

ABSTRACT

PAUL, SUJATA. First Principles Investigation of Technologically and Environmentally Important Nano-structured Materials and Devices. (Under the direction of Marco Buongiorno Nardelli).

In the course of my PhD I have worked on a broad range of problems using simulations from first principles: from catalysis and chemical reactions at surfaces and on nanostructures, characterization of carbon-based systems and devices, and surface and interface physics. My research activities focused on the application of ab-initio electronic structure techniques to the theoretical study of important aspects of the physics and chemistry of materials for energy and environmental applications and nano-electronic devices. A common theme of my research is the computational study of chemical reactions of environmentally important molecules (CO, CO₂) using high performance simulations. In particular, my principal aim was to design novel nano-structured functional catalytic surfaces and interfaces for environmentally relevant remediation and recycling reactions, with particular attention to the management of carbon dioxide.

We have studied the carbon-mediated partial sequestration and selective oxidation of carbon monoxide (CO), both in the presence and absence of hydrogen, on graphitic edges. Using first-principles calculations we have studied several reactions of CO with carbon nanostructures, where the active sites can be regenerated by the deposition of carbon decomposed from the reactant (CO) to make the reactions self-sustained. Using statistical mechanics, we have also studied the conditions under which the conversion of CO to graphene and carbon dioxide is thermodynamically favorable, both in the presence and in the absence of hydrogen. These results are a first step toward the development of processes for

the carbon-mediated partial sequestration and selective oxidation of CO in a hydrogen atmosphere.

We have elucidated the atomic scale mechanisms of activation and reduction of carbon dioxide on specifically designed catalytic surfaces via the rational manipulation of the surface properties that can be achieved by combining transition metal thin films on oxide substrates. We have analyzed the mechanisms of the molecular reactions on the class of catalytic surfaces so designed in an effort to optimize materials parameters in the search of optimal catalytic materials. All these studies are likely to bring new perspectives and substantial advancement in the field of high-performance simulations in catalysis and the characterization of nanostructures for energy and environmental applications.

Moving to novel materials for electronics applications, I have studied the structural and vibrational properties of mono and bi-layer graphene. I have characterized the lattice thermal conductivity of ideal monolayer and bi-layer graphene, demonstrating that their behavior is similar to that observed in graphite and indicating that the intra-layer coupling does not affect significantly the thermal conductance. I have also calculated the electron-phonon interaction in monolayer graphene and obtained electron scattering rates associated with all phonon modes and the intrinsic resistivity/mobility of monolayer graphene is estimated as a function of temperature.

On another project, I have worked on ab initio molecular dynamic studies of novel Phase Change Materials (PCM) for memory and 3D-integration.

We characterized high-temperature, sodium | nickel chloride, rechargeable batteries. These batteries are under consideration for hybrid drive systems in transportation applications. As part of our activities to improve performance and reliability of these batteries, we developed

an engineering transport model of the component electrochemical cell. To support that model, we have proposed a reaction kinetics expression for the REDOX (reduction-oxidation) reaction at the porous positive electrode. We validate the kinetics expression with electrochemical measurements.

A methodology based on the transistor body effect is used to estimate inversion oxide thicknesses (T_{inv}) in high- κ /metal gate, undoped, ultra-thin body SOI FINFETs. The extracted T_{inv} s are compared to independent capacitance voltage (CV) measurements.

First Principles Investigations of Technologically and Environmentally Important Nano-structured Materials and Devices

by
Sujata Paul

A dissertation submitted to the Graduate Faculty of
North Carolina State University
in partial fulfillment of the
requirements for the degree of
Doctor of Philosophy

Physics

Raleigh, North Carolina

2010

APPROVED BY:

Jerry Bernholc

Lubos Mitas

Thomas P. Pearl

Gregory Parsons

Marco Buongiorno Nardelli
Chair of Advisory Committee

DEDICATION

To Mom

BIOGRAPHY

Education

2005 -2010: PhD in Physics, Department of Physics, North Carolina State University, Raleigh, NC 27695, USA

2000 – 2003: Senior Research Fellow (SRF) at S. N. Bose National Center for Basic Sciences, Kolkata, India

1998 – 2000: MSc in Physics (Specialization: Electronics) at Kalyani University, West Bengal, India

1995 – 1998: BSc in Physics at Kalyani University, West Bengal, India

Professional Experience

May - August 2009: Summer Intern @ IBM SRDC, Albany Nanotech, Albany, NY

May - August 2008: Summer Intern @ Polymer and Chemical Technologies Division, General Electric Global Research Center, **GE**, Niskayuna, NY

May - August 2007: Summer Intern @ Physical Sciences Division, IBM T. J. Watson Research Center, **IBM**, Yorktown Heights, NY

ACKNOWLEDGMENTS

I would like to acknowledge my advisor Prof. Marco Bongiorno Nardelli for his constant support and encouragement throughout the course of my stay in North Carolina State University. I would also like to thank my committee members for taking time out of their busy schedules to critique this work.

I had an opportunity to do three industrial internships at IBM and General Electric during my tenure as a PhD student. I had the good fortune of participating in vibrant research projects at these corporate research labs in areas as diverse as Phase Change memories, electrochemistry and advanced device design for 15 nm technology nodes. For this, I'd like to acknowledge Dr. Glen J Martyna (IBM), Dr. Michael Vallance (GE), Dr. Glen Merfeld (GE) and Dr. Huiming Bu (IBM) for mentoring my progress during the summers of 2007, 2008 and 2009.

I would like to thank my parents and my husband, Kingsuk Maitra for helping me reaching my goal; friends and near ones like Nancy, Frisco, Jeff, and Cecillia made my stay at North Carolina a very memorable one. Nancy and Cecillia were always there when I needed them most.

My adopted family members at North Carolina Jill and Alan (and their siblings) offered me a home far away from home. Thank you Jill.

Finally, I'd like to thank my "unborn" baby boy for giving me an opportunity to be super excited after my graduation.

TABLE OF CONTENTS

List of Tables	x
List of Figures	xi
Chapter 1	1
1.1 <i>Introduction</i>	1
1.2 <i>Density Functional Theory (DFT)</i>	3
1.2.1 Exchange and correlation functional for DFT.....	8
1.2.2 Plane wave basis set	10
1.2.3 Pseudopotential	11
1.2.4 Computation with DFT	13
1.3 <i>Post-Processing: Tools and Capabilities</i>	16
1.4 <i>Nudged Elastic Band Method (NEB)</i>	20
1.5 <i>Density Functional Perturbation Theory (DFPT)</i>	22
1.6 <i>Ab Initio Molecular Dynamics (AIMD)</i>	25
1.7 <i>Partition Functions of Molecules and Solids (ParFuMS)</i>	28
1.8 <i>Organization of The Thesis</i>	29
<i>Figures</i>	32
<i>References</i>	37
Chapter 2: Sequestration and selective oxidation of carbon monoxide on graphene edges	40
2.1 <i>Introduction</i>	40
2.2 <i>Methods</i>	42
2.3 <i>Results and Discussion</i>	44
2.3.1 Interaction of CO with zigzag graphene edge	45

2.3.2 Interaction of CO with armchair graphene edge	48
2.3.3 Interaction of CO+H ₂ with armchair graphene edge	52
2.4 Concluding Remarks	55
Figures	57
References	68

Chapter 3: Activation of CO₂ on transition metal surfaces and oxide supported metal thin films..... 70

3.1 Introduction	70
3.2 Computational details	75
3.3 Theoretical results	78
3.3.1 Activation of CO ₂ on Pd (001)	78
3.3.2 Activation of CO ₂ on Pt (001)	81
3.3.3 Oxide Supported metal thin film	83
3.3.4 Activation of CO ₂ on 1LPd/BaO (001)	84
3.3.5 Activation of CO ₂ on 1LPt/BaO (001)	89
3.3.6 Activation of CO ₂ on 2LPd/BaO (001) and 2L Pt/BaO(001)	92
3.3.7 Activation of CO ₂ on 3LPd/BaO (001) and 3L Pt/BaO (001)	94
3.4 Conclusion	96
Tables	96
Figures	102
References	134

Chapter 4: First principles calculations of structural, vibrational properties of mono and bi-layer graphene..... 135

4.1 Introduction	135
------------------------	-----

<i>4.2 Computational Details</i>	136
<i>4.3 Band structure</i>	137
<i>4.4 Phonon dispersions</i>	139
<i>4.5 Electron phonon interaction</i>	141
<i>4.5 Conclusion</i>	142
<i>Figures</i>	143
<i>References</i>	151

Chapter 5: Ab initio molecular dynamic studies of Novel Phase

Change Materials for memory and 3D-integration 153

<i>5.1 Introduction</i>	153
<i>5.2 Methods</i>	158
<i>5.3 Liquid GST systems</i>	160
5.3.1 Liquid Ge _{0.15} Te _{0.85} : The Eutectic Alloy	160
5.3.2 Liquid GeTe	161
5.3.3 Liquid Ge ₁ Sb ₂ Te ₄	161
<i>5.4 Pressure induced transformation of Ge₂Sb₂Te₅</i>	162
<i>5.5 Pressure induced transformation of GeSb</i>	163
<i>5.6 Conclusion</i>	165
<i>Figures</i>	166
<i>References</i>	181

Chapter 6: Na / NiCl₂ Cell Positive Electrode REDOX Kinetics:

Model development and verification 183

<i>6.1 Introduction</i>	183
<i>6.2 Previous models of Sodium/metal chloride cells</i>	185
<i>6.3 The Present Kinetic Model</i>	187

6.3.1 Oxidation.....	187
6.3.2 Reduction.....	191
6.3.3 Relationship between NiCl ₂ volume fraction and passivation area density during oxidation.....	193
6.3.3.1 Homogeneous, invariant oxidation.....	194
6.3.4 Relationship between NiCl ₂ volume fraction and passivation area density during reduction.....	195
6.3.4.1 Homogeneous, Invariant Reduction.....	196
6.3.5 Verification of Kinetics Model with Smooth Electrode REDOX	197
6.3.5.1 Oxidation.....	197
6.3.5.2 Reduction.....	199
<i>6.4 Materials and Electrochemical Methods</i>	201
6.4.1 Working Electrode.....	201
6.4.2 Reference Electrode.....	202
6.4.3 Auxiliary Electrode.....	202
6.4.4 Electrolyte.....	202
6.4.5 Electrochemical characterization.....	202
<i>6.5 Results and Analysis</i>	205
6.5.1 Electrochemical Data.....	205
6.5.2 Finite Element Analysis (FEM)....	206
6.5.3 Oxidative Charge Capacity.....	210
6.5.4 Verification of Kinetic Model.....	212
<i>6.6 Conclusion</i>	214
<i>List of symbols</i>	215
<i>References</i>	219
<i>Figures</i>	221

Chapter 7: Extraction of effective oxide thickness for SOI FINFETs with high-κ/metal gates using the body effect.....	234
<i>7.1 Introduction.....</i>	<i>234</i>
<i>7.2 Theory and experiment.....</i>	<i>238</i>
<i>7.3 Discussion</i>	<i>242</i>
<i>Figures.....</i>	<i>244</i>
<i>References</i>	<i>252</i>
Chapter 8: Summary.....	254
<i>Summary</i>	<i>254</i>
<i>Figure.....</i>	<i>256</i>

LIST OF TABLES

Chapter 3: Activation of CO₂ on transition metal surfaces and oxide supported metal thin films.....	70
<i>Table 3.1 Physisorption and chemisorption binding energies of CO₂ on Pd (001) and Pt (001) surfaces.....</i>	<i>97</i>
<i>Table 3.2 Dissociation energies of CO₂ compared to different chemisorptions on Pd(001) and Pt (001) surfaces.....</i>	<i>98</i>
<i>Table 3.3 Physisorption and chemisorption binding energies of CO₂ on 1LPd/BaO (001) and 1LPt/BaO (001) surfaces.....</i>	<i>99</i>
<i>Table 3.4 Dissociation energies of CO₂ compared to different chemisorptions on 1LPd/BaO (001) and 1LPt/BaO (001) surfaces</i>	<i>100</i>
<i>Table 3.5 Energetics profile of CO₂ on surfaces: 2LPd/BaO (001), 2LPt/BaO (001), 3LPd/BaO (001) and 3LPt/BaO (001).....</i>	<i>101</i>

LIST OF FIGURES

Chapter 1: Introduction

Figure 1.1	Modeling a physical phenomenon from a broad range of perspectives, from the atomistic to the macroscopic end.....	32
Figure 1.2	Plane average and macroscopic average of 5 layer Pt (001) Surface	33
Figure 1.3	Activation energy barrier (EA), saddle point in a chemical reaction.	34
Figure 1.4	Potential energy surface, minimum energy path is depicted along with the saddle point (transition state) between reactants and products of a chemical reaction	35
Figure 1.5	Car-Parrinello Molecular Dynamics algorithm	36

Chapter 2: Sequestration and selective oxidation of carbon monoxide on graphene edges

Figure 2.1	Equilibrium energetics for a zigzag graphene edge interacting with CO molecules at high CO concentration	57
Figure 2.2	Activation energy barrier for the reaction of an oxygen atom with CO to yield CO ₂ at the zigzag graphene edge.....	58
Figure 2.3	Activation energy barrier for the reaction of an oxygen atom with CO to yield CO ₂ when the oxygen atoms are bonded to 7-5-7 carbon rings at the zigzag graphene edge	59
Figure 2.4	Activation energy barrier for the rearrangement of 7-5-7 carbon rings to 6-6-7 carbon rings at the zigzag graphene edge	60

Figure 2.5	Energetics for the interaction of an armchair graphene edge with gas phase CO molecules. Table II (inset): the reactions at different steps and the corresponding reaction energies in kcal/mol.....	61
Figure 2.6	Activation energy barrier for the reaction of an oxygen atom with CO to yield CO ₂ at the armchair graphene edge	62
Figure 2.7	Van't Hoff plot for the two main steps in the deposition of carbon on an armchair graphene edge in a CO atmosphere	63
Figure 2.8	Energetics for the competition between CO and hydrogen for the active sites on the advancing graphene edge	64
Figure 2.9	Plots of equilibrium constants vs temperature for the main reactions In Figure 2.8.....	65
Figure 2.10	Representative chemical reactions of CO and H ₂ at the armchair graphene edge involving hydroxyl and carboxyl groups.....	66
Figure 2.11	Van't Hoff plot for the reactions involving hydroxyl and carboxyl groups at the armchair graphene edge.....	67

Chapter 3: Activation of CO₂ on transition metal surfaces and oxide supported metal thin films

Figure 3.1	Adsorption geometries of CO ₂ on different sites of Pd (001) Surface	102
Figure 3.2	Relative energy diagram of “CO ₂ dissociation” of Pd (001) Surface	103
Figure 3.3	Surface LDOS of Pd (001) with adsorbed CO ₂ at different sites	104
Figure 3.4	LDOS of CO ₂ on Pd (001) surfaces.....	105
Figure 3.5	The charge density difference plot of “adsorptions of CO ₂ on Pd (001) surface”	106

Figure 3.6	Adsorption geometries of CO ₂ on different sites of Pt (001) surface.....	107
Figure 3.7	Relative energy diagram of “CO ₂ dissociation” of Pt (001) surface.....	108
Figure 3.8	Surface LDOS of Pt (001) with adsorbed CO ₂ at different sites	109
Figure 3.9	LDOS of CO ₂ on Pt (001) surfaces.....	110
Figure 3.10	The charge density difference plot of “adsorptions of CO ₂ on Pt (001) surface.....	111
Figure 3.11	Barium oxide supported metal thin films: site A is supported over O atom and Site B is supported over Ba	112
Figure 3.12	Activation of CO ₂ on 1LPd/BaO (001) surface.....	113
Figure 3.13	(a) Relative energy diagram of “CO ₂ dissociation” on 1LPd/BaO (001) surface.....	114
	(b) Optimized structures of dissociation: the energetics are given in Figure 3.13(a).....	115
Figure 3.14	Surface LDOS of 1LPd/BaO (001) with adsorbed CO ₂ at different sites.....	116
Figure 3.15	LDOS of CO ₂ on 1LPd/BaO (001)	117
Figure 3.16	Adsorption geometries of CO ₂ on different sites of Pt (001) surface.....	118
Figure 3.17	The charge density difference plot of “adsorptions of CO ₂ on 1LPd/BaO (001) surface	119
Figure 3.18	(a) Relative energy diagram of “CO ₂ dissociation” on 1LPt/BaO (001) surface.....	120
	(b) Optimized structures of dissociation: the energetics are given in Figure 3.18(a).....	121

Figure 3.19	Surface LDOS of 1LPt/BaO (001) with adsorbed CO ₂ at different sites.....	122
Figure 3.20	LDOS of CO ₂ on 1LPt/BaO (001)	123
Figure 3.21	The charge density difference plot of “adsorptions of CO ₂ on 1LPt/BaO (001) surface “	124
Figure 3.22	Barium oxide supported metal thin films.....	125
Figure 3.23	Activation of CO ₂ on 2LPd/BaO (001) surface.....	126
Figure 3.24	Activation of CO ₂ on 2LPt/BaO (001) surface.....	127
Figure 3.25	Activation of CO ₂ on 3LPd/BaO (001) surface.....	128
Figure 3.26	Activation of CO ₂ on 3LPt/BaO (001) surface.....	129
Figure 3.27	Binding energies of CO ₂ on different surfaces of Pd and Pd/BaO.	130
Figure 3.28	Binding energies of CO ₂ on different surfaces of Pt and Pt/BaO	131
Figure 3.29	Dissociation energy of CO ₂ [CO ₂ ⇌ CO + O] on different surfaces. Chemisorption energy at top site is considered as reference to calculate to dissociation energy.....	132
Figure 3.30	Dissociation of CO ₂ to CO and O atom over 2LMetal/BaO and 3LMetal/BaO. The dissociation energies are plotted in Figure 3.29.....	133

Chapter 4: First principles calculations of structural, vibrational properties of mono and bi-layer graphene

Figure 4.1	Band energy diagram of monolayer graphene along Γ KM Γ direction	143
------------	--------------------------------------------------------------------------------------	-----

Figure 4.2	Left panel: electronic band structure of bi-layer graphene in the Along $\Gamma K M \Gamma$ direction of Brillouin zone. Right panel: (a) band structure at zero gate field (b) band gap energy for the same system for an electric field with a potential energy $U=0.5$ V and (c) with potential energy $U=1.0$ V	144
Figure 4.3	Phonon dispersion of monolayer graphene along the high Symmetry direction. Following the convention, the symbol Z denotes the out of plane vibration.....	145
Figure 4.4	Left panel: phonon dispersion of bilayer graphene with A-B stacking along the high-symmetry directions. Following the convention, the symbol Z denotes the out of plane vibration; Right Panel: optical phonon dispersion near Γ and near K	146
Figure 4.5	Effect of bias on the phonon modes (at K points) of monolayer graphene.....	147
Figure 4.6	Phonon density of states for monolayer graphene	148
Figure 4.7	Electron phonon spectral (Eliashberg Function) function for monolayer graphene.....	149
Figure 4.8	Phonon linewidth for monolayer graphene	150

**Chapter 5: Ab initio molecular dynamic studies of Novel Phase Change
Materials for memory and 3D-integration**

Figure 5.1	The operation principle of a memory device based on phase changes	166
Figure 5.2	The Ge-Sb-Te ternary system. The most commonly used materials for optical recording today have been discovered in two regions in this system.....	167

Figure 5.3	Fragments of the local structure of GST around Ge atoms in the crystalline (left) and amorphous (right) state	168
Figure 5.4	Total $g(r)$ of $Ge_{0.15}Te_{0.85}$ calculated at $T=943$ K with 20ps production run (left panel) is compared with the total $g(r)$ calculated by Bichara et.al. [14] is given in the (right panel).....	169
Figure 5.5	Experimental (right) and calculated (left) total Structure factor at $T=943$ K of $Ge_{0.15}Te_{0.85}$	170
Figure 5.6	Calculated pair correlation function $g(r)$ at $T=1000$ K (left) and experimental $g(r)$ of GeTe.....	171
Figure 5.7	Calculated structure factor $S(q)$ at $T=1000$ K (left) and experimental $S(q)$ (right) of GeTe liquid	172
Figure 5.8	Calculated total pair correlation function at $T= 973$ K (left) for $Ge_1Sb_2Te_4$ in comparison to experimental $g(r)$ (right: blue curve)	173
Figure 5.9	Calculated partial pair correlation function (left) for $Ge_1Sb_2Te_4$. Partial pair correlation function calculated at $\rho = 0.0297 \text{ \AA}^3$ (black curve) in reference [19]	174
Figure 5.10	Calculated (left) and Experimental (right: blue curve) total Structure factor $S(q)$ at $T=973$ K for $Ge_1Sb_2Te_4$	175
Figure 5.11	Pressure induced transformation of $Ge_2Sb_2Te_5$: crystal to Amorphous	176
Figure 5.12	Total energy of 225 GST system with total run time of MD Simulation	177
Figure 5.13	Total structure factor calculated from the AIMD simulations and compared the result with experimental structure factor profile of crystal, liquid and amorphous $Ge_2Sb_2Te_5$	178
Figure 5.14	Schematic of a potential device based	179

Figure 5.15	A comparison of experimental and simulation structure factors for amorphous phase	180
-------------	-----------------------------------------------------------------------------------------	-----

Chapter 6: Na / NiCl₂ Cell Positive Electrode REDOX Kinetics: Model development and verification

Figure 6.1	Idealized geometry of the electrode.....	221
Figure 6.2	Cell Schematic.....	221
Figure 6.3	Chronopotentiographs for oxidation at T=300°C	222
Figure 6.4	Chronopotentiographs for oxidation at T=325°C	222
Figure 6.5	Chronopotentiographs for oxidation at T=350°C	223
Figure 6.6	Chronopotentiographs for reduction at T=300°C.....	223
Figure 6.7	Chronopotentiographs for reduction at T=325°C.....	224
Figure 6.8	Chronopotentiographs for reduction at T=350°C.....	224
Figure 6.9	FEM Model of Cell.....	225
Figure 6.10	FEM Analysis for $I = -0.009$ A and $t_{cf} = 3.82$ s. Left panel is electrolyte potential. Right panel is chloride ion concentration normalized by equilibrium concentration.	225
Figure 6.11	Chloride ion concentration predictions at T=300°C versus reduced time at current densities 3.35 (oxidation) and -3.35 (reduction) A/m ² . Terminal oxidation and reduction times were 1708.3s And 163.6 s, respectively.....	226
Figure 6.12	Effective resistance in equation 5.8.	226
Figure 6.13	ΔU corresponding to a typical discharge chronopotentiograph (300°C, -0.0005 A)	227
Figure 6.14	Maximum charge density versus nominal current density and temperature. The measurements correspond to the data in figures 6.3-6.5.....	228

Figure 6.15	Parameters for equation 5.10	229
Figure 6.16	Linear relationship between i_a ($ i_c $) and η	229
Figure 6.17	Comparison of predicted η to measurement at T=300°C.....	230
Figure 6.18	Comparison of predicted η to measurement at T=325°C.....	231
Figure 6.19	Comparison of predicted η to measurement at T=350°C.....	232
Figure 6.20	Model parameters as functions of temperature	233

Chapter 7: Extraction of effective oxide thickness for SOI FINFETs with high κ /metal gates using the body effect

Figure 7.1	(a) A bulk planar MOSFET (b) Double gate SOI (silicon on insulator) MOSFET	244
Figure 7.2	Cross section of FINFET. The fin is connected to source and drain.	244
Figure 7.3	Equivalent circuit model and TEM cross-section of fin.....	246
Figure 7.4	Upper panel: I_s - V_g sweeps for different back biases both for n and pFET, Lower panel: The close look of I_s - V_g to show the effect of VBB. Also, the IV's have been color coded to emphasize the "forward bias" regime.....	247
Figure 7.5	Evolution of threshold voltages as a function of back gate voltage. The closed symbol (square: pFET, circle: nFET) represents $ V_T $ vs back bias voltage calculated from Figure 4. Both pFET and nFET "forward bias" curves, with the different straight line fits used to extract the slopes for estimating T_{inv} 's.....	248
Figure 7.6	Representative CV sweeps for nFET and pFET.....	249
Figure 7.7	Comparison of T_{inv} s determined from back bias and CV sweeps from n and pFETs. A unity slope line illustrating the ideal case i.e $T_{INV}(IV) = T_{INV}(CV)$ is also shown.	250

Figure 7.8 Simulation study illustrating the evolution of the location of the charge centroid relative to the gate oxide/Si interface as a function of gate voltage for DC- and AC-type measurements (representative cuts are taken @ $V_g = 0.5$ & 0.9 V to illustrate the difference between the value of charge centroid for low and high gate voltages respectively under DC and AC measurement condition).....251

Chapter 8: Summary

Figure 8.1 Thesis Layout256

Chapter 1

1.1 Introduction

In this dissertation we have addressed the modeling of material properties such as structure, electronic behavior, dynamics, etc. using Density Functional Theory (DFT) as our basis. We also studied the integration with other atomistic simulation techniques, such as Molecular Dynamics (MD) and advanced applications of DFT to modern outstanding problems such as chemical reactions on catalytic surfaces.

In Figure 1.1, we have shown the multi-scale modeling a physical phenomenon from a broad range of perspectives, from the atomistic to the macroscopic end. The ab-initio methods calculate material properties from first principles, solving the quantum-mechanical Schrödinger (or Dirac) equation numerically. These methods give information on both the electronic and structural/mechanical behavior; can handle processes that involve bond breaking/formation, or electronic rearrangement (e.g. chemical reactions); can (in principle) obtain essentially exact properties without any input but the atoms conforming the system. There are some disadvantages; ab-initio methods can handle only relatively small systems and it is numerically expensive;

can only study fast processes, usually $O(10)$ ps. There are some substantial gaps exist between the dimensions of the largest systems accessible to ab-initio DFT simulations and between the maximum time span of MD simulations and the time and length scales of laboratory experiments. To bridges the gaps, strategies for multi-scale simulations are being developed over the years.

We actively worked on a broad range of problems in first principles simulations of catalysis and chemical reactions, characterization of carbon nanostructures, and surface and interface physics. The research activities were aligned on the application of ab-initio electronic structure techniques to the theoretical study of important aspects of the physics and chemistry of catalytic reactions in nano-structured media. The focus of our work is the computational study of chemical reactions of environmentally important molecules (CO , CO_2) using high performance simulations. In particular, our aim is to design novel nano-structured functional catalytic surfaces and interfaces for environmentally relevant remediation and recycling reactions, with particular attention to the management of carbon dioxide. We have also studied the electronic structure, vibrational and dynamical properties of graphene.

Moreover we have also studied the electronic structure of phase change materials (PCM) with ab-initio MD simulations.

The dissertation also contains experimental studies on two real-life systems: 1. Ni/NiCl₂ electrochemical cell; 2. ultra scaled FINFETS.

1.2 Density Functional Theory (DFT)

Density functional theory is one of the most popular and successful quantum mechanical approaches to matter. DFT has proved to be highly successful in describing structural and electronic properties in a vast class of materials, ranging from simple crystalline solids to more complex solids (including glasses and liquids) and molecules. This is a remarkable theory that allows one to replace the complicated N electron wave function $\Psi(\mathbf{r}_1, \mathbf{r}_2, \dots, \mathbf{r}_N)$ and associated Schrödinger equation by much simpler electron density. The History begins with the works of Thomas and Fermi in the 1920's. Countless modifications and improvements of the Thomas-Fermi theory have been made over the years¹. However it starts with approximations that are too crude, missing essential physics and chemistry. The situation changed in 1964 with the publication of the landmark paper by Hohenberg and Kohn². The modern formulation of DFT originated from the classic work of Kohn and Sham³. The collection of nuclei and electrons in a piece of a material is a formidable many-body problem, because of the intricate motion of the particles in the many body system.

The Hamiltonian for a system of electrons ($\{\mathbf{r}_{ij}\}$) and nuclei ($\{\mathbf{R}_{ij}\}$) is,

$$H = -\frac{\hbar^2}{2m_e} \sum_i \nabla_i^2 + \sum_{i,l} \frac{Z_l e^2}{|\mathbf{r}_i - \mathbf{R}_l|} + \frac{1}{2} \sum_{i \neq j} \frac{e^2}{|\mathbf{r}_i - \mathbf{r}_j|} - \sum_I \frac{\hbar^2}{2M_I} \nabla_I^2 + \frac{1}{2} \sum_{I \neq J} \frac{Z_I Z_J e^2}{|\mathbf{R}_I - \mathbf{R}_J|} \quad (1)$$

According to Born-Oppenheimer approximation⁴, we can drop the kinetic energy of the nuclei (4th term in eqn.(1)) due to the large difference between electron and nuclear masses. The fundamental Hamiltonian for the theory of electronic structure is,

$$H = T + V_{ext} + V_{int} + E_{II} \quad (2)$$

Where, $T = \frac{\hbar^2}{2m_e} \sum_i \nabla_i^2$ is the kinetic energy of the electrons,

$V_{ext} = \frac{1}{2} \sum_{i,l} V_l(|\mathbf{r}_i - \mathbf{R}_l|)$ is the potential acting on the electrons due to the nuclei and,

$V_{int} = \frac{1}{2} \sum_{i \neq j} \frac{e^2}{|\mathbf{r}_i - \mathbf{r}_j|}$ is the electron-electron interaction. The last term, E_{II} , is the

classical interaction of nuclei with one another, plus any other terms that contribute to the total energy of the system but are not germane to the problem of describing electrons. The systems of electrons in the external potential of atoms are described by the many body wave function, $\Psi(\mathbf{r})$. This wave function is a solution of Schrödinger equation, $H\Psi = E\Psi$. Knowing Ψ allow us to evaluate all the fundamental properties of the system. For example, a quantity of great relevance is the electron density,

$$n(\mathbf{r}) = N \int d^3\mathbf{r}_1 \dots d^3\mathbf{r}_N \psi^*(\mathbf{r}_1, \mathbf{r}_2, \dots, \mathbf{r}_N) \psi(\mathbf{r}_1, \mathbf{r}_2, \dots, \mathbf{r}_N) \quad (3)$$

The main quantity is the ground state density, which is the expectation value of H ,

$$E = \langle H \rangle = \langle T \rangle + \langle V_{\text{int}} \rangle + \int d\mathbf{r} V_{\text{ext}}(\mathbf{r}) n(\mathbf{r}) + E_{II} \quad (4)$$

The ground state wave function Ψ_0 is the state with lowest energy. This can be determined by minimizing the total energy with respect to all the parameters in $\Psi(\mathbf{r})$, with the constraints that Ψ must obey the particle symmetry and any conservation. This is the variational principle. Solving for Ψ is a formidable problem because electron-electron interactions (long range Coulomb force) induce correlations that are impossible to treat.

The approach of Hohenberg and Kohn² is to formulate DFT as an exact theory of many-body system. This is based upon two theorem: there is only one external potential $V_{\text{ext}}(\mathbf{r})$ which yield a given ground state density $n(\mathbf{r})$. The demonstration is very simple and uses a “proof by contradiction” argument². A straightforward consequences of the first HK theorem is that the ground state energy, E is also uniquely determined by the ground state density $n(\mathbf{r})$. We can write,

$$\begin{aligned} E^{(HK)}[n(\mathbf{r})] &= \langle \Psi[n] | T + V_{\text{int}} + V_{\text{ext}} | \Psi[n] \rangle = T[n(\mathbf{r})] + V_{\text{int}}[n(\mathbf{r})] + \int V_{\text{ext}}(\mathbf{r}) n(\mathbf{r}) d\mathbf{r} \\ &= F_{HK}[n] + \int V_{\text{ext}}(\mathbf{r}) n(\mathbf{r}) d\mathbf{r} \end{aligned} \quad (5)$$

The functional $F_{HK}[n(\mathbf{r})]$ is universal i.e. it is independent of the external potential $V_{\text{ext}}(\mathbf{r})$; this is good news, however it is no compensation for the fact that the

functional is not known explicitly. So it would be rather useless if not for the clever ansatz by Kohn and Sham, which provides a way to define useful approximate functional for real systems of many electrons.

The Kohn-Sham³ approach is to replace the difficult many-body system obeying the Hamiltonian in eqn.(1) with a different auxiliary system that can be solved more easily. Kohn-Sham ansatz¹ rests upon two assumptions: 1.the exact ground state density can be represented by the ground state density of an auxiliary system of non-interacting particles, i.e. the non-interacting electrons assumed to have the same density as the true interacting system. 2.The Kohn-Sham Hamiltonian is chosen to have the usual kinetic operator and an effective potential

$H_{eff}^{\sigma} = -\frac{\hbar^2}{2m_e} \nabla^2 + V^{\sigma}(\mathbf{r})$ acting on an electron of spin σ and point \mathbf{r} . The ground state

density $n(\mathbf{r})$ of the auxiliary system is,

$$n(\mathbf{r}) = \sum_{\sigma} n(\mathbf{r}, \sigma) = \sum_{\sigma} \sum_N |\Psi_i^{\sigma}|^2 \quad (6)$$

The Kohn-Sham approach to the full interacting many body problem is to write the Hohenberg-Kohn expression for the ground state energy functional (5) in the for

$$E_{KS} = T_S[n(\mathbf{r})] + E_{Hartree}[n(\mathbf{r})] + \int V_{ext}(\mathbf{r})n(\mathbf{r})d\mathbf{r} + E_{xc}[n(\mathbf{r})] \quad (7)$$

Where first term is the kinetic energy of non-interacting electrons,

$$T_S[n] = \sum_{\sigma,N} \left\langle \Psi_i^\sigma \left| -\frac{\hbar^2}{2m_e} \nabla^2 \right| \Psi_i^\sigma \right\rangle = -\frac{\hbar^2}{2m_e} \sum_{\sigma,N} |\nabla \Psi_i^\sigma|^2 \quad (8)$$

The second term (called the Hartree energy¹) contains the electrostatic interactions between clouds of charge,

$$E_{Hartree} = \frac{1}{2} \int d\mathbf{r}^3 d\mathbf{r}'^3 \frac{n(\mathbf{r})n(\mathbf{r}')}{|\mathbf{r} - \mathbf{r}'|} \quad (9)$$

The third term, called the *exchange-correlation energy*. All the many body effects of exchange and correlation are grouped into this term. So far the theory is still exact, provided we can find an “exact” expression for exchange and correlation term. Solution of the Kohn-Sham auxiliary system for the ground state¹ can be found by minimizing with respect to the independent electron wave function $\Psi_i(\mathbf{r})$,

$$\frac{\delta E_{KS}}{\delta \Psi_i^{\sigma*}(\mathbf{r})} = \frac{\delta T_S}{\delta \Psi_i^{\sigma*}(\mathbf{r})} + \frac{\delta [E_{ext} + E_{Hartree} + E_{xc}]}{\delta n(\mathbf{r}, \sigma)} \frac{\delta n(\mathbf{r}, \sigma)}{\delta \Psi_i^{\sigma*}(\mathbf{r})} = 0 \quad (10)$$

$$\text{with, } \langle \Psi_i^\sigma | \Psi_i^\sigma \rangle = \delta_{i,j} \delta_{\sigma,\sigma'}$$

The Lagrange multiplier method leads to the Kohn-Sham Schrödinger-like equation

$$(H_{KS}^\sigma - \varepsilon_i^\sigma) \Psi_i^\sigma(\mathbf{r}) = 0 \quad (11)$$

where ε_i are the eigenvalues and H_{KS} is the effective Hamiltonian

$$H_{KS}^\sigma(\mathbf{r}) = -\frac{\hbar^2}{2m_e} \nabla^2 + V_{KS}^\sigma(\mathbf{r}) \quad (12)$$

We notice that the KS equations are standard differential equations with effective potential ; any difficulty in the procedure has been confined to a reasonable guess of the exchange correlation function.

1.2.1 Exchange and correlation functional for DFT

The exact form of the exchange and correlation energy $E_{xc}[n(\mathbf{r})]$ for which Kohn and Sham equations would give exactly the same ground state answer, as the many body Schrödinger equation is not known and approximations must be used.

In the local density approximation (LDA), the local exchange-correlation energy density is taken to be the same as in a uniform electron gas of the same density^{5,6}.

LDA has turned out to be much more successful than expected. It yields results in atoms, molecules and even highly inhomogeneous systems for which an approximations based on the homogeneous electron gas would hardly look appropriate. Structural and vibrational properties of solids are in general accurately describe: the correct crystal structure is usually found to have the lowest energy, bond length, bulk moduli and phonon frequencies are accurate within few percent.

LDA also has some well known drawbacks. LDA grossly underestimate (~50%) band

gaps in insulators. LDA tends to badly overestimates (~20% and more) cohesive energies in molecules and solids. As a general rule, LDA tends to over-bind. This has some interesting consequences in systems bound by van der Waals (dispersive) forces. The van der Waals interaction is absent from LDA by construction: it is due to charge fluctuations, not to charge overlap.

LDA however overestimates the attractive potential coming from the overlap of the tails of the charge density, thus yielding apparently good results for the binding energy (but wrong dependence on the separation distance, of course), for the wrong reason. In finite systems the presence of self interaction (the interaction of an electron with the field it generates) is reflected in an incorrect long range behavior of the potential felt by an electron. For an atom, we should have $V_{xc}(\mathbf{r}) \rightarrow -1/r$ for $\mathbf{r} \rightarrow \infty$, but LDA yields instead a potential that decays exponentially.

The generalized gradient approximation (GGA) introduces a dependence of E_{xc} on the local gradient of the electron density $|\nabla n(r)|$. Many different forms of GGA functionals are available in literature¹, but for material simulations, it is good practice to use parameter-free functional derived from known expansion coefficients and sum rules of many body theory^{7,8} and to avoid empirical parameterizations popular in

molecular quantum chemistry⁹. LDA and GGA are by far the most commonly used functionals today. Quite generally, GGA calculations represent a systematic improvements, compared with the LDA. The study of reasons for the good performance and failures of LDA and GGA, as well as search for better functionals, is still a very active field.

1.2.2 Plane wave basis set

The effective one-electron Kohn-Sham equations are practically nonlinear partial differential equations that are iteratively solved by representing the electronic wave functions by a linear combination of a set of basis functions. Basis sets falls into two classes: plane-wave (PW) basis sets and local basis sets. Basis set convergence is crucial for the accuracy of the calculations, in particular for the prediction of pressure, stresses and forces.

In the following we will assume that our system is a crystal with lattice vectors \mathbf{R} and reciprocal lattice vectors \mathbf{G} . It is not relevant whether the cell is a real unit cell or real periodic crystal or it is a supercell describing an aperiodic system. The Kohn-Sham wave functions are classified by a band index and a Bloch vector \mathbf{k} in the Brillouin Zone (BZ). A PW basis set is defined as

$$\langle \mathbf{r} | \mathbf{k} + \mathbf{G} \rangle = \frac{1}{V} e^{i(\mathbf{k} + \mathbf{G}) \cdot \mathbf{r}}, \frac{\hbar^2}{2m} |\mathbf{k} + \mathbf{G}|^2 \leq E_{cut} \quad (13)$$

where V is the crystal volume, E_{cut} is a cutoff on the kinetic energy of PW's. PW's have many attractive features: they are simple to use (matrix elements of the Hamiltonian have very simple form), orthonormal by construction, unbiased (there is no freedom in choosing PW's, the basis is fixed by the crystal structure and by the energy cutoff) and it is very simple to check for convergence (by increasing the cutoff). Unfortunately the extended character of PW's makes it very difficult to accurately reproduce localized functionals such as the charge density around a nucleus or even worse, the orthogonalization wiggles of inner (core) states.

1.2.3 Pseudopotential

Core states prevent the use of the PW's. However they don't contribute in a significant manner to chemical bonding and to solid-state properties. Only outer electrons (valence) do, while core electrons are "frozen" in their atomic states. This suggests that one can safely ignore changes in core states (frozen core approximations)¹⁰. The idea of replacing the full atom with a much simpler pseudoatom with valence electrons only arises naturally. In plane-wave calculations, the electron-ion interactions must be described by pseudopotential¹¹, eliminating the need of an explicit treatment of the strongly bound and chemically inert electrons. The theory of pseudopotential is mature, but the practice of constructing transferable and efficient pseudopotentials is far from straightforward. Methods for generating

pseudopotentials by Troullier and Martins¹² (conserving the norm of the wave function) and the ultrasoft pseudopotentials introduced by Vanderbilt¹³ (which have the merit of making calculations for *d* and *f* electron metals feasible at an acceptable computational core). The Norm-conserving pseudopotentials are atomic potentials which are devised so as to mimic the scattering properties of the true atom. For a given reference atomic configurations, a norm-conserving pseudopotentials must fulfill the following condition: (1) all-electron and pseudo-wavefunctions must have the same energy and (2) they must be the same beyond a given “core-radius” r_c , which is usually located around the outermost maximum of the atomic wave function; (3) the pseudo charge and the true charge contained in the region $r < r_c$, must be the same¹¹. More complex Ultrasoft pseudopotentials have been devised are much softer than ordinary norm-conserving pseudopotentials, at the price of a considerable additional complexity.

The criterion for the quality of a pseudopotential is not how well the calculation matches experiments, but how well it reproduces the result of accurate all-electron calculations. A certain drawback of pseudopotential calculations is that because of the nonlinearity of the exchange interaction between valence and core electrons, elaborate nonlinear core corrections are required in all systems where the overlap between the valence and core electrons densities is not completely negligible. All mature codes provide extensive database of well-tested pseudopotentials⁹.

1.2.4 Computation with DFT

A variety of mature DFT codes are available nowadays to the community¹⁵. Some of them are accessible through general public licenses, whereas others are proprietary. The codes are based on different choices of basis sets, potentials, exchange-correlation functionals and algorithm for solving the Schrödinger equation. We primarily used QUANTUM ESPRESSO¹⁹ for the understanding of the nano-structured materials in this thesis. Quantum Espresso/PWSCF, is an integrated consortium of computer codes for electronic-structure calculations and materials modeling based on density-functional theory, plane waves basis sets and pseudopotentials to represent electron-ion interactions. This is free, open-source software distributed under the terms of the GNU General Public License (GPL) [<http://www.gnu.org/licenses/>]. The basic computations/simulations that can be performed using PWSCF include¹⁴:

- calculation of the Kohn–Sham (KS) orbitals and energies for isolated or extended/periodic systems, and of their ground-state energies;
- complete structural optimizations of the microscopic (atomic coordinates) and macroscopic (unit cell) degrees of freedom, using Hellmann–Feynman forces and stresses;
- ground state of magnetic or spin-polarized systems, including spin–orbit coupling

and noncollinear magnetism;

- ab initio molecular dynamics (MD), using either the Car–Parrinello Lagrangian or the Hellmann–Feynman forces calculated on the Born–Oppenheimer (BO) surface, in a variety of thermodynamical ensembles, including NPT variable-cell MD;
- density-functional perturbation theory (DFPT), to calculate second and third derivatives of the total energy at any arbitrary wavelength, providing phonon dispersions, electron–phonon and phonon–phonon interactions, and static response functions (dielectric tensors, Born effective charges, infrared spectra, Raman tensors). We will discuss this in details in section 1.5;
- location of saddle points and transition states via transition-path optimization using the nudged elastic band (NEB) method. We will come back to this part of the discussion in section 1.4;
- ballistic conductance within the Landauer–Büttiker theory using the scattering approach;
- generation of maximally localized Wannier functions and related quantities;
- calculation of nuclear magnetic resonance (NMR) and electronic paramagnetic resonance (EPR) parameters;
- calculation of K-edge x-ray absorption spectra.

There are more advanced and specialized tools and capabilities are implemented in the PWSCF software package, which are described in section 1.3.

The atomic arrangement in perfect crystal is described by a periodically repeated

unit cell. For many interesting physical systems, however, perfect periodicity is absent, but the system is either approximately periodic or periodic in one or two directions or periodic except for a small part. Examples of such systems include surfaces, point defects in crystals, substitutional alloys, heterostructures (superlattices and quantum well). In all such cases it is convenient to simulate the system with a periodically repeated fictitious supercell. The form and the size of the supercell depend on the physical system being studied. The study of point defects requires that a defect does not interact with its periodic replica in order to accurately simulate a truly isolated defect. For disordered solids, the supercell must be large enough to guarantee a significant sampling of the configuration space. For surfaces, one uses a crystal slab alternated with a slab of empty space, both large enough to ensure that the bulk behavior is recovered inside the crystal slab and that the surface behavior is unaffected by the presence of the periodic replica of the crystal slab. Even finite systems (molecules, clusters) can be studied using supercells. Enough empty space between the periodic replicas of the finite system must be left so that the interactions between them are weak. The molecule has to be put in a big unit cell, making sure the separation is big enough to avoid the artificial interactions. The use of supercells for the simulation of molecular or completely aperiodic systems (liquids, amorphous systems) has become quite common in recent years, in connection with first principles simulations (especially molecular dynamics simulations) using a Plane Wave basis set.

1.3 Post-Processing: Tools and Capabilities

For many applications in condensed matter science, the availability of a basic code for solving Schrödinger equation is not sufficient; the resulting energies, wave functions and electron (spin) densities are merely the starting point for the calculations of many different materials properties. Much current code development¹⁴ is focused on the routines for the post-processing of DFT results to yield a comprehensive description of materials. There are a number of auxiliary codes performing post-processing tasks such as plotting, averaging, and so on, on the various quantities are implemented in Quantum Espresso as well as in other advanced ab-initio electronic structure calculation codes¹⁵.

The main post-processing code (pp.x) in Quantum Espresso reads data file(s), extracts or calculates the selected quantity, writes it into a format that is suitable for plotting. Quantities that can be read or calculated are: charge density, spin polarization, various potentials, local density of states at Fermi level (E_F), local density of electronic entropy, STM (Scanning Tunneling Microscope) images¹⁶, selected squared wave function, ELF (electron localization function)¹⁷, planar averages an integrated local density of states etc. Various types of plotting (along a line, on a plane, three-dimensional, polar) and output formats (including the popular

cube format) can be specified. The output files can be directly read by the free plotting system Gnuplot¹⁸ (1D or 2D plots), or by code (plotrho.x) that comes with PWscf¹⁹ (2D plots), or by advanced plotting software XCrySDen²⁰, VMD²¹ and gOpenMol²² (3D plots).

The code (bands.x) reads data file(s), extracts eigenvalues, regroups them into bands (the algorithm used to order bands and to resolve crossings may not work in all circumstances, though). The output is written to a file in a simple format that can be directly read by plotting program (plotband.x). Unpredictable plots may result if k-points are not in sequence along lines.

The calculation of Fermi surface can be performed using the codes (kvecs_FS.x) and (bands_FS.x). The resulting file is in “xsf” format which can be read and plotted using Xcrysden²⁰. There are examples available for these calculations in PWSCF software package.

The code (projwfc.x) calculates projections of wave functions over atomic orbitals. The atomic wavefunctions are those contained in the pseudopotential file(s). The Löwdin population analysis²³ (similar to Mulliken analysis) is presently implemented. The projected DOS (or PDOS: the DOS projected onto atomic orbitals) can also be calculated and written to file(s). The auxiliary code (sumpdos.x) can be used to sum selected PDOS, by specifying the names of files containing the desired PDOS. Charge density difference [$\Delta\rho = \rho(\text{Adsorbate+Surface}) - \rho(\text{Surface}) - \rho(\text{Adsorbate})$]

can be used to explain charge transfer and bonding characteristic at the atomistic level (i.e. a molecule on a surface). A difference plot can be obtained by subtracting from a total system (e.g. an adsorbate on surface) the densities of each isolated system (e.g., the adsorbate, clean surface), keeping the atomic position same.

The work function W is defined as the minimum energy necessary to extract an electron from the metal surface. This definition calls for zero temperature and a perfect vacuum, since it is assumed that the metal is in its ground state, both before and after the electron removal²⁴. For a crystal with N electrons, if E_N is the initial energy of the metal and E_{N-1} that of the metal with one electron removed to a region of electrostatic potential V_e , we define

$$W = (E_{N-1} - V_e) - E_N \quad (14)$$

The removed electron is assumed to be at rest, and therefore possesses only potential energy. At zero temperature, the chemical potential μ by definition, $\mu = E_N - E_{N-1}$. In the limit of large systems, the chemical potential is shown to coincide with the Fermi energy E_F ²⁵. The work function, finally, is the difference between the Fermi level and the vacuum level.

$$W = V_e - E_F \quad (15)$$

The vacuum level is defined as the electrostatic potential outside the metal surface. Therefore, the calculation of work function is separated into two parts. One is to calculate the Fermi energy E_F of the slab, which can be done through self-consistent

calculation. The other part is the potential energy at the vacuum level. It is found by the macroscopic technique²⁶.

The electronic density $n(\mathbf{r})$ is the basic variable calculated by the PWScf code¹⁹ based on the DFT. We first introduce the plane-averaged electronic density,

$$\bar{n}(z) = \frac{1}{S} \int_S n(\mathbf{r}) dx dy \quad (16)$$

where z axis is chosen perpendicular to the slab surface S. The macroscopic-average electronic density $\bar{\bar{n}}(z)$ is then defined from the plane-averaged density by integration over the inter-planar distance d of the slab²⁶:

$$\bar{\bar{n}}(z) = \frac{1}{d} \int_{-\frac{d}{2}}^{+\frac{d}{2}} \bar{n}(z + z') dz' \quad (17)$$

The electrostatic potential $V_e(\mathbf{r})$ is related to the total charge density, including the ionic charge contribution, via the Poisson equation. Since these operations are linear, the plane-averaged potential $\bar{V}_e(z)$ is related to its macroscopic average $\bar{\bar{V}}_e(z)$ by a relation similar to above equation (17):

$$\bar{\bar{V}}_e(z) = \frac{1}{d} \int_{-\frac{d}{2}}^{+\frac{d}{2}} \bar{V}_e(z + z') dz' \quad (18)$$

By plotting the macroscopic average over the z-axis, the vacuum level is found. This is because the curve of the average potential is nearly flat in the vacuum provided

the vacuum is large enough. Subtracting this vacuum level from the Fermi level, we can find the value of work function for the metal surface.

The code (average.x) calculates planar and macroscopic averages of a quantity defined on a 3D-FFT mesh. The planar average is done on FFT mesh planes. It reads the quantity to average, or several quantities, from one or several files and adds them with the given weights. It computes the planar average of the resulting quantity averaging on planes defined by the FFT mesh points and by one direction perpendicular to the planes. The planar average can be interpolated on a 1D-mesh with an arbitrary number of points. Finally, it computes the macroscopic average. The size of the averaging window is given as input. In Figure 1.2, we have shown the plane average and macroscopic average of the electrostatic potential in the unit cell, as a function of the z-axis of the unit cell of five layer Pt (001) surface. The vacuum level was taken as the potential at the cell boundary. The work function of Pt (001) is 6.04 eV.

1.4 Nudged Elastic Band Method (NEB)

Calculation of transition states is an important problem in theoretical chemistry and condensed matter physics. The transition state of a chemical reaction is a particular configuration along the reaction coordinate. It is defined as the state corresponding to the highest energy along this reaction coordinate. Assuming a perfectly

irreversible reaction, colliding reactant molecules will always go on to form products. The Potential Energy Surface (PES) in a chemical reaction comes from the fact that the total energy of an atom arrangement can be represented as a curve or (multidimensional) surface, with atomic positions as variables. The identification of a lowest energy path on the PES for a rearrangement of a group of atoms from one stable configuration to another is important in chemical reactions. Such a path is often referred to as the Minimum Energy Path (MEP). The goal is locating all the relevant saddle points (Transition state) on the MEP, but saddle points are unstable and their direct location is rather a difficult task. The potential energy maximum along the MEP is the saddle point energy, which gives the activation energy barrier (as it is depicted in Figure 1.3), a quantity of central importance for estimating the transition rate within harmonic transition state theory²⁷. In Figure 1.4 we have shown the Mueller potential energy surfaces and the saddle point on the MEP between reactants and products in a chemical reaction.

Many different methods have been presented for finding reaction paths and saddle points²⁸. The Nudged Elastic Band (NEB) method²⁹ is used to find reaction pathways when both the initial and final states are known. Using this method MEP for any given chemical process may be calculated, however both the initial and final states must be known. The NEB is implemented in the Quantum Espresso package¹⁹. The code works by linearly interpolating a set of images between the known initial and final states (as a "guess" at the MEP), and then minimizes the energy of this string of

images. Each "image" corresponds to a specific geometry of the atoms on their way from the initial to the final state, a snapshot along the reaction path. Thus, once the energy of this string of images has been minimized, the true MEP is revealed. The subsequent images of the chain are connected by springs and each image feels the forces due to external potential and the springs. The elastic forces are projected along the path and external forces are projected orthogonally to the path. With this code, it is possible to calculate not only the MEP for the reaction but also the transition state (TS) configuration at the saddle point. The climbing image (CI) NEB method³⁰ has one modification, which drives the image with the highest energy up to the saddle point. This CI gives better resolution around the saddle point.

1.5 Density Functional Perturbation Theory (DFPT)

The calculation of vibrational properties of materials from their electronic structure is an important goal for materials modeling. A wide variety of physical properties of materials depend on their lattice dynamical behavior: specific heats, thermal expansion, heat conduction, phenomena related to the electron-phonon interaction such as resistivity of metals, superconductivity and temperature dependence of optical spectra are just a few of them. Vibrational frequencies can be measured accurately using infrared, Raman spectroscopy and inelastic neutron scattering.

Accurate calculations of frequencies and displacement patterns yield a lot of information on atomic and electronic structure of materials.

Density functional perturbation theory (DFPT) is a particularly powerful and flexible theoretical technique that allows calculation of such properties within the density functional framework^{31,32}. System responses to external perturbations can be calculated using DFT with the addition of some perturbing potential.

In this thesis we concentrated the calculations of phonon frequencies and electron-phonon interactions and related physical properties of different systems. We now consider the application of perturbation theory to DFT, and use this formalism to derive equations of phonons in crystalline materials. Using DFPT we can calculate phonon dispersions and Inter-atomic Force Constants (IFC) in a crystalline solid. Once the unperturbed ground state is determined (using equation 11), the phonon frequencies can be determined from the IFC i.e. the second derivative of the total crystal energy at equilibrium w.r.t. the displacements of the ions^{31,33}.

$$C_{\alpha i, \beta j}(\mathbf{R} - \mathbf{R}') = \left. \frac{\partial^2 E}{\partial u_{\alpha i}(\mathbf{R}) \partial u_{\beta j}(\mathbf{R}')} \right|_{Equil} \quad (19)$$

Here $\mathbf{R}(\mathbf{R}')$ is a Bravais Lattice vector, $i(j)$ indicates the i th (j th) atom of the unit cell and $\alpha(\beta)$ represents the Cartesian components.

Linear response theory allows us to calculate the response to any periodic

perturbation; i.e., it allows direct access to the dynamical matrix related to the IFC via a Fourier transform,

$$\tilde{D}_{\alpha i, \beta j} = \frac{1}{\sqrt{M_i M_j}} \sum_{\mathbf{R}} C_{\alpha i, \beta j}(\mathbf{R}) e^{-i\mathbf{q} \cdot \mathbf{R}} \quad (20)$$

where, M_i is the mass of the i th atom. Phonon frequencies at any \mathbf{q} are the solutions of the eigenvalue problem

$$\omega^2(\mathbf{q}) u_{\alpha i}(\mathbf{q}) = \sum_{\beta j} u_{\beta j}(\mathbf{q}) \tilde{D}_{\alpha i, \beta j}(\mathbf{q}) \quad (21)$$

Finally, the dynamical matrix and the phonon frequencies at any \mathbf{q} point can be obtained by Fourier interpolation of the real-space IFC. The IFC is related to the forces. The forces \mathbf{F}_I can be calculated by Hellmann-Feynmann theorem³⁶,

$$\mathbf{F}_I = -\frac{\partial E(\{\mathbf{R}\})}{\partial \mathbf{R}_I} = -\left\langle \Psi_{\{\mathbf{R}\}} \left| \frac{\partial H_{\{\mathbf{R}\}}}{\partial \mathbf{R}} \right| \Psi_{\{\mathbf{R}\}} \right\rangle = -\int n(\mathbf{r}) \frac{\partial V_I(\mathbf{r} - \mathbf{R}_I)}{\partial \mathbf{R}_I} - \frac{\partial E_N(\{\mathbf{R}_I\})}{\partial \mathbf{R}_I} \quad (22)$$

$$\text{So, } C_{\alpha i, \beta j}(\mathbf{R} - \mathbf{R}') = \frac{\partial^2 E}{\partial \mathbf{R}_I^\alpha \partial \mathbf{R}_J^\beta} = -\frac{\partial F^{\alpha}_I}{\partial \mathbf{R}^\beta_J} \quad (23)$$

The calculation of the IFC thus requires the knowledge of the ground state charge density, $n(\mathbf{r})$ as well as linear response to a distortion of the nuclear geometry. For a detailed and complete description of DFPT please see the reference [31].

The Electron-phonon interaction (EPI) is a subject of intensive theoretical and experimental investigations. For a quantitative understanding of physical phenomena such as electrical and thermal resistivity, transport, superconductivity

etc., a proper description of EPI is required. There are lots of developed scheme to compute EPI for a large number of systems specially metals. In the framework of the density-functional linear-response method, the electron-phonon matrix element is defined as³⁴

$$g_{\mathbf{k}+\mathbf{q}j',\mathbf{k}j}^{qv} = \langle \mathbf{k} + \mathbf{q}j' | \delta^{qv} V_{eff} | \mathbf{k}j \rangle \quad (24)$$

The electron-phonon spectral distribution functions $\alpha^2 F(\omega)$, in terms of linewidth γ_{qv} ,

$$\alpha^2 F(\omega) = \frac{1}{2\pi N(\epsilon_F)} \sum_{qv} \frac{\gamma_{qv}}{\omega_{qv}} \delta(\omega - \omega_{qv}) \quad (25)$$

where $N(\epsilon_F)$ is the electronic density of state per atom per spin at the Fermi level. The linewidth is given by the Fermi “golden rule” and this is related to electron-phonon matrix element

$$\gamma_{qv} = 2\pi\omega_{qv} \sum_{\mathbf{k}j'} |g_{\mathbf{k}+\mathbf{q}j',\mathbf{k}j}^{qv}|^2 \delta(\epsilon_{\mathbf{k}j} - \epsilon_F) \delta(\epsilon_{\mathbf{k}+\mathbf{q}j'} - \epsilon_F) \quad (26)$$

We would like to discuss the importance of these equations in Chapter 4 in detail.

1.6 Ab Initio Molecular Dynamics (AIMD)

In classical molecular dynamics, a single potential energy surface (usually the ground state) is represented in the force field. This is a consequence of the Born-Oppenheimer approximation. Under these assumptions, the dynamical behavior of

ions can be described by a classical Lagrangian

$$L = \frac{1}{2} \sum_i M_i \dot{\mathbf{R}}_i^2 - E_{tot}(\{\mathbf{R}\}) \quad (27)$$

where, M_i is the mass of the ions. The corresponding equations of motion are Newton's equations:

$$\frac{d}{dt} \frac{\partial L}{\partial \dot{\mathbf{R}}_i} - \frac{\partial L}{\partial \mathbf{R}_i} = 0, \mathbf{P}_i = \frac{\partial L}{\partial \dot{\mathbf{R}}_i} \quad (28)$$

If excited states, chemical reactions or a more accurate representation is needed, electronic behavior can be obtained from first principles by using a quantum mechanical method, such as DFT. This is known as ab Initio Molecular Dynamics (AIMD). Due to the cost of treating the electronic degrees of freedom, the computational cost of these simulations is much higher than classical molecular dynamics. This implies that AIMD is limited to smaller systems and shorter period of time. Ab-initio quantum-mechanical methods may be used to calculate the potential energy of a system on the fly, as needed for conformations in a trajectory. This calculation is usually made in the close neighborhood of the reaction coordinate. Although various approximations may be used, these are based on theoretical considerations, not on empirical fitting. Ab-Initio calculations produce a vast amount of information that is not available from empirical methods, such as density of electronic states or other electronic properties. A significant advantage of using ab-initio methods is the ability to study reactions that involve breaking or formation of covalent bonds, which correspond to multiple electronic states.

The AIMD simulation studies presented in this thesis were performed using the Car-Parrinello method³⁵. A finite basis set of plane-waves is employed to expand the Kohn-Sham orbitals of Kohn-Sham Density Functional Theory (KS-DFT)³. Car and Parrinello introduced a Lagrangian for both electronic and ionic degrees of freedom,

$$L = \frac{\mu}{2} \sum_k dr |\dot{\psi}_k(\mathbf{r})|^2 + \frac{1}{2} \sum_i M_i \dot{\mathbf{R}}_i^2 - E_{tot}(\{\mathbf{R}\}, \{\psi\}) + \sum_{k,l} \Lambda_{kl} \left(\int \psi_k^*(\mathbf{r}) \psi_l(\mathbf{r}) - \delta_{kl} \right) \quad (29)$$

which generates the following set of equations of motion,

$$\mu \ddot{\psi}_k = H \psi_k - \sum_l \Lambda_{kl} \psi_l, M_i \ddot{\mathbf{R}}_i = - \frac{\partial E_{tot}}{\partial \mathbf{R}_i} \quad (30)$$

where μ is a fictitious mass and the Lagrangian multipliers Λ_{kl} enforce orthonormality constraints. The forces acting on ions have the Hellmann-Feynmann³⁶ form:

$$F_i = - \frac{\partial E_{tot}}{\partial \mathbf{R}_i} = - \sum_k \langle \psi_k | \frac{\partial V}{\partial \mathbf{R}_i} | \psi_k \rangle \quad (31)$$

where V is the electron-ion interaction (pseudo-)potential. Highly simplified description of the molecular dynamics simulation algorithm is depicted in Figure 1.5.

The Car-Parrinello dynamics has turned out to be very successful especially in the study of low symmetry situations: surfaces, clusters, liquids, disordered materials and for the study of chemical reactions.

1.7 Partition Functions of Molecules and Solids (ParFuMS)

Calculating macroscopic properties of materials from first principles or ab-initio computations is one of the foremost goals of computational materials science. Apart from detailed information about electronic structure, the typical output of DFT calculations is the forces acting on the nuclei for a given atomic configurations. A stable atomic configuration corresponds to a minimum of the PES (as it is described in section 1.4). The forces acting on a given configuration are just the local gradient of the PES and the vibrational modes of a (local) minimum are given by the PES curvature around it. The goal of the thermodynamic approach is to use the data from electronic structure theory, i.e. the information on the PES, to calculate appropriate thermodynamic potential functions like Gibbs free energy (G). We can also calculate the partition function of systems considering the vibrational modes. Once such a quantity is known, one is immediately in the position to evaluate macroscopic system properties.

In particular, for a chemical reaction, we want to know the chemical equilibrium (What are the possible reaction products and thermodynamic properties of the reactants and products) and Kinetics (what is (are) the reaction mechanism(s) involved, Rates of these processes etc). In most cases, equilibrium is defined in terms of equilibrium constants³⁷:

$$\sum_{i=1}^c \nu_i \mu_i = 0 \Rightarrow \prod_{i=1}^c a_i^{\nu_i} = \exp\left(-\frac{\Delta G^0}{kT}\right) \equiv K_{eq} \quad (32)$$

where, ν_i = stoichiometric coefficient, μ_i = chemical potential, a_i = activity

K_{eq} is the equilibrium constant and ΔG° is the Gibbs free energy of reaction. A chemical reaction is called endothermic when $\Delta G^\circ > 0$ and exothermic when $\Delta G^\circ < 0$. A direct consequence of the important equation (32) is the van't Hoff equation, which relates the change in temperature to the equilibrium constant. In chapter 2, we have considered several chemical reactions where we calculated these thermodynamic properties.

1.8 Organization of The Thesis

The dissertation is organized as follows:

In chapter 1, we have discussed an overview of the ab initio methods and techniques, which is used in this thesis.

In chapter 2, we have studied the carbon-mediated partial sequestration and selective oxidation of carbon monoxide (CO), both in the presence and absence of hydrogen, on graphitic edges. Using first-principles calculations we have studied several reactions of CO with carbon nanostructures, where the active sites can be regenerated by the deposition of carbon decomposed from the reactant (CO) to make the reactions self-sustained. Using statistical mechanics, we have also studied

the conditions under which the conversion of CO to graphene and carbon dioxide is thermodynamically favorable, both in the presence and in the absence of hydrogen. These results are a first step toward the development of processes for the carbon-mediated partial sequestration and selective oxidation of CO in a hydrogen atmosphere.

In chapter 3, we have elucidated the atomic scale mechanisms of activation and reduction of carbon dioxide on specifically designed catalytic surfaces via the rational manipulation of the surface properties that can be achieved by combining transition metal thin films on oxide substrates. We have analyzed the mechanisms of the molecular reactions on the class of catalytic surfaces so designed in an effort to optimize materials parameters in the search of optimal catalytic materials. All these studies are likely to bring new perspectives and substantial advancement in the field of high-performance simulations in catalysis and the characterization of nanostructures for energy and environmental applications.

In chapter 4, we have studied the first principles calculations of structural, vibrational properties of mono and bi-layer graphene. We have shown the characterization of the lattice thermal conductivity of ideal monolayer and bi-layer graphene demonstrating that their behavior is similar to that observed in graphite, indicating that the intra-layer coupling does not affect significantly the thermal conductance.

We have also calculated the electron-phonon interaction in monolayer graphene and obtained electron scattering rates associated with all phonon modes and the

intrinsic resistivity/mobility of monolayer graphene is estimated as a function of temperature.

In chapter 5, we have worked on ab initio molecular dynamic studies of novel Phase Change Materials (PCM) for memory and 3D-integration. This project involved high-end numerical computation in IBM's internal "Blue-Gene" cluster and Oak Ridge National Laboratories (ORNL) supercomputing resources.

In chapter 6, we characterized high-temperature, sodium | nickel chloride, rechargeable batteries. These batteries are under consideration for hybrid drive systems in transportation applications. As part of our activities to improve performance and reliability of these batteries, we developed an engineering transport model of the component electrochemical cell. To support that model, we have proposed a reaction kinetics expression for the REDOX (reduction-oxidation) reaction at the porous positive electrode. In this chapter we validate the kinetics expression with electrochemical measurements.

In chapter 7, a methodology based on the transistor body effect is used to estimate inversion oxide thicknesses (T_{inv}) in high- κ /metal gate, undoped, ultra-thin body SOI FINFETs. The extracted T_{inv} s are compared to independent capacitance voltage (CV) measurements. Simulation studies are also conducted to understand the differences in T_{inv} values extracted using the two techniques.

In chapter 8, we would like to conclude the dissertation.

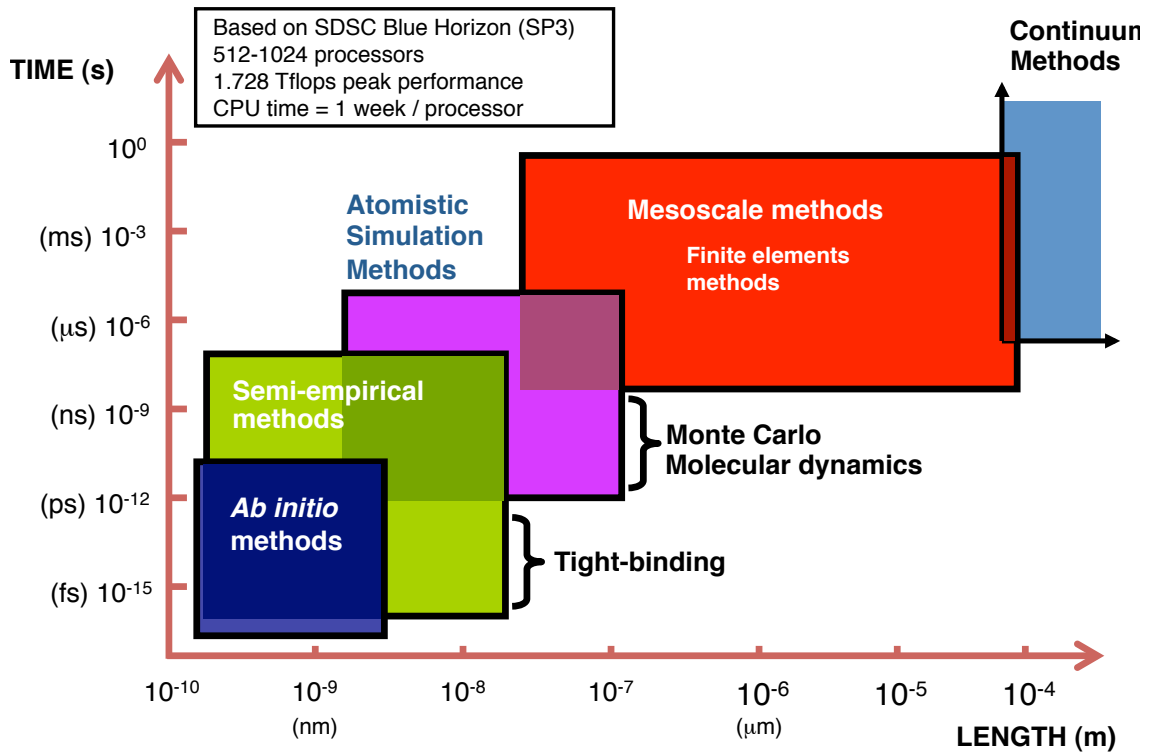


Figure 1.1. Modeling a physical phenomenon from a broad range of perspectives, from the atomistic to the macroscopic end.

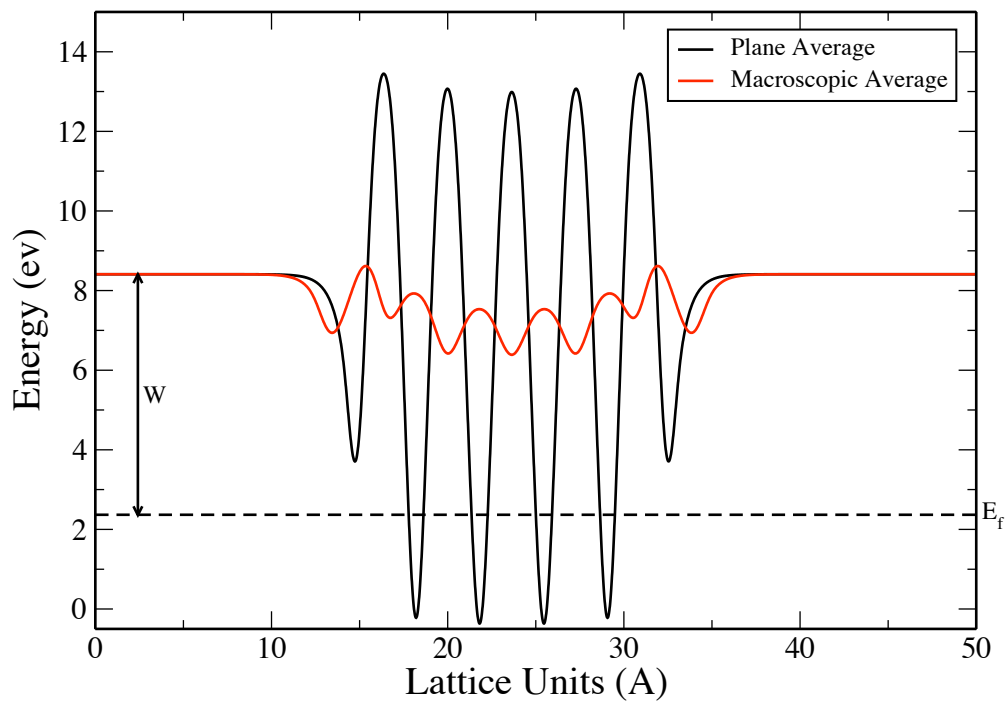


Figure 1.2. Plane average and macroscopic average of 5 layer Pt (001) surface.

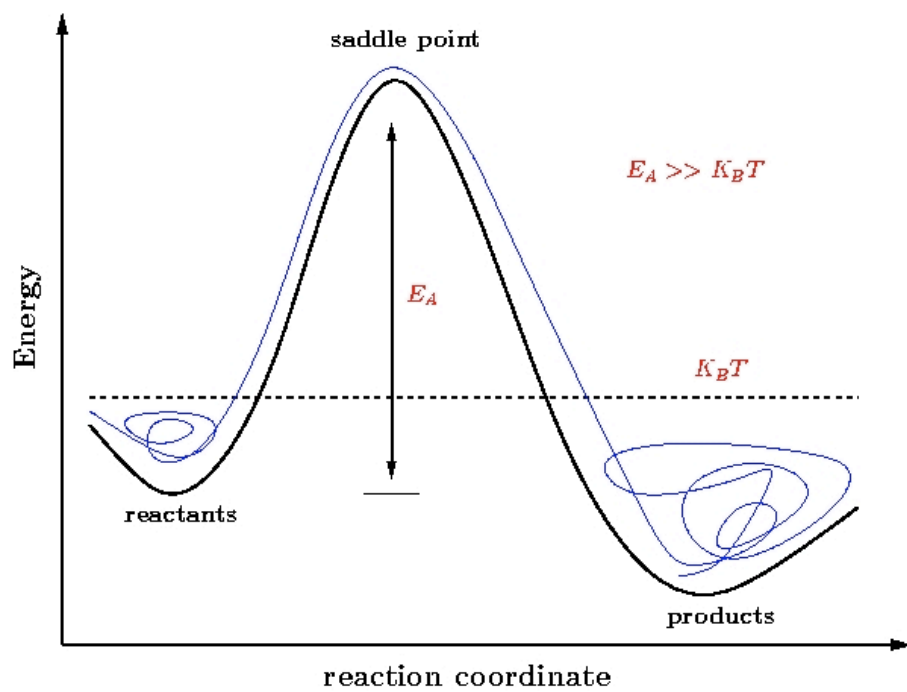


Figure 1.3. Activation energy barrier (E_A), saddle point in a chemical reaction.

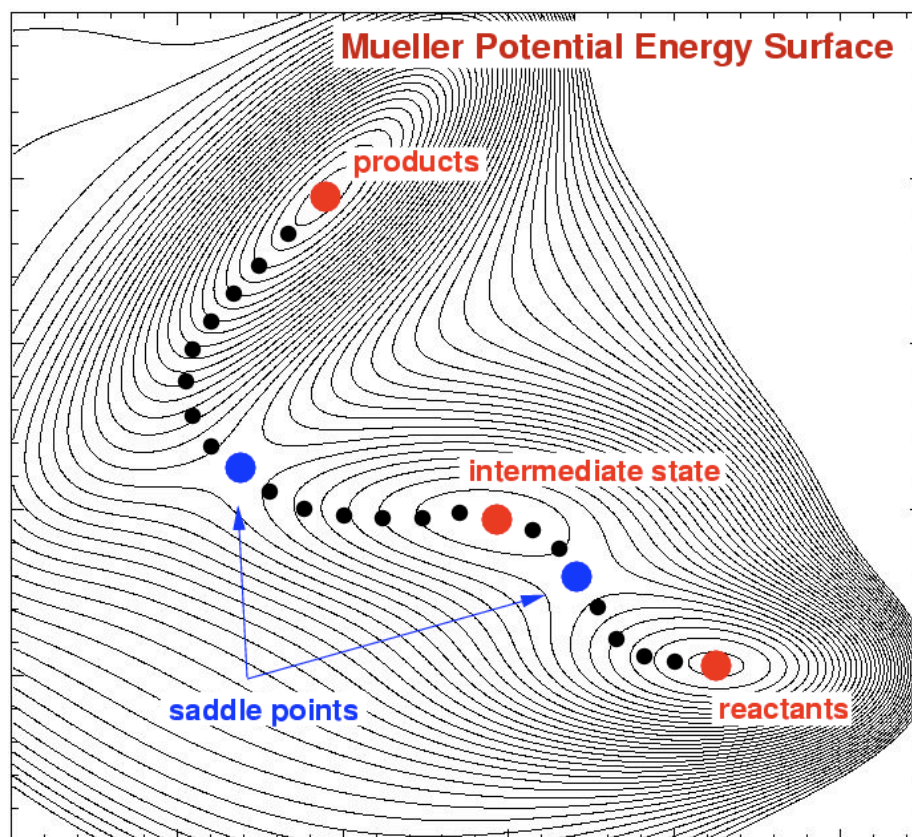


Figure 1.4. Potential energy surface, minimum energy path is depicted along with the saddle point (transition state) between reactants and products of a chemical reaction.

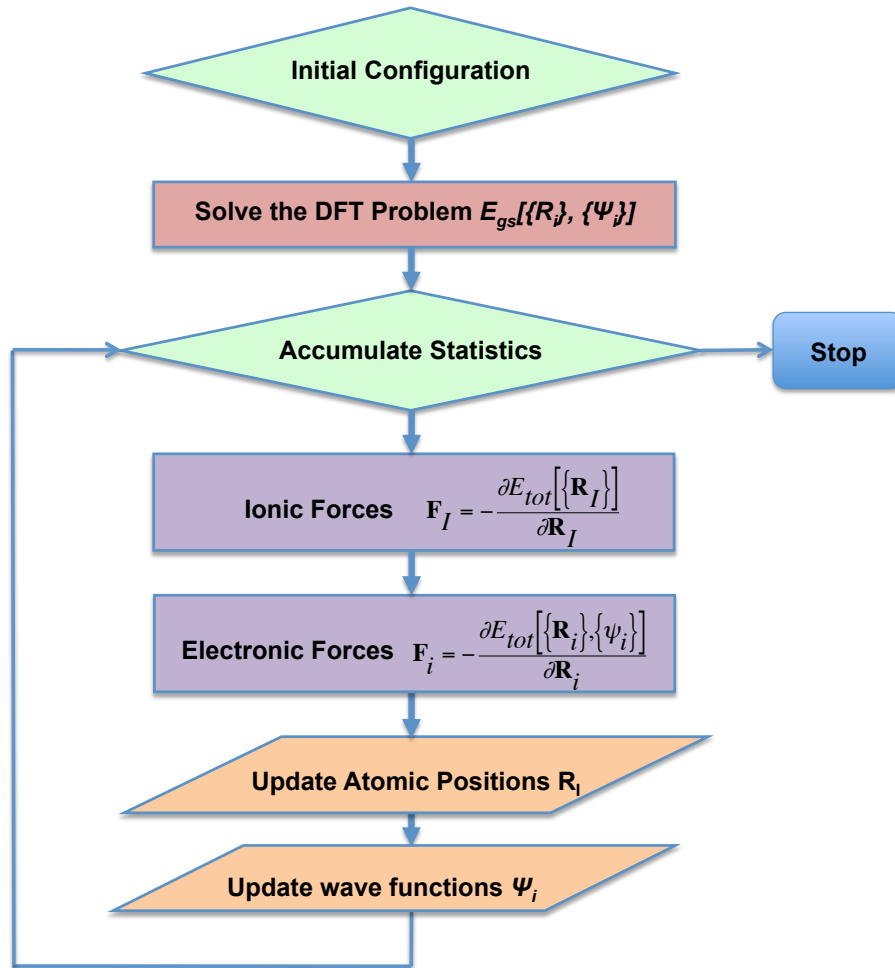


Figure 1.5. Car-Parrinello Molecular Dynamics algorithm.

References

- ¹ R. M. Martin, *Electronic structure: Basic theory and practical methods*, Cambridge University Press (2004)
- ² P. Hohenberg and W. Kohn, *Phys Rev*, **136**, B864 (1964)
- ³ W. Kohn and L. J. Sham, *Phys. Rev.*, **140**, A1133 (1965)
- ⁴ M. Born and J. Oppenheimer, *Ann. Physik*, **84**, 457 (1927)
- ⁵ J. P. Perdew and A. Zunger, *Phys. Rev. B*, **23**, 5048 (1981)
- ⁶ D. M. Ceperly and B. J. Alder, *Phys. Rev. Lett.*, **45**, 566 (1980)
- ⁷ J. P. Perdew, J. A. Chevary et.al., *Phys. Rev. B*, **46**, 6671 (1992)
- ⁸ J. P. Perdew, K. Burke et.al., *Phys. Rev. Lett.*, **77**, 3865 (1996)
- ⁹ M.R.S. Bulletin, September 2006, Volume 31, No.9
- ¹⁰ U. V. Barth and C. D. Gerlatt, *Phys. Rev. B*, **21**, 2222 (1980)
- ¹¹ W. E. Pickett, *Computer Physics Report*, **9**, 115-197 (1989)
- ¹² N. Troullier and J. L. Martins, *Phys. Rev. B*, **43**, 1993 (1991)
- ¹³ D. Vanderbilt, *Phys. Rev. B*, **41**, 7892 (1990), G. Kresse and J. Hafner, *J. Phys.: Condens Matter*, **6**, 8245 (1994)
- ¹⁴ P. Giannozzi, S. Baroni, N. Bonini, M. Calandra, R. Car, et. al., *J.Phys.:Condens.Matter*, **21**, 395502 (2009)
- ¹⁵ <http://electronicstructure.org/>
- ¹⁶ J. Tersoff and D. R. Hamann D R, *Phys. Rev. B*, **31**, 805–13 (1985)
- ¹⁷ A. D. Becke and K. E Edgecombe, *J. Chem. Phys.*, **92**, 5397–403 (1990)
- ¹⁸ <http://www.gnuplot.info/>

¹⁹ <http://www.pwscf.org/>

²⁰ A. Kokalj A 1999 J. Mol. Graph. Modelling., **17**, 176–179 (1999),
<http://www.xcrysden.org/>

²¹ W. Humphrey, A. Dalke and K. Schulten K, J. Mol. Graph. Modelling., **14**, 33–38
(1996), <http://www.ks.uiuc.edu/Research/vmd/>

²² <http://www.csc.fi/english/pages/g0openMol>

²³ A. Szabo A and N. Ostlund N, Modern Quantum Chemistry (New York: Dover),
1996

²⁴ C.J Fall, Ab initio study of the work functions of elemental metal crystals , PhD
thesis, 1999.

²⁵ F. K. Schulte, Phys. Rev. B, **50**, 15248-15260 (1994)

²⁶ C. J. Fall, N. Binggeli and A. Baldereschi, J. Phys.: Condens Matter, **11**, 2689-
2696 (1999)

²⁷ G. H. Vineyard, J. Phys. Chem. Solids **3** 121 (1957)

²⁸ M.L. McKee and M. Page, Reviews in Computational Chemistry Vol. IV, K.B.
Lipkowitz and D.B. Boyd, Eds., (VCH Publishers Inc., New York, 1993)

²⁹ G.Mills and H.Jonsson, Phys. Rev. Lett., **72**, 1124 (1994), G.Henkelman and
H.Jónsson, J. Chem. Phys., **113**, 9978 (2000)

³⁰ G. Henkelman, B. P. Uberuaga and H. Jónsson, J. Chem. Phys., **113**, 9901
(2000)

³¹ S. Baroni, S. d. Gironcoli , A. D. Corso and P. Giannozzi, Review of Modern
Physics, **73**, 515 (2001)

-
- ³² S. Baroni, P. Giannozzi and A. Testa, Phys. Rev. Lett., **58**, 1861 (1987), X.
Gonze, Phys. Rev. A, **52**, 1086 (1995); X. Gonze, Phys. Rev. A, **52**, 1096 (1995)
- ³³ N. Mounet and N. Marzari, Phys. Rev. B, 71, 205214 (2005)
- ³⁴ S. Y. Savrasov and D.Y. Savrasov, Phys. Rev. B, **54**, 16487 (1996)
- ³⁵ R. Car and M. Parrinello, Phys. Rev. Lett., **55**, 2471-2474 (1985)
- ³⁶ H. Hellmann, Einführung in die Quantenchemie. Leipzig: Franz Deuticke, page.
285 (1937), R. P. Feynman, Phys. Rev., **56**, 340 (1939)
- ³⁷ T. M. Reed and K. E. Gubbins, Applied statistical mechanics, 1973

Chapter 2

Sequestration and selective oxidation of carbon monoxide on graphene edges

2.1 Introduction

The versatility of carbon nanostructures makes them attractive as possible catalytic materials, as they can be synthesized in various shapes and chemically modified by doping, functionalization, and the creation of defects in the nanostructure. Recent research has shown how the properties of carbon nanostructures can be exploited to enhance the yield of chemical reactions such as the thermal decomposition of water¹ and the dissociation of methane into carbon and hydrogen². In this work, we consider the carbon-mediated partial sequestration and selective oxidation of carbon monoxide (CO), both in the presence and absence of hydrogen. Using first-principles calculations we study several reactions of CO with carbon nanostructures, where the active sites can be regenerated by the deposition of carbon decomposed from the reactant (CO) to make the reactions self-sustained. Using statistical mechanics, we also study the conditions under which the conversion of CO to

graphene and carbon dioxide is thermodynamically favorable, both in the presence and in the absence of hydrogen. These results are a first step toward the development of processes for the carbon-mediated partial sequestration and selective oxidation of CO in a hydrogen atmosphere.

The disproportionation reaction of carbon monoxide has been recently the focus of some attention as a means for the synthesis of carbon nanotubes^{3,4,5}. This process has been shown to be favorable at relatively high temperatures and partial CO pressures. Favorable conditions for CO sequestration from any carbon source are highly dependent on temperature, pressure and co-reactant species. In systems where CO is the main carbon bearing species, the disproportionation ($2\text{CO} \rightleftharpoons \text{C(s)} + \text{CO}_2$) and direct reduction reactions ($\text{CO} + \text{H}_2 \rightleftharpoons \text{C(s)} + \text{H}_2\text{O}$) are the primary pathways for carbon deposition. Increasing the concentration of CO by increasing the system pressure can increase the flux of the disproportionation reaction, but it may also favor side reactions such as the direct reduction, which would be undesirable in an application such as the purification of hydrogen for use in fuel cells.

In this study, we consider the sequestration of CO through disproportionation on a graphene surface, both in the absence and in the presence of hydrogen. We find

that it is possible, under certain thermodynamic conditions, to selectively deposit carbon on graphene through disproportionation rather than direct reduction, *i.e.* without converting hydrogen to water, which makes it possible to separate the H₂ from CO. We investigate the energetics of the sequestration of CO on a graphene edge using density functional theory calculations^{6,7}, studying in detail the reaction between CO and aromatic rings on graphene surfaces. In particular, we consider the adsorption of CO on edges of graphitic materials and the desorption of CO₂. Our results are a first step toward understanding the energetics of carbon deposition from a CO atmosphere, and can be used as a basis for obtaining the conditions under which such deposition can occur.

2.2 Methods

The results presented in this work were obtained using plane-wave pseudopotential⁸, density functional theory (DFT)^{6,7}, with the Perdew-Becke-Ernzerhof (PBE) exchange-correlation functional⁹. We used ultrasoft pseudopotentials^{10,11} with a plane-wave cutoff of 35 Ry and a density cutoff of 280 Ry which we found sufficient for convergence. The calculations were done using the PWSCF¹² and CPMD¹³ codes. Some reaction pathways were obtained using the Nudged Elastic Band (NEB) method^{14,15} with the climbing image¹⁶ modification to

obtain the structure of the transition states and the activation barrier. All geometries have been relaxed using the Broyden-Fletcher-Goldfarb-Shanno BFGS algorithm¹⁷. The graphene walls were modeled on an orthorhombic unit cell with periodic boundary conditions. In order to prevent interaction between periodic images in the y and z-directions, a vacuum of 10 Å was left in those directions. One end of the graphene wall was saturated with hydrogen in order to see the interactions between the gas molecules and a single edge. We considered graphene edges with different numbers of rings in order to ensure that our results were reasonably independent of the system size.

We also estimated the equilibrium constants for the various reactions in the low-pressure limit as functions of temperature. In order to do so, we computed the vibrational spectrum for both reactants and products and calculated the ideal-gas partition function as described in detail in reference¹⁸. For the solid states, only vibrational modes were included in the partition function. The standard Gibbs free energy changes ΔG^0 for all reactions were then computed from the molecular partition functions and were then used to obtain the equilibrium constants $K_{\text{eq}} = \exp(-\Delta G^0/kT)$ at different temperatures in the ideal-gas limit (Henry's law limit for adsorbed species). These values were used to construct van't Hoff plots ($\ln K_{\text{eq}}$

versus $1/T$). In all cases we treated rotations, translations, and vibrations as independent of each other. Rotations were treated quantum mechanically at low temperatures^{18,19}. The statistical mechanical approach used in this work is strictly valid only at low to moderate temperatures and pressures. We compared the ideal gas thermodynamic properties of the gaseous species (oxygen, water, carbon monoxide, carbon dioxide, and hydrogen) obtained using our approach with those obtained using the data found in the NIST database²⁰, and found reasonably good agreement for the temperature range covered in Figures 2.7, 2.9 and 2.10. For the other species considered in this work, however, there is no available data for comparison to the best of our knowledge.

2.3 Results and Discussion

The interaction between a growing surface and a chemically reactive atmosphere, especially at high temperatures and pressures, is a quite complicated problem to study since there are many possible arrangements of the atoms in the advancing edge that could lead to different energetics. Since an exhaustive study of all possible atomic configurations would be well beyond the reach of an *ab initio* study, we decided to focus on edges of only two different symmetries – zigzag and armchair –

interacting with atmospheres containing CO, and later also hydrogen. In order to obtain the relevant configurations of atoms on such edges, we investigated the reactions between gas-phase CO molecules and unsaturated edges of both zigzag and armchair symmetries. After the dangling bonds were saturated by the gas-phase species, we studied the reactions with further gas-phase molecules that would lead to a new layer of benzene rings ready for subsequent reaction. Even though the reactions in a real system would likely proceed through different (and more complex) mechanisms, we can still use the results to estimate the equilibrium energetics of the system, and thus study the conditions under which different reactions would be thermodynamically favored.

2.3.1 Interaction of CO with zigzag graphene edge

Our results regarding the interaction of carbon monoxide with an advancing zigzag edge are summarized in Figures 2.1-2.4. Figure 2.1 shows the energetics for the reactions between CO molecules in the gas phase and a zigzag graphene edge resulting in the deposition of a new layer of aromatic rings. The results in Figure 2.1 correspond to a zigzag edge with seven aromatic rings. No substantial difference in the energetics attributable to model size could be found between four-ring, five-ring,

six-ring or seven-ring models. The energetics in Figure 2.1 correspond to five reaction steps: (1) The saturation of the edge by CO molecules yielding oxygenated pentagonal structures (i to ii); (2) the reaction of this oxygenated structures with further CO from the gas phase to form CO₂ (ii to iii); (3) the deposition of another layer of CO molecules to form oxygenated 5-7-5 ring structures (iii to iv); (4) the reaction of these structures with further CO to form CO₂ (iv to v) and (5) the rearrangement of the atoms on the edge to hexagonal structures. The energetic penalty from this last rearrangement is a consequence of the zigzag symmetry of the edge – as we will see later, this does not appear in the armchair edge. Note that the extra oxygen atom in (iii), which actually completes a furan ring with the carbon on the right of the simulation box due to the periodic boundary conditions, is a consequence of doing the calculation with an odd number of rings. The overall energetics for growth, however, are not significantly different when the calculations are done with an even number of rings.

As expected, both of the steps where dangling bonds are saturated (i to ii and iii to iv) are highly exothermic. Of the steps where oxygen is removed from the edge by reaction with further gas-phase CO molecules, one (ii to iii) is endothermic and the other (iv to v) is exothermic. We also considered the possibility of desorption of the oxygen atoms as O₂ molecules but, as it would be expected, this reaction is highly endothermic and unlikely to occur at low to moderate temperatures. This is a

consequence of the larger steric hindrance experienced by the oxygen atoms bound to the heptagonal rings in (iv), which makes them less strongly bound to the graphene edge. The rearrangement of the benzene rings (v to vi) is endothermic but to a lesser extent, and the overall process is exothermic. The energy change for the overall reaction $(i) + 26\text{CO} \rightarrow (\text{vi}) + 13\text{CO}_2$, *i.e.* the deposition of a new layer of benzene rings on the graphene edge, is -820.3 kcal/mol, or -63.1 kcal/mol per CO molecule deposited, indicating that the deposition is highly favorable thermodynamically at low temperature.

In order to get an estimate of the kinetic barriers involved in the key reaction steps for the deposition of carbon on a zigzag graphene edge, we investigated the mechanisms for the reaction of gas phase CO molecules with oxygen atoms on the edge to yield CO₂ (Figures 2.2 and 2.3), and the structural rearrangement of the rings at the edge (Figure 2.4), using the Nudged Elastic Band method. We found that the removal of an oxygen atom bound to a pentagonal ring (Figure 2.2) has a very large energy barrier (~8 eV), which means that this particular reaction is very unfavorable kinetically. In contrast, the removal of an oxygen atom bound to a heptagonal ring (Figure 2.3) has a much lower energy barrier – not only are the oxygen atoms in the initial state more sterically hindered, but the transition state is a cyclic peroxide structure with no dangling bonds, which makes it much lower in energy.

Finally, the rearrangement of a heptagonal and a pentagonal ring at the graphene edge to form two hexagons, shown in Figure 2.4, has a high energy barrier (~ 2 eV). As we discuss later, this step is not necessary when the reaction happens on an armchair edge, which suggests that the growth in the zigzag direction is much less kinetically favorable.

The results in Figures 2.2-2.4 suggest that the kinetic bottleneck for the growth of a zigzag edge on a CO atmosphere is the removal of oxygen atoms bound to pentagonal rings. Even though we were unable to find a more favorable pathway for this reaction, it is possible that there is a high-pressure concerted mechanism involving more than one CO molecule with a lower activation barrier. An exhaustive search for such a mechanism would require a far larger computational effort. Alternatively, a metal catalyst could be added to promote the deposition of carbon, as has been done experimentally to grow carbon nanotubes^{4,5}.

2.3.2 Interaction of CO with armchair graphene edge

Our results regarding the interaction of gas-phase CO molecules with an armchair graphene edge are presented in Figure 2.5. Because of the symmetry of the

armchair edge, it is possible for the CO molecules to directly form hexagonal rings upon deposition. This means that no rearrangement is necessary, and all the steps where oxygen is removed by further reaction with CO are equivalent. As is the case with the zigzag edge, the saturation of the dangling bonds with CO (steps (i) → (ii) and (iii) → (iv) in Figure 2.5) is, as expected, highly exothermic. Indirectly, our results suggest that the armchair edge is significantly more stable than the zigzag edge, since the drop in energy per carbon atom added when the edge is saturated with CO is ~ 65 kcal mol⁻¹ for the zigzag edge versus ~ 45 kcal mol⁻¹ for the armchair edge. This is so even despite the fact that oxygen atoms on the edge experience higher steric hindrance in the armchair case. However, the reaction with further CO to yield CO₂ and a new exposed edge is also exothermic – both the reactions (ii) → (iii) and (iv) → (v) release approximately 75 kcal/mol. In reality, the energy differences for both of the reactions (ii) → (iii) and (iv) → (v) should be the same for a large surface. The $\sim 5\%$ difference in the values for (ii) → (iii) (-78.7 kcal mol⁻¹) and (iv) → (v) (-74.7 kcal mol⁻¹) is due to the finite size of our system. The explanation for this is similar to that for the reaction (iv) → (v) in Figure 2.1: the steric hindrance between the oxygen atoms attached to the hexagonal rings makes them easier to remove. Thus, all the steps from (i) to (v) in Figure 2.5 are exothermic and therefore thermodynamically favorable at low temperature. The overall energy released for the

deposition of 12 CO molecules to grow a new row of rings, *i.e.* $(i) + 24\text{CO} \rightarrow (v) + 12\text{CO}_2$ is 684.0 kcal/mol, or 57.0 kcal/mol per CO molecule deposited. Even though this is lower than the value for the zigzag edge, the fact that every step is endothermic suggests that the growth in the direction of the armchair edge is more favorable than the growth in the direction of the zigzag edge.

In analogy with the zigzag case, we investigated the mechanism for the reaction between an oxygenated armchair edge ((ii) in Figure 2.5) and a gas-phase CO molecule using the Nudged Elastic Band method. The results are shown in Figure 2.6. The reaction barrier, about 1.5 eV, is still quite high (Note that, as with the zigzag case, we cannot preclude the existence of a more complex high-pressure mechanism involving more than one CO molecule with a lower barrier.), but considerably smaller than the barrier for the removal of an oxygen atom from a pentagonal ring in the zigzag edge (~8 eV, Figure 2.2). This indicates that the kinetic bottleneck for the deposition of carbon from CO is much lower on an edge of armchair symmetry, and therefore the growth in this direction is not only more favorable thermodynamically, but also kinetically. This is in agreement with other theoretical studies²¹ and experimental results^{22,23,24} for the growth of carbon nanotubes. For this reason, in the rest of the paper we only consider reactions on edges of armchair symmetry. Nevertheless, for the reaction to be practical at low to moderate temperatures and pressures, our results suggest that it would still be

necessary to lower the activation barrier by using a catalyst.

In order to study the effect of temperature on the equilibrium distribution of CO and CO₂ over an advancing graphene edge, we estimated the equilibrium constant, K_{eq} , for the first two reaction steps shown in Figure 2.5. Figure 2.7 shows the results as a van't Hoff plot. As expected, since both reaction steps are highly exothermic, both reactions are very favorable at low to moderate temperatures. From the equilibrium data one would expect, based purely on thermodynamics, that significant deposition of carbon would happen below ~1000 K. However, as mentioned above, in the absence of a catalyst this is a mainly kinetically limited process.

The calculations discussed up to this point involve the interaction of pure CO with a graphene surface. We have also studied the selective oxidation of CO in the presence of hydrogen, which is of interest for the purification of fuel cell feed. For this system we considered two types of reactions: (1) The competition between hydrogen and CO for the active sites on the graphene edge, and (2) The incorporation of hydrogen from the gas phase onto the oxygenated edge to form hydroxyl and carboxyl groups on the edge.

2.3.3 Interaction of CO+H₂ with armchair graphene edge

Figure 2.8 shows the energetics for the adsorption of hydrogen on a graphene edge and subsequent displacement of graphene-bound hydrogen by carbon monoxide. As expected, the adsorption of H₂ on the graphene edge [steps (i) to (ii)] is highly exothermic, as is the adsorption of CO (steps (i) to (ii) and (iii) to (iv) in Figure 2.5). However, the binding of CO with the armchair graphene edge is slightly stronger than that of H₂, and thus the displacement of hydrogen by CO on the edge [(ii) to (iii)] is slightly exothermic. This shows that, at low to moderate temperatures, it is more favorable to deposit CO on the edge than to deposit hydrogen.

As in the case of a pure CO atmosphere, oxygen atoms can be removed from the edge by further reaction with either gas-phase CO molecules to yield CO₂ (steps (ii) to (iii) and (iv) to (v) in Figure 2.5) or with gas-phase hydrogen molecules to yield water. However, the latter reaction is less exothermic by 16.7 kcal/mol and thus, at low to moderate temperatures, the majority of the edge-bound oxygen will react with CO instead of hydrogen. We also considered a few other pathways by which water could be formed in the system, as shown in steps (ii) to (ii-a) and (ii) to (ii-b) in Figure 2.8. To detach one H₂ molecule from the edge as H₂O [(ii) to (ii-a)], the energy needed for the reaction is +112.6 kcal/mol. Even if the unsaturated bond is

saturated with CO, as in (ii-b), the reaction is still quite endothermic (+17.7 kcal/mol), and thus thermodynamically unfavorable at low to moderate temperatures. Figure 2.9 shows a van't Hoff plot for the relevant reactions in Figure 2.8 between an armchair graphene edge and a mixture of CO and H₂. From this plot it is clear that at low to moderate temperatures, carbon monoxide is preferentially bound to the active sites on the advancing edge, and the reactions that would lead to significant oxidation of hydrogen to yield water are unfavorable.

As mentioned above, we also considered some of the reactions that could occur between gas-phase hydrogen and graphene-bound oxygen atoms. The simplest and most likely of these are the formation of hydroxyl (OH) and carboxyl groups (COOH). Figure 2.10 shows the energetics of a representative set of reactions involving these functional groups. The formation of hydroxyl groups [(i) to (ii) in Figure 2.10] and the addition of CO to these hydroxyl groups to form carboxyl groups [(ii) to (iii)] are both exothermic, and therefore favorable at low to moderate temperatures. Carboxyl groups formed in this way can further react with gas phase CO to yield CO₂, or with gas-phase hydrogen to form water – both processes would result in a net deposition of carbon on the graphene edge. Both of these reactions are quite exothermic but, as it was the case with carbonyl oxygens (Figure 2.9), the reaction of the carboxyl oxygens with CO to yield CO₂ is considerably more exothermic than the reaction with hydrogen to yield water. Thus at low and moderate temperatures, we would

expect both hydroxyl and carboxyl groups to be formed on the advancing graphene edge. However, the presence of these groups does not hinder the deposition of carbon, and thus deposition is still thermodynamically favorable. Furthermore, carbon deposition is more favorable than the oxidation of hydrogen at low to moderate temperatures.

The temperature dependence of the equilibrium constant for the reactions in Figure 2.10 is shown in Figure 2.11 as a van't Hoff plot. From this plot it is clear that, at temperatures below $\sim 300\text{K}$, the deposition of both hydrogen and carbon monoxide on the edge to form hydroxyl and carboxyl groups is thermodynamically favorable, as is the oxidation of gas-phase CO by reaction with carboxyl groups. The least favorable reaction is the formation of water at the expense of gas-phase hydrogen. At moderate temperatures the formation of carboxyl groups is less favorable, but the formation of water from surface oxygen is still less favorable than the formation of carbon dioxide. Only at high temperatures (above 1500K) is the formation of water thermodynamically favored. We carried out equilibrium calculations with the equilibrium constant data from Figure 2.11 at different initial compositions, temperatures and pressures, and found that at most reasonable temperatures and pressures the equilibrium concentration of water in the gas phase is negligible. This shows that, on the basis of a thermodynamic analysis (i.e. in the presence of a

suitable catalyst to overcome kinetic barriers) the removal of CO from a hydrogen stream is possible by sequestration and partial oxidation to CO₂.

2.4 Concluding Remarks

Using a combination of statistical thermodynamics and density functional theory, we have shown that the adsorption of CO on a graphene edge is a thermodynamically favorable process at low to moderate temperatures. According to our calculations, the growth of graphene edges of armchair symmetry from gas-phase CO is both kinetically and thermodynamically more favorable than the growth of edges of zigzag symmetry, in agreement with similar observations for carbon nanotubes²¹⁻²⁴.

We have also studied the interaction between an advancing graphene edge of armchair symmetry and an atmosphere containing a mixture of carbon monoxide and hydrogen. Our calculations show that, in such a system, the deposition of carbon monoxide on the edge is slightly more favorable than the deposition of hydrogen at low and moderate temperatures. We have shown that the reaction of oxygens bound to the edge with gas phase CO to yield CO₂ is also more favorable thermodynamically than the reaction with gas phase hydrogen to form water. When

including in our model the possibility of forming hydroxyl and carboxyl groups at the edge, we find that the deposition of carbon and oxidation of carbon monoxide is still thermodynamically favorable without any loss of hydrogen due to oxidation at low and intermediate temperatures. This shows that such a setup could in principle be used to remove carbon monoxide from a stream of hydrogen.

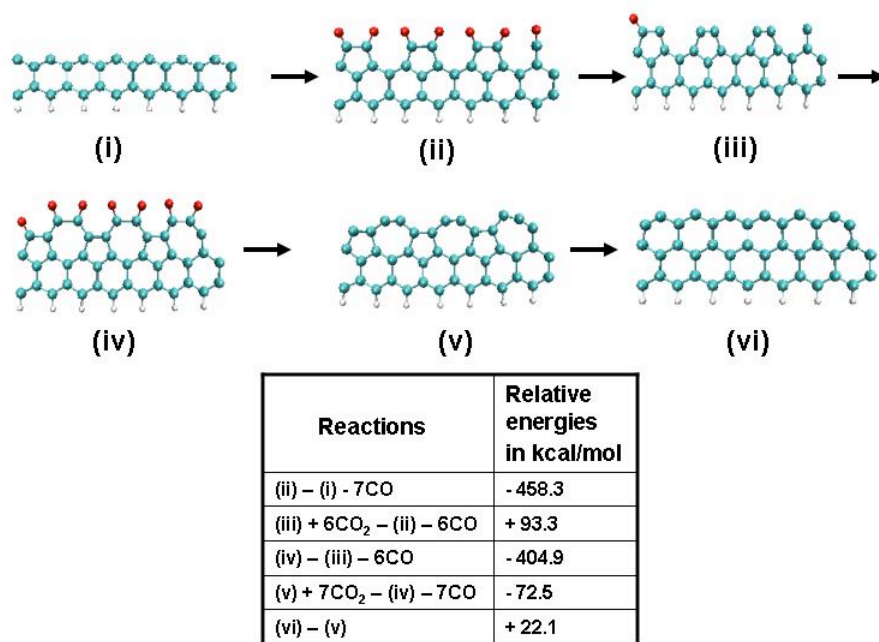


Figure 2.1. Equilibrium energetics for a zigzag graphene edge interacting with CO molecules at high CO concentration. Table I (inset): the reactions at different steps and the corresponding reaction energies in kcal/mol.

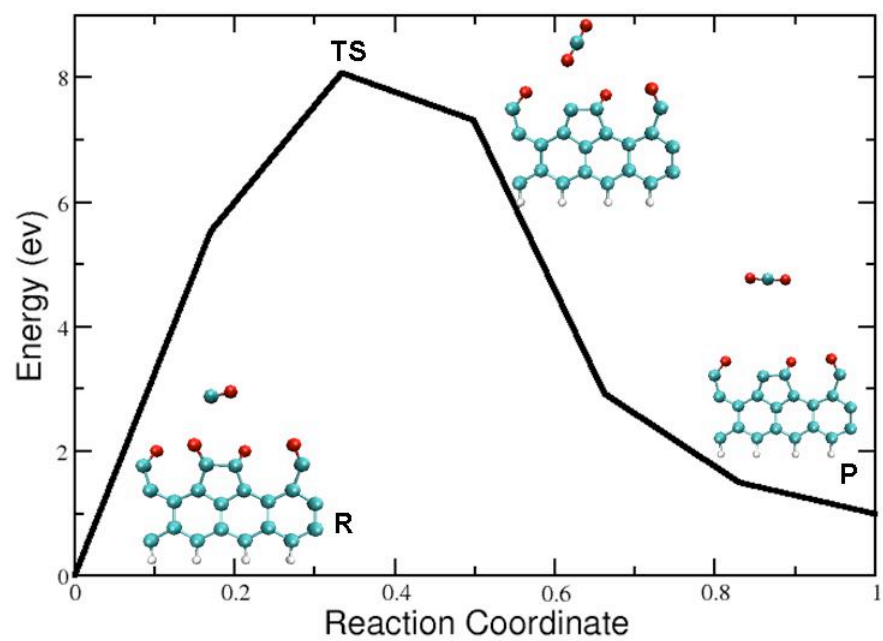


Figure 2.2. Activation energy barrier for the reaction of an oxygen atom with CO to yield CO₂ at the zigzag graphene edge.

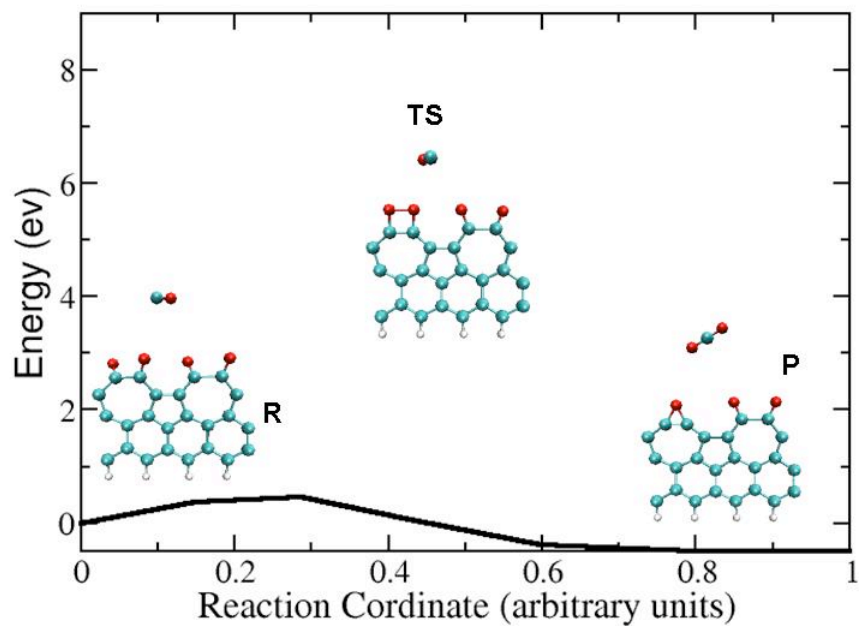


Figure 2.3. Activation energy barrier for the reaction of an oxygen atom with CO to yield CO₂ when the oxygen atoms are bonded to 7-5-7 carbon rings at the zigzag graphene edge.

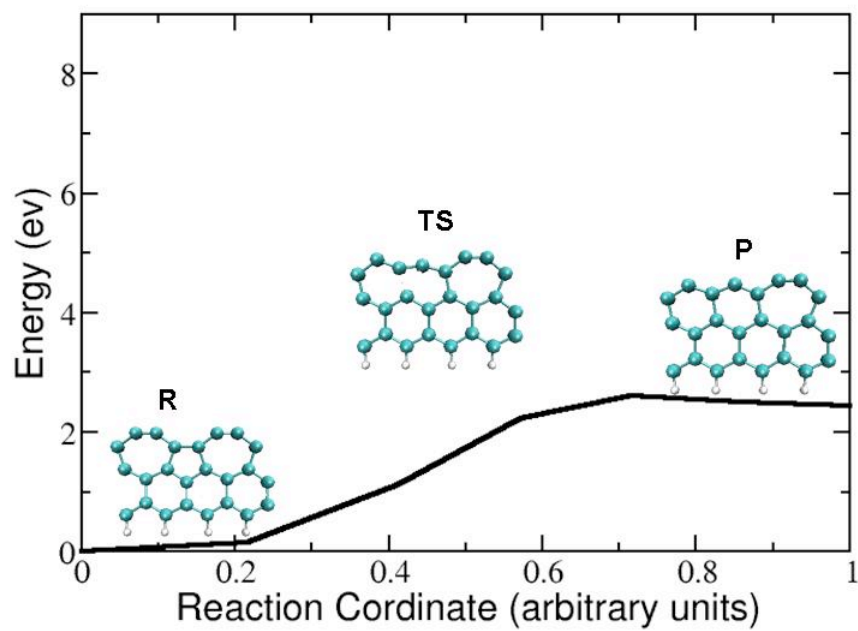


Figure 2.4. Activation energy barrier for the rearrangement of 7-5-7 carbon rings to 6-6-7 carbon rings at the zigzag graphene edge.

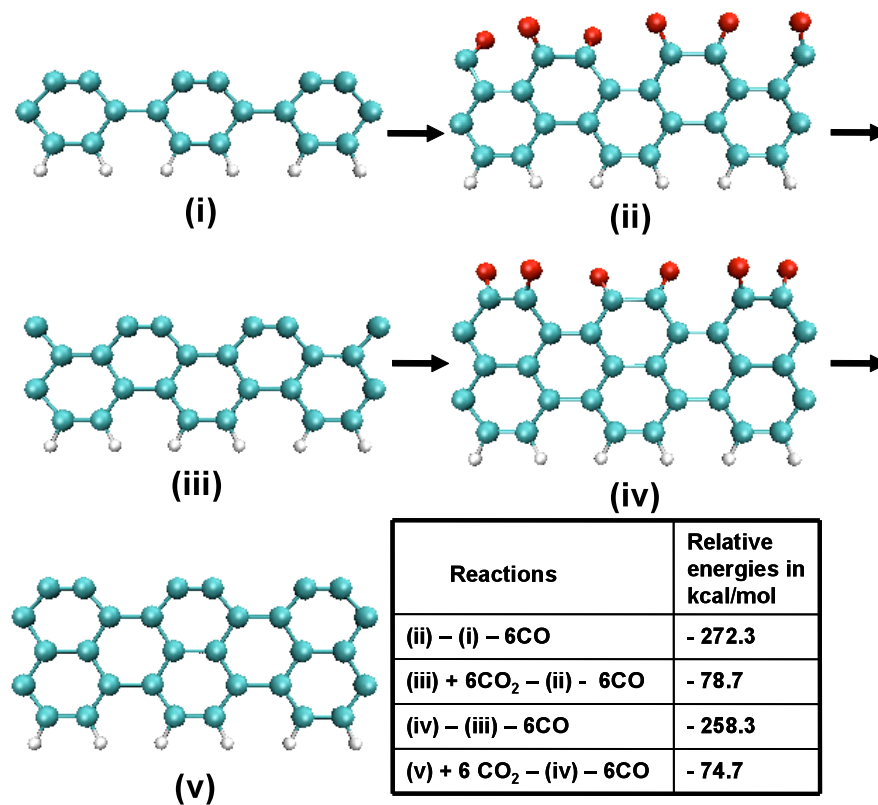


Figure 2.5. Energetics for the interaction of an armchair graphene edge with gas phase CO molecules. Table II (inset): the reactions at different steps and the corresponding reaction energies in kcal/mol.

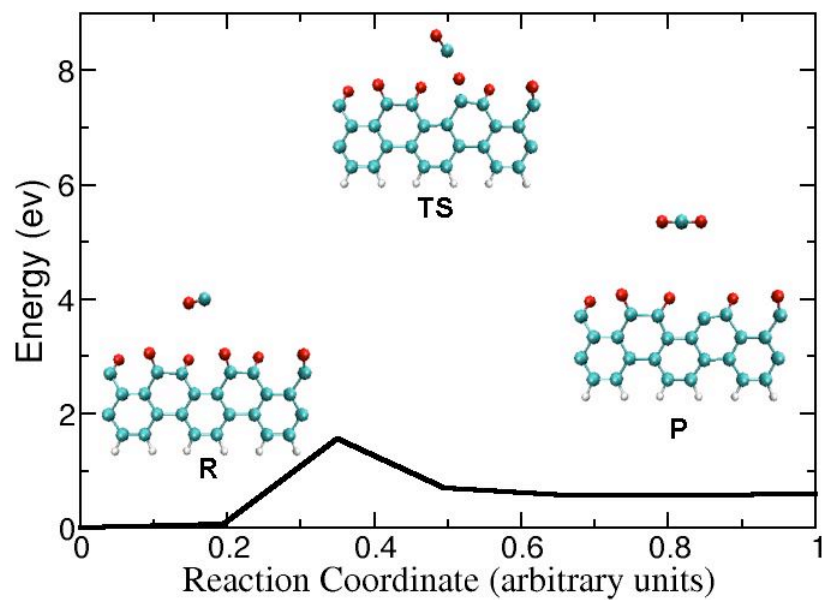


Figure 2.6. Activation energy barrier for the reaction of an oxygen atom with CO to yield CO₂ at the armchair graphene edge.

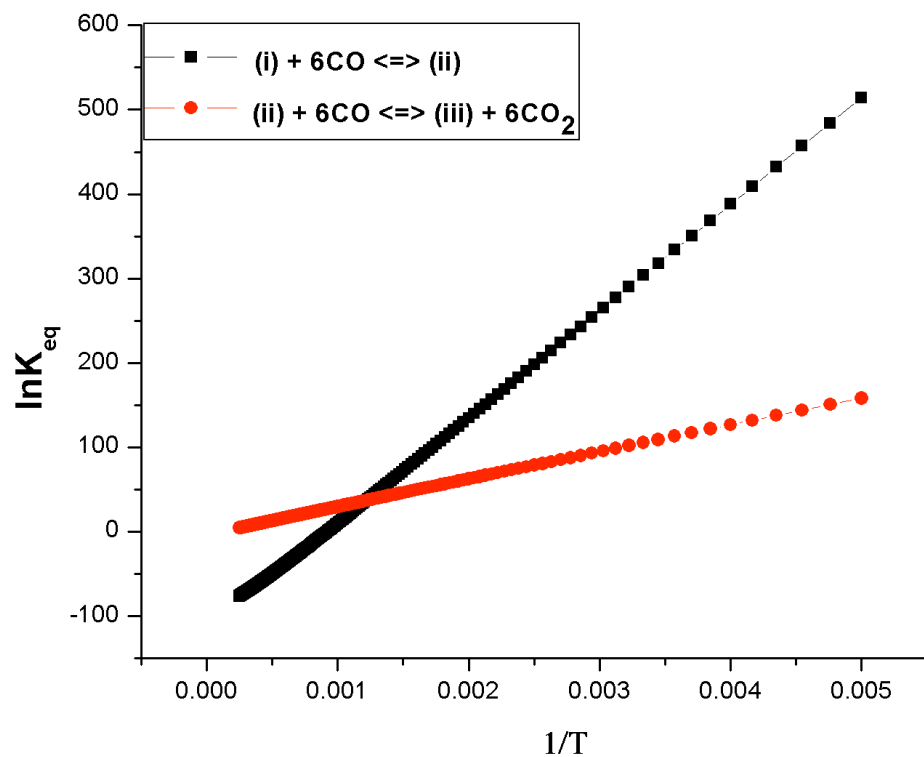


Figure 2.7. Van't Hoff plot for the two main steps in the deposition of carbon on an armchair graphene edge in a CO atmosphere.

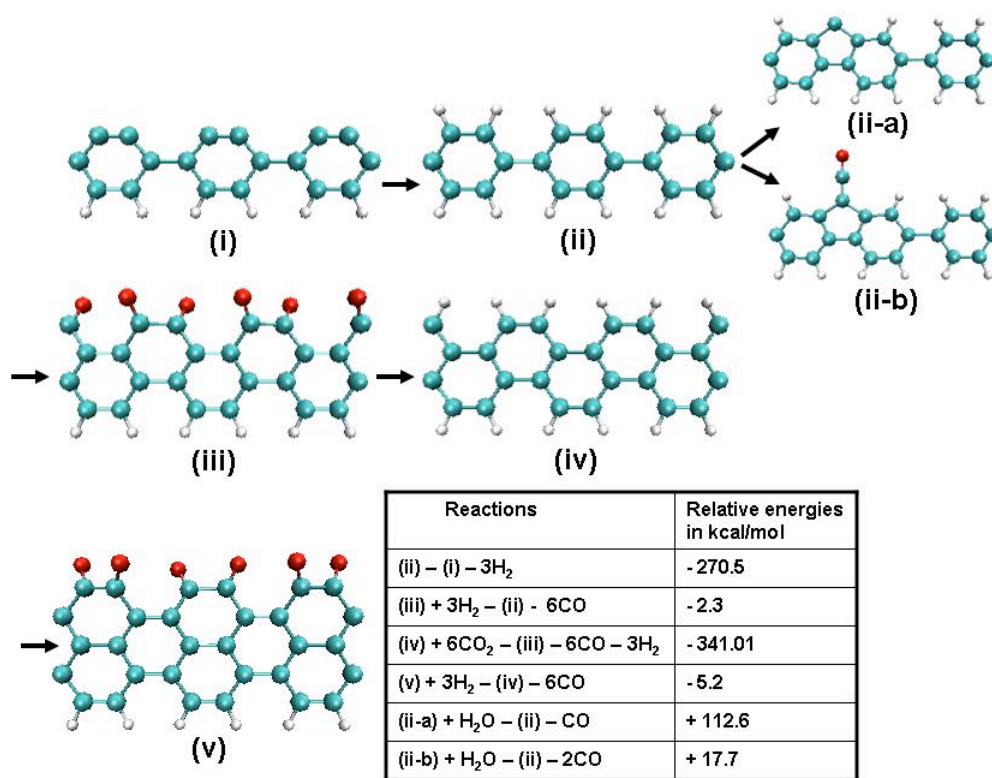


Figure 2.8. Energetics for the competition between CO and hydrogen for the active sites on the advancing graphene edge. Table III(inset): relative energies in kcal/mol for each of the reaction steps.

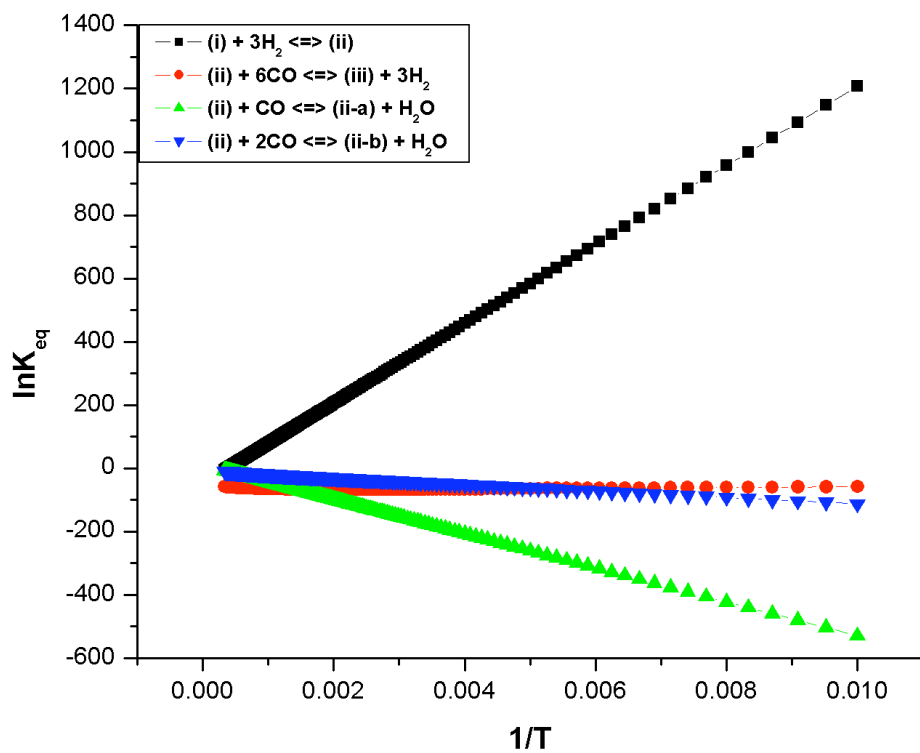


Figure 2.9. Plots of equilibrium constants vs temperature for the main reactions in Figure 2.8.

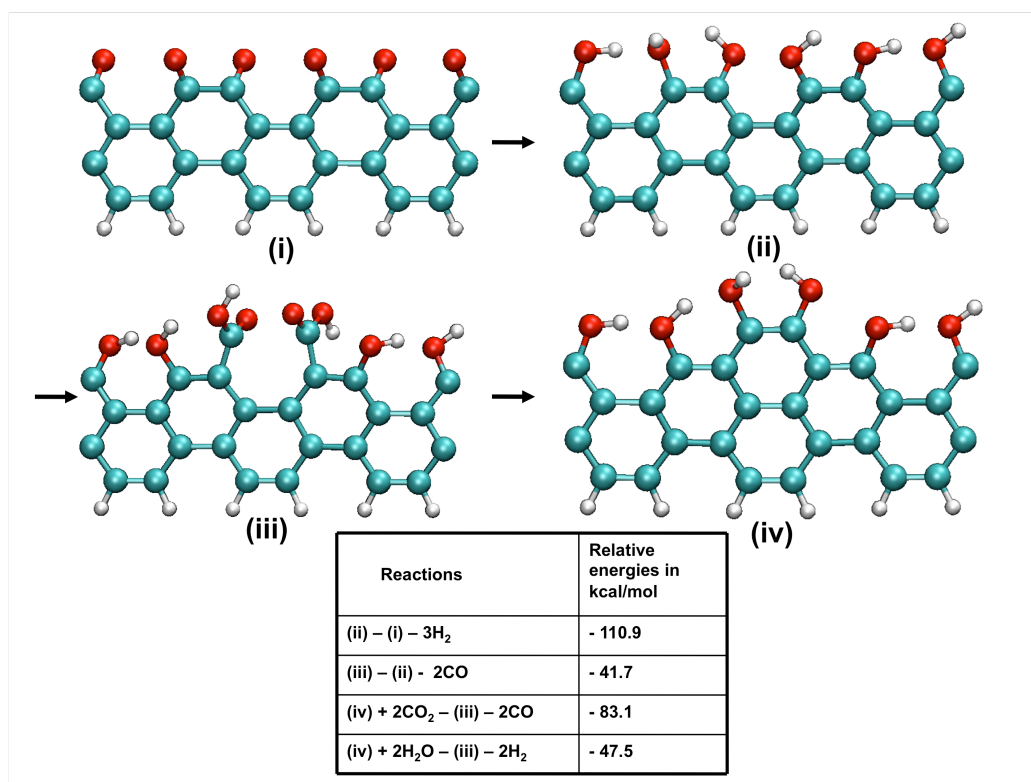


Figure 2.10. Representative chemical reactions of CO and H₂ at the armchair graphene edge involving hydroxyl and carboxyl groups. Table IV(inset): relative energies for the respective reaction steps in kcal/mol.

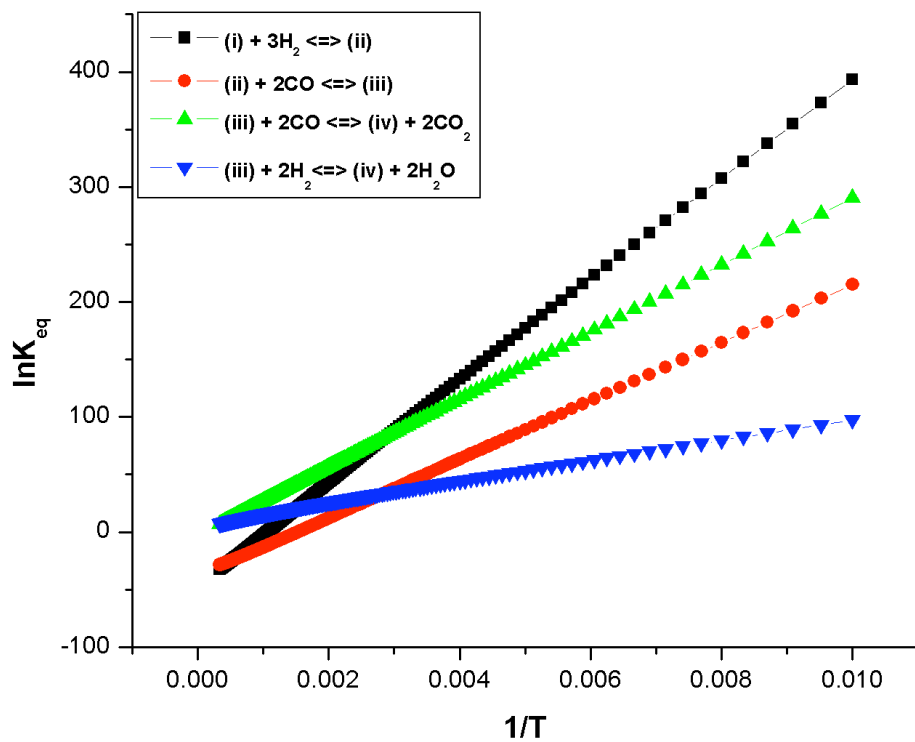


Figure 2.11. Van't Hoff plot for the reactions involving hydroxyl and carboxyl groups at the armchair graphene edge.

References

- ¹ Kostov M K, Santiso E E, George A M, Gubbins K E and Buongiorno Nardelli M, Phys. Rev. Lett., 95, 136105, 2005
- ² Huang L P, Santiso E E, Buongiorno Nardelli M and Gubbins K E, J. Chem. Phys. 130 194701, 2009
- ³ Seo K, Kim C, Kim B, Lee Y H and Song K, J. Phys. Chem. B 108 430813, 2004
- ⁴ Nikolaev P et al., Chem. Phys. Lett. 313, 91, 1999
- ⁵ Bronikowski M J et al., J. Vac. Sci. Technol. A 19, 1800, 2001
- ⁶ Parr R G and Yang W, Density Functional Theory of Atoms and Molecules (New York: Oxford University Press), 1989
- ⁷ Martin R, Electronic Structure: Basic Theory and Practical Methods (Cambridge: Cambridge University Press), 2004
- ⁸ Pickett W E, Comput. Phys. Rep. 9, 115, 1989
- ⁹ Perdew J P, Burke K and Ernzerhof M., Phys. Rev. Lett., 77, 3865, 1996
- ¹⁰ Vanderbilt D, Phys Rev. B, 41, 7892, 1990
- ¹¹ We used H.pbe.rrkus.UPF, C.pbe.rrkus.UPF and O.pbe.rrkus.UPF
<http://www.quantum-espresso.org/pseudo.php>
- ¹² Baroni S et al <http://www.pwscf.org>
- ¹³ CPMD Copyright IBM Corp 1990–2001, Copyright MPI fur Festkorperforschung Stuttgart, 1997–2001 <http://www.cpmd.org>

-
- ¹⁴ Mills G, Jonsson H and Schenter G K, Surf. Sci. 324, 305, 1995
- ¹⁵ Jonsson H, Mills G and Jacobsen K W, Classical and Quantum Dynamics in Condensed Phase Simulations ed B J Berne, G Ciccotti and D F Coker (Sinagapore: World Scientific), 1998
- ¹⁶ Henkelman G, Uberuaga B P and Jonsson H, J. Chem. Phys., 113 9901, 2000
- ¹⁷ Broyden C G , J. Inst. Math. Appl., 6, 222, 1970, Fletcher R, Comput. J. 13, 317, 1970, Goldfarb D, Math. Comput. 24, 23, 1970, Shanno D F, Math. Comput. 24, 647,1970
- ¹⁸ Reed T M and Gubbins K E, Applied Statistical Mechanics (Boston: Butterworth–Heinemann), 1973
- ¹⁹ Santiso E E ParFuMS (Partition Functions of Molecules and Solids), 2007, <http://gubbins.ncsu.edu/users/erik/parfums/>
- ²⁰ <http://webbook.nist.gov>
- ²¹ Ding F, Harutyunyan A R and Yakobson B I, Proc. Natl. Acad. Sci., 106, 2506, 2009
- ²² Luo Z, Pfefferle L D, Haller G L and Papadimitrakopoulos F, J. Am. Chem. Soc., 128, 15511, 2006
- ²³ Miyauchi Y, Chiashi S, Murakami Y, Hayashida Y and Maruyama S, Chem. Phys. Lett. 387, 198,2004
- ²⁴ Bandow S, Asaka S, Saito Y, Rao A M, Grigorian L, Richter E and Eklund P C, Phys. Rev. Lett. 80, 3779, 1998

Chapter 3

Activation of CO₂ on transition metal surfaces and oxide supported metal thin films

3.1 Introduction

Carbon dioxide is a part of our environment's natural life cycle but it is also produced artificially at ever increasing rates through hydrocarbon combustion as well as oxidation of carbon monoxide in catalytic converters. Unfortunately, there currently exists very few means of reusing and managing CO₂ due to these abiological processes and this allows for the unwanted contribution to the greenhouse molecule concentration in atmosphere. CO₂ is both very abundant and cheap carbon feedstock, but due to its low energy content as compared to carbon dioxide, it has limited use as a chemical reactant. However, when the reactions are carried out in presence of a co-reactant, the thermodynamics can be much more favorable¹. So the problem is more likely to be kinetic in origin². One possibility to overcome the kinetic barrier is to use catalyst. In both homogeneous and heterogeneous catalytic processes CO₂ chemistry has large technological interest. Most catalysts used in industry are solids, and the catalysis typically takes place on the surface of nano-

particles of active materials. The understanding of the way the solid surfaces can interact with gas phase molecules, break them down, and form new products has increased enormously. When a chemical reactions are carried out in nano-structured media, such as metal cluster, metal thin films we have at our disposal many new variables; these include the nature of the material size, shape, connectivity, defects, surface roughness etc., which can have a large impact on the free energy surface of the reaction. Through a judicious choice of these variables it should be possible to develop much improved catalytic structures.

Transition metal surfaces were used in heterogeneous catalysis extensively. The interaction of CO₂ with transition metal surfaces, were studied widely in experiments and simulations^{3,4,5}. CO₂ has several possible modes of coordination with the surface: a pure carbon coordination, a pure oxygen coordination or a mixed carbon-oxygen coordination⁶. It has been reported that the adsorption of CO₂ on metal surfaces has two state: chemisorption and physisorption. The chemisorbed state is related to the formation of CO₂^{δ-} where an electronic charge transfer occurs from the metal to the molecule. On clean metal surfaces, CO₂ molecule has physisorbed state; in it's linear un-reactive form.

The authors S. G. Wang et. al. in reference 4, have studied the factor controlling the interaction of CO₂ with different transition metals. In this paper, they found three

stable structure of CO₂ on the Pd (111) surface. The lowest binding energy for the chemisorption is 0.30 eV. On the other hand on Pt (111) surface they found only two stable chemisorption and the lowest binding energy is 1.01 eV. They predicted that the bridge-site of the surfaces is favorable for chemisorption. There are couple of recent work was reported on the adsorption of CO₂ on Ni (110), Ni (111) surfaces^{3,5,7}. The DFT cluster model for different coordination of CO₂ on Pd (111) was discussed in reference⁸.

The activation of CO₂ on transition metal surfaces is important. After the molecule is adsorbed on the surface it is also important to study the catalytic decomposition of CO₂ to CO and O over the surface. The thermal decomposition of CO₂ to CO and O is possible at very high temperatures $\text{CO}_2 = \text{CO} + \frac{1}{2} \text{O}_2$, $\Delta G=0$ at 3350 K⁹. So the thermal decomposition or direct dissociation of CO₂ is limited by both thermodynamic equilibrium and kinetic barrier. The reference¹⁰ showed the catalytic decomposition of CO₂ over Pd mixed-conducting oxide catalyst in an oxygen permeable membrane reactor.

We intend to focus on the chemical conversion of CO₂ through heterogeneous catalysis using novel, tunable surfaces and interfaces, particularly ones where there is nano-scale control over charge density at the reactive sites. In order to address the role of localized charge as well as atomic and molecular electronic states as

opposed to full bands on the adsorption and dissociation cross section for CO₂, different types of surfaces were introduced. We addressed the activation and dissociation of CO₂ on Pd (001) and Pt (001) surfaces.

We also investigated the activation and dissociation of CO₂ over monolayer and bi-layer and tri-layer Pd and Pt supported on Barium oxide (BaO). We call these surfaces as 1LPd/BaO (001), 1LPt/BaO (001), 2LPd/BaO(001), 2LPt/BaO (001), 3LPd/BaO(001) and 3LPt/BaO (001). For oxide supported metal particles catalysts, the support serves as a structural promoter that, in combination with the metal deposition conditions, determines the size and shape of the catalyst particles and thereby the types of the metal atom faces exposed¹¹. The fundamental requirement when two materials (in this case the metal-alkaline earth oxide interface) are brought together, is the ability to control the band alignment, hence the Schottky barrier¹². The structural sensitivity of the metal atoms on the oxide substrate generally arises from several factors including strain, charge transfer at the interface. This could make the corrugation of the atoms in a given surface with respect to the bulk geometry and creates special reaction sites at the surface. The presence of any chemical species (in this case CO₂ molecule) at the surface may cause morphological changes of supported metal atoms in the case of strong bonding of the molecule to the surface. Generally the activation of CO₂ on any surfaces can be affected by many factors such as binding modes, charge transfer between

molecules and surface and electronic properties of the surface etc.

We have studied the activation and dissociation of CO₂ on Pd (001), Pt (001) bulk surfaces. We used 5 layers of metal atoms in (001) direction, which can be well understood as metal thin films. Comparing the results of 5 layers with 7 and 9 layers of metal atoms, no significant difference can be found neither in terms of geometry nor in the energetics. We also studied the activation and dissociation of CO₂ on mono bi-layer and tri-layer metal surfaces supported over 5 layers of BaO. We optimize the different orientation of CO₂ as a molecule on different surfaces. To better understand the activation of CO₂ on the surface we calculated the Local Density Of States (LDOS) of the surface on which the adsorption was occurred. In free CO₂ molecule, the highest occupied molecular orbital (HOMO) is the degenerate bonding orbital and the lowest unoccupied molecular orbital (LUMO) is the degenerate anti-bonding orbital. We have studied, how the HOMO and LUMO of CO₂ changes or coupled with the LDOS of surface atoms. Along with that the charge density difference plot of the molecule on the surface gives us total insight into the local electronic structure and their mutual relationship of all the different adsorptions. In the dissociated CO₂ as CO and O, the CO always binds with the metal atoms on the surface as “metal-CO” bond. And O atom made strong bond to the surface atom too. We also calculated the activation energy barrier for the dissociations of CO₂ on different surfaces to better understand the kinetics of the process.

3.2 Computational details

The results presented in this work were obtained using plane-wave pseudopotential, density functional theory (DFT). We used the local density approximation (LDA) with Perdew-Zunger (PZ) exchange-correlation functional¹³. We used ultrasoft pseudopotentials with a plane-wave cutoff of 35 Ry and a density cutoff of 350 Ry. The calculations were done using the PWSCF codes¹⁴. The integration up to the Fermi energy is made by using a broadening technique with a smearing parameter of 0.01 Ry. The self consistent field (SCF) calculations were done with the threshold of 10^{-8} Ry. The atomic forces are relaxed with a threshold of 10^{-6} Ry/au. The mixing beta parameter was used as 0.3 to 0.5. The Brillouin zone integration was carried out with smearing techniques using 8 X 8 X 1 not shifted k-point mesh for bulk Pd (001) and Pt (001) supercell and 6 X 6 X 1 not shifted k-point mesh was used for the Pd/BaO (001) and Pt/BaO (001). All geometries have been relaxed using the Broyden-Fletcher-Goldfarb-Shanno (“BFGS”) algorithm or “damp” dynamics (quick-min Verlet).

The optimized lattice parameters for Pd (3.87 Å), Pt (3.91 Å) and BaO (3.86 Å). The geometry of metal/oxide interface is characterized by two geometrical parameters, the average distance between metal and oxide interfacial planes and the rumpling parameters¹². The super cell of Pd (001), Pt (001), Pd/BaO (001) and Pt/BaO (001)

were modeled on a tetragonal unit cell with periodic boundary conditions. In order to prevent interaction between periodic images in the z-directions, a vacuum of 14 Å was left. In x and y-direction the systems were periodic. In order to avoid spurious potential due to the vacuum at both side of the system in z-direction, we made the system symmetric in z-direction. In the case of molecules adsorbed at the surface, we put the molecules at both side of the slab to make the system completely symmetric. Since we put the two molecules at the two sides of the slab, we calculated the binding energy of the molecule to the surface as: $\Delta E_{BE} = \frac{1}{2} \{E(\text{CO}_2/\text{Slab}/\text{CO}_2) - E(\text{Slab}) - 2E(\text{CO}_2)\}$, where $E(\text{CO}_2/\text{Slab}/\text{CO}_2)$ is the total energy of the system, $E(\text{Slab})$ is the total energy of the slab and $E(\text{CO}_2)$ is the energy of the isolated linear CO_2 . For the slab geometry we use the same unit cell as we used for the whole system. The free CO_2 was calculated in a periodically repeated cubic unit cell of dimension 25 Å at Γ ($\kappa=0,0,0$). A negative ΔE_{BE} indicated the adsorption of the molecule is exothermic and a positive value of the same indicates the adsorption is endothermic. For the adsorbed geometry, calculations are done to 1/8 ML (monolayer) coverage, i.e., one atom per 8 surface atoms was considered and there were no apparent lateral interactions between the molecules at this coverage due to the periodicity. We calculated the dissociation energy when the CO_2 is dissociated as CO and O atom on the surface as follows: $\Delta E_{DE} = E(\text{CO}+\text{O}/\text{Slab}/\text{CO}+\text{O}) - 2E(\text{CO}_2) - 2E(\text{Slab})$. A positive value of ΔE_{DE} indicates the

dissociation is endothermic and a negative value means the dissociation is exothermic. Some reaction pathways were obtained using the Nudged Elastic Band (NEB) method [which is described in chapter 1], with the climbing image modification to obtain the structure of the transition states and the activation barrier.

We wanted to investigate the microscopic interactions between surface and molecule. One logical procedure to analyze the local density of states of the surfaces from the projected wave functions onto orthogonalized atomic wavefunctions. We plotted the LDOS with the energy and after we rescaled all the systems on the same plot we could see how the Fermi level of the metal was aligned with the molecular orbital. We calculated the work function, which is the most fundamental parameters of metal surfaces and interfaces to understand the adsorptions and catalysis promotion. With the adsorption of atoms or molecules, the surface electronic structure is modified and the work function can change by several eV. The charge rearrangement at the surfaces and interfaces were calculated from the differential plot of the charge density. The charge density difference is defined as: $\Delta\rho = \rho(\text{CO}_2/\text{Sab}/\text{CO}_2) - \rho(\text{Slab}) - \rho(\text{CO}_2/\text{CO}_2)$.

3.3 Theoretical results

3.3.1 Activation of CO₂ on Pd (001)

The structures of physisorbed and chemisorbed CO₂ at different sites on the surface of Pd (001) have shown in Figure 3.1. The left panel of Figure 1 depicts the different physisorption of CO₂ on the Pd surface namely (top and side view of different site adsorption are provided in the picture) (i) physisorption at top-site (ii) physisorption at diagonal-site and (iii) physisorption at bridge-site. In all these physisorptions CO₂ form a linear structure over the surface. The adsorption (physisorption) energy at the top-site of Pd is - 0.21 eV, at the diagonal-site it is - 0.23 eV and at the bridge-site it is - 0.33 eV. These adsorption energies are all exothermic and the physisorption at the bridge-site is the most favorable among the three physisorptions. On the right panel of Figure 3.1, we have shown the chemisorptions at (iv) top (v) diagonal and (vi) bridge site. The top view of top-site-chemisorption and diagonal-site-chemisorption are same as top view of respective physisorptions. The adsorption energy at top-site is - 0.22 eV, at the diagonal-site is - 0.34 eV, and at the bridge-site (top view have shown) is - 0.49 eV. The chemisorption energies at different sites are also exothermic but the bridge site adsorption is the most stable. The binding energies for different adsorptions are listed in Table 3.1.

On clean metal surfaces, CO₂ molecules adsorb in linear un-reactive form. We have also investigated the dissociations of CO₂ to CO and O (CO₂ ⇌ CO + O) on the clean metal surfaces. The dissociation can happen at very high temperatures. In Figure 3.2 we have presented the relative energy (energetics) of all the dissociation along with the chemisorptions. In Table 3.2 we have listed all the relevant energetics of dissociations and chemisorptions of Figure 3.2. In Figure 3.2, we have shown three dissociations on Pd (001) where 3.2-(i) represents the dissociation of CO₂ to CO and O, where O has formed four bonds at the bridge-site. Figure 3.2-(ii) represents the dissociation where O atom went to next top-site after dissociated from CO₂ and 3.2-(iii) represents, further diffusion of O atom away from CO. In all these dissociations CO forms metal-carbon bond to the surface at the top-site. All these dissociations are highly endothermic compared to the top site chemisorption. The bridge-site dissociation (i) is the least endothermic compared to other dissociations. We compared the dissociation energy with respect to chemisorption at top-site [Figure 3.1 (iv)], which is the most unfavorable chemisorption compared to the other chemisorptions. In Figure 3.2 we also compared the energetics of chemisorption at diagonal and bridge site. So from the most stable chemisorbed state (bridge-site), the dissociation to (i) requires highest energy to overcome. We also studied the microscopic interaction of CO₂ with the surface: one logical procedure is to analyze the local density of states (LDOS) of the surfaces and the

adsorbed CO₂. In Figure 3.3 we have shown the LDOS against the energy of different adsorptions and the Pd *d* orbitals. The zero in the energy scale is vacuum level and the arrows indicate the Fermi energies. We stacked the LDOS like this from the bottom of the Figure 3.3: free CO₂, *d* orbital LDOS of the top layer of Pd, “physisorption of CO₂ on top-site, the chemisorption of CO₂ on top-site”, “physisorption of CO₂ on diagonal-site, the chemisorption of CO₂ on diagonal-site”, “physisorption of CO₂ on bridge-site, the chemisorption of CO₂ on bridge-site”. In the respective stack we have shown the adsorbed CO₂ orbitals and frontier *d* orbitals of Pd surface. The frontier *d* orbitals of Pd surfaces are responsible for the electron transfer to the adsorbed CO₂. In free CO₂ molecule, the highest occupied molecular orbital (HOMO) is the degenerate 1π_g bonding orbital while and the lowest unoccupied molecular orbital (LUMO) is the degenerate 2π_u antibonding orbital as it is shown in Figure 3.4. CO₂ orbital hybridizations are different in physisorption and chemisorption. The surface *d* orbital did not change much of its character compared to the bare Pd (001) upon adsorptions of CO₂. In top, diagonal and bridge physisorption, the HOMO of CO₂ has less overlap with the surface *d* orbital, whereas for top, diagonal and bridge chemisorption, the HOMO of CO₂ has changed its character (split of orbitals) and has more overlap with the surface *d* orbital. This indicates that in chemisorptions the CO₂ forms with the surface and there is an electron transfer from the surface to the molecule. It is obvious that bridge site

chemisorption has more interaction compared to other sites. We have also drawn separately in Figure 3.4 the LDOS of free and chemisorbed CO₂ on surfaces. When the CO₂ is chemisorbed on the surface, the HOMO is split and the character is different than that of the free CO₂.

We also calculated the difference in electron charge density as it is depicted in Figure 3.5, which gives us an indication of charge transfer that takes place at the interface of the molecule and the surface. Charges are localized on the top site Pd atoms. We have plotted the physisorption and chemisorption at top, diagonal and bridge site in Figure 3.5. In Chemisorption, the charge transfer from Pd atom to the molecule is higher compared to physisorption.

3.3.2 Activation of CO₂ on Pt (001)

We have also considered Pt (001) surface for the activation of CO₂. As it is depicted in Figure 3.6 (left panel), we have found stable structures of physisorptions on (i) top-site, (ii) diagonal-site and (iii) bridge-site as in the case of Pd (001) surface. Similarly we found stable structures of chemisorptions at three different sites as it is depicted in the right panel of Figure 3.6. All the adsorptions are exothermic and in this case also the bridge-site physisorption is the most exothermic stable structure as it is in Pd (001) surface. The bridge-site chemisorption is the most exothermic

structure in this case too as it is on Pd (001) surface. The energetics of the adsorptions are listed in the Table 3.1.

If we compare the adsorption energy of CO₂ on Pd (001) and Pt (001) surface, we can see that both physisorption and chemisorption on Pd (001) is more exothermic than the adsorptions (physisorption and chemisorption) on Pt (001) surface. So the reactivity of CO₂ on Pd is stronger than that of Pt.

We have also investigated the dissociation of CO₂ on Pt (001) surface and the energetics have listed in Table 3.2. As in the case of Pd (001), we found different dissociation of CO₂ to CO and O atom on the Pt (001) surface too. Figure 3.7 shows the energetics of the dissociations compared to the chemisorption on top-site on Pt (001) surface. In this case the dissociation (i) where the O atom makes four bonds at the bridge site turned out to be exothermic. We have also added the other two chemisorptions (diagonal-site and bridge-site) in Figure 3.7 to compare the dissociation with all the chemisorptions. As we can see bridge-site dissociation (i) is exothermic compared to all the chemisorptions. We also found three other dissociations on Pt (001) surface, but they are all highly endothermic compared to all the chemisorptions as it was on Pd (001) case in Figure 3.2. In all these chemisorptions, the CO molecule forms a metal-carbon-oxygen bond to the surface at top-site.

We have plotted the LDOS of “surface d orbital of Pt (001)” and adsorbed CO₂ at different sites on the surface in Figure 3.8. The overlap of “HOMO of CO₂” with the surface has the same trend as we discussed at the end of section 3.3.1. The physisorbed CO₂ has less overlap with the frontier d orbital of the Pt surface atoms. The chemisorbed CO₂ orbitals has split compared to the free CO₂ and has more overlap with the d orbitals; which indicates the formation of bonds between the molecule and the surface. On Pt (001) the bridge site has the most interaction with the surface. So we can conclude that the bridge site transition metal atoms provide the charge transfer to the adsorbed molecule for the activation. We have plotted the free CO₂ and the chemisorbed CO₂ in a different Figure 3.9 to explore the split of HOMO of CO₂ molecule. The character of HOMO and LUMO of CO₂ has changed when it was chemisorbed on the surface compared to the free CO₂.

In Figure 3.10 we have shown the charge density difference plot of different geometries. It’s obvious that the chemisorbed CO₂ share more charge transfer from the surface than physisorbed CO₂.

3.3.3 Oxide Supported metal thin film

We have investigated the activation and dissociation of CO₂ on oxide supported metal (Pd and Pt) thin films. The activation and dissociation of CO₂ changes drastically when the reaction happens on the BaO supported metal thin films. Due to

the basicity of the BaO the metal layer is corrugated when deposited on the BaO (Figure 3.11). We have used 5 layers of BaO sandwiched between monolayer of metal thin films. There are two reaction sites available for CO₂. We call, site-A where metal atom is supported on O atom and site-B where metal atom is supported on Ba atom. The redistribution of charge at the interface can be seen in the charge density difference plot, which shows a transfer of charge from d_{z^2} to $d_{z^2-y^2}$ orbital of the metal (Pd and Pt) atoms bonded with the O atom in the oxide. The redistribution of charge at the Ba-Metal bond is minor and does not contribute much to the interface dipole. From the charge density difference plot (Figure 3.11) we have seen that charge is localized on site-A metal atoms and site-A is more favorable for CO₂ to interact compared to site-B.

3.3.4 Activation of CO₂ on 1LPd/BaO (001)

The energetics of the interaction of CO₂ with the surface of 1LPd/BaO structure are listed in Table 3.3 and the optimized structures are shown in Figure 3.12. We found stable structures of physisorption and chemisorption of CO₂ in its linear chain form over site-A of 1MLPd/BaO (001) surface as it is depicted in Figure 3.12 (i) and (iii). The physisorption (i) is exothermic where as the chemisorption (iii) is more exothermic. In the chemisorbed state (iii) the CO₂ makes strong bonds with the Pd

atom, which is connected to the substrate O atom. We also found the (ii) physisorption and (iv) chemisorption of CO₂ at site-B on the 1LPd/BaO (001) surface. These adsorptions are also exothermic in nature but not much favorable compared to the site-A adsorptions.

We also studied the adsorptions of CO₂ on diagonal site-A of the 1LPd/BaO (001) surface, where the CO₂ makes different bonds with the surface atoms. At the diagonal site-A, we found only the (v) chemisorption of CO₂, there is no physisorption happened at diagonal site-A. We found the diagonal chemisorption of CO₂ is exothermic. In this diagonal chemisorption the C atom of CO₂ makes bond with the surface Pd atoms and the two O atoms were diagonally placed on the surface and make bonds with the next neighbor Pd atoms.

We also found the bridge-site chemisorbed state for CO₂ on this surface as it is presented in Figure 3.12 (vi). At the bridge-site, CO₂ makes strong bonds with the surface Pd atoms and the surface atoms were restructured due to the adsorption of the molecule as it is obvious from the top site unit cell perspective from Figure 3.12 (vi). The bridge-site chemisorption is the most stable structure (exothermic) among all the adsorptions of CO₂ on 1LPd/BaO (001) surface. From Table 3.3, we can see that the diagonal and the bridge site chemisorptions are the exothermic adsorptions and the bridge-site chemisorption is the most exothermic state on this surface.

Now if we compare the above adsorptions CO_2 with the adsorption of CO_2 on bulk Pd thin film, we could immediately see the difference that the substrate makes on the activation of CO_2 . Comparing the energetics that were listed in Table 3.1 and Table 3.3, we can conclude that the most stable chemisorption on Pd (001) surface has the binding energy of - 0.49 eV at the bridge-site. Whereas the chemisorption at diagonal site-A on surface 1MLPd/BaO (001) is exothermic with a binding energy of - 1.53 eV. Not only that, the chemisorption at the bridge-site ($\Delta E_{\text{BE}} = -2.46$ eV) on the 1LPd/BaO (001) surface is more exothermic than the diagonal-site. So the activation of CO_2 is much more thermodynamically favorable on the Pd thin films over the substrate hence the substrate plays an important role to the activation of CO_2 on the surface.

We have also investigated the dissociation of CO_2 to CO and O on the oxide supported Pd thin films. The relative energy of dissociation compared to (i) chemisorption at site-A is plotted in Figure 3.13(a). All the dissociations, (ii), (iii), (v), (vi) and (viii) are exothermic compared to the chemisorbed structures (i). We also have added the other two chemisorptions: (iv) diagonal-site and (vii) bridge-site to the plot in Figure 3.13(a), to better understand the energetics profile on the 1LPd/BaO (001) surface. The structures of “dissociated CO_2 to CO and O atom” have shown in Figure 3.13(b) (ii), (iii), (v), (vi) and (viii). In all these dissociation, the CO molecule connected to the Pd atom, which stands over O atom from BaO.

The carbon from CO makes direct chemical bond to the surface Pd atom. The dissociated O atom in Figure 3.13(b) (ii) makes bond with the surface Pd atom, which is connected by “O atom in the substrate”. We named this dissociation as “Dissociation: CO + O1” in Table 3.4. The “Dissociation: CO + O2”, as named in Table 3.4, has the structure as shown in Figure 3.13(b) (iii). In Figure 3.13(b) (iii) dissociation, the O atom is connected to the next to next surface Pd atom, which is also connected to the “O atom in the substrate”. In the “Dissociation: CO + O3” as in Figure 3.13(b) (v), the CO and O form bonds with the three next to each other Pd atoms at the surface and due to the strong interaction of the molecule to the surface, the surface was reorganized in it’s optimized structure. The “Dissociation: O3 under Pd surface” has shown in Figure 3.13(b) (vi), where the O atom after dissociated from CO₂ has become part of the interface of Pd and BaO. When the dissociated O atom is part of the interface, that state is more exothermic than Figure 3.13(b) (v) where the O [O3] atom was right on the surface. The most stable dissociated structure Figure 3.13(b) (viii), is the bridge-site dissociation of CO₂, where the O atom makes three bonds with the surface Pd atoms and CO is attached to the site-A Pd atom. The monolayer of Pd is reorganized after the dissociation of CO₂ to CO and O, since the dissociated CO and O make strong bonds with the surface and changes the corrugation of the Pd layer over the BaO. We call this dissociation in Table 3.4 as “Dissociation: O atom at bridge-site”. Some of the dissociations and chemisorptions make the monolayer of Pd atoms rearranged over the substrate.

The “Dissociation: CO + O1” and “Dissociation: CO + O2” are endothermic compared to the chemisorption at diagonal-site and bridge-site, but they are slightly exothermic compared to the site-A chemisorbed state (i). The dissociation of CO₂ on the Pd thin films over substrate is thermodynamically favorable compared to the dissociation that happened on the clean bulk Pd thin films.

In Figure 3.14, we have shown the (LDOS) stack of local electronic structure of the surface and CO₂ on the surface as well. The free CO₂ with HOMO and LUMO is in the lower panel; clean top layer Pd Surface d orbital LDOS is the second panel; in the third row from bottom it shows how the Pd d orbital has changed due to the substrate BaO and this surface provide the electron transfer when CO₂ interacts. Here we considered only the Pd site, which is bonded with the O atom below. We have shown LDOS for surface and adsorbant when CO₂ chemisorbed or physisorbed on 1LPd/BaO. In the bridge site chemisorption the hybridization of CO₂ orbitals with the top Pd layer d orbital is significantly different than other cases. The profile of HOMO and LUMO of CO₂ has changed depending on the adsorption on the surface. In Figure 3.15 we have also depicted the LDOS of free CO₂ and chemisorbed CO₂ separately to better understand the split of the orbitals.

Figure 3.16 shows the charge density difference profile of different adsorptions. The charge transfer from dz^2 orbital of Pd to CO₂ molecule is higher in the case of chemisorption.

3.3.5 Activation of CO₂ on 1LPt/BaO (001)

Similarly we have also studied the activation of CO₂ on the surface of monolayer of Pt supported over 5 layer of BaO as it is shown in Figure 3.17. The energetics of the interaction of CO₂ with the surface of 1LPt/BaO structure is listed in Table 3.3. We found stable structures of physisorption of CO₂ in its linear chain form over site-A of 1MLPt/BaO (001) surface as it is depicted in Figure 3.17 (i), (ii) and (iv). The adsorptions [(i), (ii) and (iv)] at site-A are exothermic; site-A and site-B physisorptions are comparable. Site-A diagonal physisorption is the most exothermic among the three physisorptions. The chemisorption at site-A (iii) is twice more exothermic than the physisorptions as it is obvious from Table 3.3. In the chemisorbed state (iii) the CO₂ makes bonds with the Pd atom, which is connected to the substrate O atom. Now if we compare the chemisorptions at site-A on 1LPt/BaO with the 1LPd/BaO surface we see the same trend in the stable structures (bond lengths and angles); but site-A chemisorptions on 1LPd/BaO is energetically more stable than site-A chemisorption on 1LPt/BaO. We can also conclude that the nature of chemisorptions on the metal thin film over substrate is energetically more favorable than the adsorptions on the bulk metal thin film surface. We also found the (ii) physisorption of CO₂ at site-B on the 1LPt/BaO (001) surface, but there is no chemisorption was found at site-B.

We also studied the adsorptions of CO₂ on diagonal site of the 1LPt/BaO (001) surface, where the CO₂ makes different bonds with the surface atoms. At the diagonal site-A, we found both (iv) physisorption and (v) chemisorption of CO₂, unlike the case in 1LPd/BaO (001), there is no physisorption happened at diagonal site-A. We found the diagonal chemisorption of CO₂ Figure 3.17 (v) is less favorable than the 1LPd/BaO surface. The diagonal chemisorption on both surfaces [1LPd/BaO (001) and 1LPt/BaO (001)] are exothermic, and binding energies are different as it is listed in Table 3.3. In this diagonal chemisorption of CO₂, the C atom makes bond with the surface Pd atoms and the two O atoms were diagonally placed on the surface and make bonds with the next neighbor Pd atoms similar to the case of 1LPd/BaO (001) surface. Where as the diagonal chemisorptions on the bulk thin metal surfaces, the O atoms were floating on the surface without making any bonds to the surface [see Figure 3.1 (v) and Figure 3.6 (v)].

We also found the bridge-site chemisorbed state for CO₂ on this surface as it is presented in Figure 3.17 (vi). At the bridge-site, CO₂ makes strong bonds with the surface Pd atoms and the surface atoms were restructured due to the adsorption of the molecule as it is obvious from the top site unit cell perspective from Figure 3.17 (vi). The bridge-site chemisorption is the most stable structure (exothermic) among all the adsorptions of CO₂ on 1LPt/BaO (001) surface. From Table 3.3, we can see that the diagonal and the bridge site chemisorptions are the exothermic adsorptions

and the bridge-site chemisorption is the most exothermic state on this surface. Now in comparison to the adsorptions on the 1LPd/BaO (001) surface, we found similar trend for the 1LPt/BaO (001) case too. The most stable bridge-site chemisorption on the 1LPt/BaO (001) surface is little more exothermic than the 1LPd/BaO surface. From the energetics profile [Table 3.3], it is obvious that the adsorption on the 1LPt/BaO surface is energetically more favorable than that of 1LPd/BaO (001) on bridge site.

We have also investigated the dissociation of CO₂ to CO and O on the oxide supported Pt thin films. The relative energy of dissociation compared to (i) chemisorption at site-A is plotted in Figure 3.18(a). All the dissociations, (ii), (iii), (iv), (vi) and (viii) are exothermic compared to the chemisorbed structures (i). We also have added the other two chemisorptions: (v) diagonal-site and (vii) bridge-site to the plot in Figure 3.18(a), to better understand the energetics profile on the 1LPt/BaO (001) surface. The structures of dissociated CO₂ to CO and O atom have shown in Figure 3.18(b) (ii), (iii), (iv), (vi) and (viii). In all these dissociation, the CO molecule connected to the Pt atom, which stands over O atom from BaO. The carbon from CO makes direct chemical bond to the surface Pt atom. From Table 3.4, we can see that the “(iii) Dissociation: CO + O1” is slightly more exothermic than “(ii) Dissociation: CO + O2”, unlike the case in 1LPd/BaO (001).

On 1LPt/BaO (001) surface, the “(vi) Dissociation: CO + O3” is more exothermic than “(iv) Dissociation: O3 under Pt surface”, unlike the case in Pd (001). The

dissociations (ii), (iii) and (iv) are endothermic compared to the diagonal-site and bridge-site chemisorptions but exothermic compared to the (i) chemisorption at site-A (reference site). On 1LPt/BaO (001) surface also, the “(viii) Dissociation: O atom at bridge-site” is most stable and hence the energetically favorable compared to all chemisorptions. The “Dissociation: O atom at bridge-site” on 1LPt/BaO (001) is twice as exothermic than that of the case on 1LPd/BaO (001) surface.

In Figure 3.19, we have plotted the LDOS of adsorbed CO₂ and d orbital of monolayer Pt over BaO; along with the free CO₂ and bare Pt surface. In Figure 3.20 only the chemisorbed CO₂ on 1LPt/BaO surface and free CO₂ LDOS is plotted to better understand the local electronic structure. In Figure 3.21, the charge density difference is plotted for 1LPt/BaO surface. The trends in all these three figures are similar to Figure 3.14, 3.15 and 3.16.

3.3.6 Activation of CO₂ on 2LPd/BaO (001) and 2L Pt/BaO (001)

We have also investigated the activation of CO₂ on bi-layer metal (both Pd and Pt) supported over BaO. In this case we considered 5 layer of BaO sandwiched between two layers of metal. Figure 3.22 shows the structure of the bi-layer metal supported over oxide. At the interface of metal and the BaO, there is charge transfer similar to the Figure 3.11.

But adding another layer of metal on top screened the charge accumulation on the surface metal atoms. The top layer of metal lost the corrugation and behaves more like the surface of bulk metal thin film. The reaction sites for CO₂ on this surface again are the same as site-A and site-B, as we described in section 3.3.3 and also we have the bridge site available on the surface as reaction site.

In Figure 3.23, we have shown all the different adsorptions of the CO₂ molecule on the 2LPd/BaPO (001) surface. The energetics are listed in Table 3.5. The physisorption and chemisorption of CO₂ at site-A [(i) and (iv)] are both exothermic. The binding energies of CO₂ on 2LPd/BaO (001) (physisorption) are comparable to the adsorption of CO₂ on Pd (001) and Pt (001) surfaces. The physisorption of CO₂ at site-A on 2LPd/BaO (001) is more endothermic than the physisorption of CO₂ at site-A on 1LPd/BaO(001) and 1LPt/BaO(001). We also found physisorption at (ii) diagonal-site, which is similar to all other physisorptions and exothermic in nature. We found stable structure of physisorption at bridge-site (iii) in Figure 3.23, which is the only exothermic physisorption we could find among all the other surfaces. In this bridge-site physisorption, upon adsorption of the molecule the top layer of Pd atoms is reorganized, but the Pd atom layer close to the interface remains the same. We found chemisorption at diagonal site in Figure 17 (v), which is exothermic and due to the strong interaction of the molecule with the surface, the top layer of atoms

was reorganized. In this case the interaction of the CO₂ with the interface seems strong too, since we can see some reorganization at the interface too as can be seen from Figure 3.23 (v). In Figure 3.23 (vi), we have the stable structure of chemisorption at bridge site. This is the most stable and energetically favorable chemisorption we found among all the other chemisorptions on all the other surfaces we investigated so far. In this (vi) chemisorption the top layer of Pd atoms are reorganized locally around the CO₂ molecule as can be seen from the top view perspective of the unit cell in Figure 3.23 (vi). The Pd atoms close to the interface do not change upon the adsorption of the CO₂ at the surface.

We found the three types of chemisorptions of CO₂ on 2LPt/BaO (001); all are exothermic. The top, diagonal and bridge site chemisorptions of CO₂ on 2LPt/BaO (001) have shown in Figure 3.24.

3.3.7 Activation of CO₂ on 3LPd/BaO (001) and 3L Pt/BaO (001)

We have also investigated the activation of CO₂ on 3 layer metals over BaO. In Figure 3.25, we have shown the chemisorption structure of CO₂ on 3LPd/BaO (001) surface. The energetics is described in Table 3.5. The bridge site chemisorption is the most favorable as it was in the case of bulk Pd (001) surface. In Figure 3.26 we have shown the chemisorption of CO₂ on 3LPt/Bao (001) surface. The energetics is

listed in Table 3.5. From the binding energy profile we can conclude the activation of CO_2 on 3LPt/BaO (001) is less favorable than the 3LPd/BaO (001) surface.

In Figure 3.27 we have plotted the chemisorption binding energy of CO_2 on mono, bi and tri layer metals over BaO substrate and also the bulk Pd (001) surface. Bridge site chemisorption is the most favorable adsorption in all the surfaces. The monolayer Pd over BaO is the most active catalytic surface for CO_2 adsorption. As we add more metal layers on top of one another, the substrate effect is diminished. The tri-layer Pd system behaves like the bulk Pd surface on the adsorption of CO_2 . In Figure 3.28, we have shown the binding energies of CO_2 on different surfaces of Pt and Pt/BaO.

In Figure 3.29 we have shown the dissociation energy of CO_2 to CO and O atom on all the surfaces. The chemisorption at top site is considered as reference in the calculation of dissociation energy. The dissociation on monolayer of metal over substrate is the most exothermic and hence thermodynamically favorable. The dissociation energy saturates as we add more and more metal layers over the substrate.

In Figure 3.30 we have shown the optimized geometries of the dissociated CO_2 on 2LPd/BaO, 2LPt/BaO, 3LPd/BaO and 3LPt/BaO. On 3L metal/BaO, CO and O forms same kind of bond as in Bulk Metal surface.

3.4 Conclusion

Using first principles simulations based on Density Functional Theory, we have investigated the adsorption and activation properties of CO₂ on a variety of transition metal surfaces and oxide supported metal thin films. We focused on the chemical conversion of CO₂ through heterogeneous catalysis using surfaces and interfaces where there is nano-scale control over charge density at the reactive sites. The activation of CO₂ on clean metal surfaces is possible at very high temperatures and the situations changes drastically when reaction happens on oxide supported metal thin film. The chemical reactivity of the molecule on the surface depends on the charge rearrangement at the metal-alkaline earth oxide interface. We want to understand the possible catalytic systems and characterize the relevant geometrical and electronic parameters related to the reaction mechanisms, rates and yield.

Table 3.1. Physisorption and chemisorption binding energies of CO₂ on Pd (001) and Pt (001) surfaces.

Surface	Binding Mode	Adsorption	ΔE_{BE} (ev)	
Pd (001)	Top-site	Physisorption	- 0.21	
	Top-site	Chemisorption	- 0.22	
	Diagonal-site	Physisorption	- 0.23	
	Diagonal-site	Chemisorption	- 0.34	
	Bridge-site	Physisorption	- 0.33	
	Bridge-site	Chemisorption	- 0.49	
	Pt (001)	Top-site	Physisorption	- 0.17
		Top-site	Chemisorption	- 0.06
Diagonal-site		Physisorption	- 0.18	
Diagonal-site		Chemisorption	- 0.08	
Bridge-site		Physisorption	- 0.24	
Bridge-site		Chemisorption	- 0.33	

Table 3.2. Dissociation energies of CO₂ compared to different chemisorptions on Pd (001) and Pt (001) surfaces.

Surface	Adsorption/Dissociation	$\Delta E_{BE}/\Delta E_{DE}$ (ev)
Pd (001)	Chemisorption at top-site	0.00
	(i) Dissociation: O atom at bridge-site	+ 0.59
	(ii) Dissociation: CO + O1	+ 1.93
	(iii) Dissociation: CO + O2	+ 1.95
	Chemisorption at diagonal-site	- 0.12
	Chemisorption at bridge-site	- 0.27
Pt (001)	Chemisorption at top-site	0.00
	(iii) Dissociation: CO + O2	+ 0.97
	(iv) Dissociation: CO + O3	+ 0.91
	(ii) Dissociation: CO + O1	+ 0.84
	(i) Dissociation: O atom at bridge-site	- 0.42
	Chemisorption at diagonal-site	- 0.02
	Chemisorption at bridge-site	- 0.27

Table 3.3. Physisorption and chemisorption binding energies of CO₂ on 1LPd/BaO (001) and 1LPt/BaO (001) surfaces.

Surface	Binding Mode	Adsorption	ΔE_{BE} (ev)
1LPd/BaO (001)	Site-A	Physisorption	- 0.26
	Site-A	Chemisorption	- 0.98
	Diagonal Site-A	Chemisorption	- 1.53
	Bridge Site-A	Chemisorption	- 2.46
	Site-B	Physisorption	- 0.23
	Site-B	Chemisorption	- 0.23
1LPt/BaO (001)	Site-A	Physisorption	- 0.23
	Site-A	Chemisorption	- 0.61
	Diagonal Site-A	Physisorption	- 0.45
	Diagonal Site-A	Chemisorption	- 1.54
	Bridge Site-A	Chemisorption	- 2.98
	Site-B	Physisorption	- 0.26

Table 3.4. Dissociation energies of CO₂ compared to different chemisorptions on 1LPd/BaO (001) and 1LPt/BaO (001) surfaces.

Surface	Adsorption/Dissociation	$\Delta E_{BE}/\Delta E_{DE}$ (ev)
1MLPd/BaO (001)	Chemisorption at site-A (reference state)	0.00
	Dissociation: CO + O1	- 0.04
	Dissociation: CO + O2	- 0.10
	Chemisorption at diagonal-site	- 0.55
	Dissociation: CO+O3	- 0.57
	Dissociation: O3 under Pd surface	- 0.72
	Chemisorption at bridge-site	- 0.94
	Dissociation: O atom at bridge-site	- 1.26
1MLPt/BaO (001)	Chemisorption at site-A (reference state)	0.00
	Dissociation: CO + O2	- 0.27
	Dissociation: CO + O1	- 0.37
	Dissociation: O3 under Pt surface	- 0.76
	Chemisorption at diagonal-site	- 0.93
	Dissociation: CO+O3	- 1.88
	Chemisorption at bridge-site	- 2.38
	Dissociation: O atom at bridge-site	- 2.50

Table 3.5. Energetics profile of CO₂ on surfaces: 2LPd/BaO (001), 2LPt/BaO (001), 3LPd/BaO (001) and 3LPt/BaO (001).

Surface	Binding Mode	Adsorption	ΔE_{BE} (ev)
2LPd/BaO (001)	Site-A	Physisorption	- 0.19
	Site-A	Chemisorption	- 0.61
	Diagonal Site-A	Physisorption	- 0.26
	Diagonal Site-A	Chemisorption	- 1.29
	Bridge Site-A	Physisorption	- 1.09
	Bridge Site-A	Chemisorption	-1.64
	Site-B	Physisorption	- 0.19
	Site-B	Chemisorption	- 0.17
3LPd/BaO (001)	Top Site-A	Chemisorption	- 0.25
	Diagonal Site-A	Chemisorption	- 0.64
	Bridge Site-A	Chemisorption	- 0.87
2LPt/BaO	Top Site-A	Chemisorption	- 0.80
	Diagonal Site-A	Chemisorption	- 1.03
	Bridge Site-A	Chemisorption	- 1.18
3LPt/BaO (001)	Top Site-A	Chemisorption	- 0.17
	Diagonal Site-A	Chemisorption	- 0.67
	Bridge Site-A	Chemisorption	- 0.47

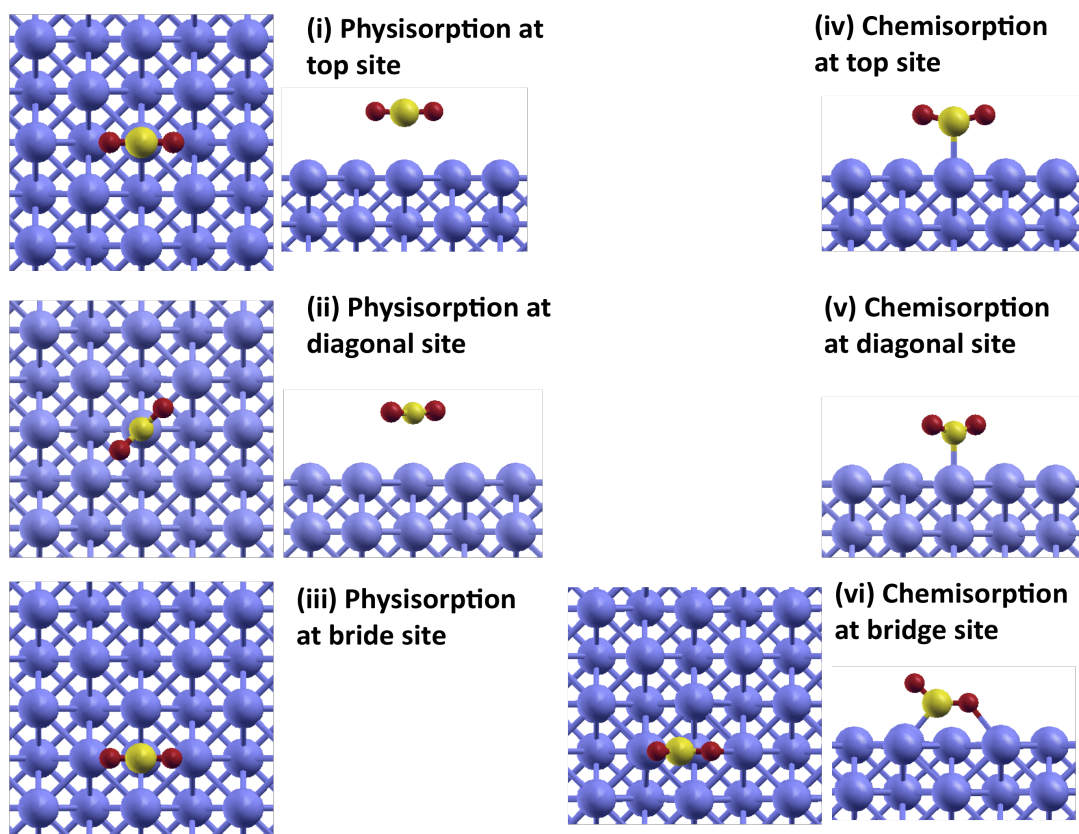


Figure 3.1. Adsorption geometries of CO₂ on different sites of Pd (001) surface.

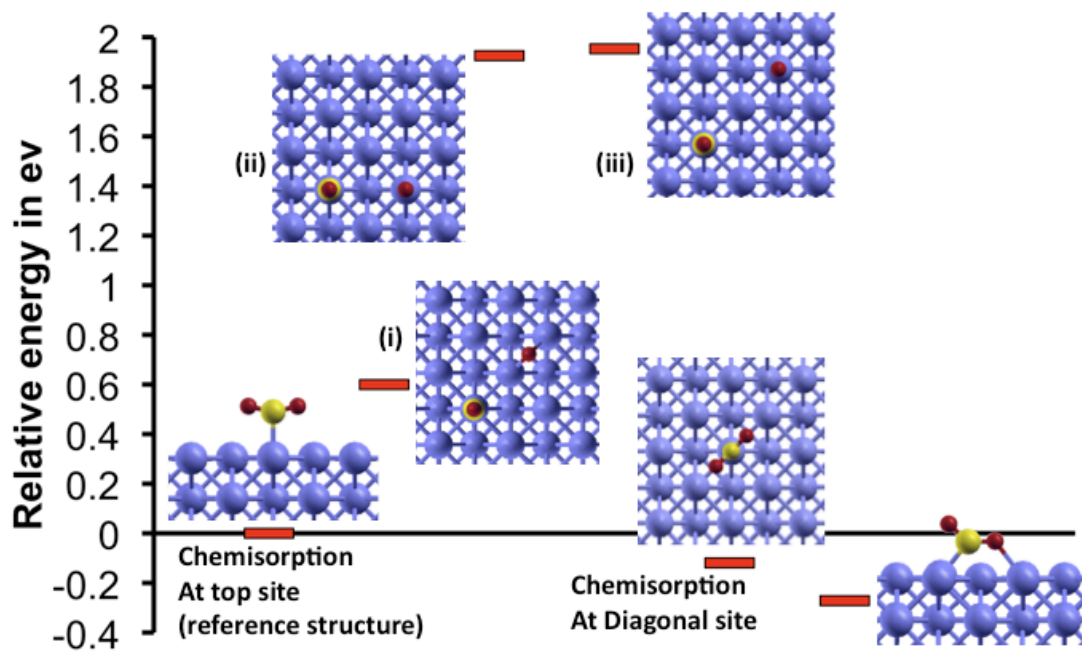


Figure 3.2. Relative energy diagram of “CO₂ dissociation” of Pd (001) surface.

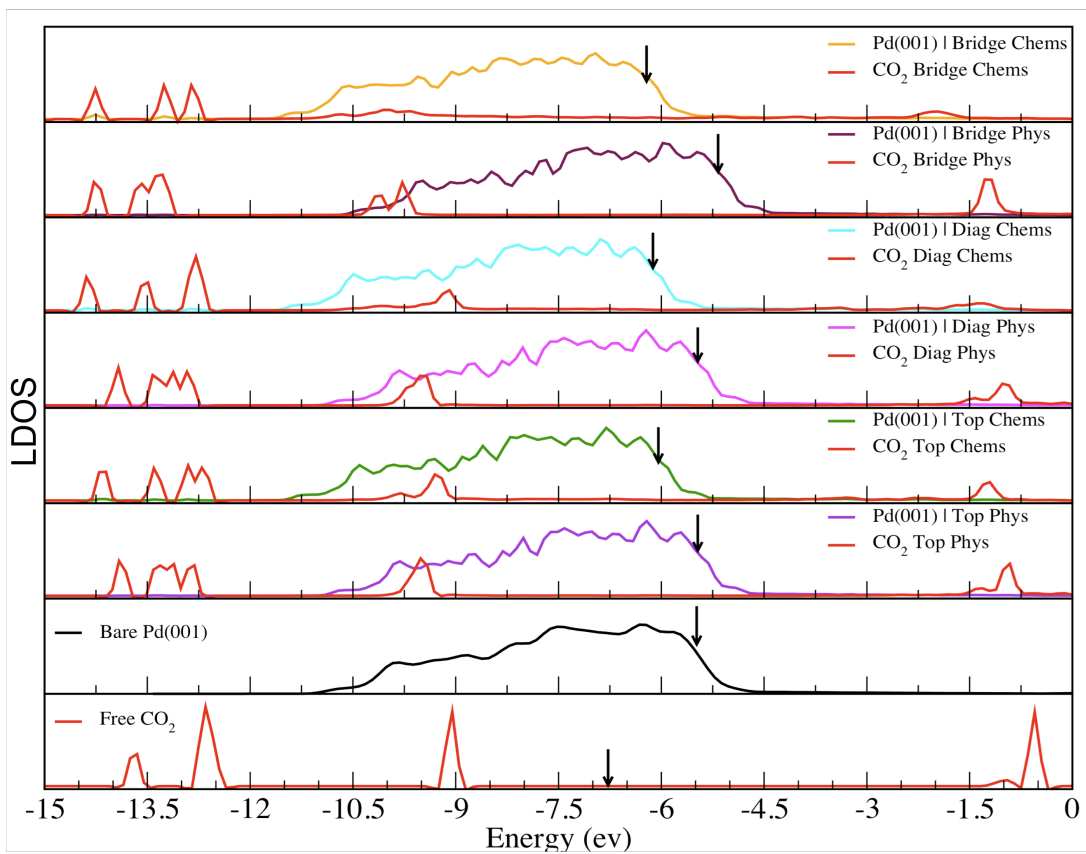


Figure 3.3. Surface LDOS of Pd (001) with adsorbed CO₂ at different sites.

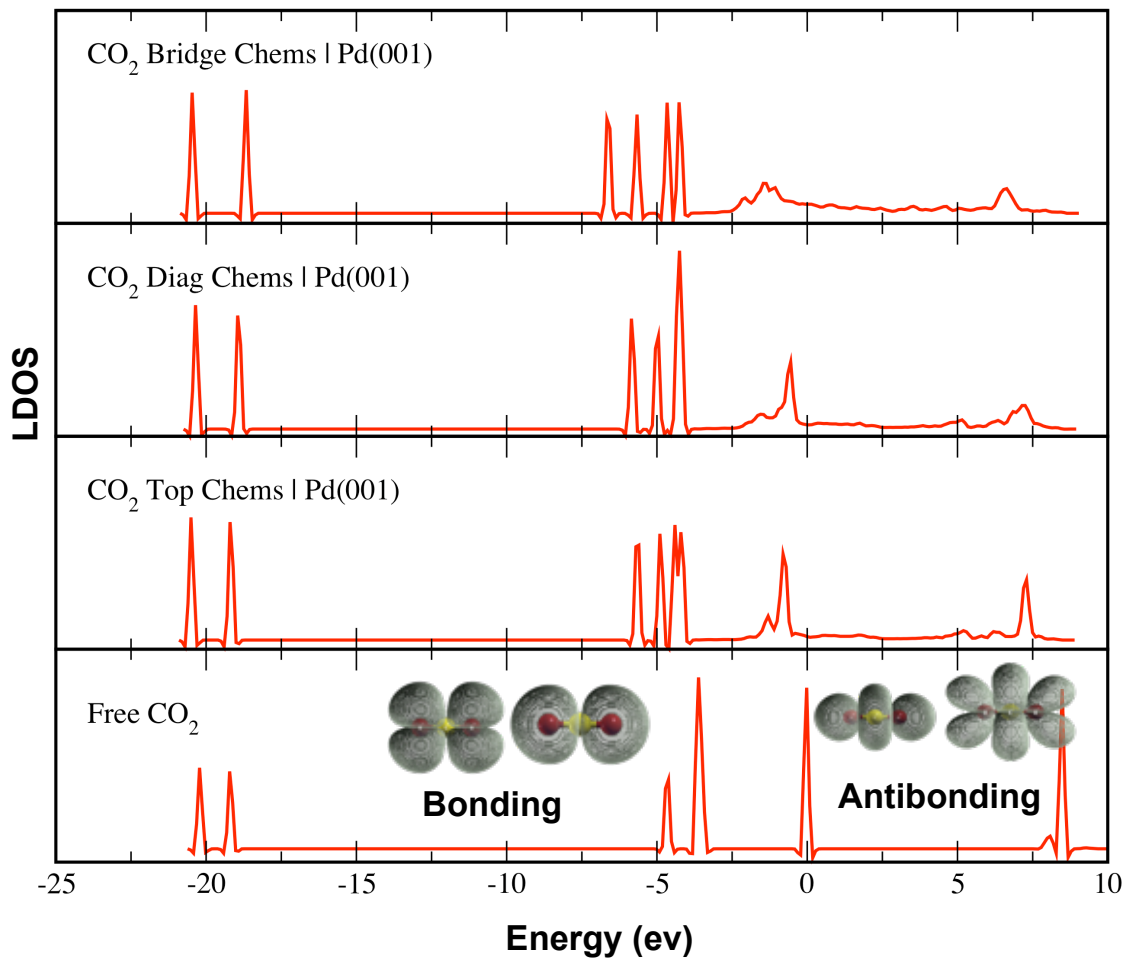
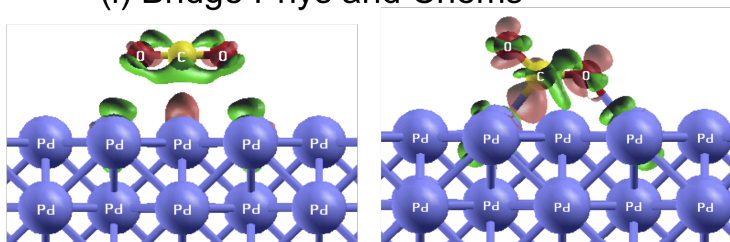
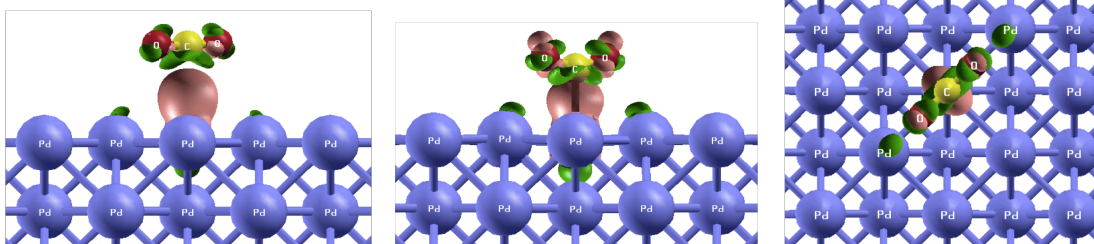


Figure 3.4. LDOS of CO₂ on Pd (001) surfaces.

(i) Bridge Phys and Chems



(ii) Diagonal Phys and Chems



(iii) Top Phys and Chems

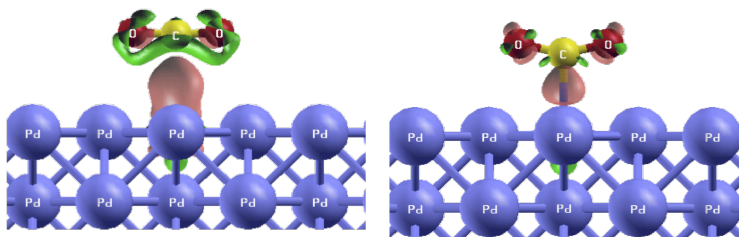


Figure 3.5. The charge density difference $[\rho(\text{Surface+adsorbant}) - \rho(\text{Surface}) - \rho(\text{adsorbant})]$ plot of “adsorptions of CO_2 on Pd (001) surface”. Pink = more positive, Green = more negative.

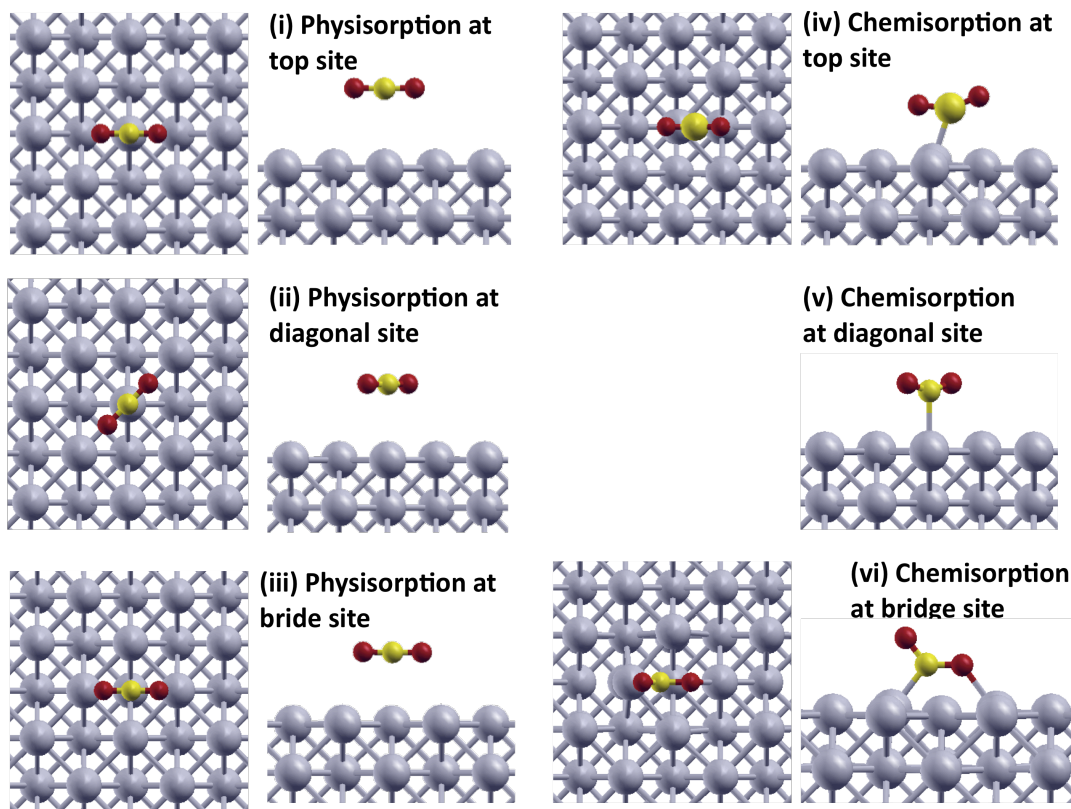


Figure 3.6. Adsorption geometries of CO₂ on different sites of Pt (001) surface.

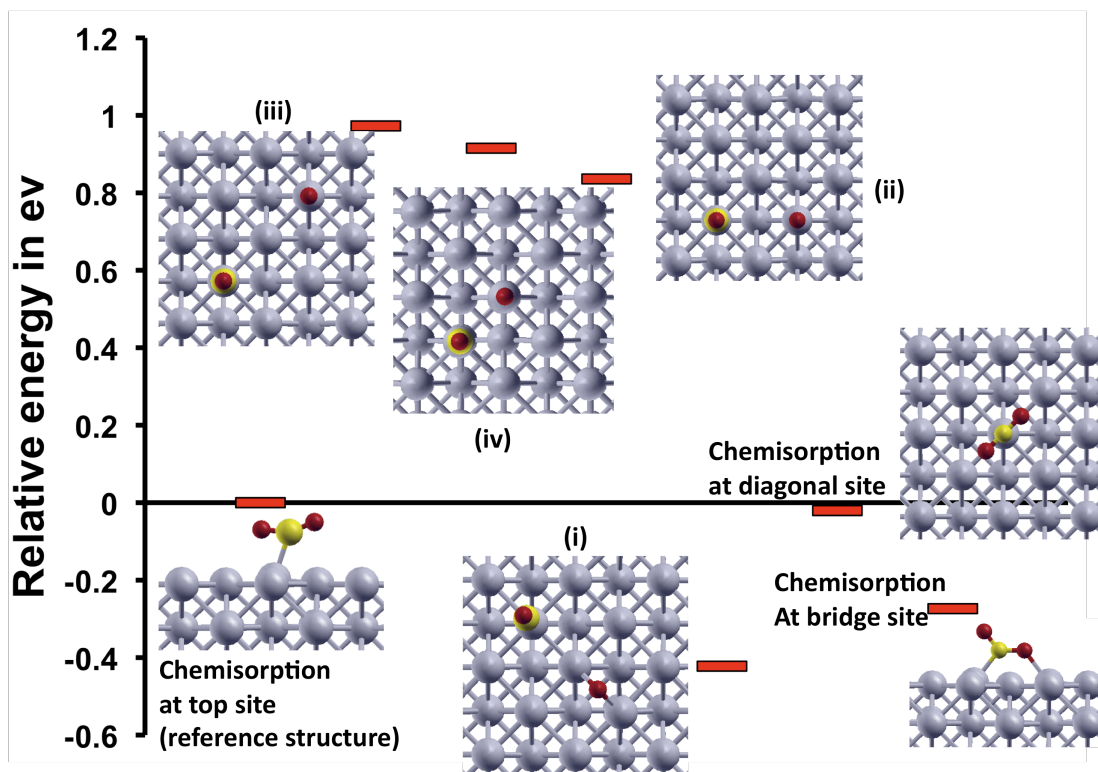


Figure 3.7. Relative energy diagram of “CO₂ dissociation” of Pt (001) surface.

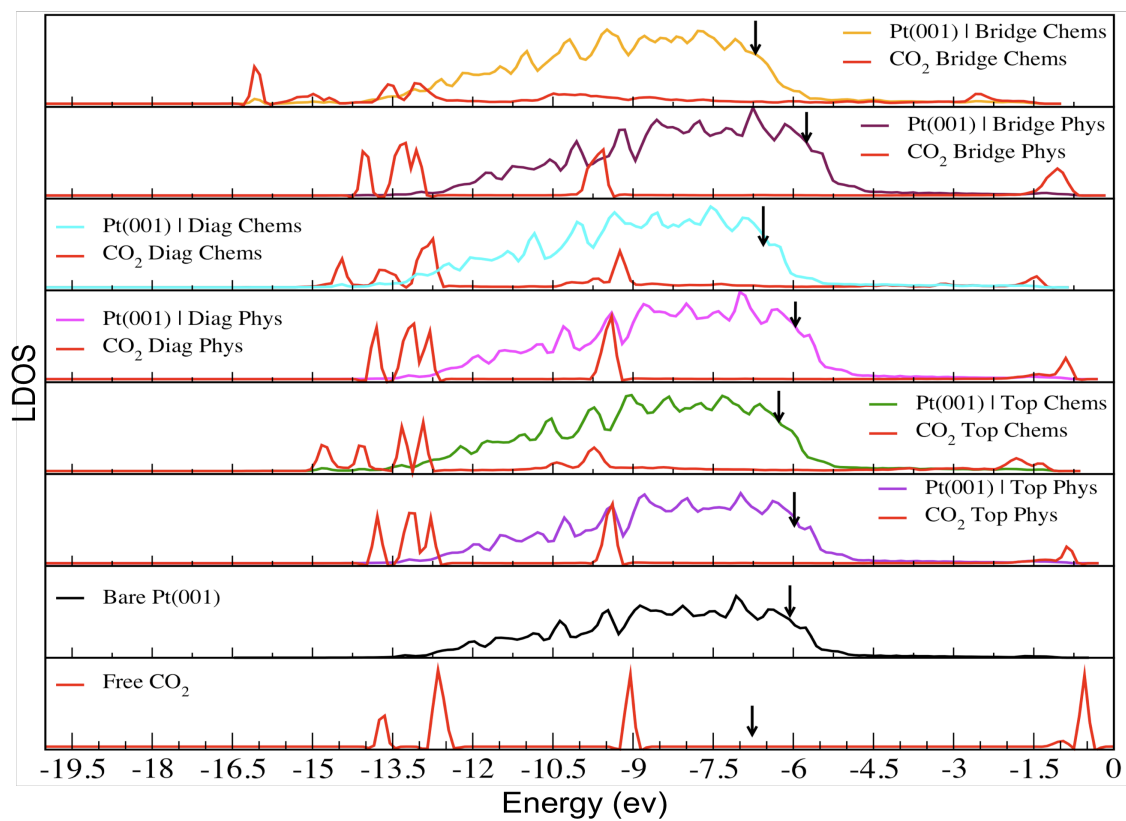


Figure 3.8. Surface LDOS of Pt (001) with adsorbed CO₂ at different sites.

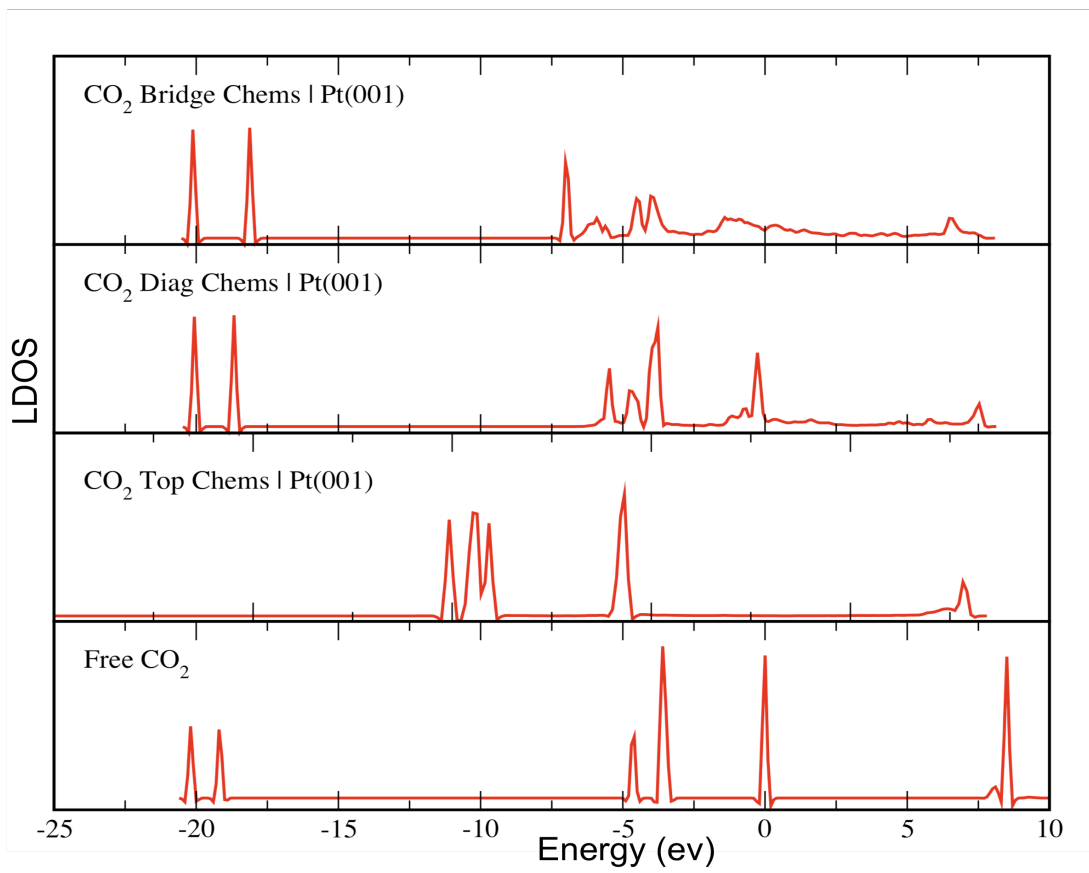


Figure 3.9. LDOS of CO₂ on Pt (001) surfaces.

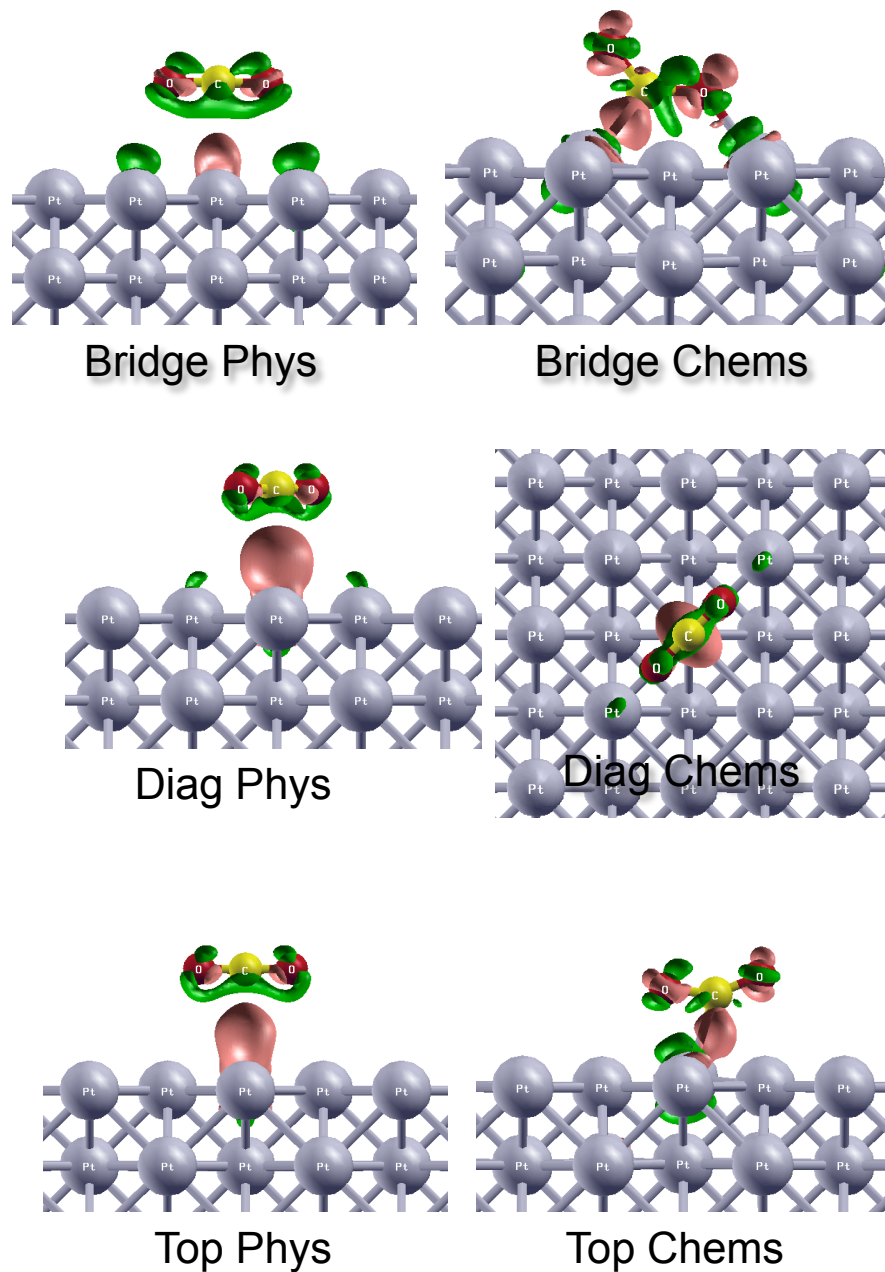


Figure 3.10. The charge density difference $[\rho(\text{Surface+adsorbant}) - \rho(\text{Surface}) - \rho(\text{adsorbant})]$ plot of “adsorptions of CO₂ on Pt (001) surface”. Pink = more positive, Green = more negative.

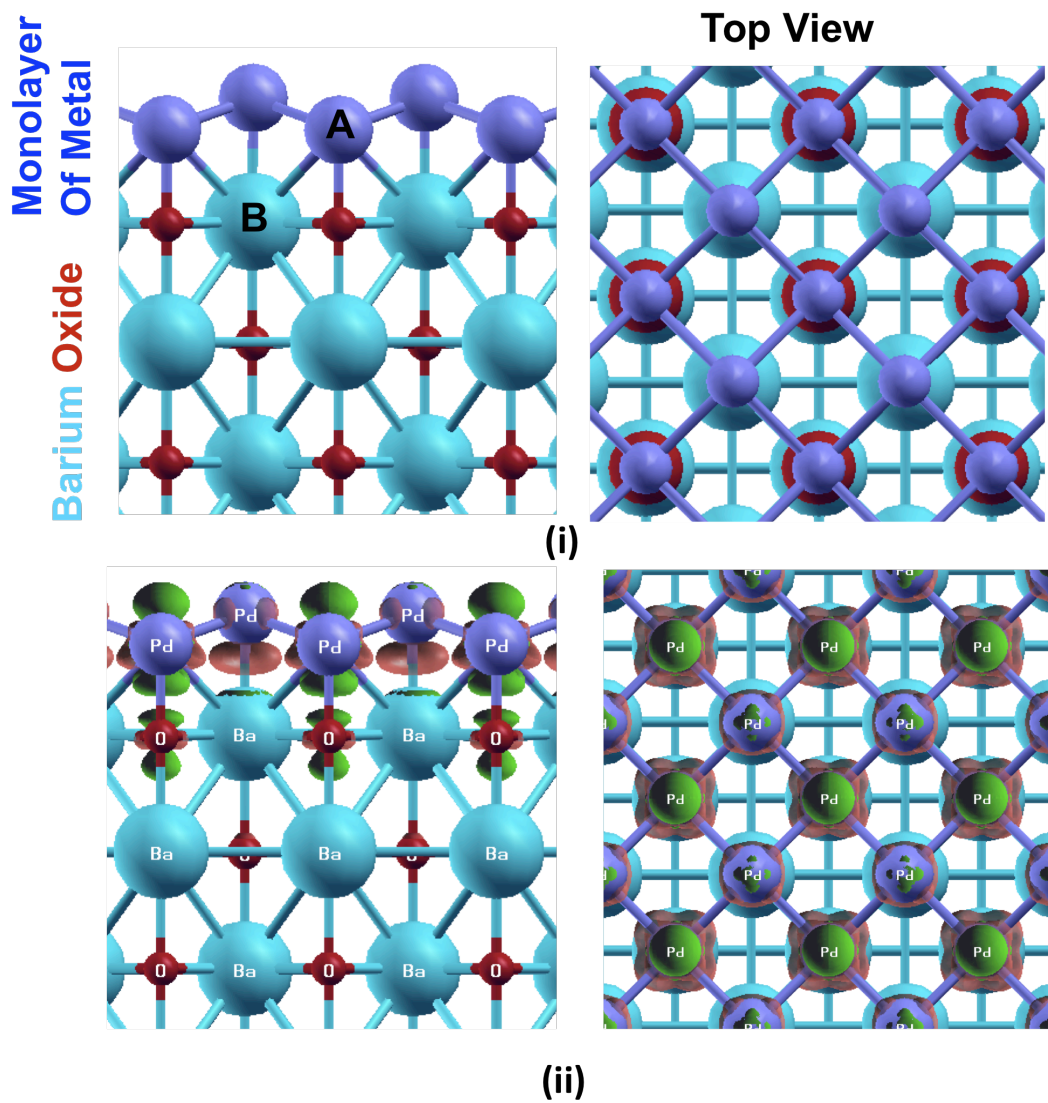


Figure 3.11. Barium oxide supported metal thin films: site A is supported over O atom and Site B is supported over Ba.

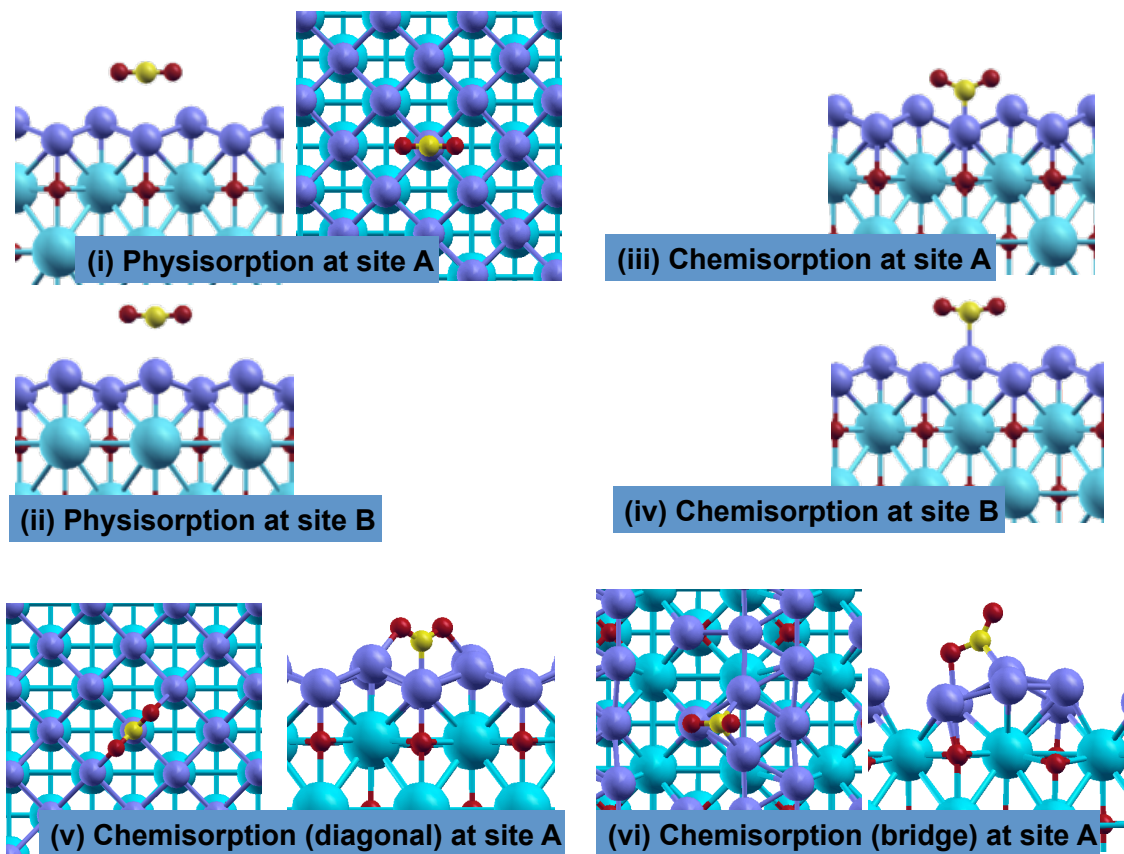


Figure 3.12. Activation of CO_2 on 1LPd/BaO (001) surface: (i) physisorption at site A (v) chemisorption at diagonal site; (vi) chemisorption at bridge site have shown in top and side view.

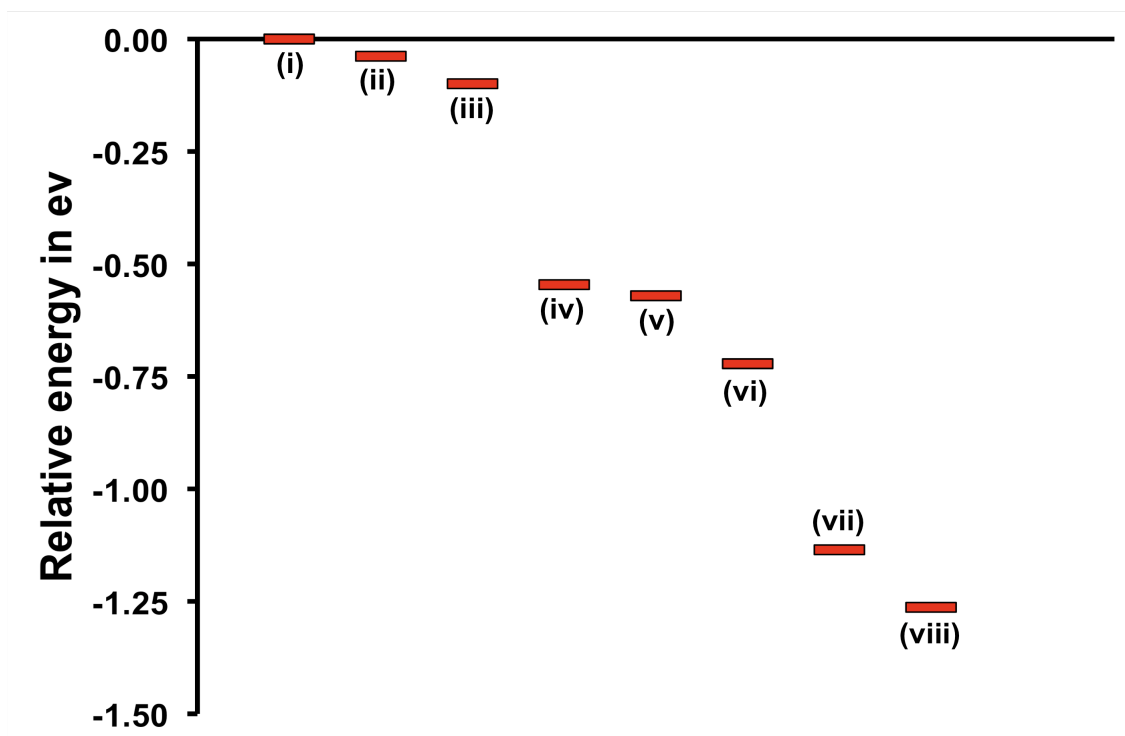


Figure 3.13(a). Relative energy diagram of “CO₂ dissociation” on 1LPd/BaO (001) surface.

(i) Chemisorption at top (reference)

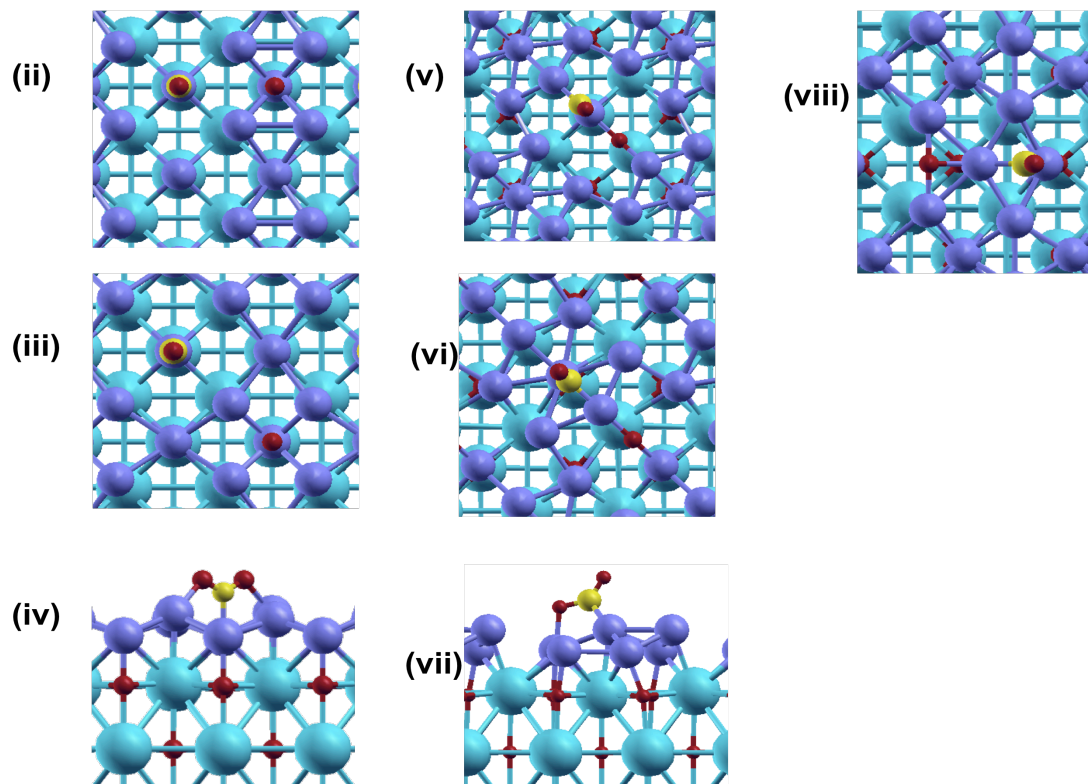


Figure 3.13(b). Optimized structures of dissociation: the energetics are given in Figure 3.13(a).

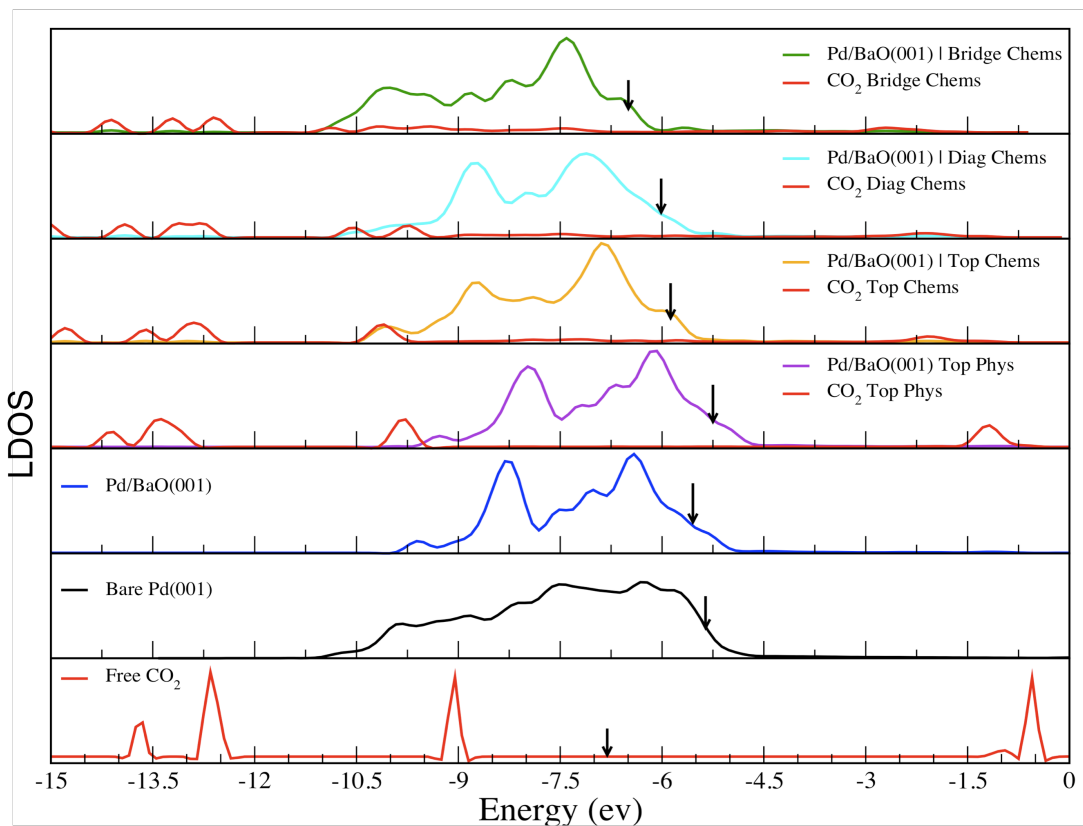


Figure 3.14. Surface LDOS of 1LPd/BaO (001) with adsorbed CO₂ at different sites. From the bottom, the LDOS of free CO₂, LDOS of bare Pd (001) surface, LDOS of Pd monolayer over BaO; LDOS of CO₂ at different sites and d orbital of monolayer Pd on 1LPd/BaO (001) surface.

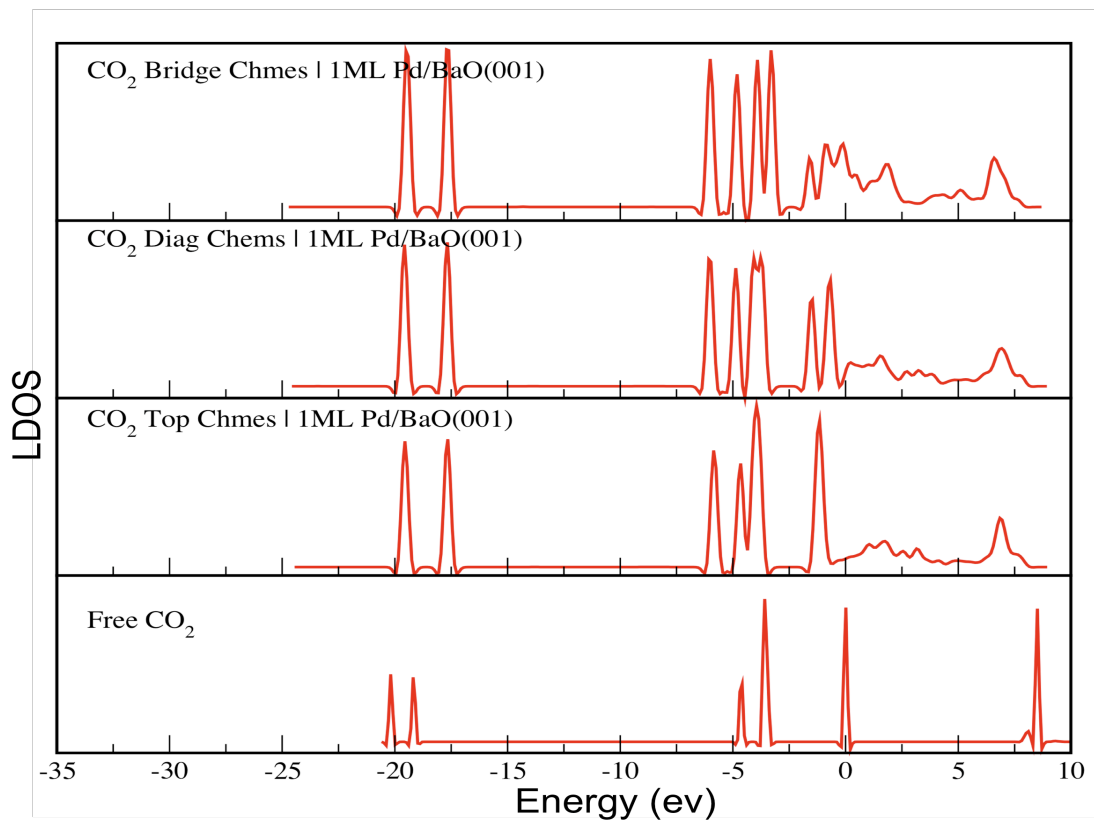


Figure 3.15. LDOS of CO₂ on 1LPd/BaO (001).

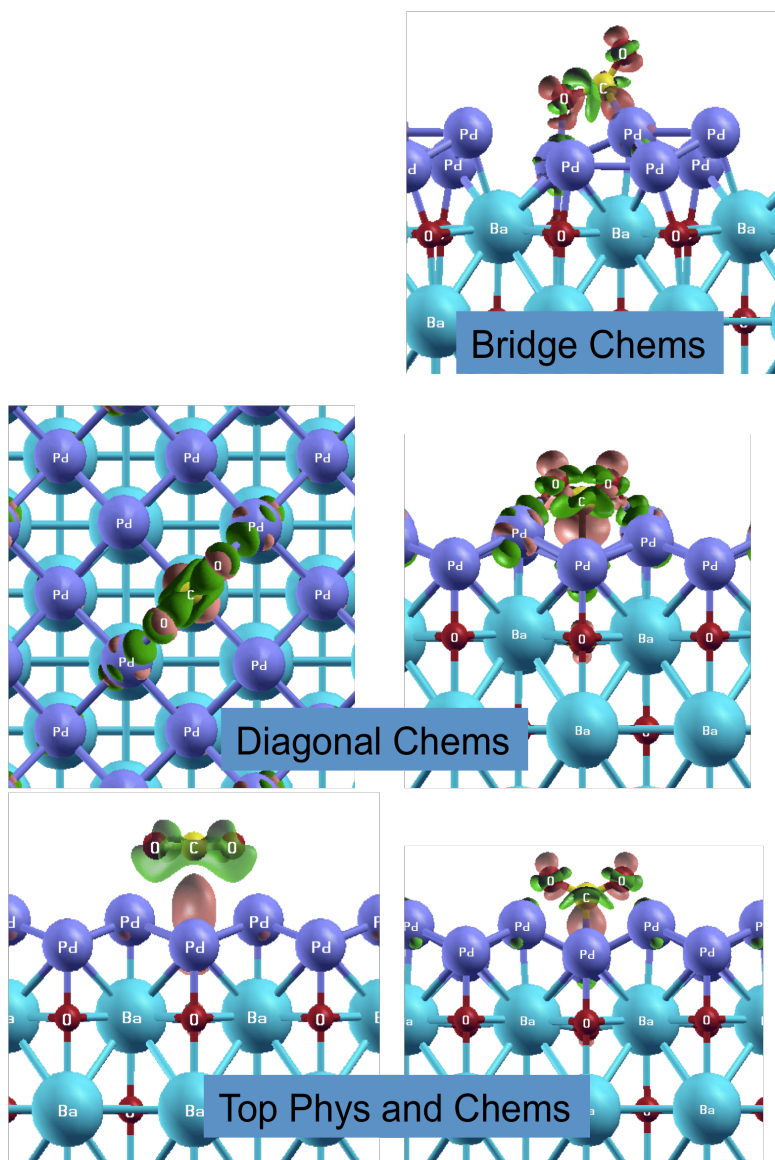


Figure 3.16. The charge density difference plot of “adsorptions of CO₂ on 1LPd/BaO (001) surface”. Pink = more positive, Green = more negative.

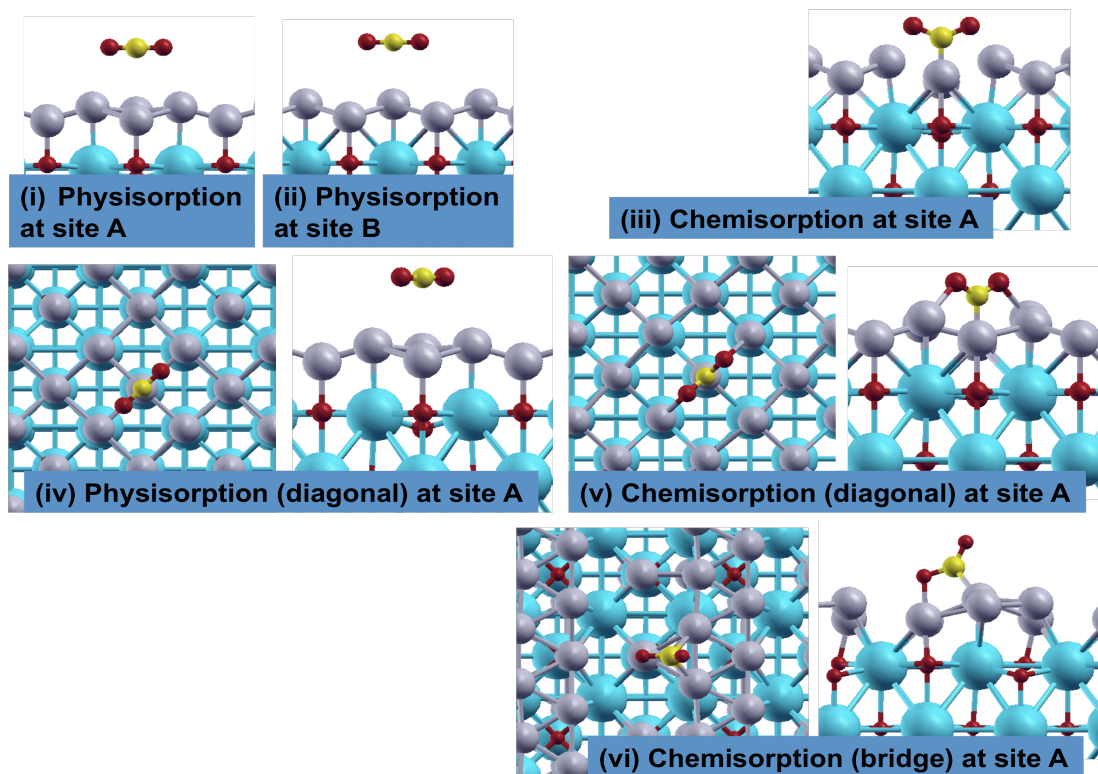


Figure 3.17. Activation of CO_2 on 1LPt/BaO (001) surface: (iv) physisorption at diagonal site (v) chemisorption at diagonal site; (vi) chemisorption at bridge site have shown in top and side view.

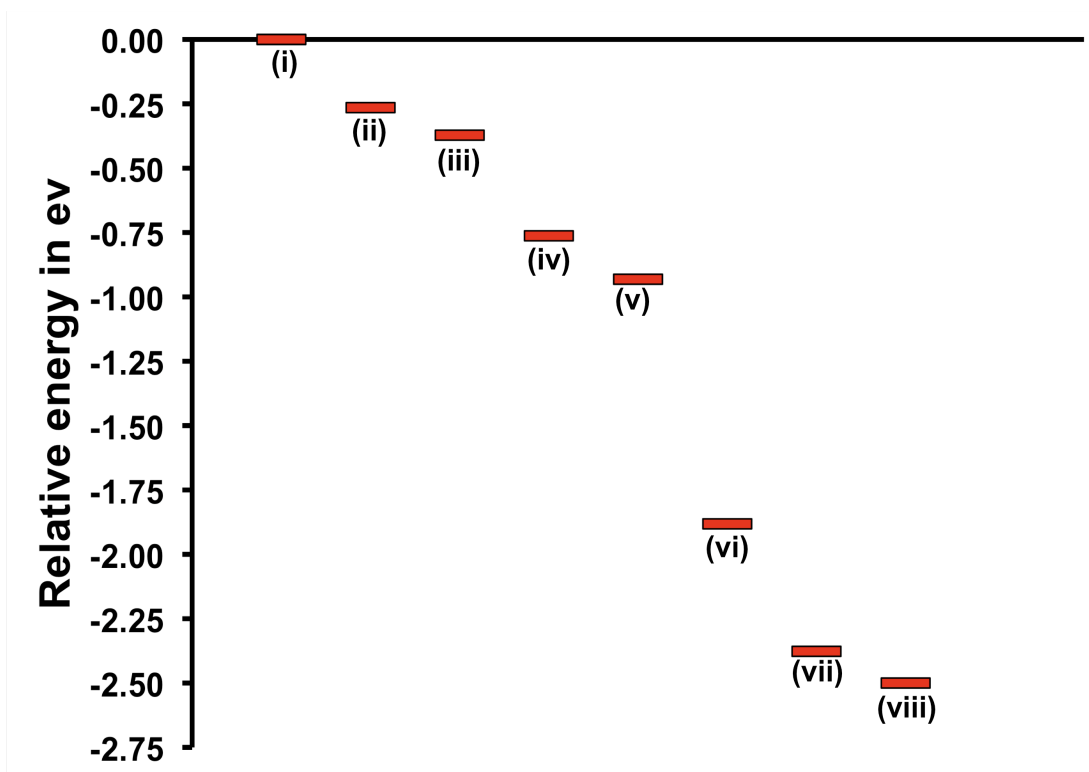


Figure 3.18(a). Relative energy diagram of “CO₂ dissociation” on 1LPt/BaO (001) surface.

(i) Chemisorption at top (reference)

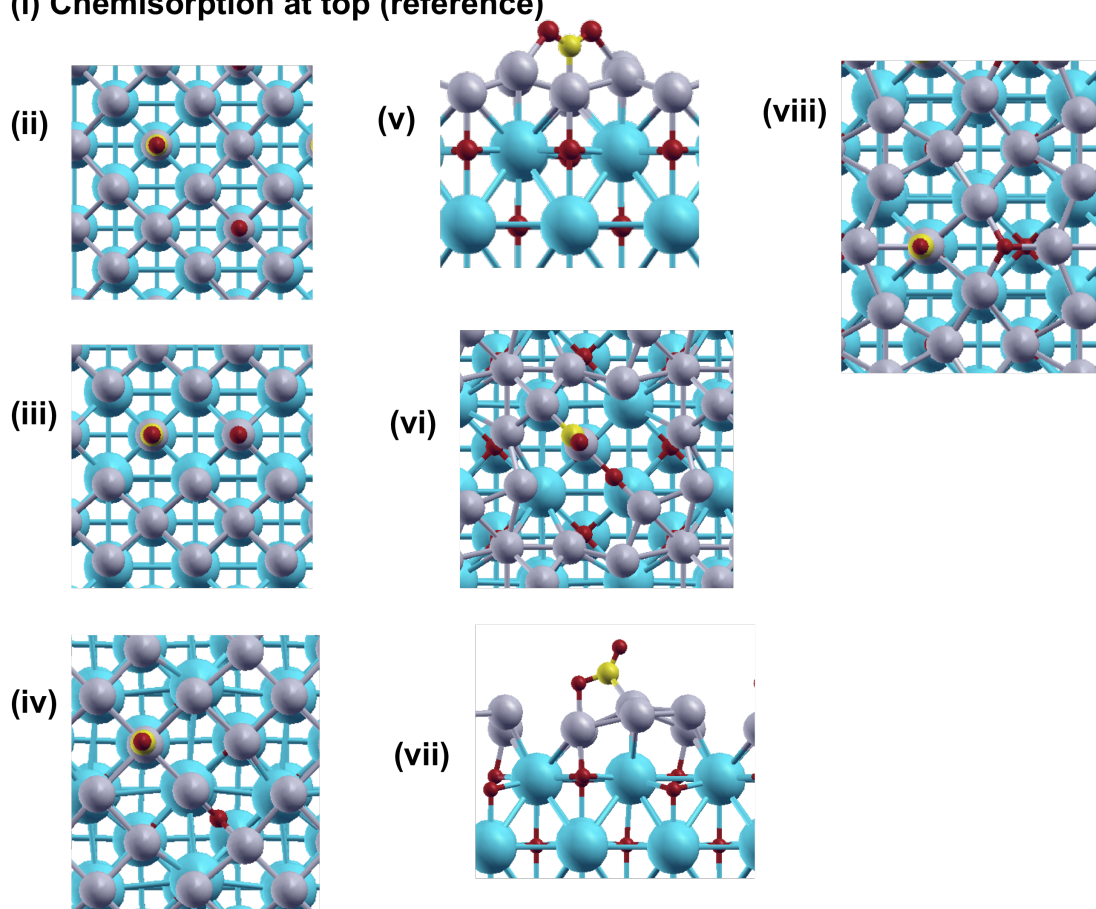


Figure 3.18(b). Optimized structures of dissociation: the energetics are given in Figure 3.18(a).

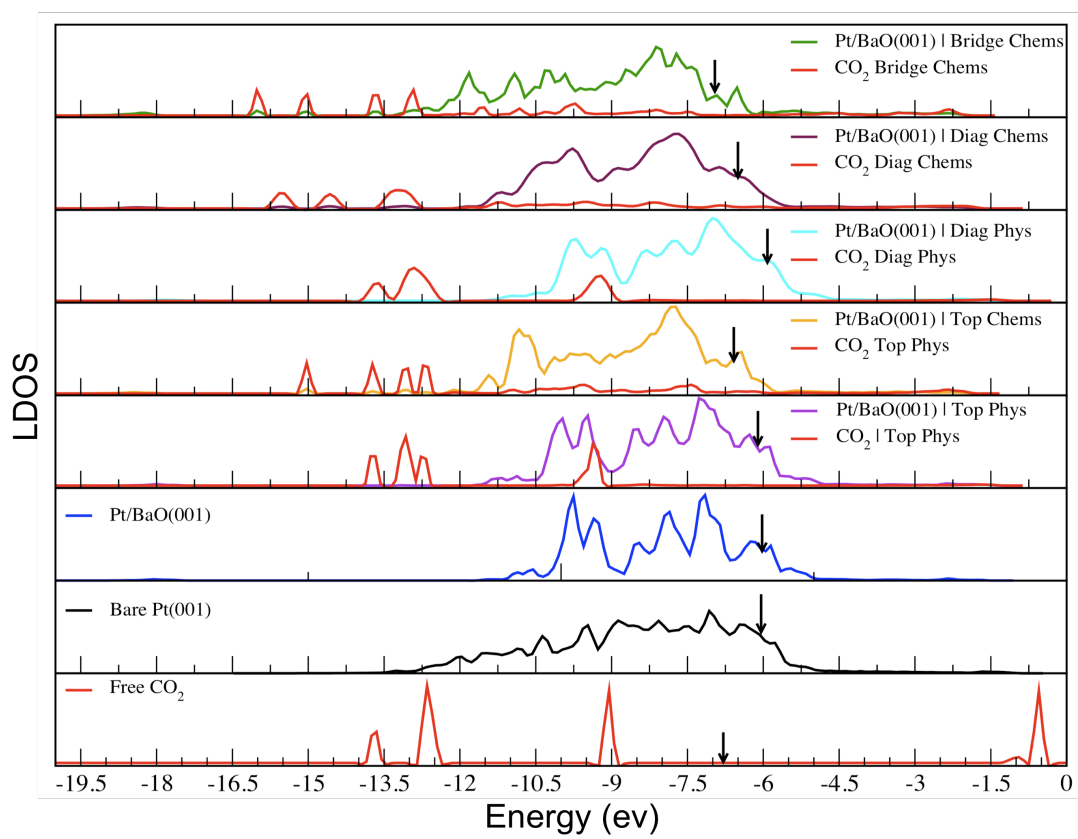


Figure 3.19. Surface LDOS of 1LPt/BaO (001) with adsorbed CO₂ at different sites. From the bottom, the LDOS of free CO₂, LDOS of bare Pt (001) surface, LDOS of Pt monolayer over BaO; LDOS of CO₂ at different sites and d orbital of monolayer Pt on 1LPt/BaO (001) surface.

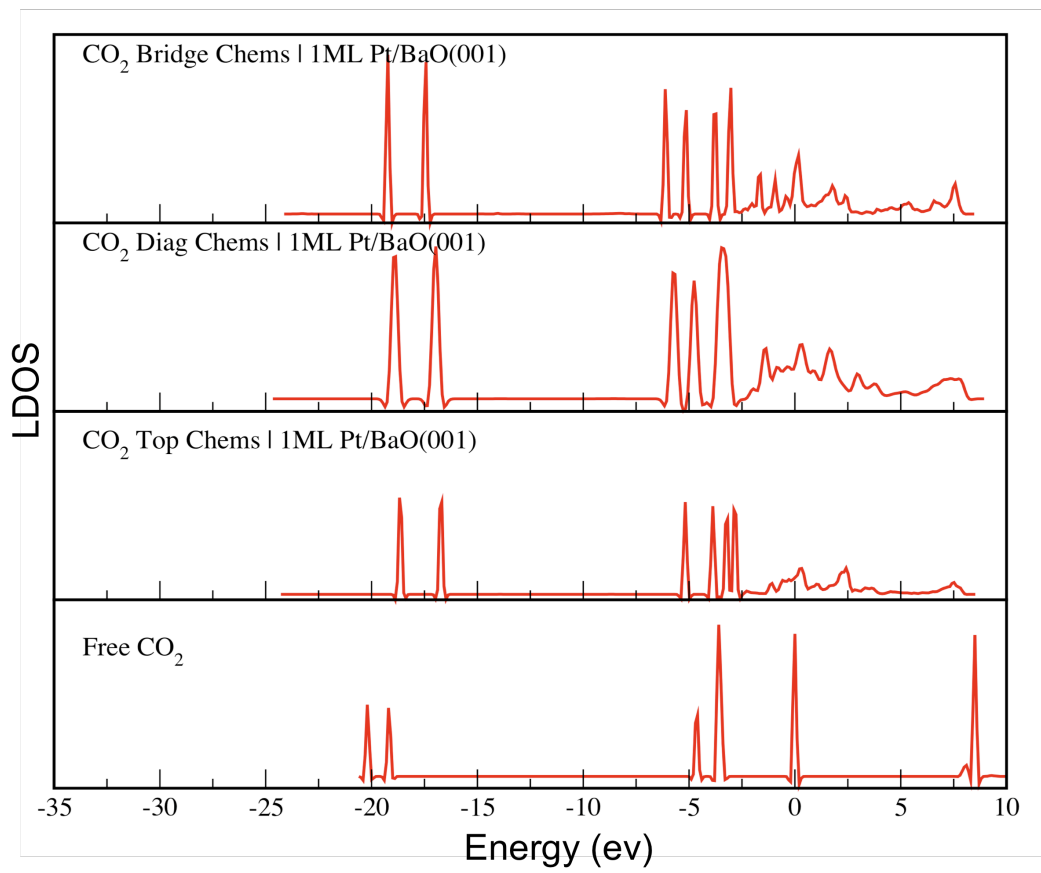


Figure 3.20. LDOS of CO₂ on 1Pt/BaO (001) surface.

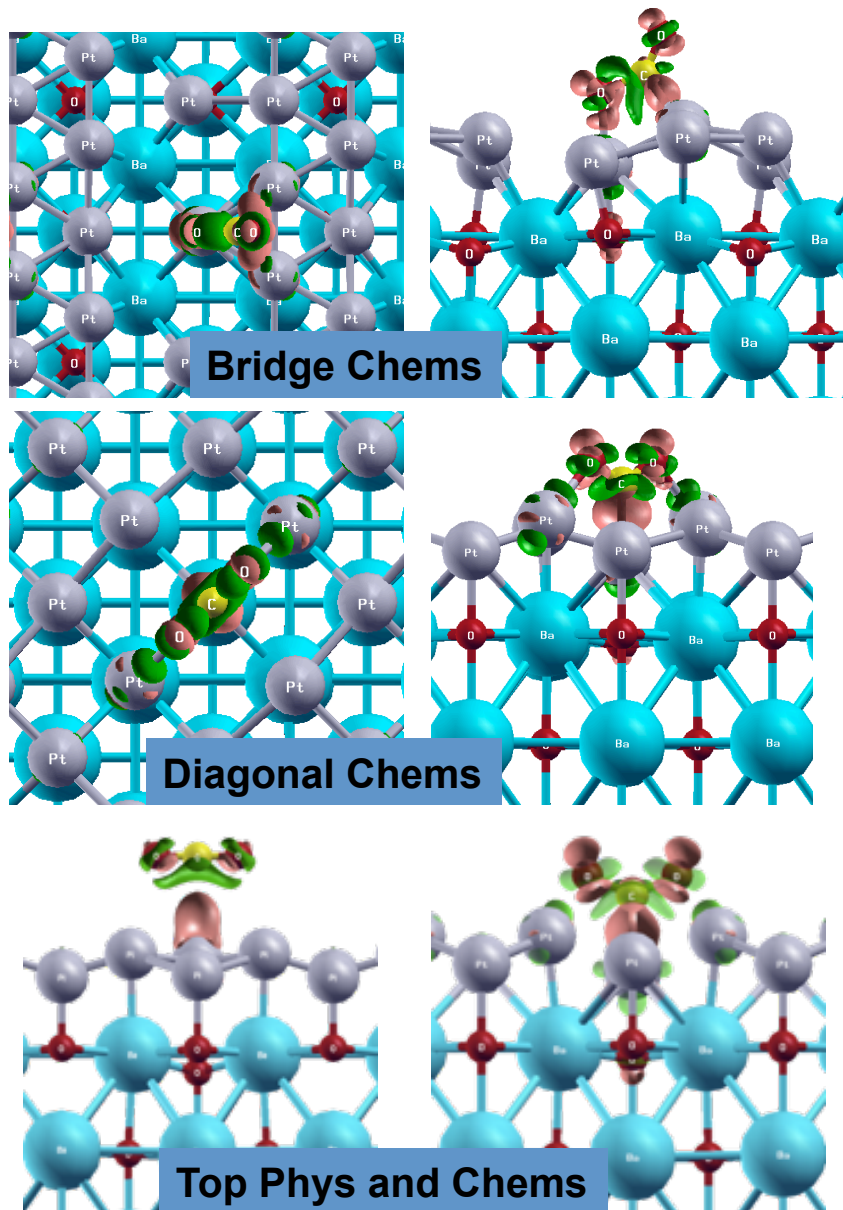


Figure 3.21. The charge density difference plot of “adsorptions of CO₂ on 1LPt/BaO (001) surface”. Pink = more positive, Green = more negative.

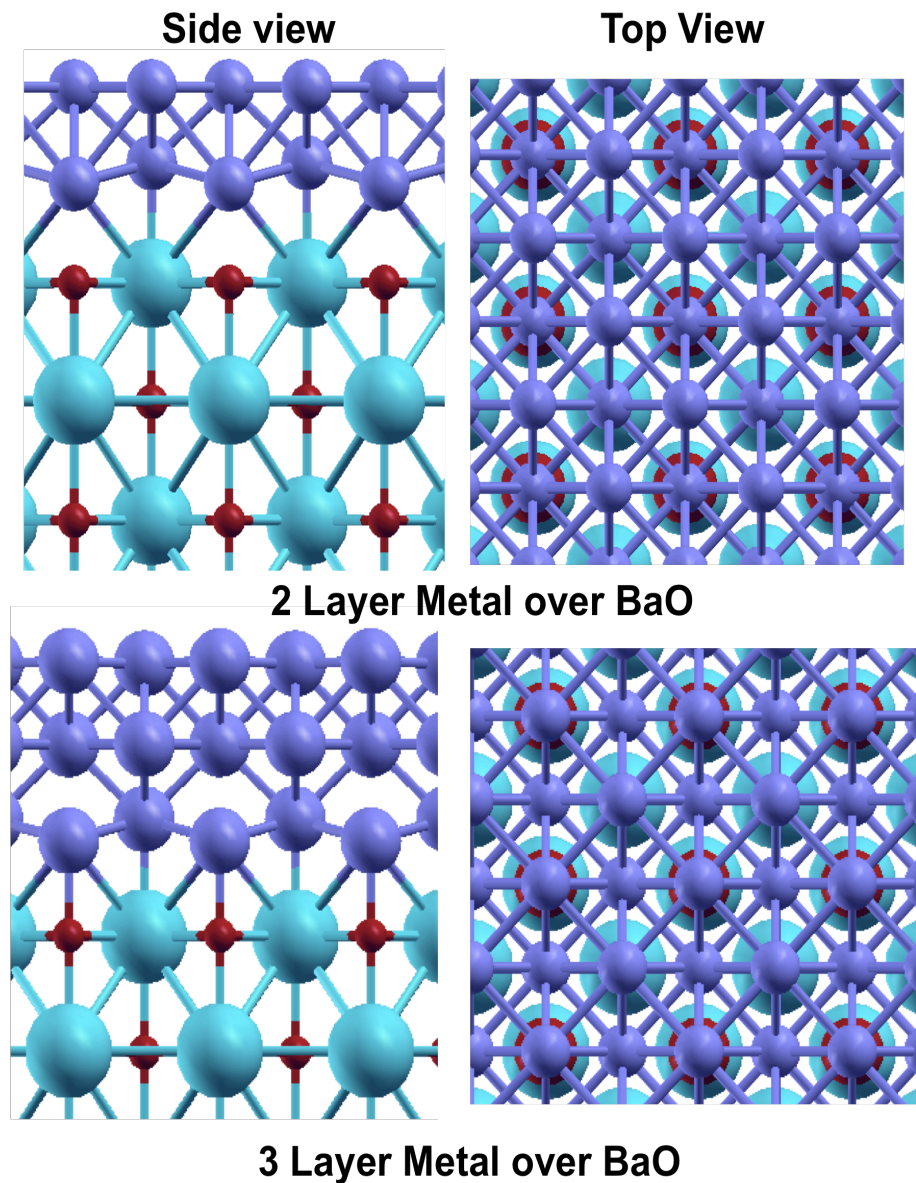


Figure 3.22. Barium oxide supported metal thin films. Upper panel: two layer metals over BaO, Lower panel: three layer metals over BaO. The site where the metal is supported over O atom is the most active site for the adsorption of CO₂. Refer to Figure 3.11.

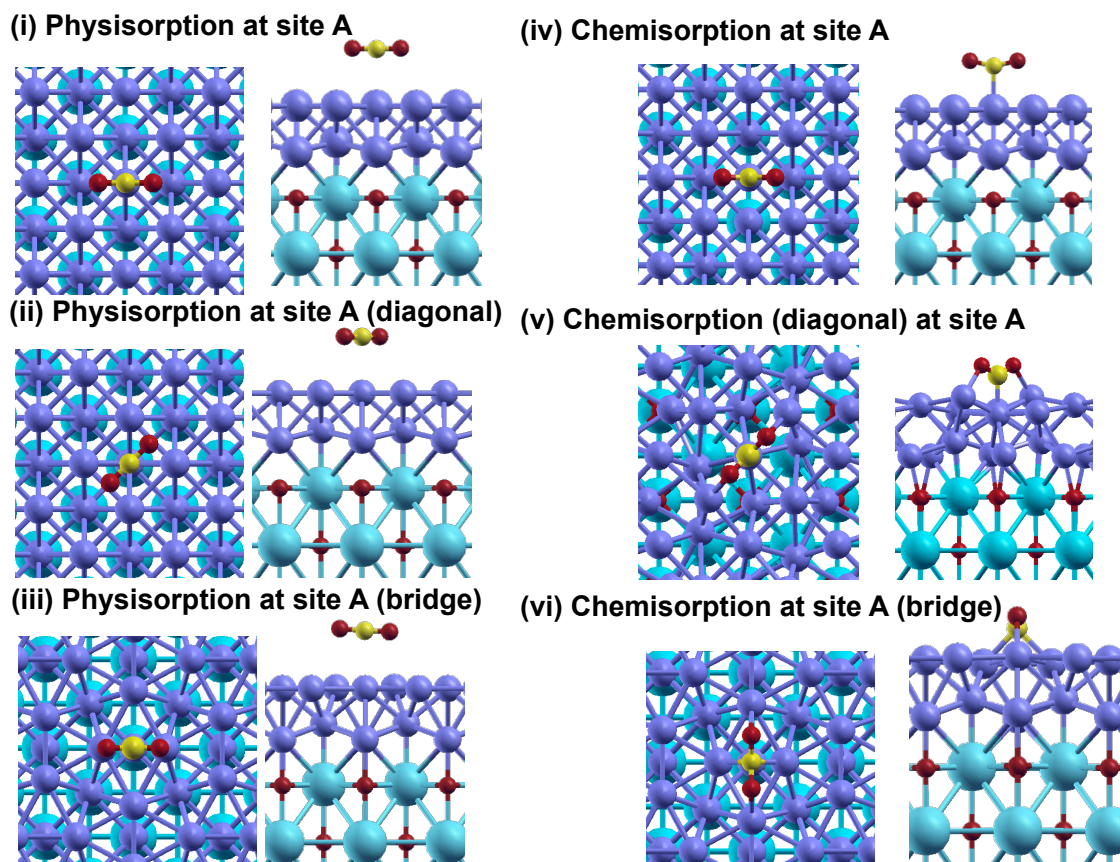
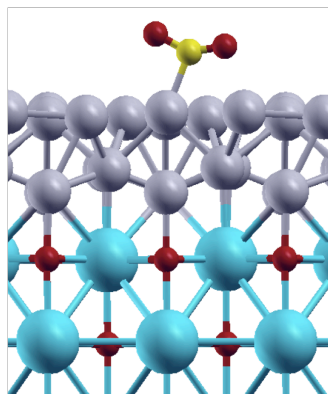
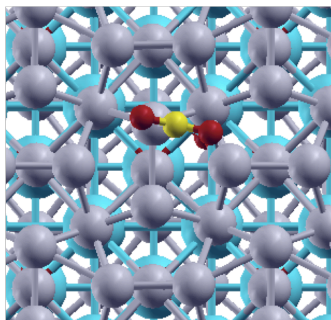
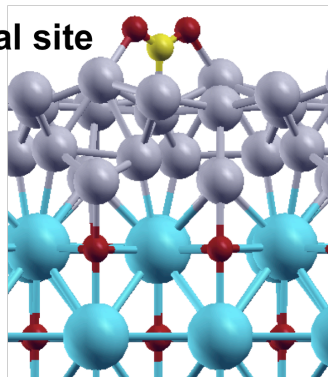
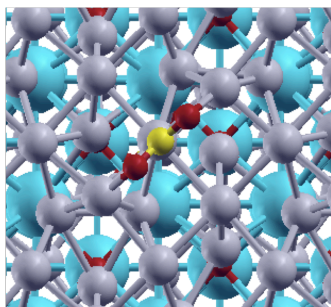


Figure 3.23. Activation of CO₂ on 2LPd/BaO (001) surface.

(i) Chemisorption at top site



(ii) Chemisorption at diagonal site



(iii) Chemisorption at bridge site

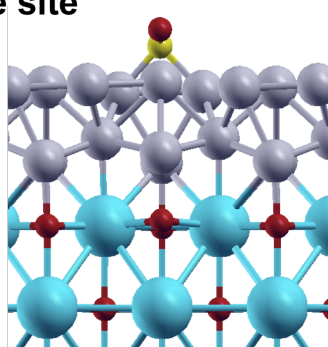
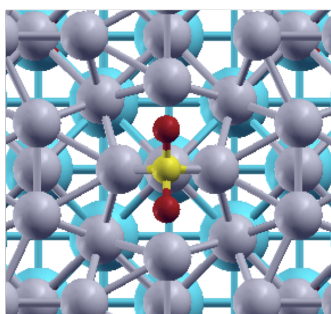
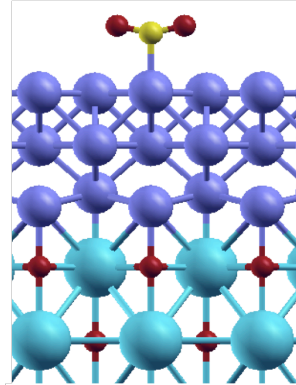
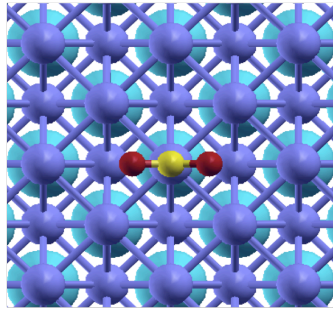
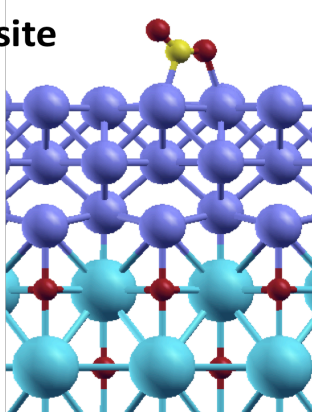
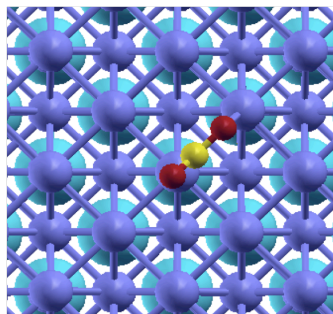


Figure 3.24. Activation of CO₂ on 2LPt/BaO (001) surface.

(i) Chemisorption at top site



(ii) Chemisorption at diagonal site



(iii) Chemisorption at bridge site

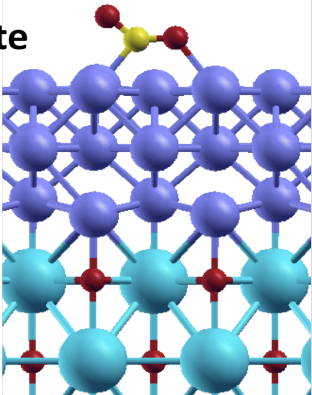
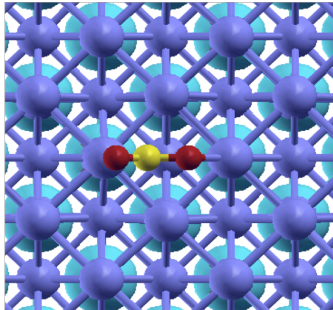
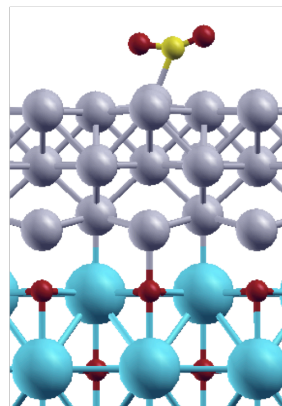
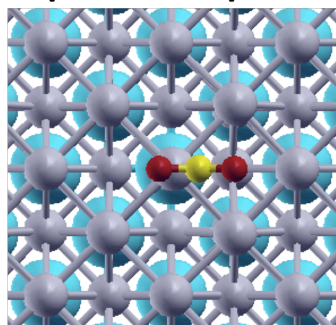
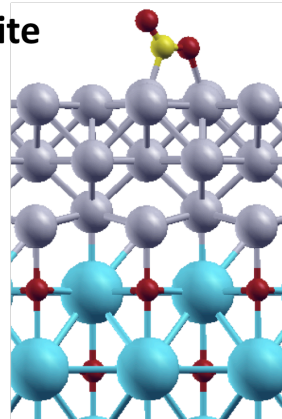
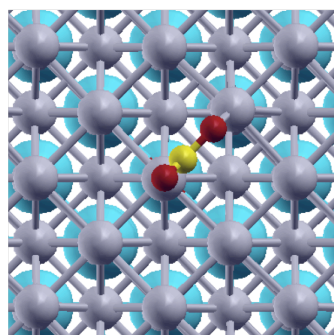


Figure 3.25. Activation of CO₂ on 3LPd/BaO (001) surface.

(i) Chemisorption at top site



(ii) Chemisorption at diagonal site



(iii) Chemisorption at bridge site

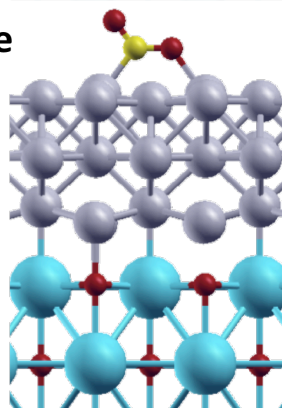
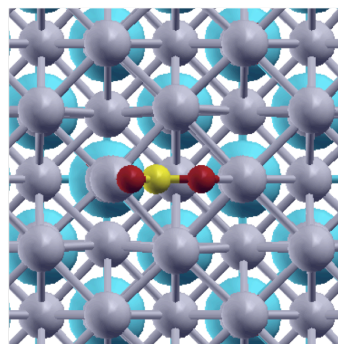


Figure 3.26. Activation of CO₂ on 3LPt/BaO (001) surface.

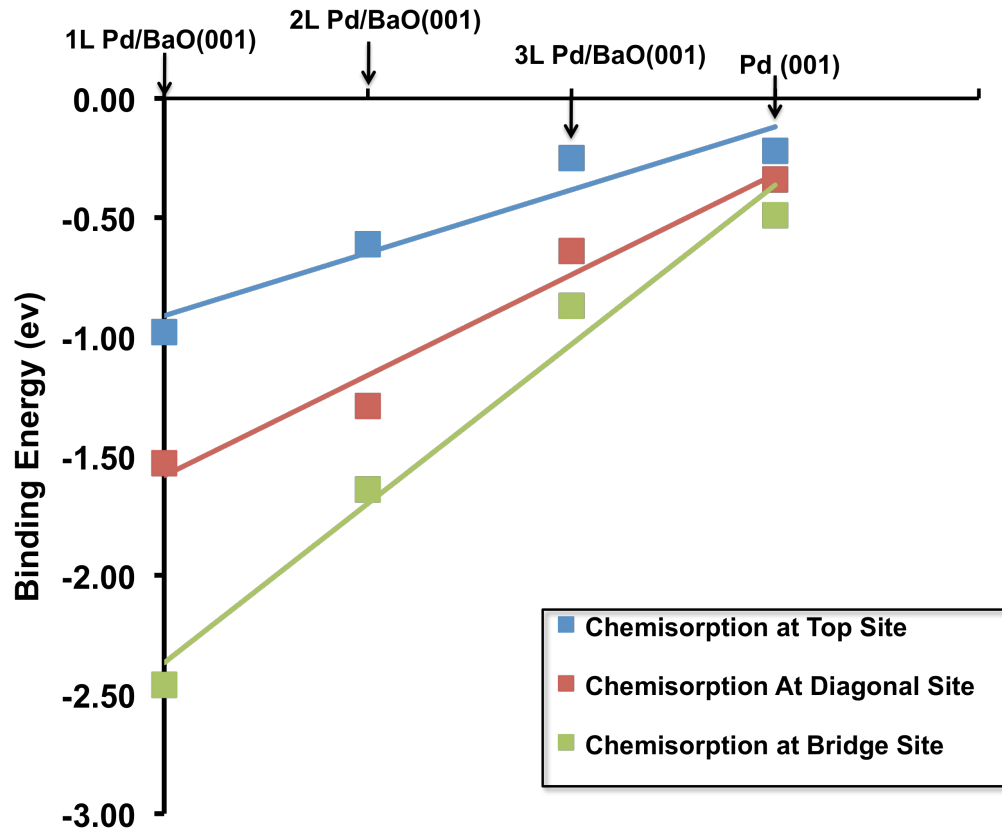


Figure 3.27. Binding energies of CO₂ on different surfaces of Pd and Pd/BaO.

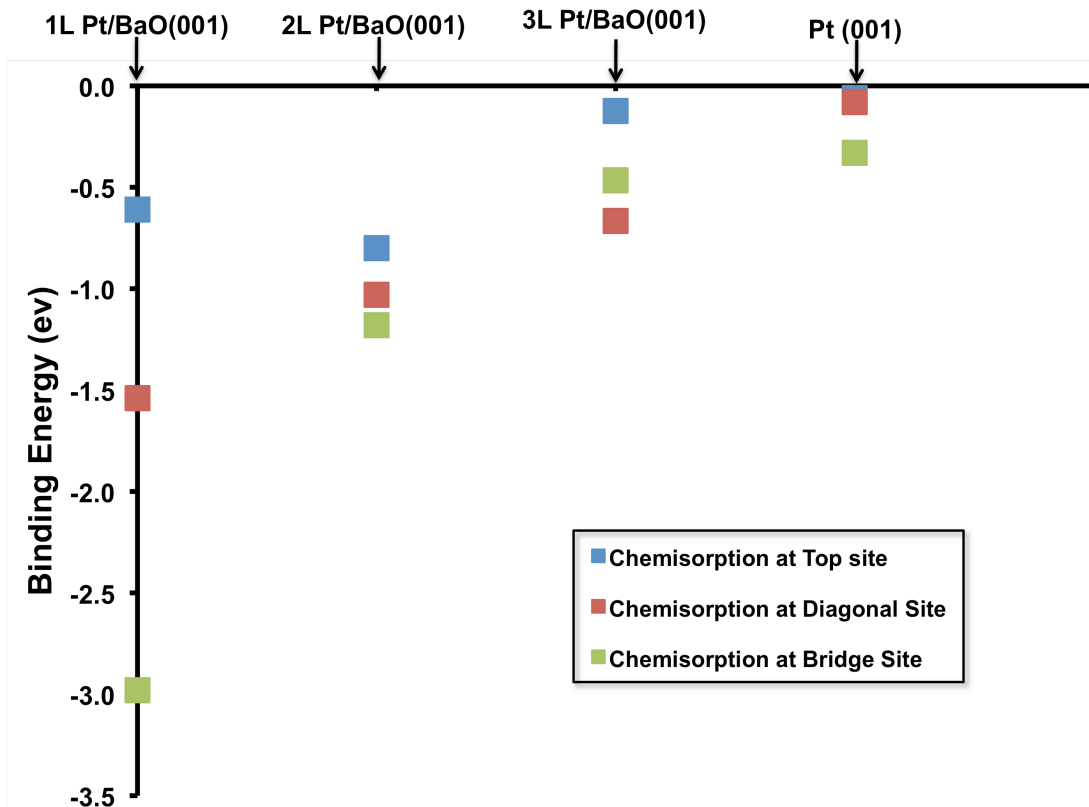


Figure 3.28. Binding energies of CO₂ on different surfaces of Pt and Pt/BaO.

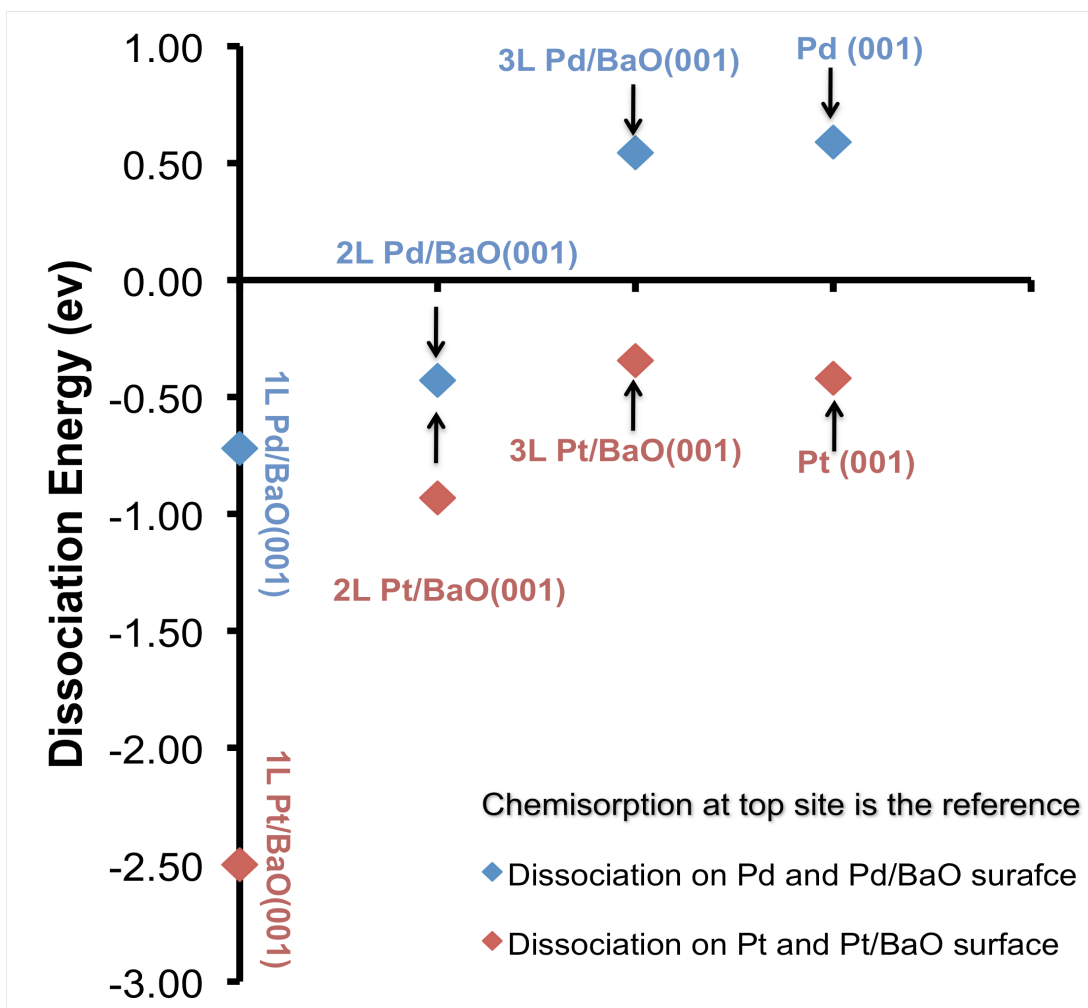


Figure 3.29. Dissociation energy of CO_2 [$\text{CO}_2 \rightleftharpoons \text{CO} + \text{O}$] on different surfaces. Chemisorption energy at top site is considered as reference to calculate to dissociation energy.

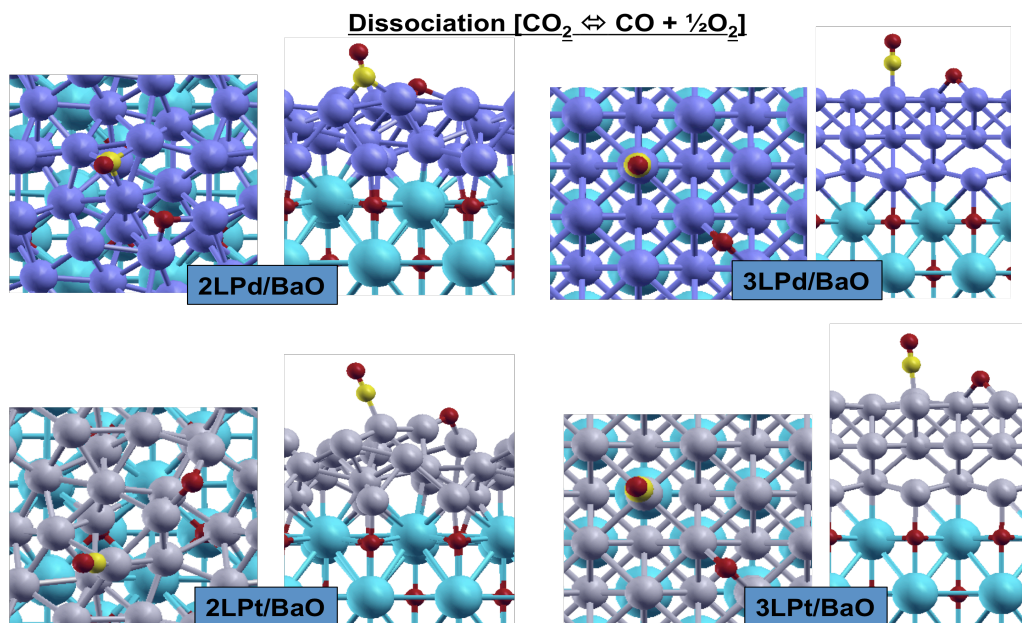


Figure 3.30. Dissociation of CO₂ to CO and O atom over 2LMetal/BaO and 3LMetal/BaO. The dissociation energies are plotted in Figure 3.29.

References

- ¹ S. Inoue, N. Yamazaki, Organic and bio-organic chemistry of carbon dioxide, Tokyo, 1982
- ² H. J. Freund, M. W. Roberts, Surface Science Report, **25**, 225, 1996
- ³ X. Ding, L. De. Rogatis et.al., Physical Review B, **76**, 195425 (2007)
- ⁴ S. G. Wang, X. Y. Liao et.al., Journal of Physical Chemistry C, **111**, 16934, 2007
- ⁵ S. G. Wang, D. B. Cao et.al., Journal of Physical Chemistry B, 109, 18956, 2005
- ⁶ H. J. Freund and R. P. Messmer, Surface Science, **172**, 1, 1986
- ⁷ A. Ding, V. Pagan et. al., Materials Science and Engineering C, 27, 1355-1359, 2007
- ⁸ M. P. Habas et. al., Surface Science, 431, 208-219, 1999
- ⁹ Martin M. Halmann, Chemical fixation of Carbon Dioxide, 1993
- ¹⁰ W. Jin et al., Environment Science Technology, **42**, 3064-3068, 2008
- ¹¹ B. Hammer, Phy. Rev Lett., 89, 016102, 2002
- ¹² M. Nunez and M. B. Nardelli, Phys. Rev. B, 73, 235422, 2006
- ¹³ J.P. Perdew and A. Zunger. Phys. Rev. B, 23, 5048, 1981
- ¹⁴ <http://www.pwscf.org/>

Chapter 4

First principles calculations of structural, vibrational properties of mono and bi-layer graphene

4.1 Introduction

Graphene is a one-atom-thick planar sheet of sp^2 -bonded carbon atoms that are densely packed in a honeycomb crystal lattice¹. In recent years monolayer and few-layer graphene have attracted great attention due to the unique properties. Graphene is quite different from most conventional three-dimensional materials. Intrinsic graphene is a semi-metal or zero-gap semiconductor. Understanding the electronic structure of graphene is the starting point for finding the band structure of graphite. It was realized early on that the E-K relation is linear for low energies near the six corners (K points) of the two-dimensional hexagonal Brillouin zone, leading to zero effective mass for electrons and holes². Due to this linear “dispersion” relation at low energies, electrons and holes near these six points, two of which are inequivalent, behave like relativistic particles described by the Dirac equation for spin 1/2 particles^{3,4}. Hence, the electrons and holes are called Dirac fermions, and

the six corners of the Brillouin zone are called the Dirac points³. The peculiar electronic structure of graphene⁵ implies that electrons have a negligible effective mass around the K point of the Brillouin zone (Dirac Point) and thus a high electrical conductivity. Besides their unusual electronic structure, vibrational properties and phonon spectra are also of fundamental interest from which many physical properties such as thermal conductivity and heat capacity can be derived. Furthermore phonons are crucial for studying the electrical transport properties. Electrons excited by optical methods can be scattered into another state by electron-phonon coupling (EPC). EPC is a key physical parameter for ballistic transport^{6,7}, quantum Hall effect⁸, Raman spectra and phonon dispersions.

4.2 Computational Details

In the present analysis, we take advantage of the PWSCF package of the QUANTUM-ESPRESSO distribution⁹ to model the characteristic graphene lattice dynamics. DFT calculations were performed with LDA Troullier-Martin (TM) norm-conserving pseudopotentials¹⁰. The wave functions and the charge density are expanded using energy cutoff of 55 Ry and 220 Ry respectively. We used 48×48×1 Monkhorst-Pack meshes adopted for Brillouin-zone sampling with 0.02 Ry Fermi-Dirac smearing in the electronic occupation. The calculation also employs the theoretical lattice parameter $a=2.46 \text{ \AA}$, which is in excellent agreement with the

experimental value at 300 K. For bilayer graphene, the Bernal stacking is considered with the interlayer distance set to the theoretical minimum of 3.36 Å. The dynamical matrix is explicitly calculated on $6 \times 6 \times 1$ q-point mesh. We carefully and extensively check the convergence in the energy cut-off and phonon frequencies with the K-point sampling of the Brillouin zone and the inter-layer vacuum spacing of mono and bi-layer graphene.

4.3 Band structure

The honeycomb lattice of graphene has two carbon atoms per unit cell. Each atom has one s and three p orbitals. The s orbital and two in-plane p orbitals are tied up in graphene's strong covalent bonding and do not contribute to its conductivity. The remaining p orbital, oriented perpendicular to the molecular plane, is odd under inversion in the plane and hybridizes to form π (valence) and π^* (conduction) bands¹¹. In the Bloch band description of graphene's electronic structure, orbital energies depend on the momentum of charge carriers in the crystal Brillouin zone. First, the band structure of the single layer graphene (SLG) is reproduced in Figure 4.1¹². SLG is then characterized by the linear dispersion of the π bands near Fermi level (E_F) represent massless fermions. The Fermi energy separates occupied and empty states. In a neutral graphene sheet, this is the energy where valence and conduction band meets. The bands from conical valleys that touch at two of the high

symmetry points, conventionally labeled K and K', in the Brillouin zone. Near these points the energy varies linearly with the magnitude of momentum measured from the Brillouin zone corners. The four other Brillouin zone corners are related to K and K' by reciprocal lattice vectors and do not represent distinct electronic states. When several SLGs interact to form a few layer graphene (FLG), the former anti-symmetric π bands are split whereas the σ ones are much less affected, as shown for an AB bilayer in Figure 4.2. Bands of FLGs containing more layers behave similarly (not shown). Magnification of the band structure of bi-layer graphene, in the vicinity of the K point, is presented in Figure 4.2 (a). The valence band (VB) and conduction band (CB) of the AB bi-layer only admit two contact points, avoiding any deep domain of coexistence of electrons and holes. We also conducted ab initio density functional theory study of the influence of an external electric field on graphene bi-layer (AB stacking) which is depicted in Figure 4.2 (a), (b) and (c). The electric field was applied along z direction. Figure 4.2 (a) shows the DFT energy band structure of bilayer graphene in the absence of an applied external electric field. When $E_{\text{ext}}=0$ eV, the low-energy band dispersion is nearly parabolic at two in-equivalent corners, K and K', of the hexagonal BZ. The valence and conduction bands meet at the Fermi level. In the absence of an external electric field, bi-layer graphene, like single-layer graphene, is a zero-gap semiconductor. At finite electric field, $E=1.542$ V/nm, however, the low-energy bands near the K point split, and the band gap is 0.23 eV as it is shown in Figure 4.2 (b). When the external electric field is higher ($E=3.08$

V/nm), the band gap is 0.46 eV as it is shown in Figure 4.2 (c). Therefore, gated graphene bi-layer systems are gate-voltage tunable narrow gap semiconductors¹³. However, as the strength of the applied field increases, the band gap continues to grow at the K point.

4.4 Phonon dispersions

Subsequent anticipation of the superior performance in device applications also makes it imperative to investigate the thermal properties of the graphene systems. Accordingly, a detailed knowledge of phonon dynamics is essential to accurately evaluate the lattice thermal conductivity [specifically, the energy, the group velocity and the lifetime for all wave vector]¹⁹. This can be provided by the first-principles calculations within the density-functional theory (DFT) and the density-functional perturbation theory (DFPT) as it was explained in Chapter 1 in this thesis.

Figure 4.3 provides the calculated phonon dispersion along the high-symmetry directions for monolayer and Figure 4.4 provides the phonon dispersion of bilayer graphenes with the typical A-B stacking. Compared to the available experimental and theoretical data in the literature^{14,15,16,17,18} they are in excellent agreement as summarized in Table I in reference 19 for the monolayer case. Our calculation also

seems to support the Kohn-like anomaly in the dispersion of the highest optical branches at the Γ and K points¹⁹. As for bi-layer graphene, the phonon band structure exhibits a very similar behavior except the so-called layer-breathing mode (denoted as ZO') that gives a nonzero frequency in the long wavelength limit (ZO'=78 cm⁻¹). This occurs when the c-directional vibration of carbon atoms in adjacent 2D layers becomes out of phase (i.e., optical mode). In graphite the corresponding mode has a frequency of 95 cm⁻¹. All other branches (namely, those except ZO' and ZA) for bi-layer are doubly degenerate with only small splitting that arise from the weak interlayer coupling. The right panel of Figure 4.4, we have shown the detailed dispersions for the high optical branches near Γ and K.

Our result¹⁹ estimates that the intrinsic thermal conductivity of both materials is around 2200 Wm⁻¹K⁻¹ at 300 K, a value close to the one observed theoretically and experimentally in graphite along the basal plane²⁰. It also illustrates the expected T⁻¹ dependence at higher temperatures. The little variation between monolayer and bi-layer thermal conductivities suggests that the number of layers may not affect significantly the in-plane thermal properties of these systems. The intrinsic thermal conductivity also appears to be nearly isotropic for graphene.

Figure 4.5 shows the phonon dispersion at K point under bias (at finite electric field, E=1.542 V/nm). Under a gate electric field, the frequencies of some phonon modes

at K show substantial dependence on monolayer graphene, suggesting potentially strong electron-phonon coupling. In the next section we will discuss the electron-phonon interaction on graphene.

4.5 Electron phonon interaction

The electron-phonon interaction in monolayer graphene is investigated using density functional perturbation theory. In this approach, the interaction potential can be obtained from the self-consistent electron response to atomic displacements caused by a phonon. As such, the outcome can account for non-adiabatic coupling between electrons and phonons. We obtained the scattering matrix elements for electron interaction with all of the relevant phonon modes. From the scattering matrix element we calculated the crucial quantities such as the electron-phonon spectral function, phonon density of states and phonon line-width. To determine the scattering rate of an electron due to the interaction with the phonons, the matrix elements $g_{\mathbf{k}+\mathbf{q}^j, \mathbf{k}j}^{\mathbf{q}^j}$ (Equation 24 in Chapter 1) are extracted from the self-consistent electron-phonon calculation. The detail of the electron-phonon matrix element is presented in the reference²¹. The phonon density of states is depicted in Figure 4.6. The peak of phonon density of states at higher frequency is dominant. In Figure 4.7 we have presented the electron-phonon spectral function (as it is described in Equation 25 in

Chapter 1). Figure 4.8 shows the phonon line-width of TO and LO mode along the high symmetry direction. Transport properties of materials are determined by the electron-phonon interaction in the material. The electron-phonon interaction is the process by which an electron in state is scattered to a state by the perturbation in the potential caused by a phonon q . As the phonon “moves” through a material, the motion of the ions is screened by the charge density. Assuming the ground state of the unperturbed system is known, the potential for the perturbed system can be viewed as a first order perturbation on the ground state potential ($V_{\text{eff}} = V_{\text{scf}} + \Delta V_q$). The scattering matrix elements, which describe the transition from the state $|\kappa\rangle$ to the state $|\kappa+q\rangle$, are the transitions through this ΔV_q . The spectral function measures contributions of phonons of frequency ω to scattering electrons at the Fermi level.

4.6 Conclusion

In this chapter we have presented the band structure, phonon dispersions and electron-phonon interactions of graphene. We calculated the thermal conductivity of mono and bi-layer graphene¹⁹. We presented a set of simple formulas which qualitatively explain the electron-phonon interaction in graphene. Our first principles analysis clearly illustrates that all in-plane phonons play an important role in electron-phonon interactions in graphene and must be considered for transport studies at room temperature²¹.

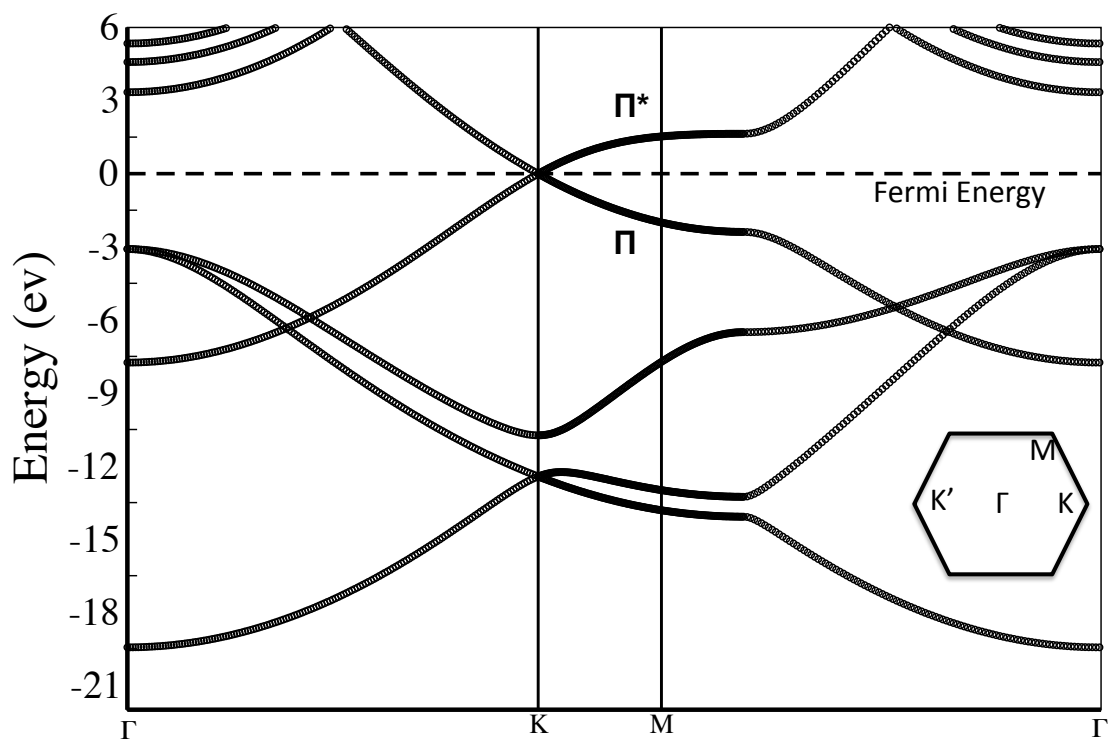


Figure 4.1. Band energy diagram of monolayer graphene along Γ KM Γ direction.

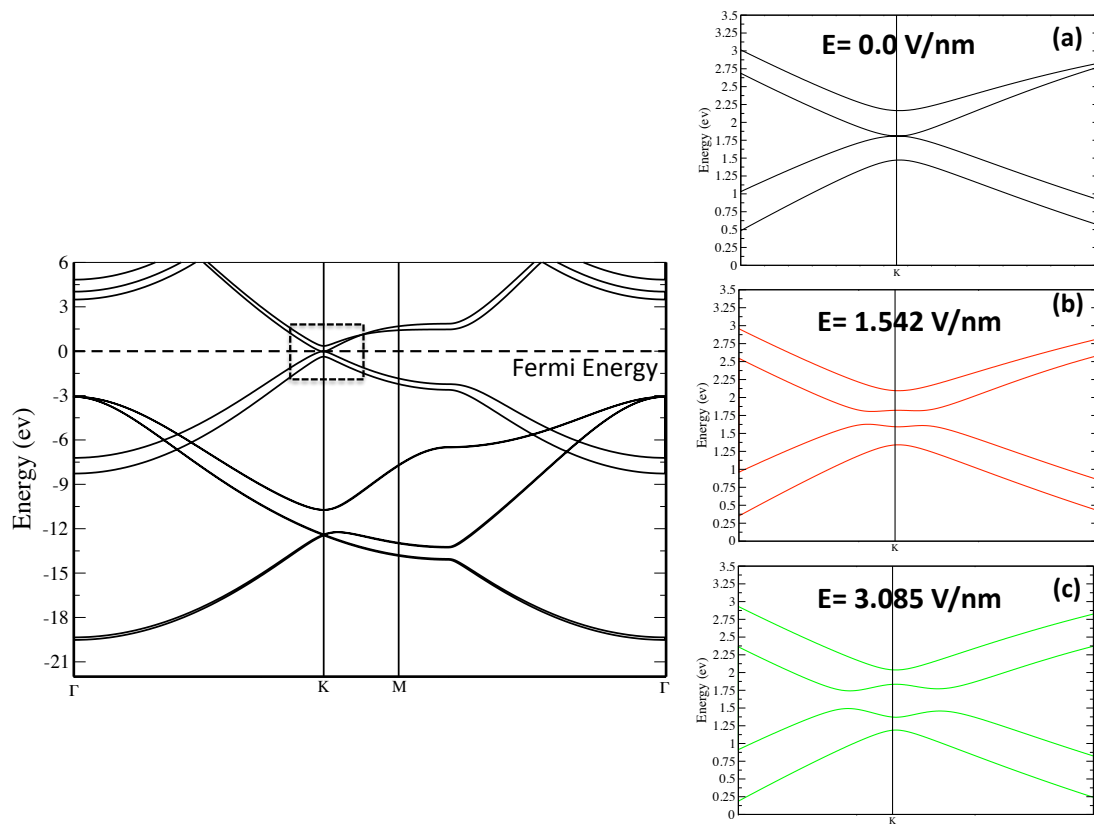


Figure 4.2. Left panel: electronic band structure of bi-layer graphene in the along Γ KM Γ direction of Brillouin zone. Right panel: (a) band structure at zero gate field (b) band gap energy for the same system for an electric field with a potential energy $U = 0.5$ V and (c) with potential energy $U = 1.0$ V.

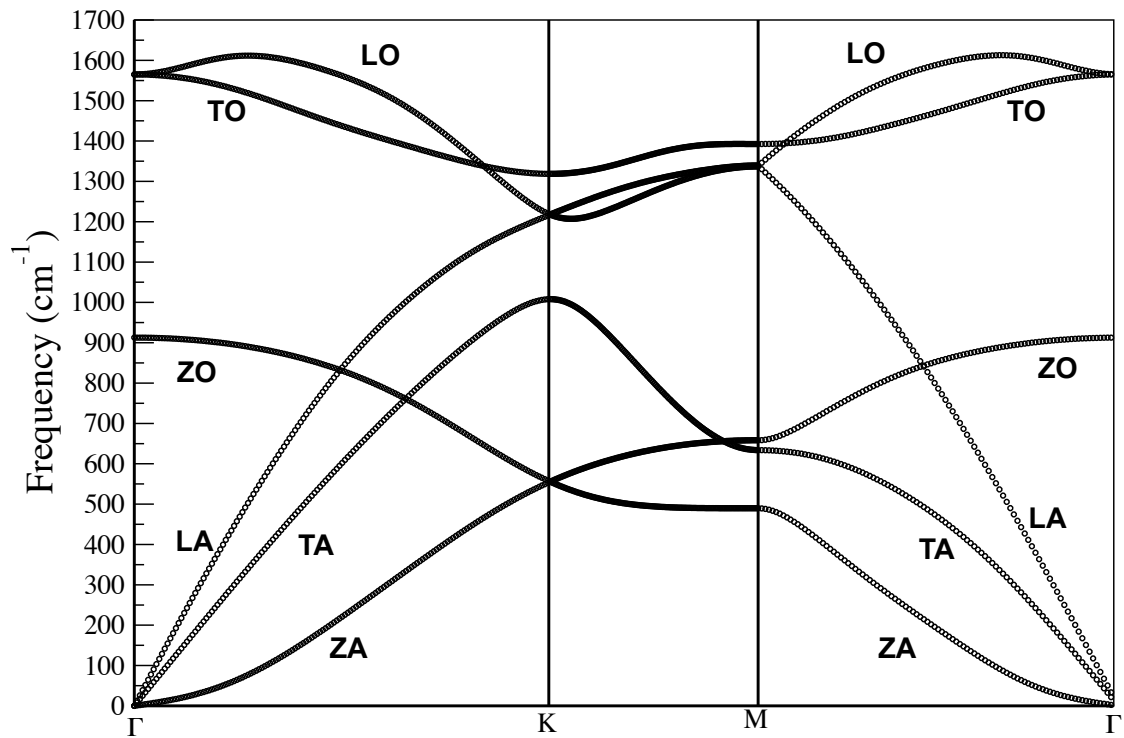


Figure 4.3. Phonon dispersion of monolayer graphene along the high-symmetry direction. Following the convention, the symbol Z denotes the out of plane vibration.

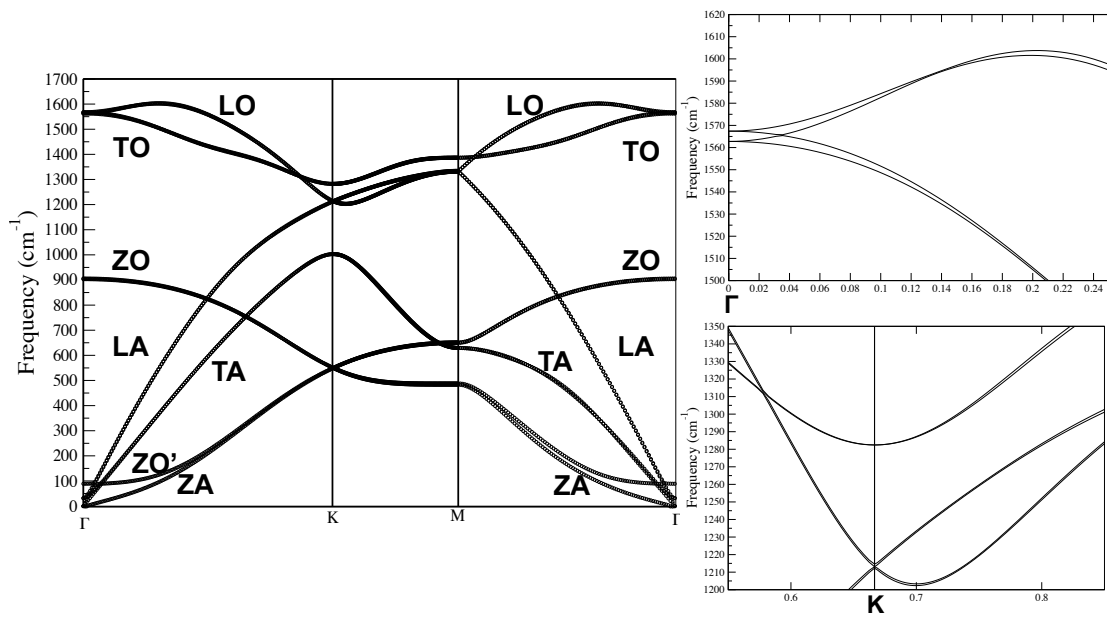


Figure 4.4. Left panel: phonon dispersion of bilayer graphene with A-B stacking along the high-symmetry directions. Following the convention, the symbol Z denotes the out of plane vibration; Right Panel: optical phonon dispersion near Γ and near K.

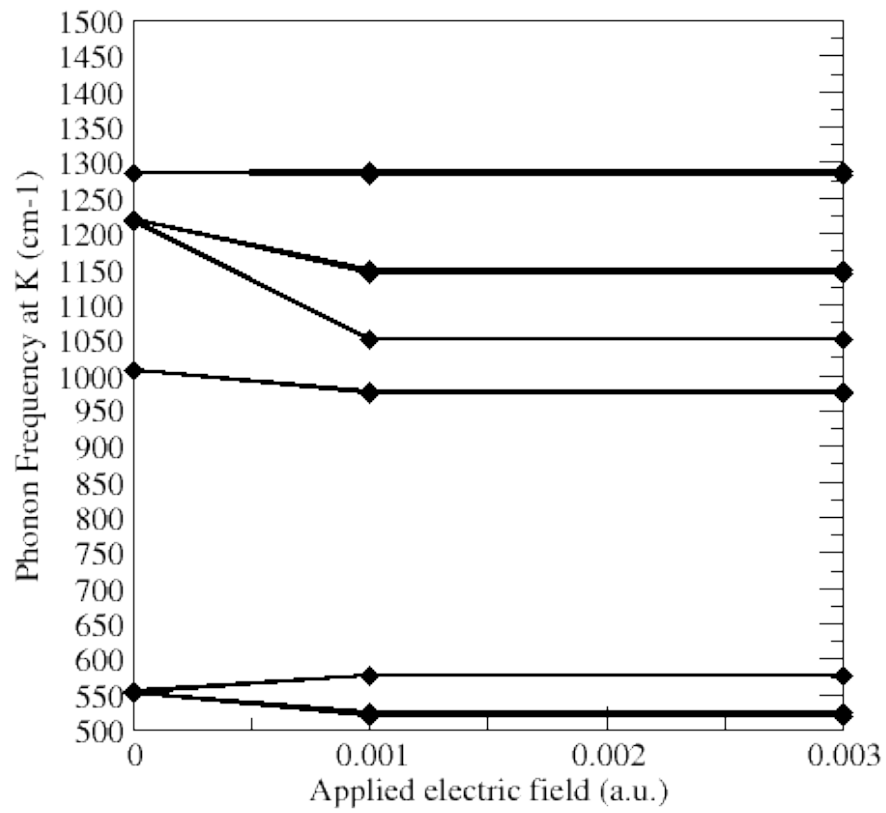


Figure 4.5. Effect of bias on the phonon modes (at K points) of monolayer graphene.

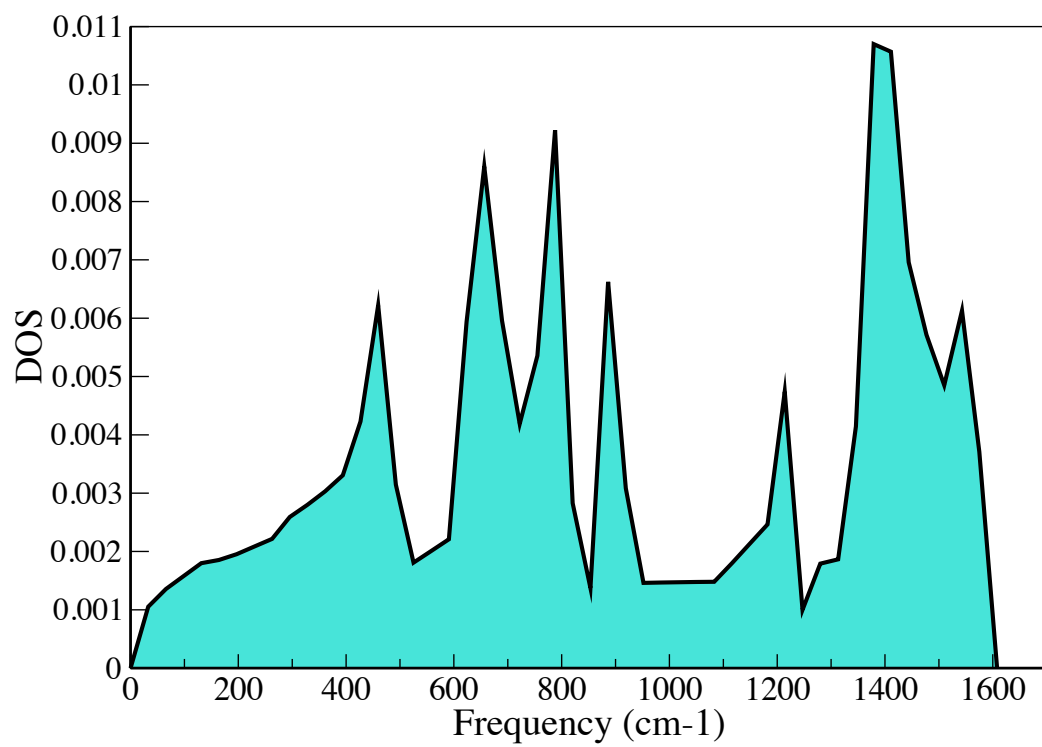


Figure 4.6. Phonon density of states for monolayer graphene.

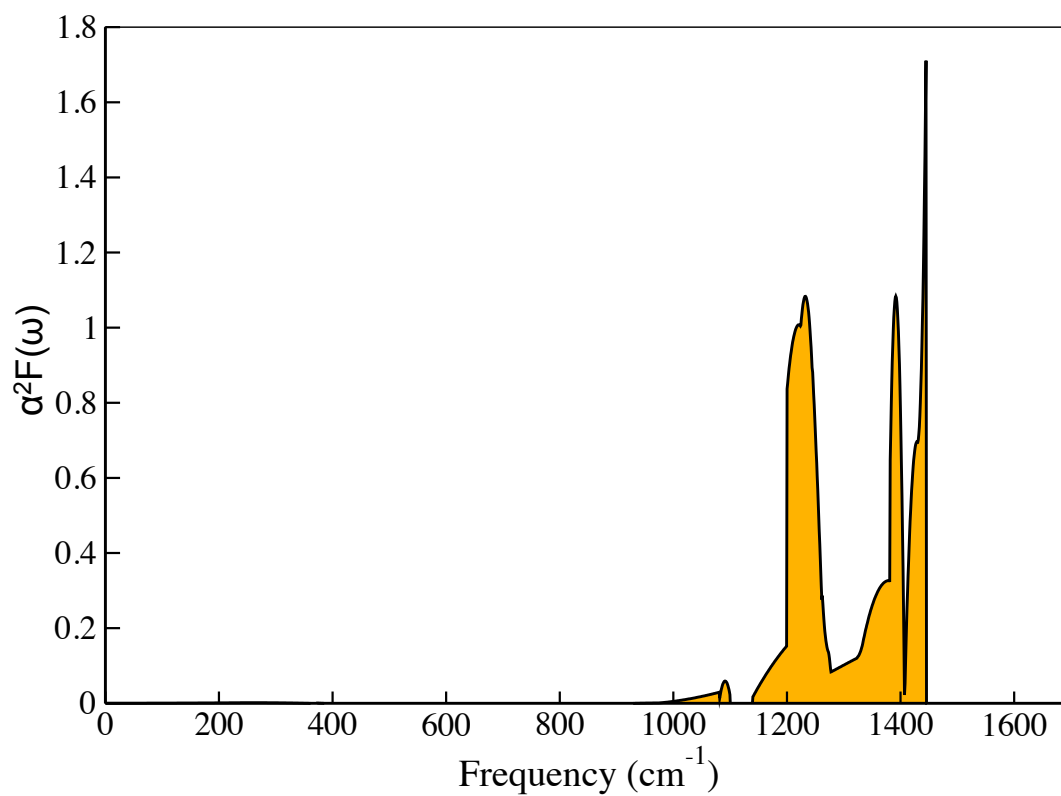


Figure 4.7. Electron phonon spectral (Eliashberg Function) function for monolayer graphene.

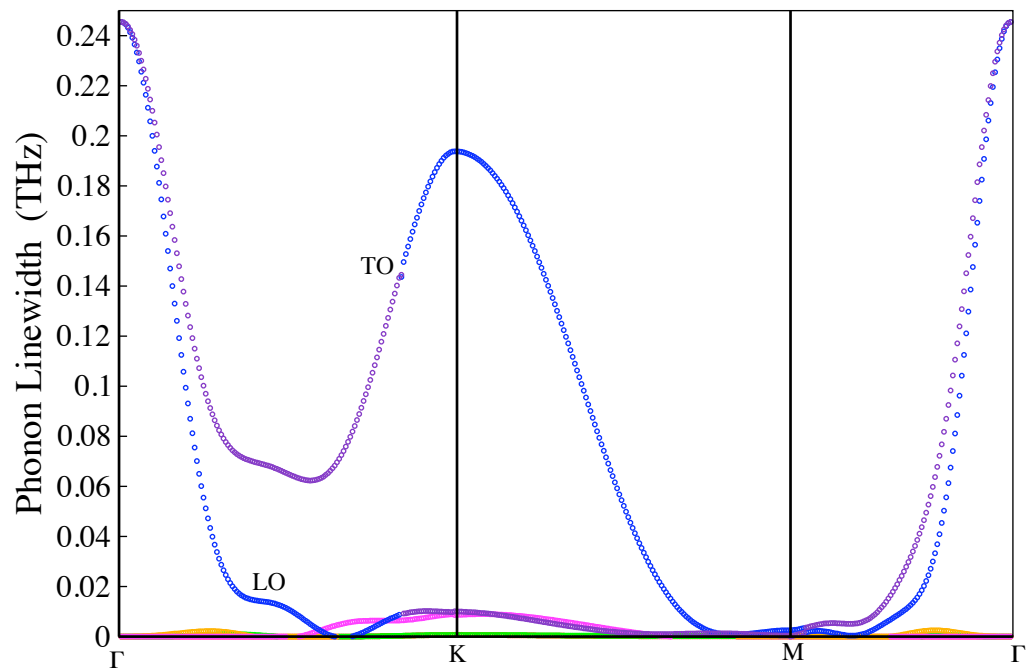


Figure 4.8. Phonon linewidth for monolayer graphene.

References

- ¹ A. K. Geim and K. S. Novoselov, *Nature Mater*, 6, 183 (2007)
- ² P. R. Wallace, *Physical Review* 71, 622 (1947)
- ³ G. W. Semenoff, *Physical Review Letters* 53, 5449 (1984)
- ⁴ P. Avouris, Z. Chen, and V. Perebeinos, *Nature Nanotechnology* 2 (10) 605 (2007)
- ⁵ M. I. Katsnelson, *Materials Today*, 10, 20 (2007)
- ⁶ C. Berger, Z. M. Song et.al., *J. Phys. Chems B.*, 108, 19912 (2004)
- ⁷ C. Berger, Z. Song et.al., *Science*, 312, 1191 (1006)
- ⁸ K. S. Novoselov, A. K. Geim et;al., *Nature*, 438, 197 (2005)
- ⁹ <http://www.quantum-espresso.org>
- ¹⁰ N. Troullier and J. L. Martin, *Phys. Rev. B*, 43, 1993 (1991)
- ¹¹ *Physics today*, August 2007
- ¹² S. Latil and L. Henrard, *Phys. Rev. Lett.*, 97, 036803 (2006)
- ¹³ H. Min, B. Sahu, S. K. Banerjee, A. H. MacDonald, *Phys. Rev. B*, 75, 155115 (2007)
- ¹⁴ N. Mounet and N. Marzari, *Phys. Rev. B* 71, 205214 (2005)
- ¹⁵ J. Yan, W. Y. Ruan and M. Y. Chou, *Phys. Rev. B*, 77, 125401 (2008)
- ¹⁶ C. Oshima, T. Aizawa, R. Souda, Y. Ishizawa, and Y. Sumiyoshi, *Solid State Commun.* 65, 1601 (1988)
- ¹⁷ J. Maultzsch, S. Reich, C. Thomsen, H. Requardt, and P. Ordejón, *Phys. Rev. Lett.* 92, 075501 (2004)

¹⁸ H. Yanagisawa, T. Tanaka, Y. Ishida, M. Matsue, E. Rokuta, S.Otani, and C.

Oshima, Surf. Interface Anal. 37, 133 (2005)

¹⁹ B. D. Kong, S. Paul, M. Buongiorno Nardelli and K. W. Kim, Phys. Rev. B, 80, 033406 (2009)

²⁰ P. G. Klemens and D. F. Pedraza, Carbon 32, 735 (1994)

²¹ K. M. Borysenko, J. T. Mullen, E. A. Barry, S. Paul, Y. G. Semenov, J. M. Zavada,

M. Buongiorno Nardelli, and K. W. Kim, 1<http://arxiv.org/abs/0912.0562v2>

Chapter 5

Ab initio molecular dynamic studies of Novel Phase Change Materials for memory and 3D-integration

5.1 Introduction

The novel and versatile phase change materials (PCM) are promising candidates for new technologies such as nonvolatile memories (PRAM) and programmable switches in 3D integration and planar logic. They are currently widely used in CD-RW and DVD-RW rewritable disks^{1,2,3,4,5}. PCM are typically alloys of Ge, Sb, and Te (GST), which can coexist in an amorphous, high resistivity phase or in a crystalline, low resistivity phase (see Figure 5.1)^{6,7}. The states are inter-converted by thermal cycling. The amorphous state is realized by rapidly quenching from the melt, while the crystalline phase is formed by annealing below the melting temperature for a longer time. The heat pulses can be generated by lasers, as in CD/DVD applications, or by electric resistive heating in the applications of interest here.

Different GST compositions are optimal for different applications as it is described in Figure 5.2. While PCM are clearly promising materials with important applications, there are huge gaps in our understanding of the GST materials and their amorphous-crystalline phase transition. The well-known $\text{Ge}_2\text{Sb}_2\text{Te}_5$, in its rock-salt structure phase, may be thought of as an FCC lattice of Te interpenetrated by a disordered FCC lattice of Ge, Sb and vacancies. Why is this material 100 times more resistive than the similar GeSb_4 ? In the amorphous phase of $\text{Ge}_2\text{Sb}_2\text{Te}_5$ ^{8,9}, EXAFS shows that there is a radical change in the local environments, which has been interpreted as driven by a change in the Ge coordination shell from distorted, octahedral (NaCl phase) to tetrahedral (amorphous phase), as shown in the Figure 5.3¹. Can this type of local-environment driven, glass transition be understood theoretically? Also we have to consider if the concept is extensible to other compositions? The 1000-10000-fold increase in resistivity on going to the amorphous state seems to arise from the opening of an energy gap. We shall attempt to learn about the mechanism of gap opening, which can be observed in a standard DFT computation even if value of the gap, itself, is more difficult to estimate. In the context of these tentative structural pictures, can the wide range in the key electrical transport properties be interpreted primarily as carrier number changes or mobility changes? The electrical breakdown, which plays a critical role in

PRAM function, has been attributed to mid-gap states. What is the nature of these states? Is the Anderson negative-U picture valid? Can the remarkably low thermal conductivity of GST, which is also crucial for PRAM function, be understood theoretically? All the fundamental questions, why the system would turn semiconducting on executing this local structure rearrangement and what is the driving force behind this process, still remain unanswered.

In order to better understand the switching dynamics of phase change materials, we would like to explore the equilibrium phase diagram of GST, in particular along the $(\text{GeTe})_{1-x}(\text{Sb}_2\text{Ge}_3)_x$ pseudo-binary line (Figure 5.2). This line contains the industrially relevant $\text{Ge}_1\text{Te}_2\text{Sb}_4$ and $\text{Ge}_2\text{Te}_2\text{Sb}_5$ compositions. Previous results on the pseudo-binary can be rationalized as follows: The metallic, rock-salt-type structures, in which Ge is octahedrally coordinated, have better packing and are thus favored at high pressure as compared to the spinel-type structures, which have been suggested to describe the local order in the disordered, insulating phase. In spinel-type phases, the Ge is tetrahedrally coordinated. The spinel structure has larger entropy and would thus be favored at high temperature, because there are two tetrahedral positions that could be occupied for each octahedral position.

We thus believe that there is a diagonal line in the PT phase diagram of commercially used GST alloys, which is crossed at ambient pressures from rock-salt

to spinel upon heating from room temperature to 1000K. The reason for the relatively weak pressure-dependence of this transition along the pseudo-binary line may be that replacing 3 Ge atoms with 2 Te atoms (plus a vacancy) is an almost volume-conserving substitution, which does not dramatically alter the competition between the system's propensity to reduce its volume and its desire to increase its entropy. Validating this hypothesis requires the simulation of various GST compositions (at least 101, 124, and 125) at various pressures and temperatures. Assessing the spinodal lines in the phase diagram at isolated points is computationally demanding, however, crucial for the understanding of the phase change dynamics. Equilibrated configurations, whether rock-salt-type or spinel-type local order can be used to assess how the electronic properties depend on the local order. The results of these simulations have the potential to provide the guidance, necessary for the structural properties of GST to be tuned in a rational fashion.

A massively parallel machine such as BG/L was ideal for treating ensemble-based models for these disordered GST systems - even the rock-salt crystal structure of $\text{Ge}_2\text{Sb}_2\text{Te}_5$ has random site occupation on one sublattice. The deepest tool is the Car-Parrinello ab initio MD approach, in which the electronic and ionic structures are simultaneously solved for. This approach, applied to many ensembles of a few hundred atoms in parallel can handle both the randomized crystal structures and the

melt as a model for the amorphized phase. In this way an ensemble-based model for the structures of both crystalline and amorphous phases, unknown at present in any detail, will be generated, and the basic electronic structure determined. Using the well-known Kubo-Green formalism in conjunction with theoretical modeling to reduce the problem's complexity, transport properties can be determined. Many different PCM compositions will be of interest to the IBM PRAM and 3DI communities, and long time simulations were required to study the amorphous state with its long relaxation times.

The basic properties of the technologically important GST phase change materials are not well understood. Structural models of the disordered crystalline and amorphous phases, generated by ab initio MD, will enable understanding of the chemical bonding in these materials very different in these two phases and the implications for electronic structure and for the strongly material-dependent transport properties, placing this field firmly within Condensed Matter Physics, rather than as at present, a branch of Materials Science and Engineering. Developing a better basic scientific background for the materials will enable better choices of composition, tailored to specific applications, from the GST phase diagram, and give insight into the utility of introducing various dopants.

GST or germanium, antimony, tellurium alloys are widely used technologically. In order to better understand these compounds, the liquid state of the binary compounds $\text{Ge}_{0.15}\text{Te}_{0.85}$ (the Eutectic alloy), $\text{Ge}_{0.15}\text{Sb}_{0.85}$ and GeTe as well the ternary $\text{Ge}_1\text{Sb}_2\text{Te}_4$ and $\text{Ge}_2\text{Sb}_2\text{Te}_5$ compound were studied. Also liquid state is very close to amorphous materials, so we chose to test the model and study the structure of the liquid GST materials in different composition. Section 5.3 covers the testing of the functional and pseudopotentials of different GST systems. We compared our AIMD data with relevant experimental data. In section 5.4 we would like to discuss the pressure induced amorphization (crystal to amorphous transition) of $\text{Ge}_2\text{Sb}_2\text{Te}_5$. In section 5.5 we have presented the pressure induced crystallization of GeSb material [22].

5.2 Method

The results presented in this work were obtained using ab initio molecular dynamics (AIMD). The plane wave based Density Functional Theory (DFT) calculations were performed in the Generalized Gradient Approximation (GGA) using Becke GGA exchange functional and LYP GGA correlation functional as implemented in the PNY code¹⁰. In order to verify that the trends found were not an artifact of the

particular choice of pseudopotential, calculations with both BHS (Bachelet, Hamamnn and Schulter)¹¹ and MT (Martin and Troullier)¹² pseudopotentials which share Kleinman and Bylander¹³ form were performed. We found closer match with BHS pseudopotentials calculations when we compared with experimental data. The plane wave energy cutoff was taken equal to 25 Ry and simulations were performed at the Gamma-point of the Brilloun Zone. Canonical conditions (NVT) were maintained for AIMD production runs of length t=6 ps using Nose Hoover chain thermostats. Initial configurations were generated from a randomly substituted NaCl lattice. Each systems was then thermalized at T=6000K for t=3 ps after which the temperature was rescaled to the target temperature. After an equilibration run of t=3 ps at the target temperature, production runs of length t=6 ps were carried out. The production simulations were divided into two t=3 ps portions in order to evaluate the quality of the sampling.

MD methods allow us to follow the coordinates r_i and velocities v_i of all atoms, and insight into the local order can be found from the distributions of the bond (θ_{ijk}) and dihedral angles (γ_{ijkl}). The radial distribution function (RDF) or pair correlation function $g(r)$ is a spherically averaged distribution of inter-atomic vectors,

$$g(r) = \frac{1}{\rho^2} \left\langle \sum_i \sum_{i \neq j} \delta(r_i) \delta(r_j - r) \right\rangle \quad (1)$$

where, ρ is the density. Partial radial distribution functions $g_{\alpha\beta}(r)$ are calculated by restricting the analysis to the elements α and β . The local structure can also be characterized by average coordination numbers found by integrating $g_{\alpha\beta}(r)$ to the first minima R_{\min} .

$$n_{\alpha\beta} = \int_0^{R_{\min}} dr 4\pi r^2 \rho_{\alpha\beta}(r) g_{\alpha\beta}(r) \quad (2)$$

We calculate the structure factor $S(q)$ by Fourier transforming the $g_{\alpha\beta}(r)$ to give the partial structure factors $S_{\alpha\beta}(q)$.

$$s(q) = 1 + \frac{4\pi\rho_0}{q} \int_0^{\infty} [g(r) - 1] \sin(qr) r dr \quad (3)$$

Equations (1), (2) and (3) give precise definitions of the regions where there are few atoms (vacancies, voids, cavities). The model considered here has proved very successful in a series of investigations involving structure factor. Despite the limited statistical description, the agreement with the experiments was very satisfactory.

5.3 Liquid GST systems

5.3.1 Liquid $\text{Ge}_{0.15}\text{Te}_{0.85}$: The Eutectic Alloy

In the following, we present the results obtained for the liquid state of eutectic composition of the GeTe binary alloy $\text{Ge}_{0.15}\text{Te}_{0.85}$ at $T=943$ K, well above the eutectic

temperature^{14,15,16}. System contains 56 (8 Ge and 48 Te) atoms. The system was studied under periodic boundary conditions (PBCs) at the experimental density, $\rho = 0.0285 \text{ \AA}^{-3}$. In Figure 5.4, we have shown the pair correlation function of the above liquid system. As can be seen in Figures 5.4 and figure 5.5, the functional does an excellent job predicting the experimental pair correlation function and structure factors. In the upper panel of Figure 5.4 we have shown the optimized liquid $\text{Ge}_{0.15}\text{Te}_{0.85}$ system.

5.3.2 Liquid GeTe

Here, a system of 64 atoms is studied under PBCs at $T=1000 \text{ K}$ with the size of the super cell fixed to correspond to the experimental density $\rho = 0.0335 \text{ \AA}^{-3}$ ^{17,18}. The partial structure factors (Figure 5.7) were calculated from the Fourier transform of the partial correlation function (Figure 5.6). The overall agreement with experiment is good; especially the first peak is at 3 \AA^{-1} . In the upper panel of Figure 5.6 we have shown the optimized liquid GeTe system.

5.3.3 Liquid $\text{Ge}_1\text{Sb}_2\text{Te}_4$

Computer simulation studies of systems containing 63 atoms (9 Ge, 18 Sb, 36 Te and 1 vacancy) in a periodic box at the experimental density, $\rho = 0.0297 \text{ \AA}^{-3}$, were

performed to model $\text{Ge}_1\text{Sb}_2\text{Te}_4$ in its liquid state at $T=973\text{ K}^{19}$. The agreement with the experimental plot of $g(r)$ and $S(q)$ with the calculated one (Left panel of Figure 5.8 and 5.10) are quite satisfactory. We could also compare our calculated the partial pair correlation (Figure 5.9) function with the one in reference [19] and the comparison is fair enough. In the upper panel of Figure 5.8 we have shown the optimized liquid $\text{Ge}_1\text{Sb}_2\text{Te}_4$ system.

5.4 Pressure induced transformation of $\text{Ge}_2\text{Sb}_2\text{Te}_5$

Pressure is an important parameter in thermodynamics and it can be surmised to have a strong effect on phase stability. Here we report on the results of pressure-induced structural changes in GST. The 225 lattice is a 2-site NaCl type structure with Te on Cl sub-lattice and Ge + Sb + vacancy on the Na sub-lattice. Computer simulation studies of systems containing 58 atoms (14 Ge, 12 Sb, 32 Te and 6 vacancy) in a periodic box at the experimental density, $\rho = 0.0315\text{ \AA}^{-3}$, were performed to model $\text{Ge}_2\text{Sb}_2\text{Te}_5$ in its liquid state at $T=300\text{ K}^{20}$. In Figure 5.11 we have showed the crystal of 225 GST goes to amorphous under pressure about 6 GPa. This result is same as it is described in reference ^{20, 21}. In Figure 5.12, we have demonstrated the energy profile of the process of amorphization of the GST

structure. The energy drops 0.27eV/atm as it moves from crystal to amorphous state. The mechanism seems to be pressure driven collapse of the octahedral coordination. We have also calculated the total structure factor of the crystal, liquid and amorphous 225 GST systems (Figure 5.13) and we found satisfactory structure information as it was reported in reference [21].

5.5 Pressure induced transformation of GeSb

Here, we demonstrate the causal link between the atomic and electronic structure during the phase change by choosing a very simple binary compound GeSb, having 2 critically important advantages²². First, it is nearly vacancy free. Unlike the complex ternary $\text{Ge}_2\text{Sb}_2\text{Te}_5$ that has a large number of vacancies [7], GeSb has only 1 (Sb) lattice with Ge substituting on the Sb sites. This is critical because during the phase-change process, along with the (orders of magnitude) jump in resistivity, there is a volume (density) change. The GeSb amorphous state is $\approx 8\%$ less dense than the crystalline form, so, by Le Chatelier's principle, applying pressure (decreasing volume) should induce a change from the amorphous to the crystalline form. This will give us an isothermal path to induce the phase change. We note that pressure-induced crystallization of GeSb has no analog in the 225 materials. Instead, under

pressure, there is the contrary phenomenon of amorphization. This process is clearly controlled by the high vacancy concentration intrinsic to the 225-crystal structure, where pressure then acts to “squeeze out” these vacancies, irreversibly denaturing the crystalline 225. Second [22], the crystallization velocity in GeSb is very high. This—in addition to the isothermal means of reaching the amorphous state being simpler—significantly reduces the demand on computational resources required to track the process by using ab initio MD (AIMD) and to test the MD results against the experimental data. In Figure 5.14 we have shown the Schematic of a potential device based on pressure switching. In order to validate the simulation studies, comparisons were made both to experimental and theoretical studies in the literature as well as our own experimental data sets. As can be seen in Figure 5.15, the functional does an excellent job predicting the experimental structure factors for amorphous materials. GS could be used in devices driven by mechanical pressure changes enabled by piezoelectric materials provided the reverse transformation can be generated. This new class of devices would potentially be low power and switch rapidly. We also are explored the crystalline to amorphous transformations under tensile load critical to a functional device and the readers can find the detailed description in reference [22].

5.6 Conclusion

We used our modeling to generate new insights into other GST compounds and help design materials with improve performance. We also data mine structural data from the equilibrium simulations. We compared correlation function and structure factors of crystal, amorphous, and liquid GST systems. We also found transition pathways for the amorphous to crystal transformations including studies of tensile load.

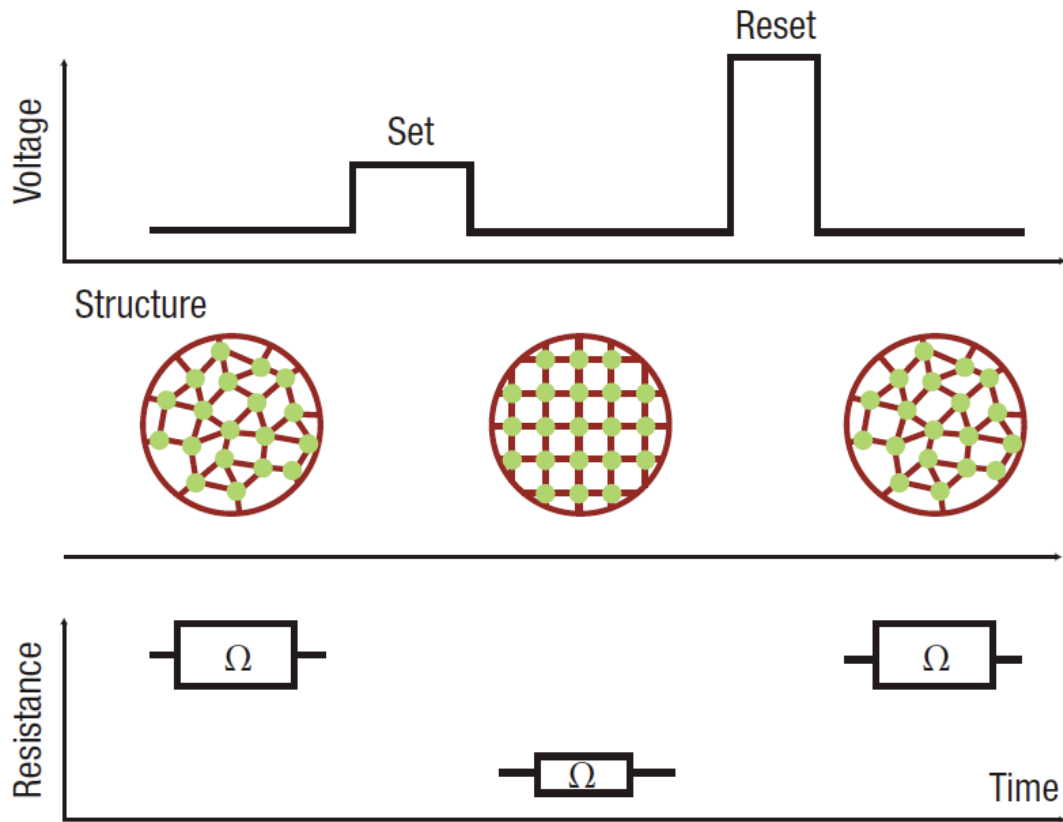


Figure 5.1. The operation principle of a memory device based on phase changes.

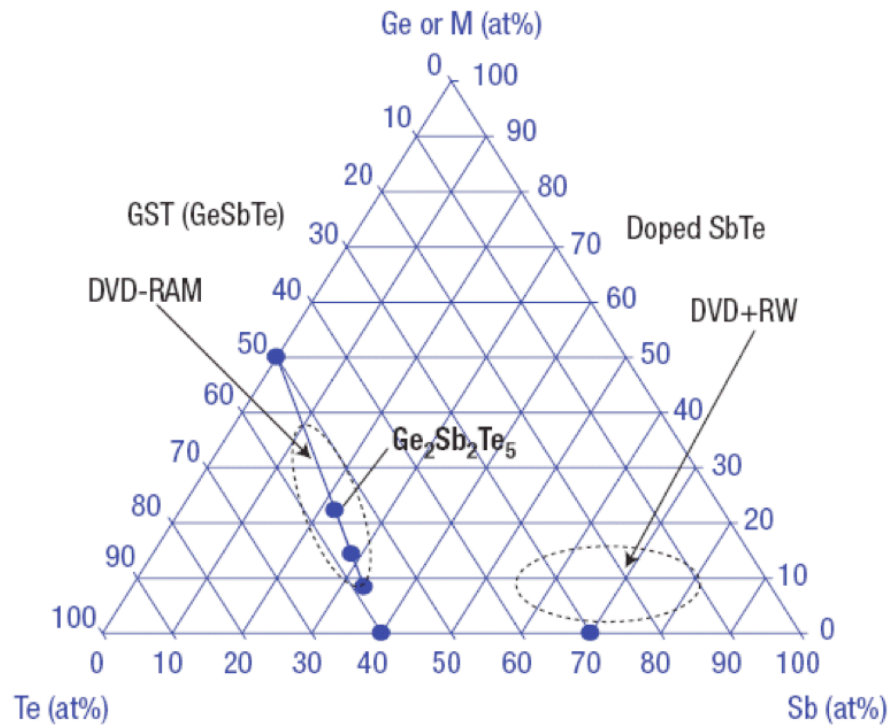


Figure 5.2. The Ge-Sb-Te ternary system. The most commonly used materials for optical recording today have been discovered in two regions in this system.

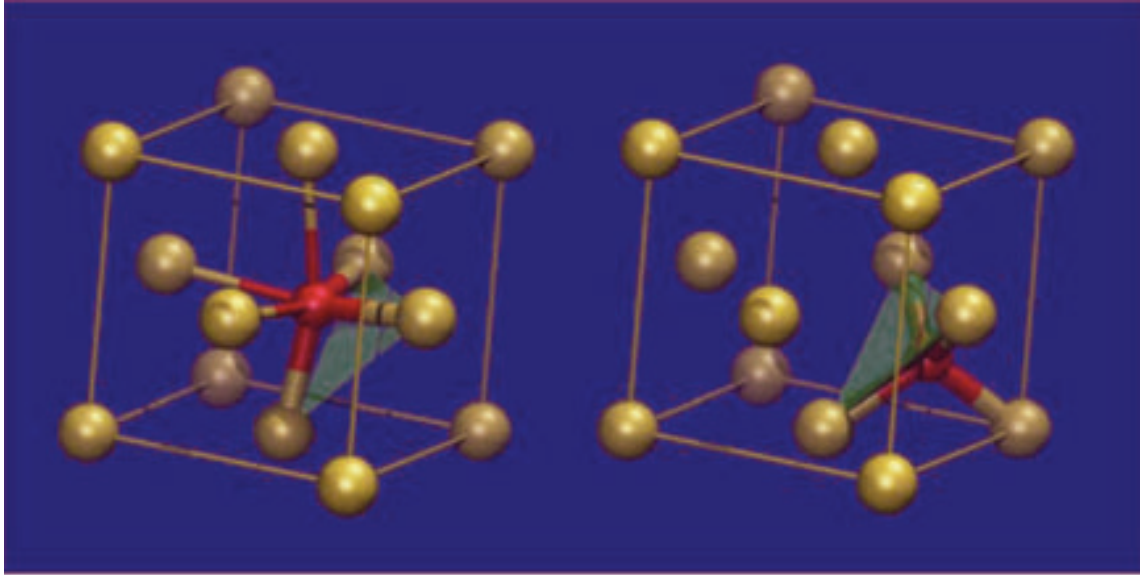


Figure 5.3. Fragments of the local structure of GST around Ge atoms in the crystalline (left) and amorphous (right) states. Stronger covalent bonds are shown as thicker lines whereas weak interblock bonds are shown as thinner lines. Notice that the stronger covalent bonds remain intact on the umbrella-flip structural transformation rendering the Ge sublattice random. It is this nature of the structural change that makes the medium fast and stable.

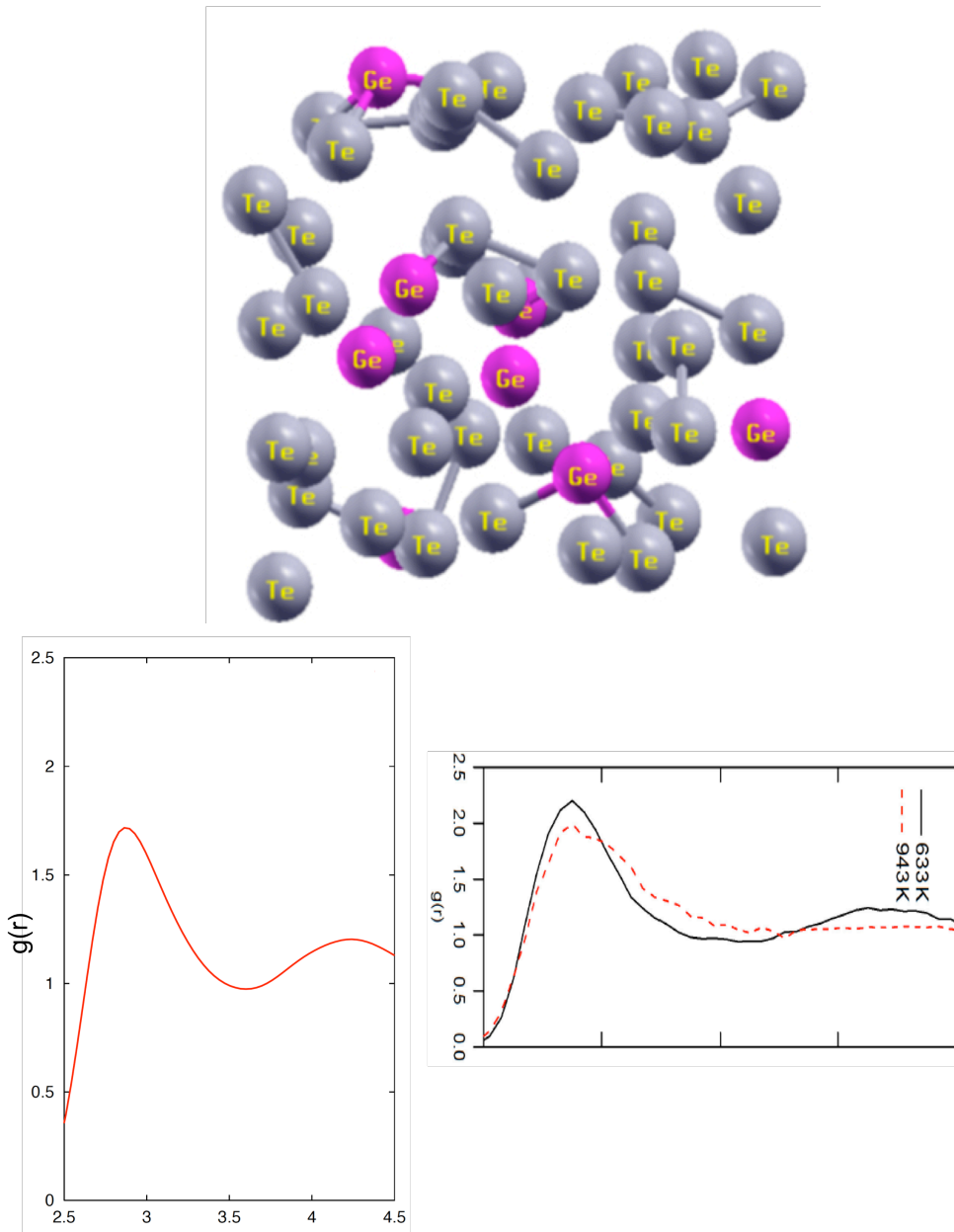


Figure 5.4. Total $g(r)$ of $\text{Ge}_{0.15}\text{Te}_{0.85}$ calculated at $T=943$ K with 20ps production run (left panel) is compared with the total $g(r)$ calculated by Bichara et.al. [14] is given in the (right panel).

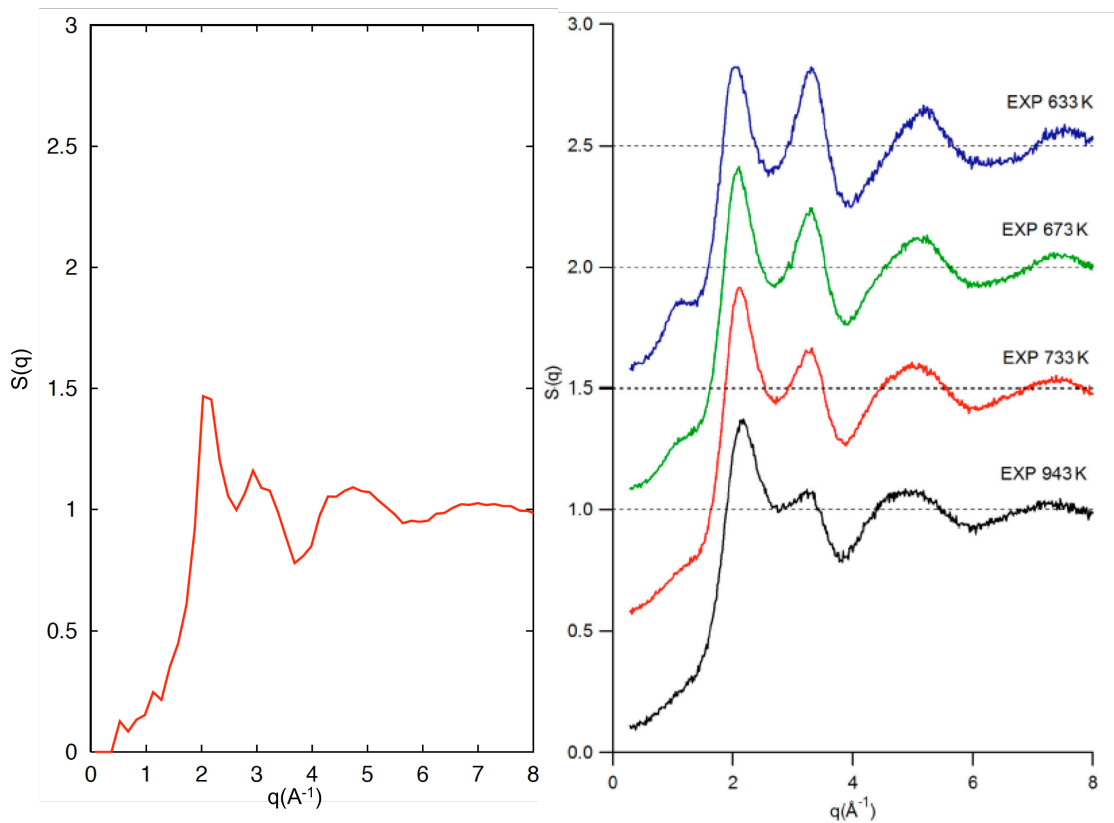


Figure 5.5. Experimental (right) and calculated (left) total Structure factor at $T=943\text{K}$ of $\text{Ge}_{0.15}\text{Te}_{0.85}$.

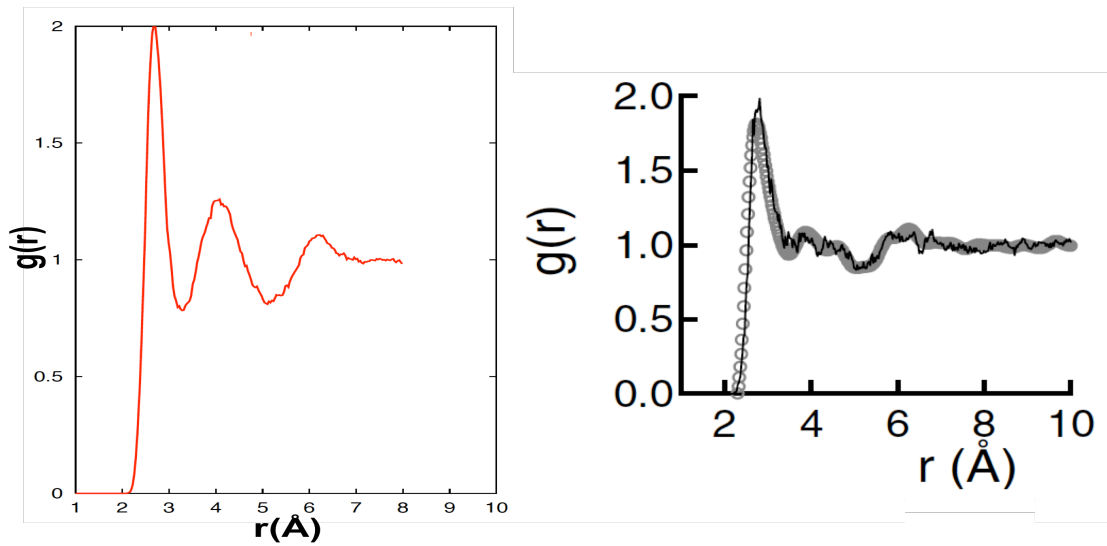
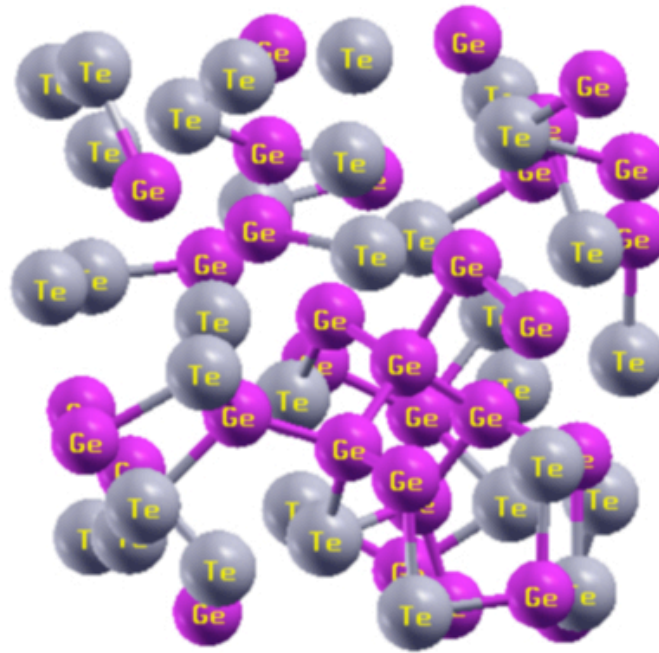


Figure 5.6. Calculated pair correlation function $g(r)$ at $T=1000$ K (left) and experimental $g(r)$ of GeTe.

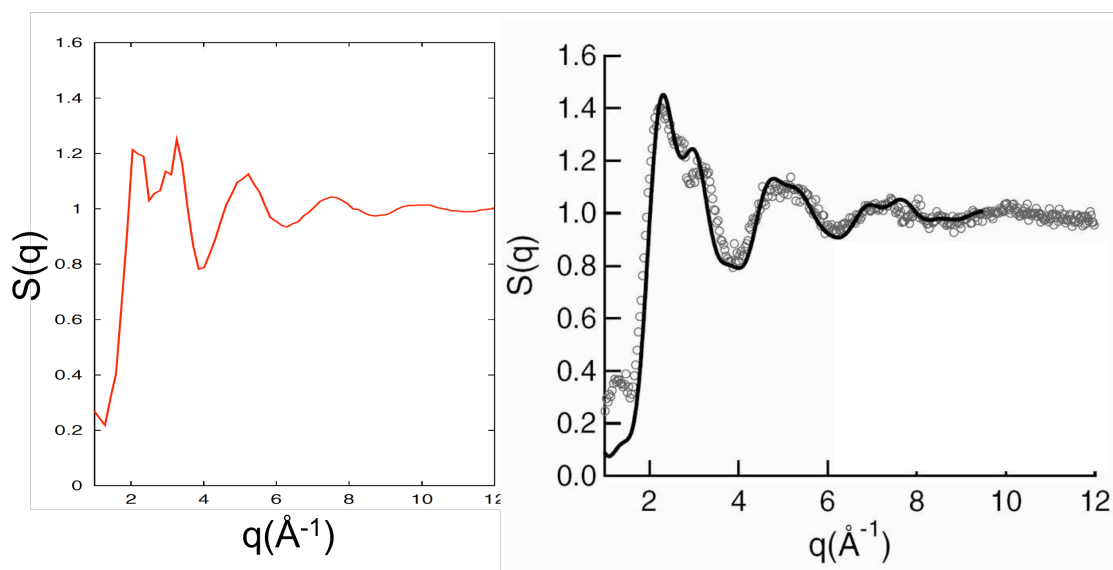


Figure 5.7. Calculated structure factor $S(q)$ at $T=1000$ K (left) and experimental $S(q)$ (right) of GeTe liquid.

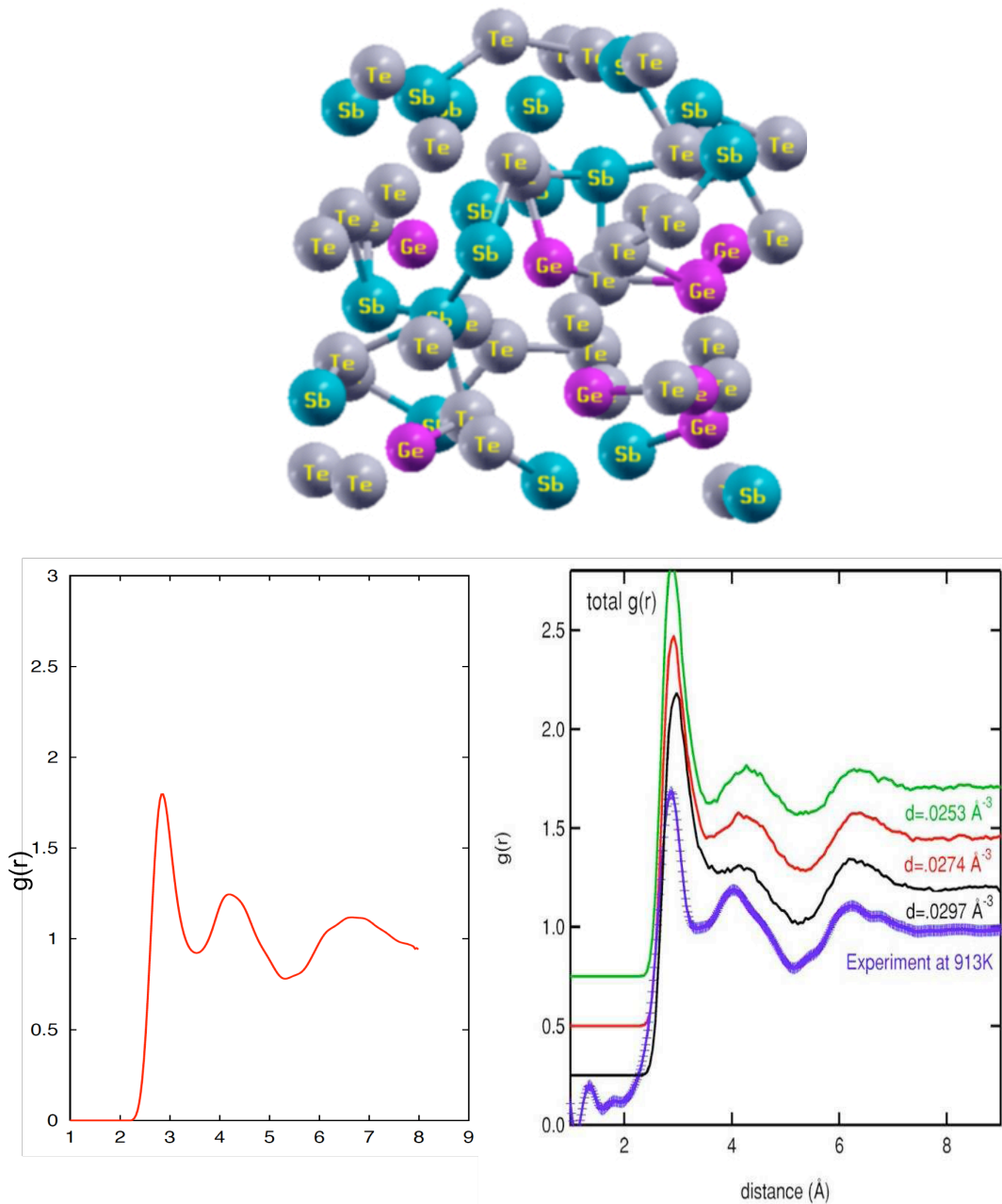


Figure 5.8. Calculated total pair correlation function at $T=973\text{ K}$ (left) for $\text{Ge}_1\text{Sb}_2\text{Te}_4$ in comparison to experimental $g(r)$ (right: blue curve).

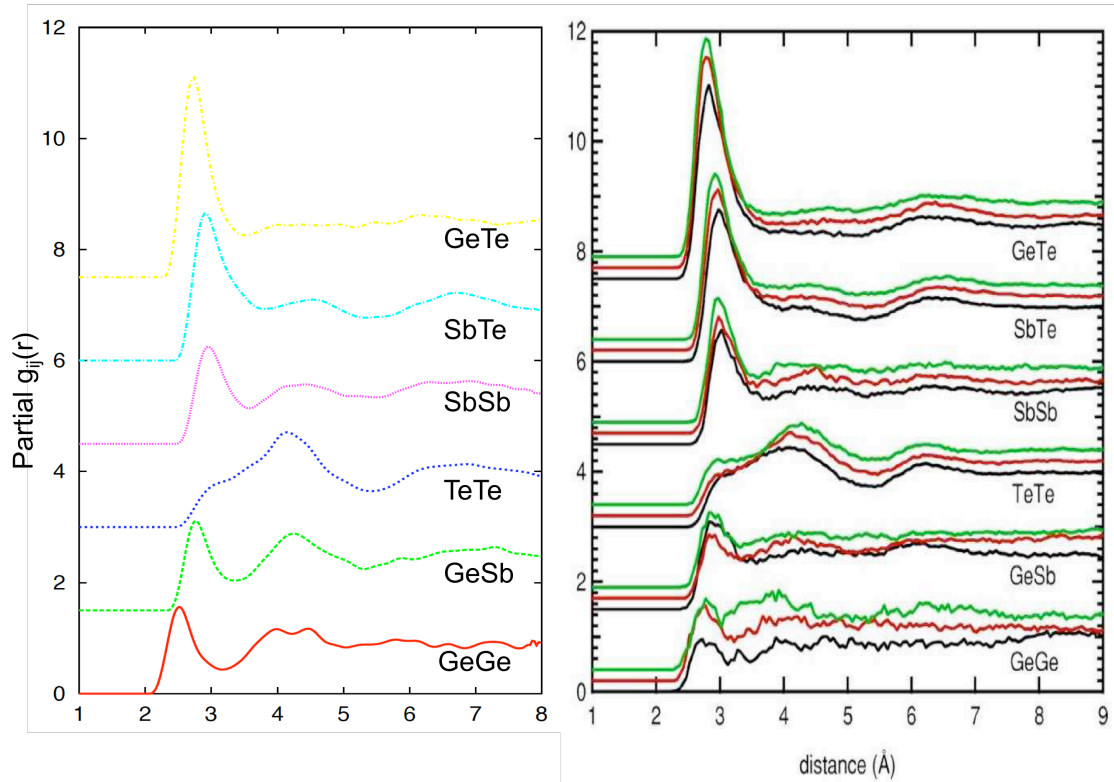


Figure 5.9. Calculated partial pair correlation function (left) for $\text{Ge}_1\text{Sb}_2\text{Te}_4$.

Partial pair correlation function calculated at $\rho = 0.0297 \text{ \AA}^{-3}$ (black curve) in reference [19].

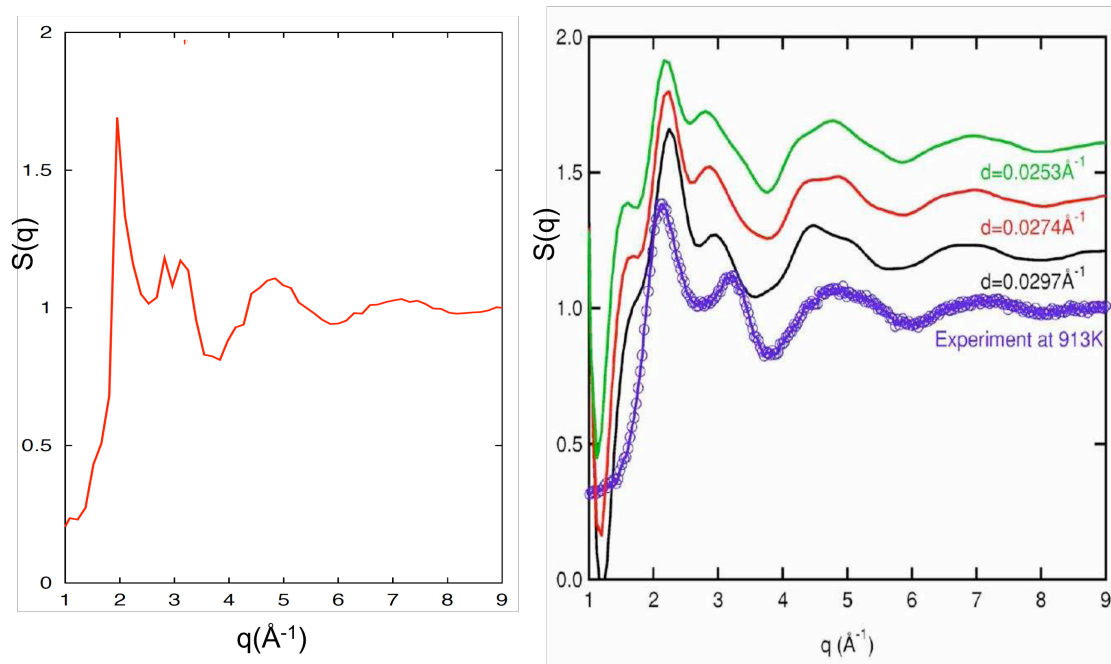


Figure 5.10. Calculated (left) and Experimental (right: blue curve) total Structure factor $S(q)$ at $T=973$ K for $\text{Ge}_1\text{Sb}_2\text{Te}_4$.

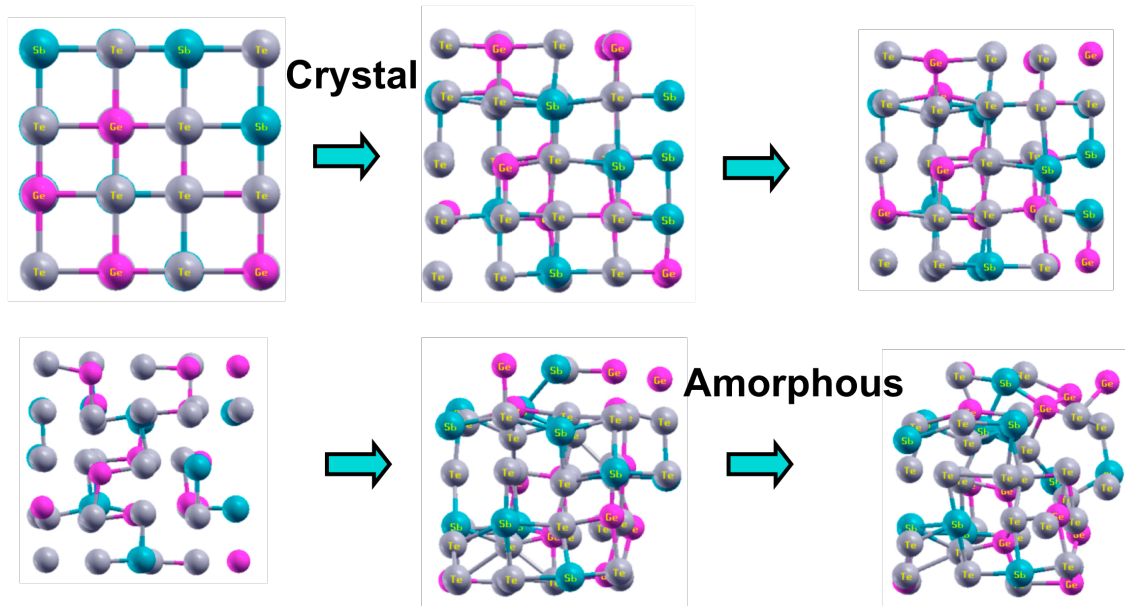


Figure 5.11. Pressure induced transformation of $\text{Ge}_2\text{Sb}_2\text{Te}_5$: crystal to amorphous.

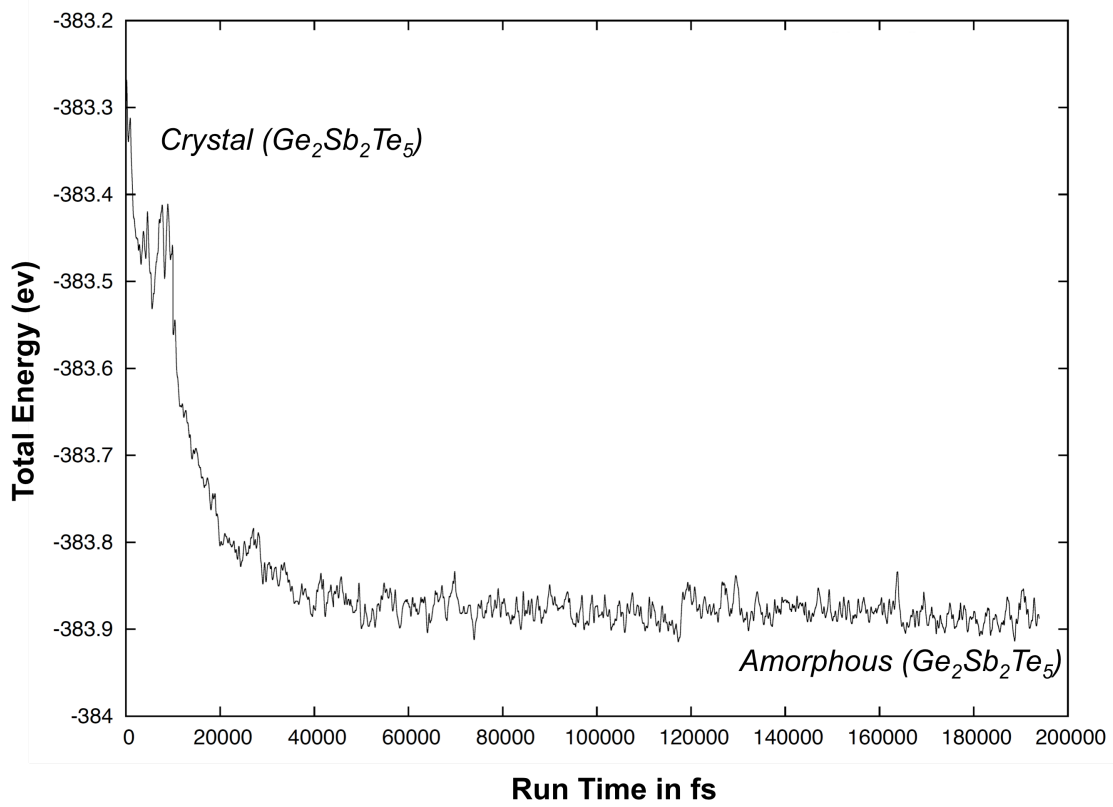


Figure 5.12. Total energy of 225 GST system with total run time of MD simulation.

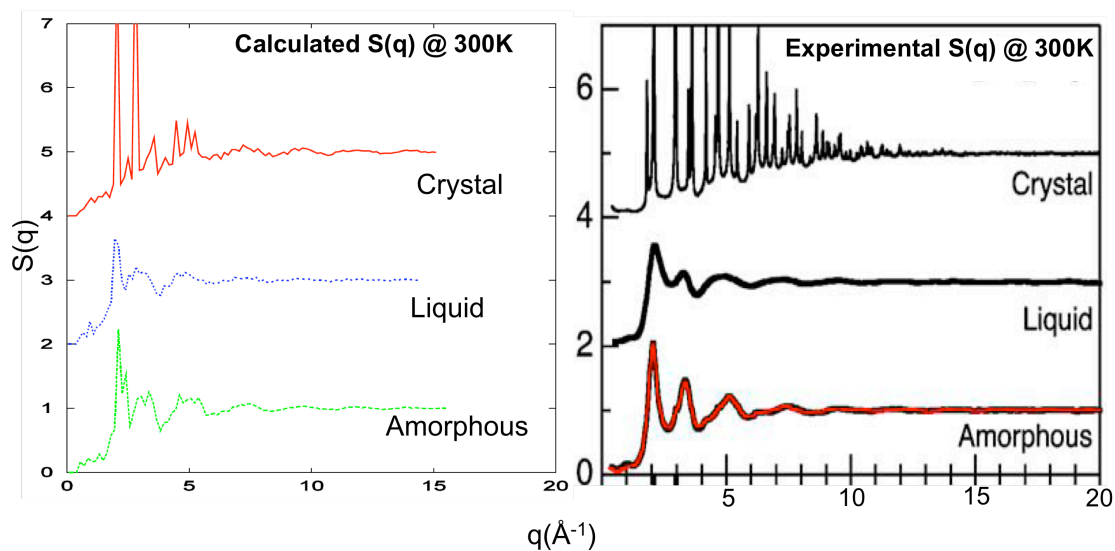


Figure 5.13. Total structure factor calculated from the AIMD simulations and compared the result with experimental structure factor profile of crystal, liquid and amorphous $\text{Ge}_2\text{Sb}_2\text{Te}_5$.

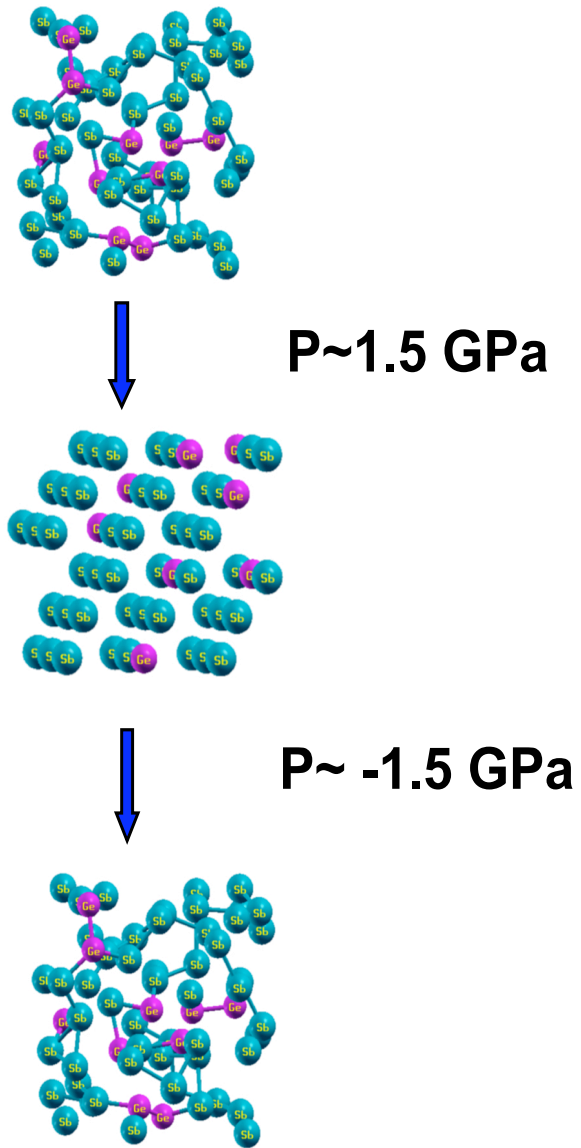


Figure 5.14. Schematic of a potential device based on pressure switching.

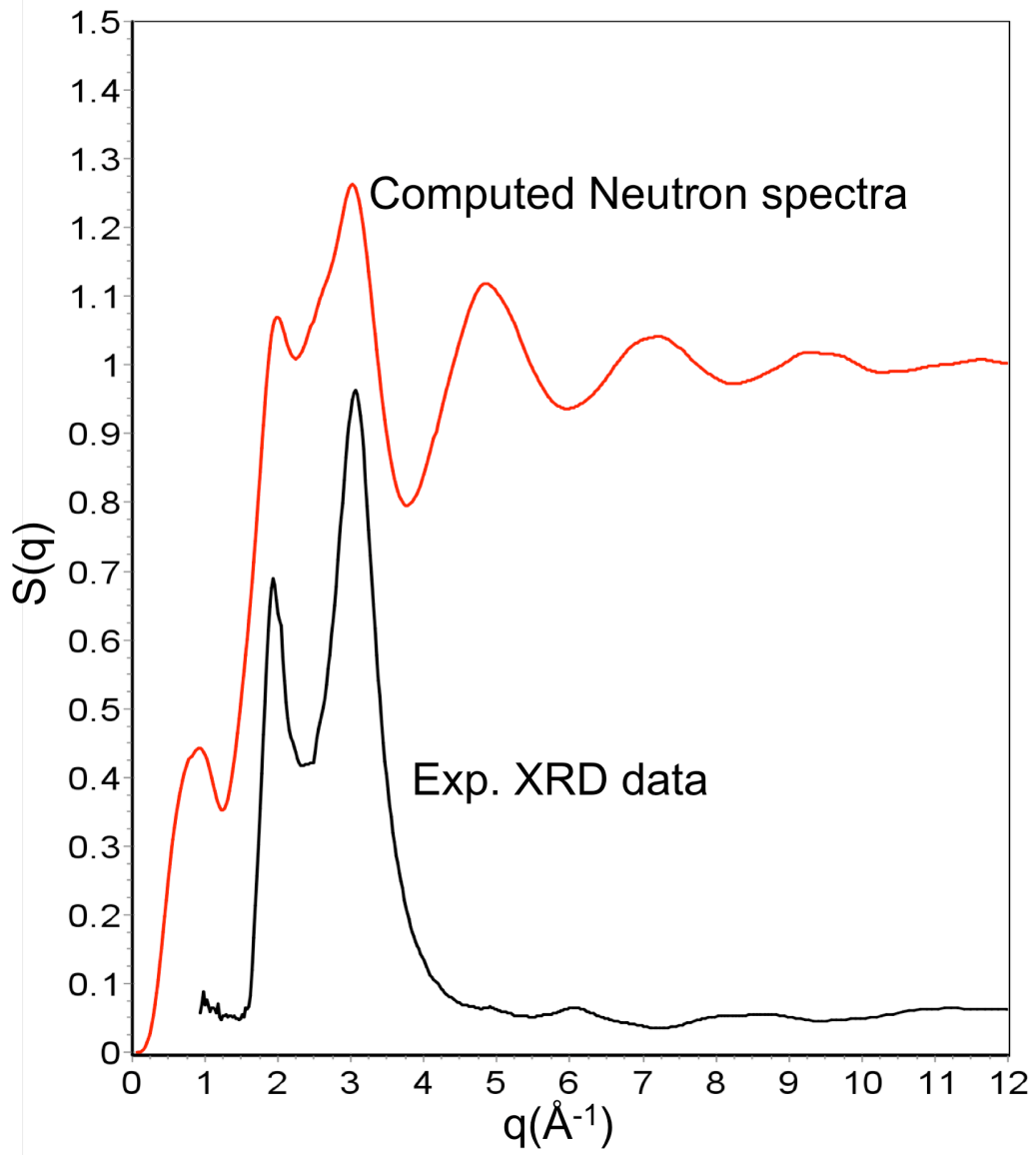


Figure 5.15. A comparison of experimental and simulation structure factors for amorphous phase.

References

- ¹ A. V. Kolobov, P. Fons, A. I. Frenkel, A. L. Ankudinov, J. Tominaga and T. Uruga, Nature Materials, Vol. 3, October 2004
- ² A. V. Kolobov, P. Fons, J. Tominaga and T. Uruga, Journal of Non-Crystalline Solids, Vol. 352 (2006) 1612-1615
- ³ Z. Sun, J. Zhou and R. Ahuja, Physical review Letter, Vol. 96, 055507 (2006)
- ⁴ M. Wuttig and C. Steimer, Applied Physics A, Vol. 87, 411-417 (2007)
- ⁵ Y. C. Chen, C. T. Rettner, S. Raoux et.al., Ultra-Thin Phase Change Bridge Memory Device Using GeSb, IEDM 2006
- ⁶ M. Wuttig, Nature Materials, Vol. 4, April 2005
- ⁷ M. Wuttig and N. Yamada, Nature Materials, Vol. 6, November 2007
- ⁸ S. Shamoto, N. Yamada, T. Matsunaga, Th. Proffen et.al., Applied Physics Letters, 86, 081904 (2005)
- ⁹ T. Matsunaga, N. Yamada and y. Kubota, Acta Cryst., (2004), B60, 685-691
- ¹⁰ http://homepages.nyu.edu/~mt33/PINY_MD/PINY.html
- ¹¹ G. B. Bachelet, D. R. Hamann and M. Schlüter, Physical Review B, Vol. 26, No. 8, 1982, 4199-4228
- ¹² N. Troullier and J. L. Martins, Physical review B, Vol. 43, No. 3, 1991, 1993-2006
- ¹³ L. Kleinman and D. M. Bylander, Physical review Letters, Vol. 48, No. 20, 1982, 1425-1428

-
- ¹⁴ C. Bichara, M. Johnson and J. Y. Raty, Physical Review Letter, Vol. 95, 267801 (2006)
- ¹⁵ C. Bergman, C. Bichara, J. P. Gaspard and Y. Tsuchiya, Physical review B, Vol. 67, 104202 (2003)
- ¹⁶ M. V. Coulet, D. Testemale, J. L. Hazemann, J. P. Gaspard and C. Bichara, Physical Review B, Vol. 72, 174209 (2005)
- ¹⁷ R. Y. Raty, V. V. Godlevsky, C. Bichara et.al., Physical Review B, Vol. 65, 115205 (2001)
- ¹⁸ R. Y Raty et.al., Physical Review Letter, Vol. 85, 1950, 2000
- ¹⁹ C. Bichara, M. Johnson and J. P. Gaspard, Physical Review B, Vol. 75, 060201 (2007)
- ²⁰ S. Kohara, K. Kato, S. Kimura and H. Tanaka, Applied Physics Letter, Vol. 89, 201910 (2006)
- ²¹ A. V. Kolobov, J. Haines, A. Pradel et.al., Physical Review Letter, Vol. 97, 035701 (2006)
- ²² D. Shakhvorostov et. al., Proceedings of National Academy of Science, July 7, 2009 vol. 106, no. 27, page, 10907-1091110.1073/PNAS.0812942106

Chapter 6

Na / NiCl₂ Cell Positive Electrode REDOX Kinetics: Model development and verification

6.1 Introduction

A new class of high-temperature, rechargeable batteries based on a liquid sodium negative electrode and a transition metal chloride as positive electrode have emerged for hybrid-drive systems in transportation applications¹⁻³. These systems evolved from the high-temperature, sodium | sulfur cell⁴. The Na | NiCl₂ cell is always fabricated in a completely discharged state, that means the positive electrode is created from a mixture of common salt (NaCl) and Nickel (Ni). The initial charge decomposes NaCl to sodium and chlorine ions and the chlorine ions combining with the Ni form NiCl₂, so we refer the positive electrode as Ni/NiCl₂. Of particular interest is the Na | NiCl₂ cell, which uses a secondary electrolyte of molten sodium tetrachloroaluminate (NaAlCl₄) in the positive electrode to provide ionic contact with a mixture of Ni, NiCl₂, and NaCl. The active cathode, NiCl₂, is

essentially insoluble in the molten electrolyte. β'' alumina, in the form of a closed-end tube, separates the positive and negative electrodes. β'' alumina, considered to be the primary electrolyte in this cell, is a sodium-ion conductor^{5, 6}. The cell reactions (discharge is left to right) are as follows:

Positive electrode:



Negative electrode:



Net reaction:



Where this value of equilibrium potential U is characteristic of NaCl-saturated NaAlCl_4 at 300°C .

A considerable amount of experimental work has been performed on these cells⁷. Excellent performance characteristics have been demonstrated with both $\text{Na} | \text{FeCl}_2$ and $\text{Na} | \text{NiCl}_2$ ⁸⁻¹³. To develop further understanding of the high-temperature, sodium-nickel chloride, electrochemical-energy storage cell, a detailed description of the reaction kinetics in the porous positive electrode is required. The electrode comprises a micro-dispersed mixture of Ni, NiCl_2 and NaCl. The pore volume is impregnated with NaCl-saturated molten NaAlCl_4 . The reversible electrode reaction as it is described in equation 1.1, where the solubility of NiCl_2 in NaAlCl_4 is slight in the operating temperature range, around 300°C . For this reason, NiCl_2 can be

approximated as insoluble. Any kinetics model for this reaction is necessarily complex, since the model must account for geometric changes that occur during the reaction's progression. Because of the geometric complexity, the forward and reverse reactions need not follow the same pathway. Furthermore, experiments indicate that the kinetics may not strictly follow Butler-Volmer form with respect to over potential dependence. Rather, the electrode demonstrates a bias potential, perhaps associated with the breakdown of a weak, insulating layer at the electrode surface.

In order to construct an engineering transport model of the electrochemical cell, it is necessary to model the heterogeneous reaction kinetics in the positive electrode, i.e., equation 1.1. We proposed such a model and in this paper and we validate the model with electrochemical measurements.

6.2 Previous models of Sodium/metal chloride cells

Sudoh and Newman^{14,15} derived a REDOX reaction rate equation for the porous Fe / FeCl₂ positive electrode in the sodium-ferrous chloride battery. The Newman model assumes that transfer of FeCl₂ between the Fe surface and the FeCl₂ surface occurs via a mobile species r , which transfers through the molten salt electrolyte. Newman concludes that the rate of r transfer is proportional to the specific surface area of Fe, and to the specific surface area of FeCl₂. Newman assumes that the rate of r

transfer between the FeCl₂ phase and the molten-salt electrolyte is driven by the difference in the instantaneous concentration of r and its equilibrium concentration, in such a way that the instantaneous concentration always tends towards the equilibrium concentration. Newman assumes that the rate of r transfer between the Fe surface and the molten-salt electrolyte is driven by the difference in instantaneous concentration of r and its pseudo-concentration at the Fe surface. The resulting expression is:

$$j = \frac{\exp\left(\frac{(1-\beta)nF}{RT}\eta\right) - \exp\left(-\frac{\beta nF}{RT}\eta\right)}{\frac{1}{i_0 a_m (c_2/c_{2e})^{2\beta}} + \frac{1}{nFc_{re}} \left(\frac{1}{k_m a_m} + \frac{1}{k_s a'_s}\right) \exp\left(-\frac{\beta nF}{RT}\eta\right)} \quad [2.1]$$

Equation 2.1 predicts that both metal oxidation and reduction must occur at infinitesimal rate for finite values of over-potential, if either a_m or a_s becomes zero. In experiments, replacing the Fe electrode with a Ni electrode, this is not the case. Newman provided typical values for the material parameters in equation 2.1 with no experimental verification. The chemical species represented by r was not identified, and its equilibrium concentration was not measured.

Orchard and Weaving¹⁶ proposed the following reduction kinetics expression for the sodium-ferrous chloride cell:

$$j_c = j_{c0} \left(\frac{\epsilon_s}{\epsilon_{s0}}\right)^{2/3} \left[\exp\left(\frac{(1-\beta)nF}{RT}\eta\right) - \exp\left(-\frac{\beta nF}{RT}\eta\right) \right] \quad [2.2]$$

Where j_c (charge/time-volume) is the reduction current density and j_{c0} is the

characteristic reduction rate. ε_s and ε_{s0} (volume/volume) are the NiCl_2 volume fraction and the NiCl_2 volume fraction at full charge. This kinetic expression was used in a shell model¹⁷ and fit to discharge data for a sodium-ferrous chloride cell. The results were $j_{c0} = 0.12 \text{ A/cm}^3$ and $\beta = 0.2175$ at 265°C in a porous electrode with 1177 coul/cm^2 of charge capacity at full charge. The authors did not provide an expression for oxidation kinetics. Equation 2.2 does not predict a dependence on c_2 , nor does the model account for mass-transfer limited operation. Shortcomings in these literature models motivated the present proposal of an alternate kinetic expression for Ni electrode REDOX. Model development is described in section 6.3. A strategy for experimental set up is described in section 6.4. In section 6.5 we discussed the results.

6.3 The Present Kinetic Model

The electrode is a collection of Ni surfaces, partially covered by NiCl_2 crystalline lamellae. Figure 6.1 is a schematic of the idealized geometry.

6.3.1 Oxidation

As oxidation proceeds, the NiCl_2 coverage increases, until the Ni surfaces cannot be

further oxidized. The concentration of oxidation-active sites on the Ni surface λ_a (number/volume) is assumed to follow equation 3.1:

$$\lambda_a = \lambda_{a0} \left(\frac{a_m}{a_{m0}} \right)^{m_a} \quad [3.1]$$

Where λ_{a0} is the concentration of REDOX active sites in the discharged state. As in equation 2.1, a_m is the electrolyte-wetted, Ni area density, and a_{m0} is the value in the discharged state. The exponent m_a has a value on the order of 1. Implicit in equation 3.1 is the assumption that the active oxidation sites are on the electrolyte-wetted Ni surface, rather than under the NiCl₂ lamella. This assumption is consistent with the observed passivation behavior of Ni electrodes, wherein constant-current oxidation proceeds at relatively constant η throughout most of the oxidation cycle, then rises asymptotically. The fraction of oxidation-active sites occupied by mobile species **r** is χ_m . NiCl₂ lamellae grow by transfer of **r** from the oxidation sites to adsorption sites on the growth planes of the NiCl₂ lamellae, where the fraction of occupied sites is χ_s . The following kinetic relationship describes the transfer rate

j_{a1} (charge/time-volume):

$$j_{a1} = nFk_{a1}\lambda_a(\chi_m - \chi_s) \quad [3.2]$$

Where k_{a1} (1/time) is the mass-transfer coefficient. Implicit in equation 3.2 is thermodynamic equivalency of the adsorption sites on the NiCl₂ growth planes and

the oxidation sites on the Ni surface, since the driving force for transfer is relative coverage. The rate of conversion of adsorbed r to crystalline NiCl₂ j_{a2} is:

$$j_{a2} = nFk_{a2}\mu_a\lambda_a(\chi_s - \chi_e) \quad [3.3]$$

Where χ_e is the equilibrium fraction of occupied sites on the growth planes, k_{a2} (1/time) is the mass-transfer coefficient, and μ_a is a proportionality factor relating the concentration of adsorption sites on the NiCl₂ growth planes to the concentration of oxidation sites on the electrolyte-wetted Ni surface. Assuming pseudo-steady-state behavior, $j_{a2} = j_{a1} = j_a$, and equations 3.2 and 3.3 can be combined to eliminate χ_s :

$$\chi_m = \chi_e + \frac{j_a}{nF\lambda_a} \left(\frac{1}{k_{a1}} + \frac{1}{\mu_a k_{a2}} \right) \quad [3.4]$$

The oxidation rate, using Butler-Volmer kinetics, is:

$$\frac{j_a}{nF\lambda_a} = k_a \exp\left[\frac{(1-\beta)nFV}{RT}\right] \left(\frac{c_2}{c_{2e}}\right)^2 - k_c \exp\left[-\frac{\beta nFV}{RT}\right] \left(\frac{\chi_m}{\chi_e}\right) \quad [3.5]$$

k_a and k_c (1/time) are the anodic and cathodic rate constants, respectively. V (electric potential) is the electrode potential, relative to an arbitrary reference electrode. For $j_a = 0$, $\chi_m = \chi_e$ according to equation 3.2, and $V \equiv U$, the equilibrium electrode potential. From equations 3.4 and 3.5:

$$U = -\frac{RT}{nF} \ln \left[\frac{k_a}{k_c} \left(\frac{c_2}{c_{2e}} \right)^2 \right] \quad [3.6]$$

Substituting the definition of over potential $\eta \equiv V - U$, from equations 3.5 and 3.6:

$$j_a = nF\lambda_a k_a^\beta k_c^{1-\beta} \left(\frac{c_2}{c_{2e}} \right)^{2\beta} \left[\exp\left(\frac{(1-\beta)nF}{RT} \eta \right) - \frac{\chi_m}{\chi_e} \exp\left(-\frac{\beta nF}{RT} \eta \right) \right] \quad [3.7]$$

From equations 3.4 and 3.7:

$$j_a = \frac{\left(\frac{a_m}{a_{m0}} \right)^{m_a} \left[\exp\left(\frac{(1-\beta)nF}{RT} \eta \right) - \exp\left(-\frac{\beta nF}{RT} \eta \right) \right]}{\frac{1}{j_{a0}(c_2/c_{2e})^{2\beta}} + \frac{1}{\Lambda_a} \exp\left(-\frac{\beta nF}{RT} \eta \right)} \quad [3.8]$$

$$j_{a0} \equiv nF\lambda_{a0} k_a^\beta k_c^{1-\beta}$$

$$\frac{1}{\Lambda_a} \equiv \frac{1}{nF\lambda_{a0}\chi_e} \left(\frac{1}{k_{a1}} + \frac{1}{\mu_a k_{a2}} \right)$$

j_{a0} (charge/time-volume) is the characteristic oxidation rate and Λ_a (charge/time-volume) is the characteristic anodic mass transfer rate. In the case of a weak, insulating film covering the electrode surface, a bias potential η_0 is required to breakdown the film. Substituting $\eta - \eta_0$ for η :

$$j_a = \frac{\left(\frac{a_m}{a_{m0}} \right)^{m_a} \left[\exp\left(\frac{(1-\beta)nF}{RT} (\eta - \eta_0) \right) - \exp\left(-\frac{\beta nF}{RT} (\eta - \eta_0) \right) \right]}{\frac{1}{j_{a0}(c_2/c_{2e})^{2\beta}} + \frac{1}{\Lambda_a} \exp\left(-\frac{\beta nF}{RT} (\eta - \eta_0) \right)} \quad \text{for } \eta \geq \eta_0 \quad [3.9]$$

$$j_a = 0 \quad \text{for } \eta < \eta_0$$

If $\eta - \eta_0 \ll RT/(1-\beta)nF$ and $\eta - \eta_0 \ll RT/\beta nF$, then the exponential expressions

can be represented as truncated Taylor series:

$$j_a = \frac{\left(\frac{a_m}{a_{m0}}\right)^{m_a} \frac{nF}{RT}(\eta - \eta_0)}{\frac{1}{j_{a0}(c_2/c_{2e})^{2\beta}} + \frac{1}{\Lambda_a} \left(1 - \frac{\beta nF}{RT}(\eta - \eta_0)\right)} \quad \text{for } \eta \geq \eta_0 \quad [3.10]$$

If oxidation (versus transfer of r) is rate limiting, i.e., $\Lambda_a \gg j_{a0}$, then the above equation becomes:

$$j_a = j_{a0}(c_2/c_{2e})^{2\beta} \left(\frac{a_m}{a_{m0}}\right)^{m_a} \frac{nF}{RT}(\eta - \eta_0) \quad \text{for } \eta \geq \eta_0 \quad [3.11]$$

Defining superficial areal oxidative current density as $i_a \equiv j_a/a_{m0}$ (charge/time-area) and characteristic areal oxidation current density as $i_{a0} \equiv j_{a0}/a_{m0}$, the above equation becomes:

$$i_a = i_{a0}(c_2/c_{2e})^{2\beta} \left(\frac{a_m}{a_{m0}}\right)^{m_a} \frac{nF}{RT}(\eta - \eta_0) \quad \text{for } \eta \geq \eta_0 \quad [3.12]$$

6.3.2 Reduction

The electrode is a collection of Ni surfaces, partially covered by NiCl₂ crystalline lamellae. As reduction proceeds, the NiCl₂ coverage decreases, until the Ni surfaces are fully reduced. The concentration of reduction-active sites on the Ni surface λ_c (number/volume) is assumed to follow equation 3.13:

$$\lambda_c = \lambda_{c0} \left(\frac{a_s}{a_{s0}} \right)^{m_c} \quad [3.13]$$

Where λ_{c0} is the concentration of reduction-active sites in the fully charged state. a_s (area/volume) is the NiCl₂-wetted, Ni area density, and a_{s0} is that value in the fully charged state. The exponent m_c has a value on the order of 1. Implicit in equation 3.13 is the assumption that the active reduction sites are adjacent to the NiCl₂-wetted Ni surface, *i.e.*, r transfers primarily along the NiCl₂ lamellae, rather than through the electrolyte. This assumption is consistent with the observed reduction behavior of NiCl₂-passivated electrodes, wherein the magnitude of η during constant-current reduction is essentially the same for NiCl₂-free and NiCl₂-saturated electrolytes, until the NiCl₂ passivation layer is nearly depleted. The derivation is analogous to that for oxidation kinetics. The results, comparable to equations 3.9 to 3.12, are:

$$j_c = \frac{\left(\frac{a_s}{a_{s0}} \right)^{m_c} \left[\exp\left(\frac{(1-\beta)nF}{RT} (\eta + \eta_0) \right) - \exp\left(-\frac{\beta nF}{RT} (\eta + \eta_0) \right) \right]}{\frac{1}{j_{c0} (c_2/c_{2e})^{2\beta}} + \frac{1}{\Lambda_c} \exp\left(-\frac{\beta nF}{RT} (\eta + \eta_0) \right)} \quad \text{for } \eta + \eta_0 \leq 0$$

$$j_c = 0 \quad \text{for } \eta + \eta_0 > 0 \quad [3.14]$$

$$j_{c0} \equiv nF \lambda_{c0} k_a^\beta k_c^{1-\beta}$$

$$\frac{1}{\Lambda_c} \equiv \frac{1}{nF \lambda_{c0} \chi_e} \left(\frac{1}{k_{c1}} + \frac{1}{\mu_c k_{c2}} \right)$$

If $-(\eta + \eta_0) \ll RT/(1 - \beta)nF$ and $-(\eta + \eta_0) \ll RT/\beta nF$, then:

$$j_c = \frac{\left(\frac{a_s}{a_{s0}}\right)^{m_c} \frac{nF}{RT} (\eta + \eta_0)}{\frac{1}{j_{c0}(c_2/c_{2e})^{2\beta}} + \frac{1}{\Lambda_c} \left(1 - \frac{\beta nF}{RT} (\eta + \eta_0)\right)} \quad \text{for } \eta + \eta_0 \leq 0 \quad [3.15]$$

If reduction (versus transfer of r) is rate limiting, i.e., $\Lambda_c \gg j_{c0}$, then:

$$j_c = j_{c0}(c_2/c_{2e})^{2\beta} \left(\frac{a_s}{a_{s0}}\right)^{m_c} \frac{nF}{RT} (\eta + \eta_0) \quad \text{for } \eta + \eta_0 \leq 0 \quad [3.16]$$

Defining superficial current density as $i_c \equiv j_c/a_{s0}$ and characteristic reduction current density as $i_{c0} \equiv j_{c0}/a_{s0}$:

$$i_c = i_{c0}(c_2/c_{2e})^{2\beta} \left(\frac{a_s}{a_{s0}}\right)^{m_c} \frac{nF}{RT} (\eta + \eta_0) \quad \text{for } \eta + \eta_0 \leq 0 \quad [3.17]$$

6.3.3 Relationship between NiCl₂ volume fraction and passivation area density during oxidation

We observe that charge capacity of a given area of Ni electrode is a decreasing function of the charging current density. We propose the following parametric equation:

$$\delta_s \equiv \frac{d\varepsilon_s}{da_s} = \frac{b_1 a_m}{j_a + b_2 a_{m0}} = \frac{b_1 A_m}{i_a + b_2} \quad [3.18]$$

$$A_m \equiv \frac{a_m}{a_{m0}}$$

δ_s (length) is the apparent passivation layer thickness (see figure 6.1) and ε_s

(volume/volume) is the NiCl_2 volume fraction. b_1 (charge/time-length) and b_2 (charge/time-area) are material parameters.

Noting that $a_{m0} = a_{s0} = a_0 = a_m + a_s$:

$$-\frac{\partial a_m}{\partial t} = \frac{\partial a_s}{\partial t} = \frac{da_s}{d\varepsilon_s} \frac{\partial \varepsilon_s}{\partial t} = \frac{1}{\delta_s} \frac{\partial \varepsilon_s}{\partial t} = \frac{1}{\delta_s} \frac{j_a \hat{V}_s}{nF} \quad [3.19]$$

\hat{V}_s is the molar volume of condensed-phase NiCl_2 (volume/number). Dividing equation 3.19 by a_0 and substituting from equation 3.18:

$$-\frac{\partial A_m}{\partial t} = \frac{i_a + b_2}{b_1 A_m} \frac{i_a \hat{V}_s}{nF} \quad [3.20]$$

6.3.3.1 Homogeneous, invariant oxidation

If j_a (and i_a) is homogeneous and invariant, then equation 3.20 can be integrated:

$$A_m = \sqrt{1 - \frac{i_a + b_2}{b_1} \frac{2\hat{V}_s}{nF} i_a t_a} \quad [3.21]$$

t_a (time) is the oxidation time. Defining t_{af} as the terminal oxidation time when

$a_m = 0$, equation 3.21 yields:

$$i_a t_{af} = \frac{b_1}{i_a + b_2} \frac{nF}{2\hat{V}_s} \quad [3.22]$$

$i_a t_{af}$ (charge/area) is the areal charge density capacity at superficial current density

i_a . By measuring the areal charge density capacity of an electrode at various nominal current densities i_a , equation 3.22 can be used to determine values for b_1 and b_3 . This is repeated at various temperatures of interest. This determination is best done with a set of smooth electrodes, since the experimental requirement of homogeneous and invariant j_a is most easily met for simple geometries. In that case:

$$i_a = \frac{I_a}{A} \quad [3.23]$$

I_a (charge/time) is the oxidation transfer current and A (area) is the electrode area.

Substituting equation 3.22 into equation 3.21:

$$A_m = \sqrt{1 - \frac{t_a}{t_{af}}} \quad [3.24]$$

6.3.4 Relationship between NiCl₂ volume fraction and passivation area density during reduction

Where q (charge/volume) is the charge density, the average NiCl₂ passivation layer thickness $\langle \delta_s \rangle$ is calculated as:

$$\langle \delta_s \rangle = \frac{q \hat{V}_s}{n F a_s} \quad [3.25]$$

The rate of change of a_s is given by:

$$\frac{\partial a_s}{\partial t} = \frac{da_s}{d\varepsilon_s} \frac{\partial \varepsilon_s}{\partial t} = \frac{1}{\delta_s} \frac{\partial \varepsilon_s}{\partial t} = \frac{1}{\delta_s} \frac{j_c \hat{V}_s}{nF} = \frac{1}{\langle \delta_s \rangle} \frac{j_c \hat{V}_s}{nF} \quad [3.26]$$

Reduction occurs simultaneously at multiple locations on the collection of passivated surfaces. Here we have assumed that these locations are randomly distributed, allowing the substitution of $\langle \delta_s \rangle$ for δ_s . Dividing both sides by a_0 :

$$\frac{\partial A_s}{\partial t} = \frac{1}{\langle \delta_s \rangle} \frac{i_c \hat{V}_s}{nF} \quad [3.27]$$

$$A_s \equiv \frac{a_s}{a_0}$$

6.3.4.1 Homogeneous, Invariant Reduction

If j_c (and i_c) is homogeneous and invariant:

$$A_s = A_{s_i} + \frac{1}{\langle \delta_s \rangle} \frac{i_c \hat{V}_s}{nF} t_c \quad [3.28]$$

$$A_{s_i} \equiv \frac{a_{s_i}}{a_0}$$

t_c (time) is reduction time. a_{s_i} is the initial passivation area density (area/volume) at the start of reduction. t_{cf} is the terminal reduction time, when $a_s = 0$.

Substituting into equation 3.28: $A_s = A_{si} \left(1 - \frac{t_c}{t_{cf}} \right)$ [3.29]

6.3.5 Verification of Kinetics Model with Smooth Electrode REDOX

6.3.5.1 Oxidation

For a smooth nickel electrode, arranged in a cell so as to experience a constant, uniform oxidation current i_a , equation 3.30 describes the electrode oxidation kinetics. Equation 3.30 is the combination of equations 3.12 and 3.24.

$$i_a = i_{a0} (c_2/c_{2e})^{2\beta} \left(\sqrt{1 - \frac{t_a}{t_{af}}} \right)^{m_a} \frac{nF}{RT} (\eta - \eta_0) \quad [3.30]$$

Equation 3.30 is based on the simplifying assumptions of inherent in equation 3.11.

However, the more general kinetics expression of equation 3.9 can be used. The following protocol is applicable in either case. For each choice of i_a , t_{af} is estimated from:

$$\lim_{t_a \rightarrow t_{af}} \frac{d\eta}{dt_a} = \infty \quad [3.31]$$

The reduced chloride ion concentration at the electrode surface, c_2/c_{2e} , must be measured or predicted as a function of t_a . If the oxidation current is periodically and briefly interrupted, the instantaneous, open-circuit, electrode potential, relative to the stable reference electrode, can be used to estimate c_2/c_{2e} using:

$$\Delta U = -\frac{RT}{nF} \ln \left(\frac{c_2}{c_{2e}} \right) \quad [3.32]$$

Where ΔU is the concentration-driven perturbation of equilibrium potential at the electrode. In this case, we have assumed that $U = -(RT/nF)\ln(k_a/k_c)$. In practice, this technique is prone to error. Time-dependent relaxation of the electrode double-layer polarization and finite instrument rise time may both lead to erroneous estimates of ΔU . A second method to estimate c_2/c_{2e} versus t_a is to solve the time-dependent diffusion equation for the cell geometry, using the Fickian diffusion constant for the NaCl / NaAlCl₄ solution. For low values of i_a , the value of c_2/c_{2e} will not be far from 1. Measured cell potential $V_c(t)$, relative to the stable reference electrode, must be corrected for U , ΔU and IR drop between the working electrode and the reference:

$$\eta(t_a) = V_c(t_a) - IR(t_a) - U - \Delta U(t_a) \quad [3.33]$$

IR drop for a given value of i_a will be nearly time-independent, so long as changes in electrolyte composition in the cell are small. IR drop may be estimated by solving the D.C. conduction equation for the cell geometry, using the conductivity for the NaCl / NaAlCl₄ solution.

The procedure outlined above is repeated for a range of i_a values. The reduced chloride concentration data and the corrected over-potential data are then used with equation 3.30 to numerically or graphically estimate the values of i_{a0} , β , m_a and η_0 . If the values of c_2/c_{2e} do not vary appreciably from 1 during oxidation,

determination of β will be difficult. In that case, an arbitrary value between 0 and 1 can be assigned with little error.

6.3.5.2 Reduction

For a NiCl_2 passivated electrode, arranged in a cell so as to experience a constant uniform reduction current i_c , equation 3.34 describe the electrode oxidation kinetics.

Equation 3.34 is the combination of equations 3.17 and 3.29 with $A_{si} = 1$.

$$i_c = i_{c0} (c_2/c_{2e})^{2\beta} \left(1 - \frac{t_c}{t_{cf}}\right)^{m_c} \frac{nF}{RT} (\eta + \eta_0) \quad [3.34]$$

While equation 3.34 is based on the simplifications inherent in equation 3.16, we could have based our analysis on the more general equation 3.14. The following protocol would be unchanged. The electrolyte should be essentially free of dissolved NiCl_2 at the start of the reduction current; in typical characterization cells, the volume of electrolyte is relatively large, and the quantity of dissolved NiCl_2 can be orders of magnitude greater than the quantity of NiCl_2 passivation coating, even at temperatures where NiCl_2 is sparingly soluble in the electrolyte. Testing in the presence of dissolved NiCl_2 leads to data distortion, as NiCl_2 diffuses to the electrode simultaneously with reduction of the passivation coating. In particular, it is very difficult to estimate t_{cf} using:

$$\lim_{t_c \rightarrow t_{cf}} \frac{d\eta}{dt_c} = -\infty \quad [3.35]$$

In porous electrodes, where the Ni surface area is high and the volume of electrolyte is low, the quantity of NiCl₂ in the passivation layer is much larger than the quantity of dissolved NiCl₂, even at saturation, so dissolved NiCl₂ has a small role in electrode kinetics.

To execute a reduction experiment, starting with electrolyte free of NiCl₂, a smooth Ni electrode is oxidized to passivation at a high oxidation current, such that oxidation is completed in a matter of seconds. The oxidized electrode is immediately reduced at a selected constant, uniform current density i_c . In this fashion, distortions due to NiCl₂ dissolution are minimized, except at low i_c combined with high T ; NiCl₂ solubility is enhanced at high T (350°C and above)¹³. Data reduction follows the methodology described for oxidation currents in section 6.3.5.1. Because material parameters β and η_0 are common to equations 3.30 and 3.34, it is recommended that these two equations be fit to a combined set of oxidation and reduction data simultaneously.

As part of a simulation study of the Na – NiCl₂ storage cell, a kinetics model for the electrochemical insertion reaction at the Ni / NiCl₂ electrode has been developed (Readers are encouraged to consult the reference¹⁸). The model includes Butler-Volmer REDOX kinetics, breakdown of a weak coating layer, and mass transfer between the Ni surface and the growth face of the NiCl₂ crystalline lamellae. The

model assumes that all REDOX occurs at the Ni-electrolyte interface. The model further assumes that mass transfer of the mobile Ni^{++} species occurs predominantly via surface diffusion, rather than diffusion through the electrolyte. Rationale is provided to support these assumptions. A parametric approach to the modeling of electrode passivation during oxidation is presented. Under certain conditions, including low over potential and rapid mass transfer, the model can be simplified. An experimental strategy is described for verification of the model in section 6.4.

6.4 Materials and Electrochemical Methods

We constructed an electrochemical cell. The external vessel was a closed-end tube constructed of Pyrex glass, permitting visual observation, by lifting the cell out of the heating mantle. The tube was partially filled with molten NaAlCl_4 . The cell included three electrodes: working (WE), reference (RE) and auxiliary (AE). Figure 6.2 is a schematic of the cell. The cell was closed at the top with a stopper. Three holes were formed in the stopper, and lengths of hollow Pyrex tubing were fitted into these holes. The three electrode leads passed through these Pyrex guides.

6.4.1 Working Electrode

Straight Ni wire (Alfa Aesar Item #43133, 1.0×10^{-3} m diameter, 99.98% metals basis) was used as the WE in the cell. Prior to insertion in the cell, the Ni wire was degreased in methanol, then lightly polished with polishing paper. After the

electrolysis experiment, the WE was extracted from the cell and its wetted length was measured, in order to calculate the wetted area, typically $6 \times 10^{-5} \text{ m}^2$, and the nominal current density. A fresh nickel wire was used for each oxidation and each reduction measurement.

6.4.2 Reference Electrode

The RE was a straight aluminum wire (Alfa Aesar Item #43427, $1.0 \times 10^{-3} \text{ m}$ diameter, 99.9995% metal basis) positioned in a closed-end Pyrex tube of $4 \times 10^{-3} \text{ m}$ OD. The Pyrex tube was filled with NaCl-saturated NaAlCl₄ melt. Pyrex is a sodium-ion conductor.

6.4.3 Auxiliary Electrode

The AE, a coiled aluminum wire (same commercial source as RE), was built inside of a closed-end, circular, β " alumina tube (Ionotec #A1). The β " alumina tube was filled with NaCl-saturated NaAlCl₄ melt. The surface area of the AE was an order of magnitude higher than the electrolyte-wetted surface of the WE.

6.4.4 Electrolyte

NaAlCl₄, produced by reaction between NaCl and sublimated AlCl₃, was used as received (Sigma-Aldrich #451584, 99.99% anhydrous).

6.4.5 Electrochemical characterization

The Ni/NiCl₂ electrode was oxidized and reduced between 1.4 and 0.4 V limits, relative to the Al reference electrode. Equilibrium potential U for the

Al | NaAlCl₄/NaCl (sat) | β" alumina | NaAlCl₄/NaCl (sat) | NiCl₂ was 0.993 V. Chronopotentiographs of the WE were performed at nominal current densities ranging from ±3.0 A/m² to ±160 A/m². Nominal current density was calculated assuming that the entire wetted surface of the WE was electrochemically active. As we have described previously in section 6.3.5, the WE surface becomes passivated by the formation of adjacent NiCl₂ crystals. Working electrode capacity increases with cycling during the first 10-12 cycles, likely due to electrochemically induced surface roughening; we always used virgin wire, as mentioned above, to eliminate this source of variability.

A Solartron 1287 programmable current source was used for electrochemical characterization. The test cell was mounted in a Glas-col cylindrical heating mantle with integrated thermocouple. That thermocouple was used to control temperature with a Fisher 753 Digi-Sense digital temperature controller. We have performed the whole experiments inside of a glove box in an argon gas environment, where we fixed the moisture and the oxygen level during the experiments. We scavenged cationic impurities from the WE compartment, particularly Ni⁺⁺, by immersing Al wire into the melt between measurements. The Al wire was removed before measurement began. Just prior to measurement, with the WE positioned in the cell, we reduced oxidized impurities on the wire, in situ, with reducing current -0.005 A until WE potential dropped to 0.4 V with respect to the RE.

Oxidation experiments were run as a series of chronopotentiographs at currents in

the range 0.0002 to 0.009 A. Prior to oxidation, the wires were conditioned as described above. Oxidation ended when WE potential rose above 1.4 V. Nominal oxidation current density was calculated using the WE surface area based on measured immersion length. These experiments were repeated at three temperatures, 300, 325 and 350°C. NiCl₂, the oxidation product, is sparingly soluble in the molten electrolyte, although the solubility increases with increasing temperature¹³. In the electrochemical cell, where Ni surface area is high and electrolyte volume is small, NiCl₂ dissolution is not an important factor. In the present measurement cell, Ni area is low and electrolyte volume is high, so NiCl₂ dissolution during oxidation can alter the test results. For this reason, we did not extend our measurements to lower currents (longer times) or higher temperatures. In fact, at 350°C, the lowest oxidation currents were not possible. In those cases the chronopotentiographs exhibited diffusion-controlled oxidation at the end of test.

Reduction measurements were done on fully oxidized wires. These wires were prepared by oxidizing virgin wires with a 0.005 A transfer current. Prior to oxidation, the wires were conditioned as described above. Reduction chronopotentiographs were measured immediately following this oxidation, so as to minimize NiCl₂ dissolution. The experiment ended when the WE potential fell below 0.4 V. Similar oxidation and reduction charge capacities assured that loss of adsorbed NiCl₂ by dissolution is minimal. A series of chronopotentiographs, at currents from -0.0002

to -0.009 A, were measured.

6.5 Results and Analysis

6.5.1 Electrochemical Data

Figures 6.3-6.8 show $V_c - U$ versus t_a/t_{af} (oxidation) or t_c/t_{cf} (reduction). Here V_c is the WE potential and U is the equilibrium WE potential for the case of NaCl-saturated electrolyte. t_a , t_{af} , t_c and t_{cf} are oxidation time, terminal oxidation time, reduction time, and terminal reduction time, respectively. The oxidation chronopotentiographs in figures 6.3, 6.4 and 6.5 exhibit non-systematic behavior early in the oxidation process, corresponding to the first 5% of the time axis. We have not been able to ascertain the cause of this behavior, whether due to capacitance, reduced contaminants on the WE or instrumental problems. We exclude this portion of the data when comparing experiment to model.

The discharging chronopotentiographs in figures 6.6, 6.7 and 6.8 exhibit a persistent, systematic trend, wherein the reduction process begins at non-negative values of $V_c - U$ (not shown in figures), followed by rapid decrease in $V_c - U$. The curvature $d^2(V_c - U)/d(t_a/t_{af})^2$ is persistently positive well into the reduction process, corresponding to more than 60% of the reduced time axis. All models, including the present one, predict negative curvature during reduction. We believe that the cause

of this behavior is the protocol -- rapid oxidation, immediately followed by reduction measurement. During rapid oxidation, dissolved chloride ion at the surface of the WE is consumed, via the reverse of equation 1.1, at a rate faster than replacement chloride ion can diffuse to the surface. This likely resulted in acidification of the electrolyte near the WE via equation 5.1:



Whereby, in the absence of chloride ion, the electrolyte itself becomes a chloride ion donor. To support this hypothesis, we have done a simulation of the cell using finite element analysis. This analysis is described below in section 6.5.2.

6.5.2 Finite Element Analysis (FEM)

Comsol Multiphysics¹⁹ was used to analyze transport phenomena in the electrochemical cell. This analysis was used to correct the measured chronopotentiographs for ohmic loss and the influence of chloride ion concentration on equilibrium potential. As is described below in section 6.5.4, chloride ion concentration, as predicted by this analysis, is also used in the kinetic model.

We solved coupled models for electric potential and chloride ion concentration in the electrolyte. We modeled the electrolyte as a binary mixture of NaAlCl_4 and NaCl . Electrical conductivity of the electrolyte κ was calculated as a function of temperature and composition, using the equation proposed by Sudoh and

Newman¹⁴. The binary diffusion coefficient D was estimated from pulse-relaxation experiments done in our laboratory. The following equation was used:

$$D = D_{ref} \exp\left[\frac{E_a}{R} \left(\frac{1}{T_{ref}} - \frac{1}{T}\right)\right]$$

$$E_a = 20900 \frac{J}{mole} \quad (5.2)$$

$$D_{ref} = 4.90 \times 10^{-9} \frac{m^2}{s}$$

$$T_{ref} = 573.15^\circ K$$

The composition of NaCl-saturated electrolyte, as a function of temperature, was taken from Torsi and Mamantov²⁰. Chloride ion concentration c_2 was modeled as a function of time and position using the following mass balance:

$$\frac{\partial c_2}{\partial t} + \vec{\nabla} \cdot (-D \vec{\nabla} c_2) = 0 \quad (5.3)$$

The electric potential in the molten electrolyte φ_2 was modeled as a function of time and temperature using the following charge balance:

$$-\vec{\nabla} \cdot \kappa \vec{\nabla} \varphi_2 = 0 \quad (5.4)$$

The initial value of c_2 was set equal to the equilibrium concentration, calculated as described above.

The cell was modeled in two dimensions. The cell model is show in figure 6.9, along with FE meshing. The boundary conditions were as follows. For the diffusion equation: insulating at the AE, insulating at the RE, uniform constant flux normal to

the interface at the WE. For the electric potential equation: $\varphi_2 = 0$ at the AE, insulating at the RE, uniform current density normal to the interface at the WE.

The analysis was repeated for each of the chronopotentiographs, using the calculated nominal current density i_2 . The chloride ion flux at the WE was calculated as $-i_2/F$. In each case, the analysis was run over the same time interval as the chronopotentiographs. Figure 6.10 shows typical analysis output. These plots show φ_2 and c_2/c_{2e} at the end of discharge for one of the chronopotentiographs: -0.009 A and $t_{cf} = 3.82$ s. c_{2e} is the equilibrium concentration of chloride ion.

The FEM analysis was used to correct the measured potential for ohmic loss and perturbation of the equilibrium potential ΔU , due to change in concentration of chloride ion in the molten electrolyte at the WE surface. ΔU was calculated using equation 3.32. Equation 3.32 is reasonably accurate for melt compositions close to the NaCl-saturated equilibrium. Because the FEM predicts small variation in c_2 around the perimeter of the WE, the average value of c_2 was used in equation 3.32:

$$\frac{\int_{WE} c_2 ds}{\int_{WE} ds} \quad (5.5)$$

Where integration is performed around the perimeter. Typical c_2/c_{2e} results are shown in Figure 6.11. Ohmic loss IR is defined as:

$$IR = \varphi_2|_{WE} - \varphi_2|_{RE} \quad (5.6)$$

The FEM predicts some variation in φ_2 on the perimeter of the WE and RE. In equation 5.6, we have used:

$$\varphi_2|_{WE} = \frac{\int_{WE} \varphi_2 ds}{\int_{WE} ds}, \quad \varphi_2|_{RE} = \frac{\int_{RE} \varphi_2 ds}{\int_{RE} ds} \quad (5.7)$$

We found that the value of IR from equation 5.6 was essentially constant during oxidation and reduction, and proportional to i_2 , because the conductivity of the electrolyte did not change much during the chronopotentiograph. For this reason, we introduced effective resistance $\hat{\rho}$:

$$IR = i_2 \hat{\rho}(T) \quad (5.8)$$

Calculated values for $\hat{\rho}$ are given in figure 6.12. The Corrected electrode overpotential η is calculated from the measured electrode potential V_c using equations 3.32 and 5.6 in (As it was also described in equation 3.33):

$$\begin{aligned} \eta(t_a) &= V_c(t_a) - IR - U - \Delta U(t_a), \\ \eta(t_c) &= V_c(t_c) - IR - U - \Delta U(t_c) \end{aligned} \quad (5.9)$$

Returning to the problem described at the end of the section 6.5.1, that of acidification of the melt during the pre-oxidation of the WE, which precedes the reduction chronopotentiographs, we simulated that process with the FEM model. In this case, both the oxidation and the ensuing reduction processes were modeled, then compared to the reduction process alone. In figure 6.13 we plot the

concentration-driven change in equilibrium potential ΔU at the WE surface, as a function of time. In the case shown, the reduction current was -0.0005 A. The concentration-driven change in equilibrium potential is modeled with and without the influence of the preceding oxidation. Note that the two curves do not come together until late in the reduction measurement.

To calculate an accurate value of η , the corrections shown in equation 5.9 should not introduce significant error. At the start of discharging, the value of ΔU is not known with high accuracy, because equation 3.32 provides only approximate values of ΔU for acidic melts. Equation 3.32 assumes the electrolyte to be a binary mixture, which is not true of acidic melts, as described in equation 5.1 and reference 20, as well as by Boxall, *et al*²¹. The ΔU predictions of equation 3.32 need not be highly inaccurate to cause large error in η . At early reduction times, the electrode over-potential is low, but the ΔU correction is high. Therefore, small error in the evaluation of ΔU will result in large error in η . Rather than depending on equation 3.32 values of ΔU , we chose to disregard the experimental discharge data at low t_c/t_{cf} , when comparing the model to the experimental data.

6.5.3 Oxidative Charge Capacity

Charge density capacity of the Ni electrode depends on the oxidation rate, as depicted in Figure 6.14. We believe that charge density is limited by passivation of

the surface due to the deposition of NiCl₂ crystals. We find that charge density capacity increases with temperature, but decreases with oxidation rate. From the section 6.3.3.1, in equation 3.22), we proposed a parametric equation to describe the observed trends.

$$i_2 t_{af} = \frac{b_1}{i_2 + b_2} \frac{nF}{2\hat{V}_s} \quad (5.10)$$

$i_2 t_{af}$, the product of applied current density at the WE and the final oxidation time, is equal to the charge capacity density. \hat{V}_s , is the condensed-phase molar volume of NiCl₂ and b_1 and b_2 are fitting parameters. The resulting equation fits are shown along with the measured data in figure 6.14. Figure 6.15 shows the temperature-dependent values for b_1 and b_2 . The effective average thickness of the NiCl₂ crystalline layer on the passivated Ni surface is $i_2 t_{af} \hat{V}_s / nF$. So for example, 1.4×10^4 coul/m² charge density capacity corresponds to 2.7×10^{-6} m effective average NiCl₂ thickness. This corresponds to the largest charge capacity that we measured, although equation 5.10 predicts larger charge capacities at lower current densities. In *post mortem* analysis of battery cells quenched in the charged state, we find lamellar NiCl₂ crystals with lateral dimensions on the order of 4×10^{-6} m, a dimension which is compatible with the predictions of equation 5.10.

6.5.4 Verification of Kinetic Model

For arbitrary t_a/t_{af} (t_c/t_{cf}) ratios, we constructed Tafel plots²² from the data in figures 6.3-6.8. We found linear dependence between η and i_2 , focusing on the five lowest current densities. These current densities are of prime interest, because they correspond to the exchange current densities that occur in the porous positive electrode of the Na | NiCl₂ battery, according to FEM analysis. Figure 6.16 shows one such example. Here we use i_a and i_c to refer to oxidation and reduction current densities, respectively.

From figure 6.16, the plotted lines do not intersect the baseline at $\eta = 0$. This observation suggests that a bias potential η_0 is operative, although we do not know its physical origin. Hypothetically, the Ni surface may be covered with a weak, insulating coating that must be broke down, before electrolysis can occur.

In our kinetic model, we have proposed REDOX kinetics of the Ni/NiCl₂ electrode. The model is rather general; both electron insertion and mass transport to and from the electrode surface have been included. Butler Volmer potential dependence has been included. The model also includes a bias potential η_0 , as describe above. In that derivation, we also provide a simplified expression which assumes that the effective over-potential $\eta - \eta_0$ is small, relative to RT/nF and that NiCl₂ transport to and from the electrode surface is not rate limiting. Although the model is applicable

to a porous electrode subjected to an arbitrary REDOX history, the model has been re-stated for the case of invariant, homogeneous exchange current density at a smooth, monolithic electrode. The resulting simplified expressions are:

$$\begin{aligned}
 i_a &= i_{a0} (c_2/c_{2e})^{2\beta} \left(\sqrt{1 - \frac{t_a}{t_{af}}} \right)^{m_a} \frac{nF}{RT} (\eta - \eta_0) \quad \text{for } \eta - \eta_0 > 0 \\
 i_a &= 0 \quad \text{for } \eta - \eta_0 \leq 0 \\
 i_c &= i_{c0} (c_2/c_{2e})^{2\beta} \left(1 - \frac{t_c}{t_{cf}} \right)^{m_c} \frac{nF}{RT} (\eta + \eta_0) \quad \text{for } \eta + \eta_0 < 0 \\
 i_c &= 0 \quad \text{for } \eta + \eta_0 \geq 0
 \end{aligned} \tag{5.11}$$

Where i_{a0} and i_{c0} are the characteristic oxidation and reduction exchange current densities, similar to the equilibrium exchange current densities in the classic Butler-Volmer equation. β is the symmetry factor, with a value between 0 and 1 and m_a and m_c are exponents on the order of 1.

In cases where the ratio c_2/c_{2e} is not far from 1, as in the present case, the choice of β is not critical. In the present case we have set $\beta = 1$. c_2/c_{2e} in equation 5.11 was obtained from FEM analysis. The other 5 parameters were determined by graphically fitting equations 5.11 to the corrected η data. The graphical technique was chosen, because of the ease of excluding suspect data from the fit, as was discussed in section 6.5.2 and 6.5.3. The comparisons of data and model are shown in figures 6.17-6.19.

The resulting parameter values are shown in figure 6.20. Especially at longer times,

the model agrees with experiment reasonably well. No satisfactory fit could be found with $\eta_0 = 0$. For all temperatures and rates, excluding initial reduction data, model and data predictions are, for the most part, within 5 mV; cell over-potentials in the batteries are typically on the order of 100 mV, or more, so the present kinetic model will provide acceptable fidelity when used in finite-element modeling.

6.6 Conclusion

The kinetic model, which is based on rational reaction engineering assumptions, is capable of predicting over-potential for the Ni electrode. The material parameters of this model have been evaluated over the temperature and current density ranges of interest. Oxidation of Ni results in passivation, limiting charge density. The charge capacity increases with decreasing current density. A parametric equation from the model fits the measured trends well.

Current densities of interest are small relative to the characteristic exchange current densities (i_{a0} , i_{c0}), which motivated us to use a linearized kinetic equation, rather than the Butler-Volmer formalism. The fit of the model to the data dictates that $i_{a0} \neq i_{c0}$. This is a manifestation of the physics, where geometric change accompanies electrolysis. Again, the fitting procedure indicates that the electrode exhibits a bias potential during oxidation and reduction, hypothetically related to breakdown of a weak, insulating barrier film of undetermined origin.

The model shows good agreement with experiment. Predicted over-potential is typically within 5 mV of experiment over a broad temperature and exchange current density range. The chosen experimental method leads to erroneous reduction data at the beginning of reduction. This data was excluded during model fitting.

Acknowledgements

We would like to thank Glen Merfeld and Chuck Iacovangelo for financial support and technical advice. Dave Bogdan was instrumental in the experimental design.

List of Symbols

Roman

a_m	Electrolyte-wetted Ni surface area density, cm^{-1}
a_{m0}	a_m at full discharge
a_s	NiCl_2 -wetted Ni surface area density, cm^{-1}
a'_s	NiCl_2 surface area density, cm^{-1}
a_{si}	a_s at start of reduction
a_{s0}	a_s at full charge
a_0	Total Ni surface area density, cm^{-1}
A	Smooth electrode area, cm^2 (eq 28)

A_m	Relative electrolyte-wetted Ni area
A_s	Relative NiCl ₂ -wetted Ni area
A_{si}	Relative NiCl ₂ -wetted Ni area at start of reduction
b_1	First thickness parameter, A/cm
b_2	Second thickness parameter, A/cm ²
c_2	Concentration of Cl ⁻ ion, mole/cm ³
c_{2e}	Saturation concentration of Cl ⁻ ion, mole/cm ³
c_{re}	Saturation concentration of mobile Ni ⁺⁺ species r , mole/cm ³
F	Faraday's constant, 96,485 coul/mole
i_a, i_c	Superficial areal current density, A/cm ²
i_{a0}, i_{c0}	Characteristic oxidation, reduction areal current densities, A/cm ²
$i_a t_{af}$	Areal charge density capacity, coul/cm ²
i_0	Equilibrium exchange current density, A/cm ²
I_a	Oxidative transfer current, A
IR	Ohm's law potential drop between working and reference electrodes,
j	Transfer current density, A/cm ³
j_a, j_c	Oxidation, reduction transfer current density, A/cm ³
j_{a0}, j_{c0}	Characteristic oxidation, reduction current densities, A/cm ³
j_{a1}, j_{a2}	Anodic mass transfer rates, A/cm ³

k_{a1}, k_{a2}	Anodic transfer coefficients, s^{-1}
k_{c1}, k_{c2}	Cathodic transfer coefficients, s^{-1}
k_a, k_c	Anodic, cathodic insertion rate constants, s^{-1}
k_m, k_s	Mass transfer coefficients, cm/s
m_a, m_c	Oxidation, reduction-active site concentration sensitivity factors
n	Number of electrons transferred in electrode reaction
q	Charge density, coul/cm ³
R	Gas constant, 8.314 V·coul/mole·°K
t_a, t_c	Oxidation, reduction times, s
t_{af}, t_{cf}	Terminal oxidation, reduction times, s
T	Temperature, °K
U	Equilibrium potential, V
V	Electrode potential, V
V_c	Cell potential, V
\hat{V}_s	Molar volume of condensed phase NiCl ₂ , cm ³ /mole
Greek	
β	Symmetry factor
δ_s	Apparent NiCl ₂ layer thickness, cm
$\langle \delta_s \rangle$	Average NiCl ₂ passivation layer thickness, cm

ΔU	Concentration-driven perturbation of equilibrium potential, V
ε_s	NiCl ₂ condensed phase volume fraction
η	Electrode over potential, V
η_0	Threshold over potential, V
λ_a, λ_c	Oxidation, reduction-active site concentrations, mole/cm ³
$\lambda_{a0}, \lambda_{c0}$	Oxidation, reduction-active site concentrations at full discharge, charge, mole/cm ³
Λ_a, Λ_c	Characteristic anodic, cathodic mass transfer rates, A/cm ³
μ_a	Ratio of r adsorption sites on NiCl ₂ growth faces vs oxidation-active sites on electrolyte-wetted Ni
μ_c	Ratio of r adsorption sites on NiCl ₂ growth faces vs reduction-active sites on electrolyte-wetted Ni
χ_e	Occupied fraction of r adsorption sites on NiCl ₂ growth faces at equilibrium
χ_m	Occupied fraction of REDOX-active sites on electrolyte-wetted Ni
χ_s	Occupied fraction of r adsorption sites on NiCl ₂ growth faces

References

- ¹ D. J. L. Brett et.al., Transactions of the ASME, 3 (2006) 254
- ² J. L. Sudworth, Journal of Power Science, 100 (2001) 149
- ³ R.C. Galloway and S. Haslam, Journal of Power Science, 80, (1999), 164
- ⁴ J. L. Sudworth and A. R. Tilley, The Sodium Sulfur Battery, Chapman and Hall, 2001
- ⁵ G. R. Belton and P. T. Morzenti , Journal of Metals , 22 Issue: 12, (1970), A26
- ⁶ T.C. Girija, A. V. Virkar, Journal of Power Sources 180 (2008) 653
- ⁷ K. Kronsbein, Investigation and modeling of the ZEBRA systems to optimize state of charge detection, Thesis, May 2004, Institut für Werkstoffe der Elektrotechnik, Universität Karlsruhe
- ⁸ R. J. Bones, J. Coetzer , R. C. Galloway and D. A. Teagle, Journal of Electrochemical society, 134, No. 10 (1987) 2379
- ⁹ R. J. Bones, D. A. Teagle, S. D. Brooker and F. L. Cullen, Journal of Electrochemical Society, 136, No. 5 (1989) 1274
- ¹⁰ J. Prakash, L. Redey and D. R. Vissers, Journal of Power Science, 84 (1999) 63-69
- ¹¹ J. Prakash, L. Redey and D. R. Vissers, Ionics, 6 (2000) 210
- ¹² J. Prakash, L. Redey and D. R. Vissers, Journal of Power Science, 87 (2000) 195-200

-
- ¹³ Jai Prakash, Laszlo Redey, and Donald R. Vissers, *Journal of The Electrochemical Society*, **147**, No. 2 (2000) 502-507.
- ¹⁴ M. Sudoh and J. Newman, *Journal of Electrochemical Society*, 137, (1990), 876
- ¹⁵ R. Pollard and J. Newman, *Journal of Electrochemical Society*, 126, no. 10 (1979) 1713
- ¹⁶ S. W. Orchard and J. S. Weaving, *Journal of Applied Electrochemistry*, 23 (1993) 1214-1222
- ¹⁷ T. M. O'Sullivan, C. M. Bingham and R. E. Clark, Zebra battery technologies for all electric smart car, SPEEDAM 2006, International symposium on Power Electronics, electrical Drives, Automation and motion
- ¹⁸ M. valance and R. E. White, Excerpt from the proceedings of the COMSOL conference, Boston, 2008
- ¹⁹ <http://www.comsol.com/>
- ²⁰ G. Torsi and G. Mamantov, *Inorganic Chemistry*, Volume 10, No. 9 (1971) 1900-1902.
- ²¹ L. G. Boxall, H. L. Jones and R. A. Osteryoung, *Journal of the Electrochemical Society: Electrochemical Science and Technology*, 120, No. 2 (1973) 223-231.
- ²² J. S. Newman and K.E. Thomas-Alyea, *Electrochemical Systems*, 3rd Edition, Prentice Hall, 2004.

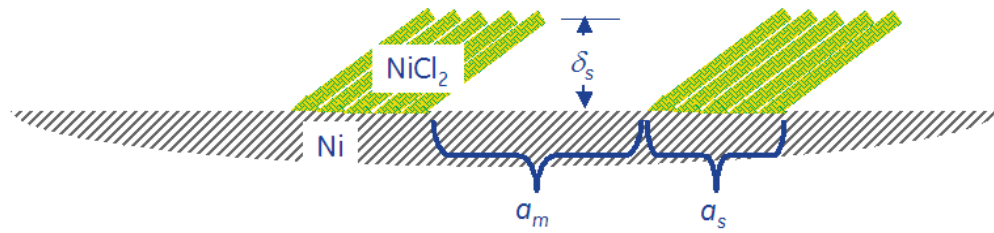


Figure 6.1. Idealized geometry of the electrode

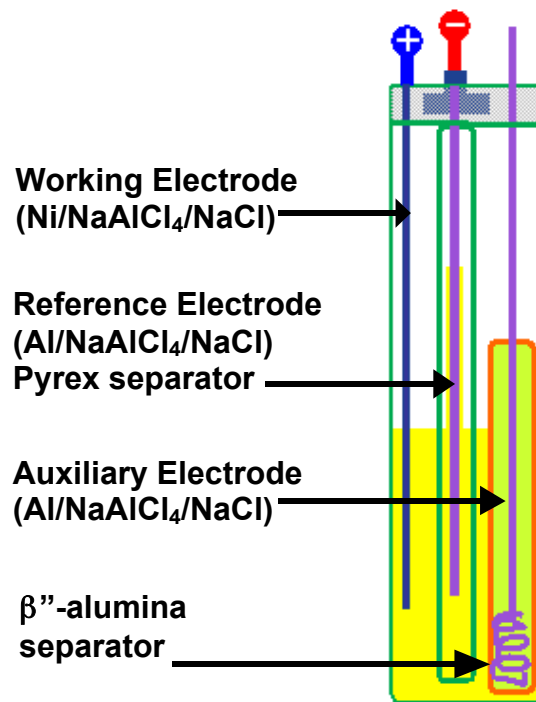


Figure 6.2. Cell Schematic

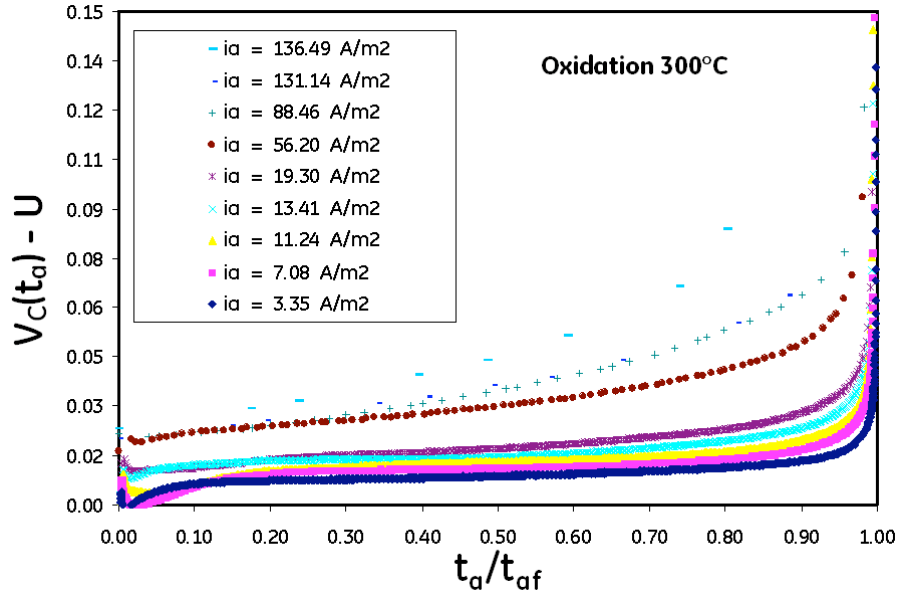


Figure 6.3 Chronopotentiographs for oxidation at $T=300^\circ\text{C}$

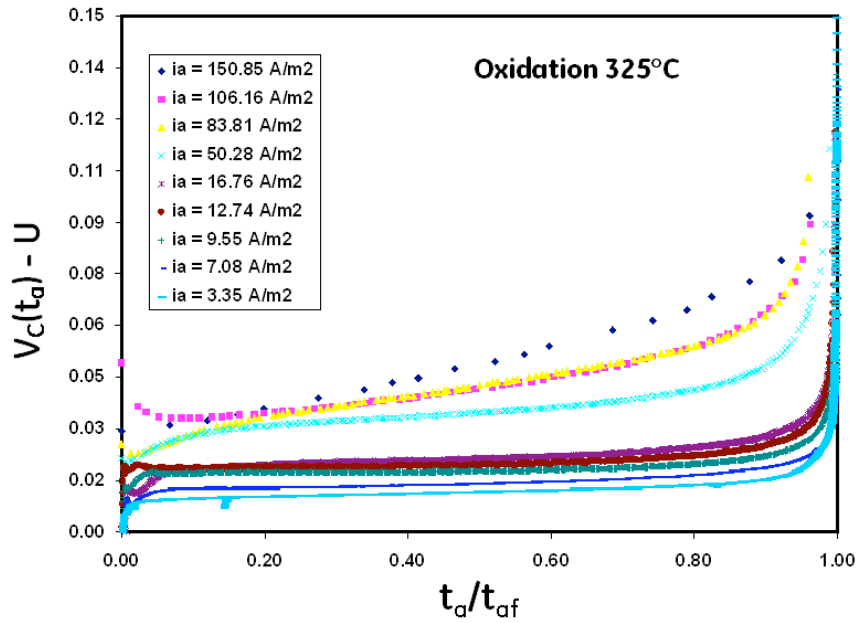


Figure 6.4. Chronopotentiographs for oxidation at $T=325^\circ\text{C}$

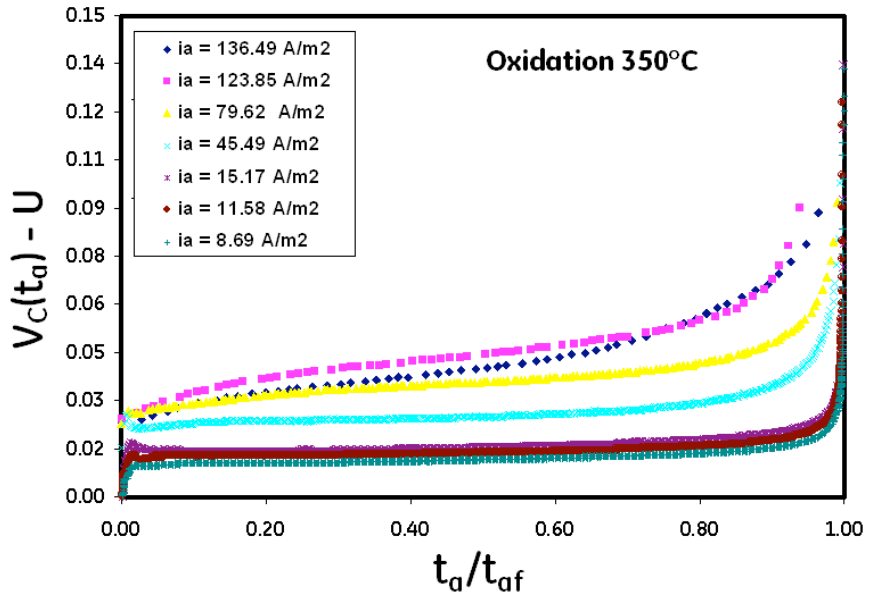


Figure 6.5. Chronopotentiographs for oxidation at $T=350^\circ\text{C}$

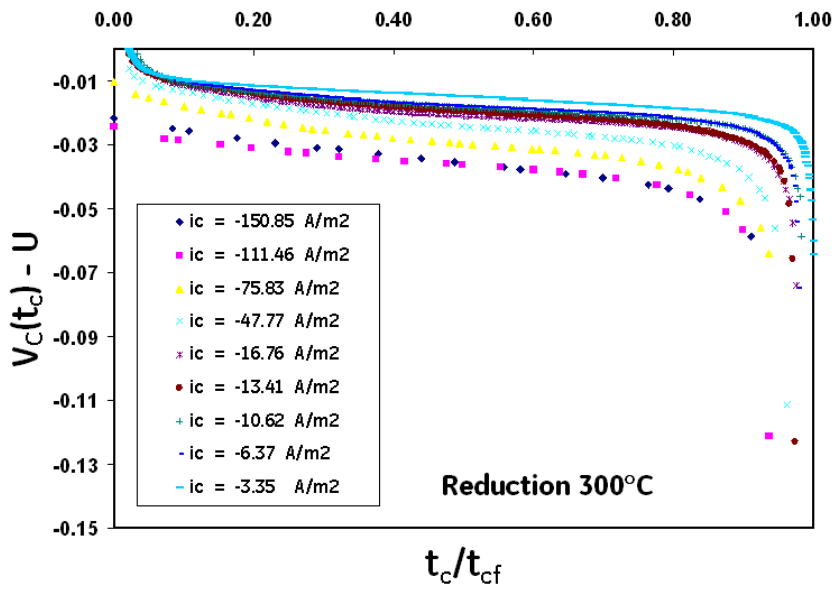


Figure 6.6. Chronopotentiographs for reduction at $T=300^\circ\text{C}$

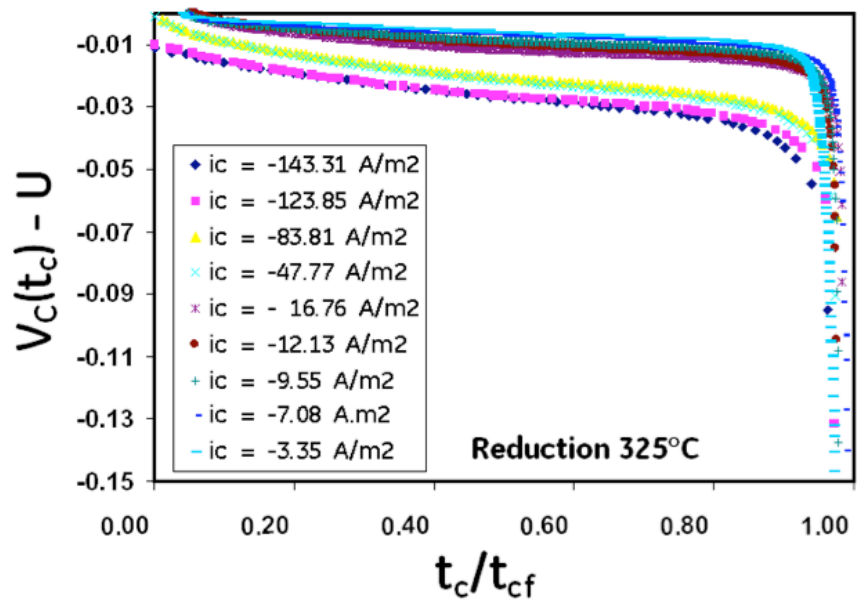


Figure 6.7. Chronopotentiographs for reduction at T=325°C

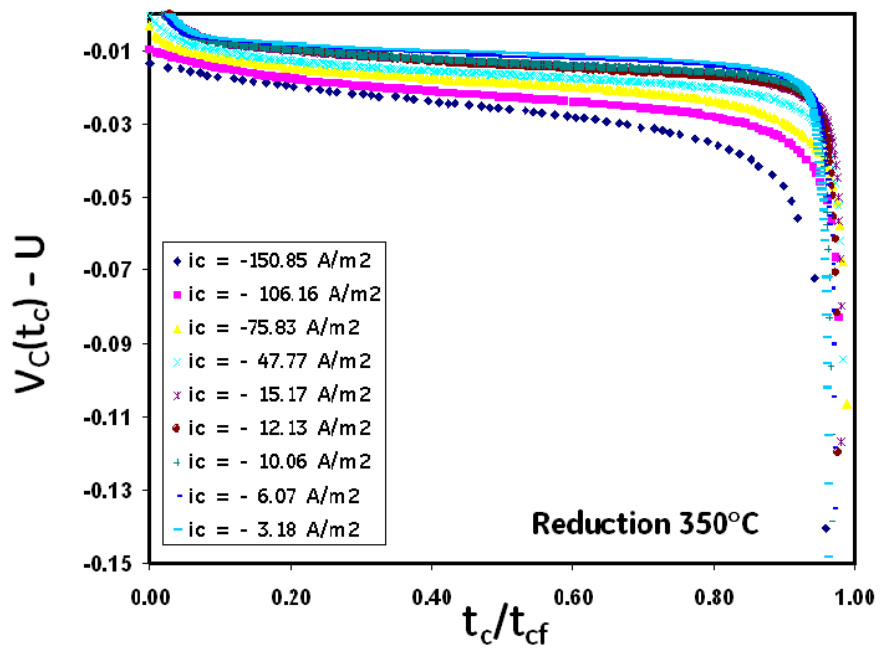


Figure 6.8. Chronopotentiographs for reduction at T=350°C

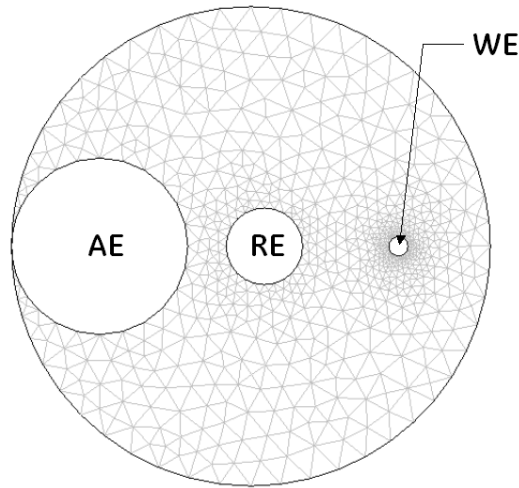


Figure 6.9. FEM Model of Cell

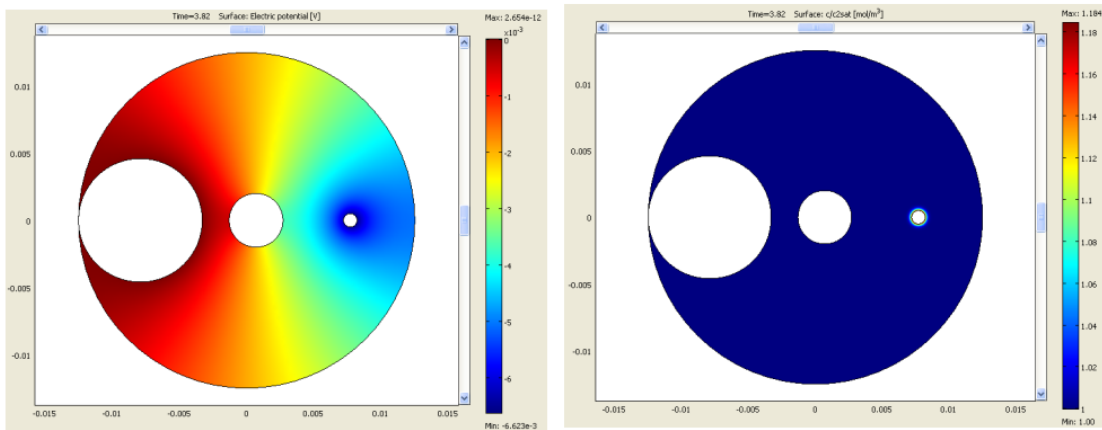


Figure 6.10. FEM Analysis for $I = -0.009$ A and $t_{cf} = 3.82$ s. Left panel is electrolyte potential. Right panel is chloride ion concentration normalized by equilibrium concentration.

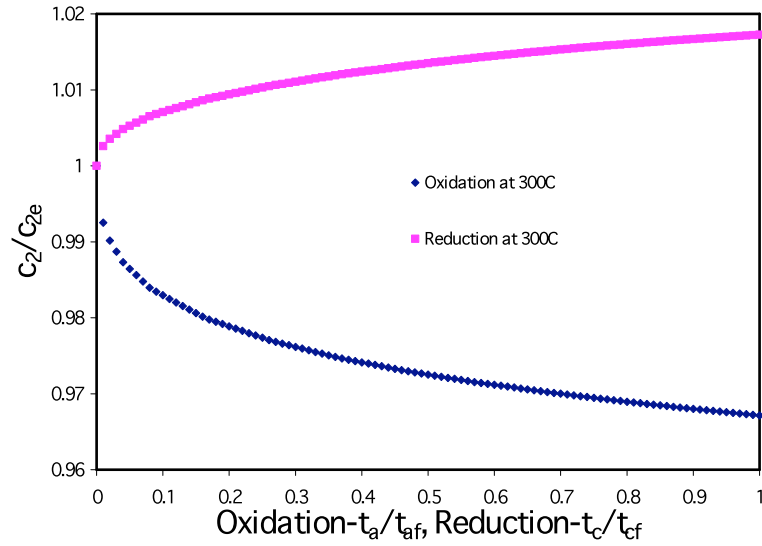


Figure 6.11. Chloride ion concentration predictions at $T=300^\circ\text{C}$ versus reduced time at current densities 3.35 (oxidation) and -3.35 (reduction) A/m^2 . Terminal oxidation and reduction times were 1708.3 and 163.6 s, respectively.

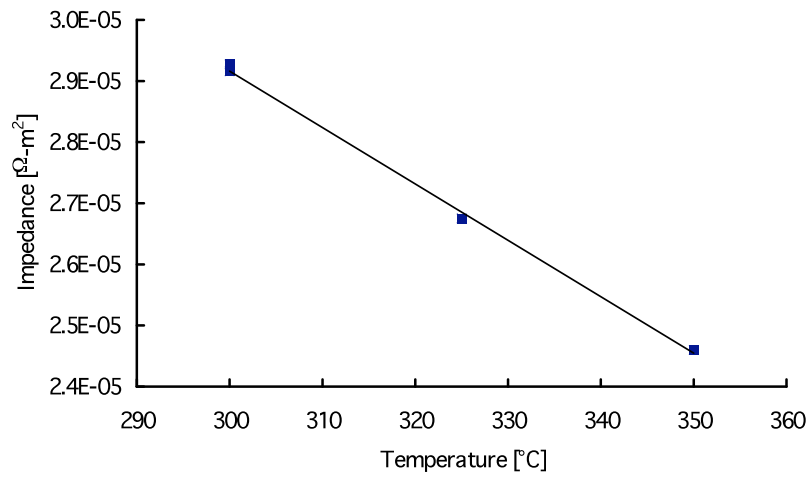


Figure 6.12. Effective resistance in equation 5.8.

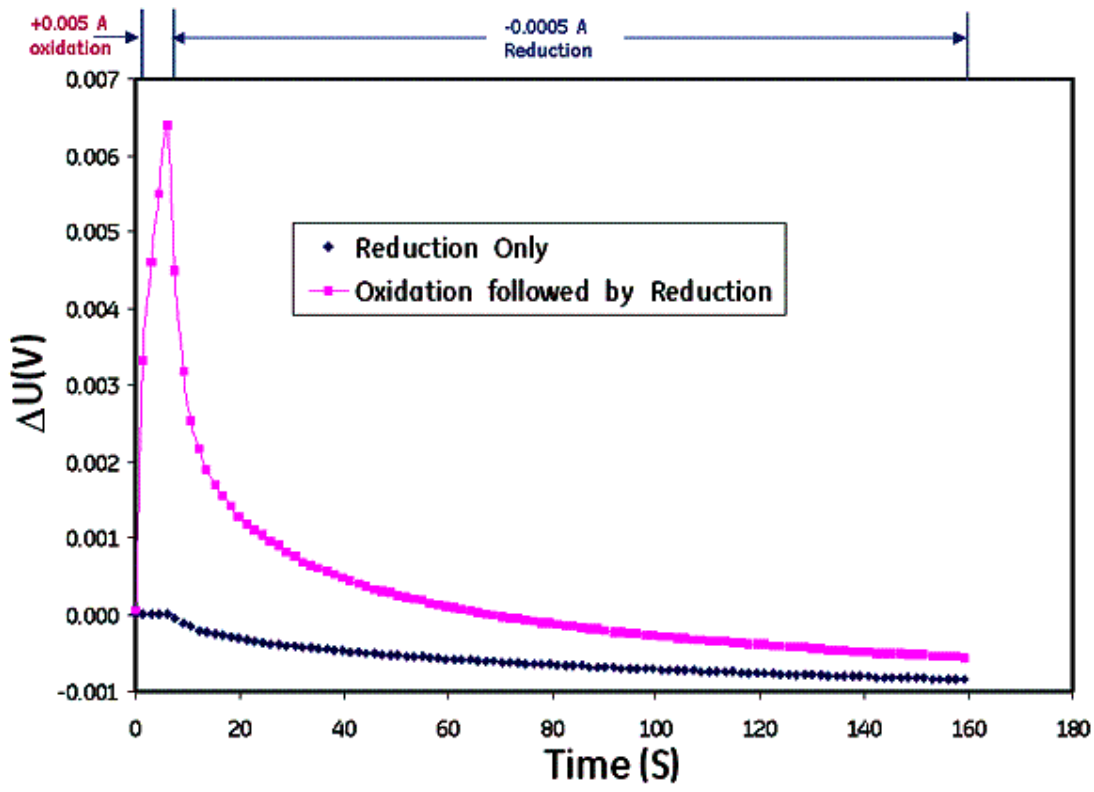


Figure 6.13. ΔU corresponding to a typical discharge chronopotentiograph (300°C, -0.0005 A).

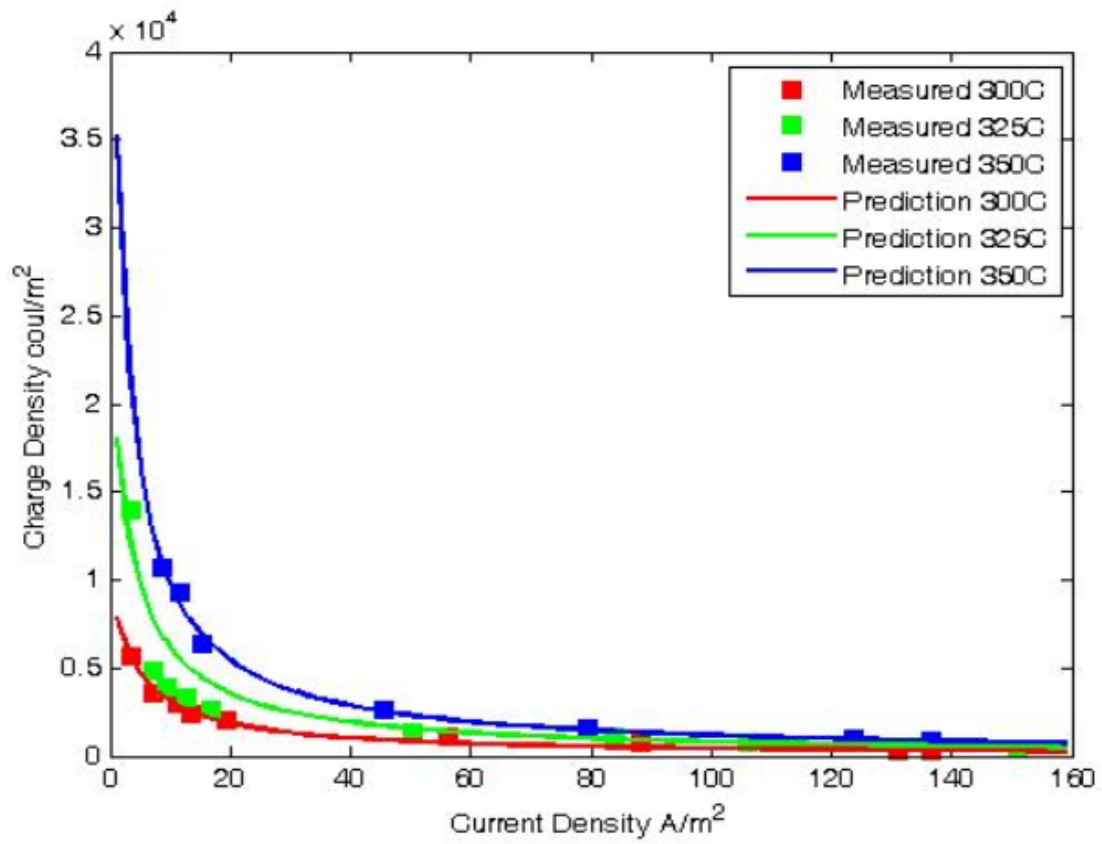


Figure 6.14. Maximum charge density versus nominal current density and temperature. The measurements correspond to the data in figures 6.3 and 6.5.

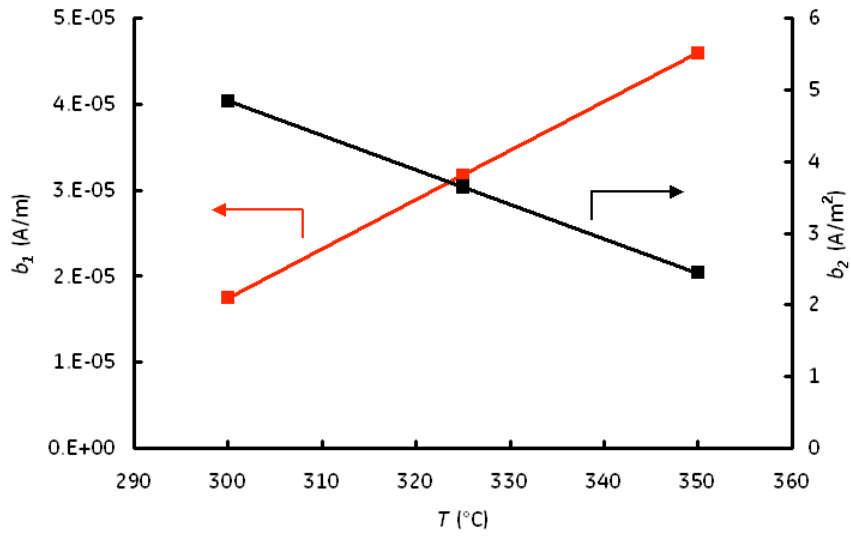


Figure 6.15. Parameters for equation 5.10.

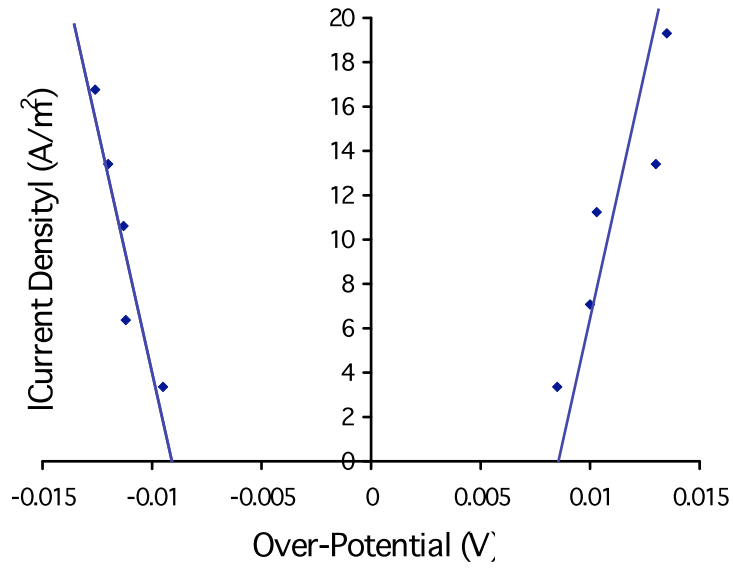


Figure 6.16. Linear relationship between i_a ($|i_c|$) and η .

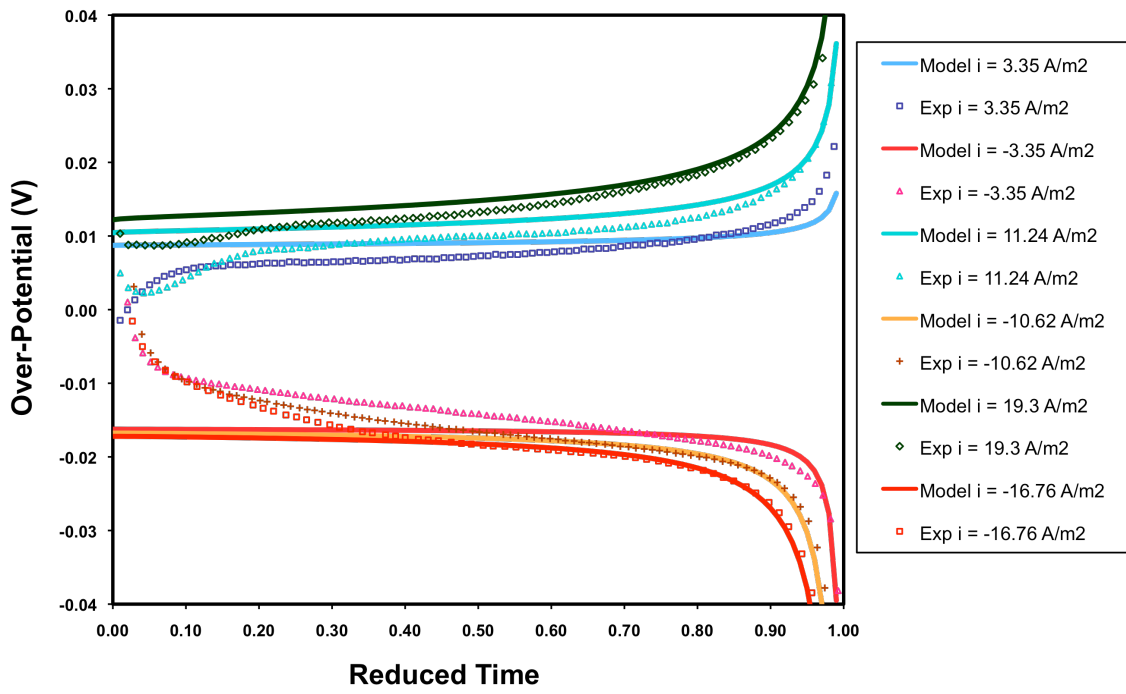


Figure 6.17. Comparison of predicted η to measurement at T=300°C.

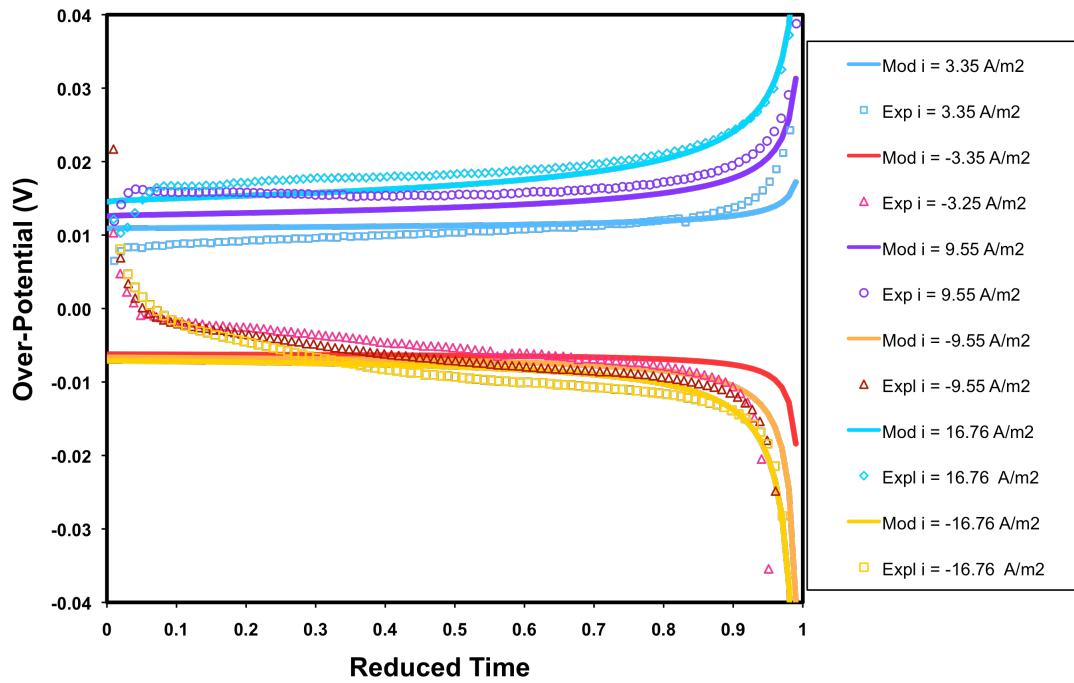


Figure 6.18. Comparison of predicted η to measurement at $T=325^{\circ}\text{C}$.

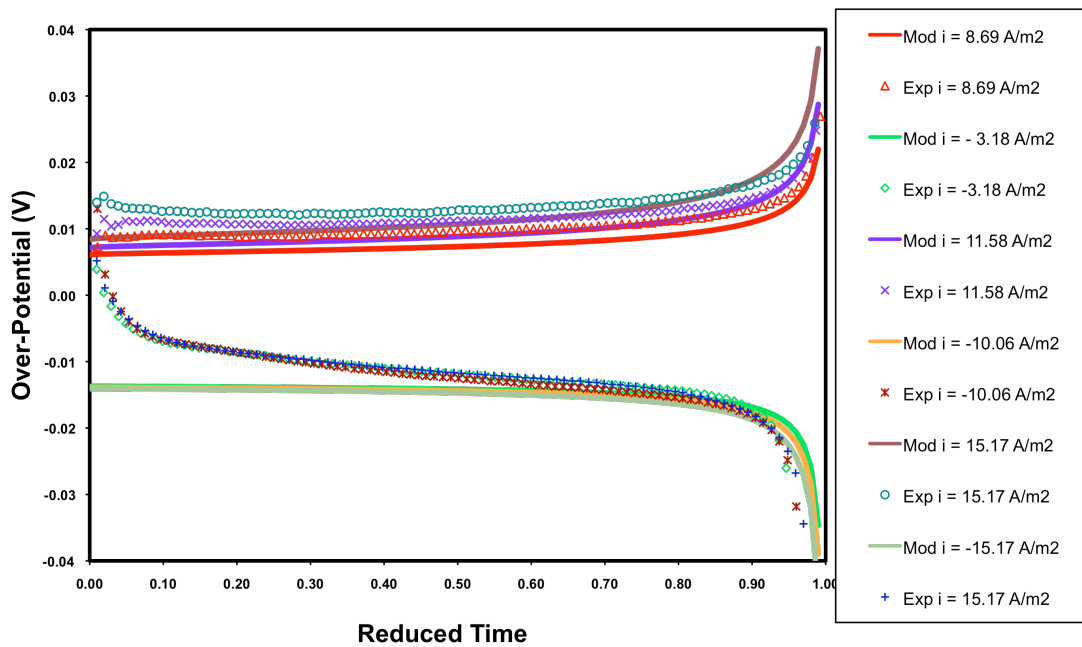


Figure 6.19. Comparison of predicted η to measurement at $T=350^{\circ}\text{C}$.

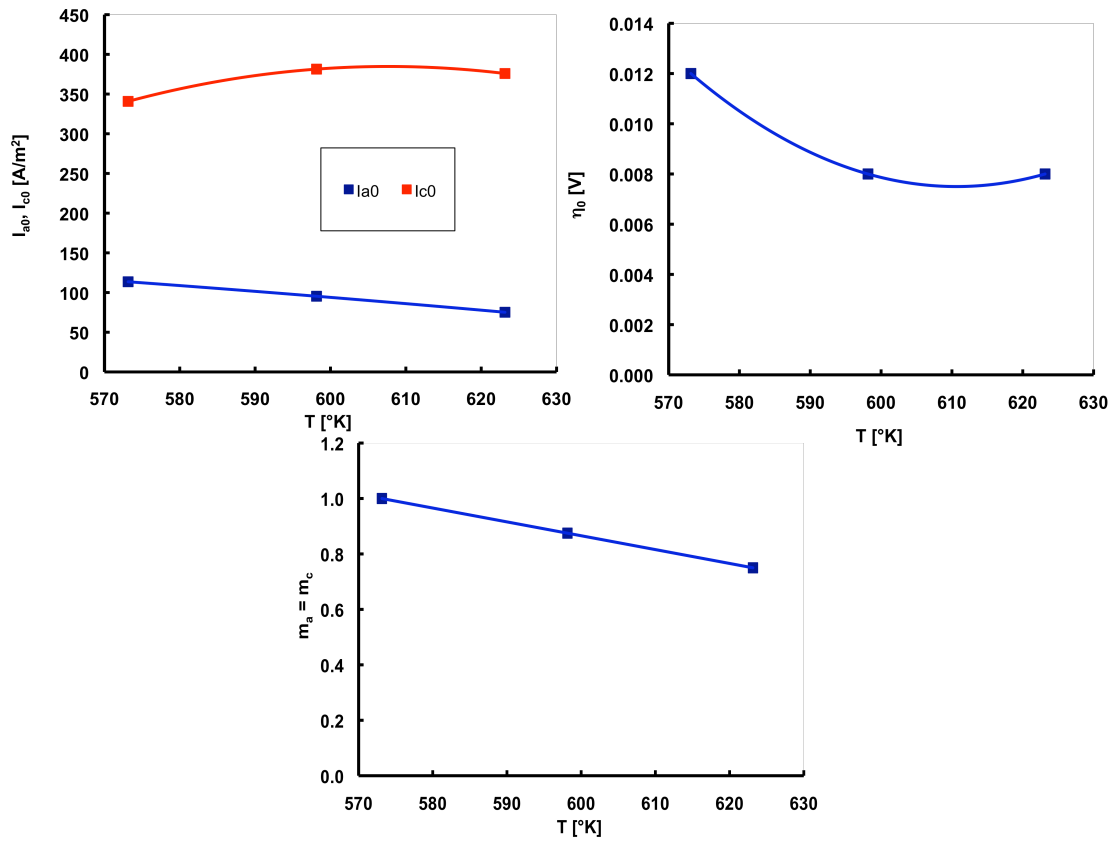


Figure 6.20. Model parameters as functions of temperature.

Chapter 7

Extraction of effective oxide thickness for SOI FINFETs with high- κ /metal gates using the body effect

7.1 Introduction

Planar transistors have been the core of integrated circuits for several decades, during which the size of the individual transistors has steadily decreased. Since the fabrication of MOSFET, the minimum channel length has been shrinking continuously. The motivation behind this decrease has been an increasing interest in high speed devices and in very large scale integrated circuits. As the dimensions of transistors are shrunk, the close proximity between the source and the drain reduces the ability of the gate electrode to control the potential distribution and the flow of current in the channel region. This is the undesirable effect called the “short-channel effects (SCE)”. The sustained scaling of conventional bulk device requires innovations to circumvent the barriers of fundamental physics constraining the

conventional MOSFET device structure.

Alternative device structures based on silicon-on-insulator (SOI) technology have emerged as an effective means of extending MOS scaling beyond bulk limits for mainstream high-performance or low-power applications. Partially depleted (PD) SOI was the first SOI technology introduced for high-performance microprocessor applications. The fully depleted (FD) SOI device structures may be better or worse than the bulk MOSFETs, depending on the silicon film thickness, buried oxide thickness and doping concentration. The SCE can be reduced in FD SOI device by using a thin buried oxide and an underlying ground plane¹. Concurrently, material enhancements, such as the use of a) high-k gate material and b) strained Si channel for mobility and current drive improvement, have been actively pursued². In Figure 7.1 we have showed the different type of MOSFETs both planar and multi-gate (FIN) MOSFETs.

A much more efficient device configuration is obtained by using the double-gate transistor structure. In a multi-gate device, the channel is surrounded by several gates on multiple surfaces, allowing more effective suppression of "off-state" leakage current³. Multiple gates also allow enhanced current in the "on" state, also known as drive current. These advantages translate to lower power consumption and enhanced device performance. Nonplanar devices are also more compact than conventional planar transistors, enabling higher transistor density, which translates

to smaller overall microelectronics. Dozens of multigate transistor variants may be found in the literature¹. The non-planar FinFET device structures promise to be the potential future technology/device choices. The term FinFET was coined by University of California, Berkeley researchers (Profs. Chenming Hu, Tsu-Jae King-Liu and Jeffrey Bokor⁴) to describe a nonplanar, double-gate transistor built on an SOI substrate, based on the earlier DELTA (single-gate) transistor design⁵. The distinguishing characteristic of the FinFET is that the conducting channel is wrapped around a thin silicon "fin", which forms the body of the device. The dimensions of the fin determine the effective channel length of the device.

In current usage the term FinFET has a less precise definition. Among microprocessor manufacturers, AMD, IBM, and Motorola describe their double-gate development efforts as FinFET development whereas Intel avoids using the term to describe their closely related tri-gate architecture. In the technical literature, FinFET is used somewhat generically to describe any fin-based, multigate transistor architecture regardless of number of gates. In Figure 7.2, we have depicted a double gate FinFET as used in this study. In Figure 7.2, the "fin" is connected to source and drain¹.

The effective oxide thickness (T_{inv}) under inversion, is a key parameter of both device electrostatics and transport. It is a measure of the capacitance influence of

gate voltage on charge induced in the device channel, and includes the actual electrostatic dielectric thickness plus the quantum effect in channel where there is a charge centroid. The centroid occurs below the channel dielectric interface because the charge can not be forced directly against the interfacial layer.

In this work, we develop a novel T_{inv} (inversion oxide thickness) extraction methodology for the aforementioned FINFET devices (Figure 7.2). It is worth noting that this methodology leverages current-voltage (IV) sweeps as opposed to more conventional capacitance-voltage (CV) technique for extraction of this important device/technology parameter. It is also instructive to note that T_{inv} is an important parameter when it comes to making a predictive projection of short channel behavior of any MOSFET device geometry. Capacitance measurement on vertical device structure remains a challenge due to the parasitic capacitance and variability. New methodology is needed for electrical parameter calculation/extraction based on capacitance measurement.

The measurement of inversion oxide thickness (T_{inv}) using the conventional CV technique is a challenge for ultra thin body SOI FINFETs. Design of FinFET devices for advanced CMOS technology nodes necessitates that individual fins be very thin for good short channel control. FinFET devices have very small capacitance which

makes a capacitance measurement of T_{inv} difficult. In this work, we leverage a technique published by Frei et.al.⁶ to extract T_{inv} values from DC current voltage measurements making use of the body effect in SOI FINFETs. This obviates the need for special capacitance structures for T_{inv} estimation, and being fast (as opposed to using very long integration times to extract very small capacitance values) may be integrated relatively easily in an automated inline test environment. Also, this enables direct estimation of T_{inv} on actual transistors, a requirement more critical in high-K/metal gate stacks where T_{inv} may vary between different device structures/geometries.

7.2 Theory and experiment

FDSOI (fully depleted SOI with undoped body) FINFETs (double gate) with high- κ /metal gates are fabricated using a sidewall image transfer flow⁷ with tight fin pitch (52 nm) on [100] Si substrates, so that the channel transport orientation is [110]. A transmission electron micrograph (TEM) of an individual fin device is shown in the inset of Figure 7.3 (height of the fin, $H_{fin} = 30$ nm, and width of the fin, $D_{fin} = 11$ nm). An equivalent circuit of this structure (taking into account a buried oxide (BOX = 140 nm) recess (r) of 1 nm, $d_s = 4.5$ nm) is depicted in Figure 7.3. Different capacitive

components of this device under back gate bias are described by the following equations⁶:

$$C_{G-CH} = 2C_{OX} = 2 \frac{\epsilon_{OX}}{T_{inv}} \quad (1)$$

$$C_{CH-GND} = \frac{C_{BOX} \times 2C_{fin}}{C_{BOX} + 2C_{fin}} \quad (2)$$

with, $C_{BOX} = \frac{\epsilon_{OX}}{T_{BOX}} \left[\frac{D_{fin} - 2d_s}{D_{fin}} \right]^*$ and $C_{fin} = \frac{C_{Si}}{\pi} \ln \left(\frac{D_{fin}}{r} \right)$, where $C_{Si} = \frac{\epsilon_{Si}}{t_{Si}}$ and $t_{Si} = H_{fin}$

where C_{G-CH} is the gate-to-channel capacitance and C_{CH-GND} is the channel-to-ground capacitance. C_{fin} is extracted considering two plate capacitors perpendicular to each other as shown in Figure 7.3 [6]. C_{fin} and C_{BOX} are related to the body factor as shown in the following equations:

$$n = 1 + \frac{C_{CH-GND}}{C_{G-CH}} \quad (3)$$

$$1 - n = \frac{dV_t}{dV_{BB}} \quad (4)$$

It is instructive to note that Equations (1)-(4) illustrate that T_{inv} is directly proportional to the slope $\left(\frac{dV_t}{dV_{BB}} \right)$ of the threshold voltage with respect to back-gate bias plot. In

Figure 7.4, we have shown an example of source current and gate voltage sweeps for different back gate bias. For pFET we consider the forward bias regime as $V_{BB}=0$ to -10 V and for nFET the forward bias regime is $V_{BB}=0$ to +10 V. Figure 7.5 clearly

illustrates the linear evolution of threshold voltage as a function of back-gate bias. We consider 3 splits for pFET and 3 splits for nFET. The slope of the respective nFET and pFET curve is used to estimate the value of T_{inv} [Equation (4)]. Physically, the slope represents the sensitivity of the threshold voltage (V_t) to the back-gate bias voltage⁸. Adequate care was taken to ensure that the back-bias sweep did not stress the devices, causing additional threshold voltage shift. Hysteresis of current voltage sweeps was monitored to confirm that the back-bias sweeps did not induce gate dielectric charging. The current voltage sweeps were restricted to the sub-threshold regime to prevent the risk of gate charging from high gate biases in the high- κ /metal gate stacks.

To independently bench mark the accuracy of the back-bias IV technique, CV measurements were performed on the same devices to extract the values of T_{inv} (Figure 7.6)^{9,10}. Sufficiently long channel FinFETs (LGate = 230 nm with 52 fins) were used for this study to ensure that depletion capacitances (C_d in the equivalent circuit diagram in Figure 7.3) did not interfere with the capacitive response. Measurements were made on multiple pFET and nFET devices having different T_{inv} . Figure 7.6 depicts two representative CV curves for an nFET and pFET device. Due to the very small capacitances of these devices (capacitance values on the order of 50 fF), long integration times (frequency = 100 kHz) with multiple averaging were used. The T_{inv} values were extracted @ $V_g = 0.9$ V. Figure 7.7 provides a

comparison of the T_{inv} values extracted by the two methods. There is an apparent difference between the T_{inv} s extracted from these two techniques. Generally speaking, the T_{inv} values extracted from back-bias IV technique are higher than those extracted using CVs (Figure 7.7 shows the values of extracted T_{inv} s from the two different techniques). It is easy to conjecture that this difference primarily comes from the different extraction regions of the gate voltage window used in the measurements namely: the T_{inv} extracted from the back-bias IV technique is from the sub-threshold region of operation (where body factor is usually defined), whereas the T_{inv} determined from the CV measurement is in the strong inversion region.

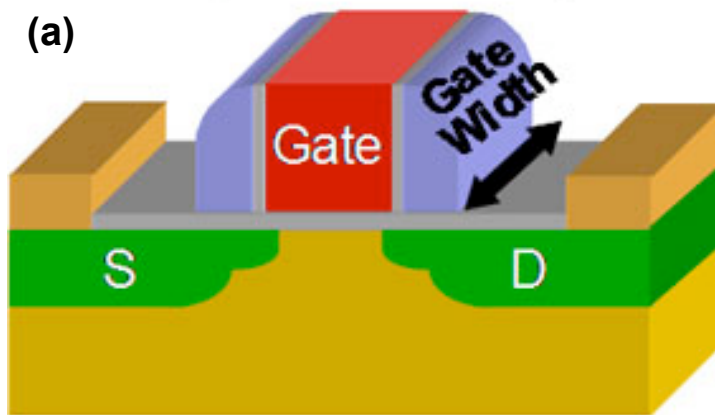
Extensive device simulations were carried out using well calibrated device simulator Fielday with MLDA quantum mechanical correction to confirm this explanation of the difference. As illustrated in Figure 7.8, the location of the charge centroid from the gate oxide/Si interface is a strong function of gate bias. X_{dc} and X_{ac} are locations of the charge centroid representative of IV and CV techniques respectively. Figure 7.8 also illustrates the relative difference in charge centroid values estimated by the two different techniques at different bias ranges^{11,12}, thereby confirming our hypothesis on the difference observed in estimated T_{inv} values obtained from back-bias IV (DC, @ $V_g \sim V_t$) and CV (AC, $V_g \sim 0.9$ V) technique.

7.3 Discussion

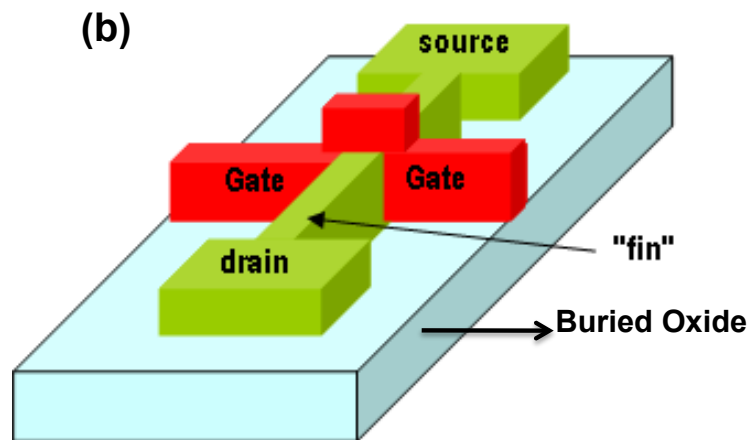
A simple methodology for T_{inv} extraction, based on the capacitive coupling effects between the channels of an SOI FINFETs, its gate, and a substrate bias is evaluated. The sensitivity of the technique to change in T_{inv} for both n and pFETs is illustrated. Device simulations were performed to understand the differences in extracted T_{inv} values by the back-bias IV and the conventional CV technique.

At $V_g \sim V_t$, the fin is in volume inversion and the equations (2) and (3) are not valid. This is the fundamental reason why the proposed T_{inv} extraction method is not accurate, particularly for p-channel MOSFETs whose inversion-charge centroid is located further away from the gate-dielectric interface (as compared to n-channel MOSFETs). Our simulations in Figure 7.8, point in this direction. Hence, we propose this technique to be used as a quick T_{inv} screening methodology in automated in-line test. This method has the ability to provide comparative estimate of T_{inv} from split to split on the actual transistors (even for short channel ones). This is particularly useful for high-K/metal gate SOI FINFET's where T_{inv} may vary between the transistors and the capacitor structures. On top of that, being an IV based methodology, this is quicker. Because of the difference in the relative location of the charge centroids, the accuracy of this method may be in question. This is why, this method needs

thorough calibration: a comparison between experimental data and simulations across different experimental splits show that the difference between the T_{inv} extracted by the BB IV and CV technique may be quantified.

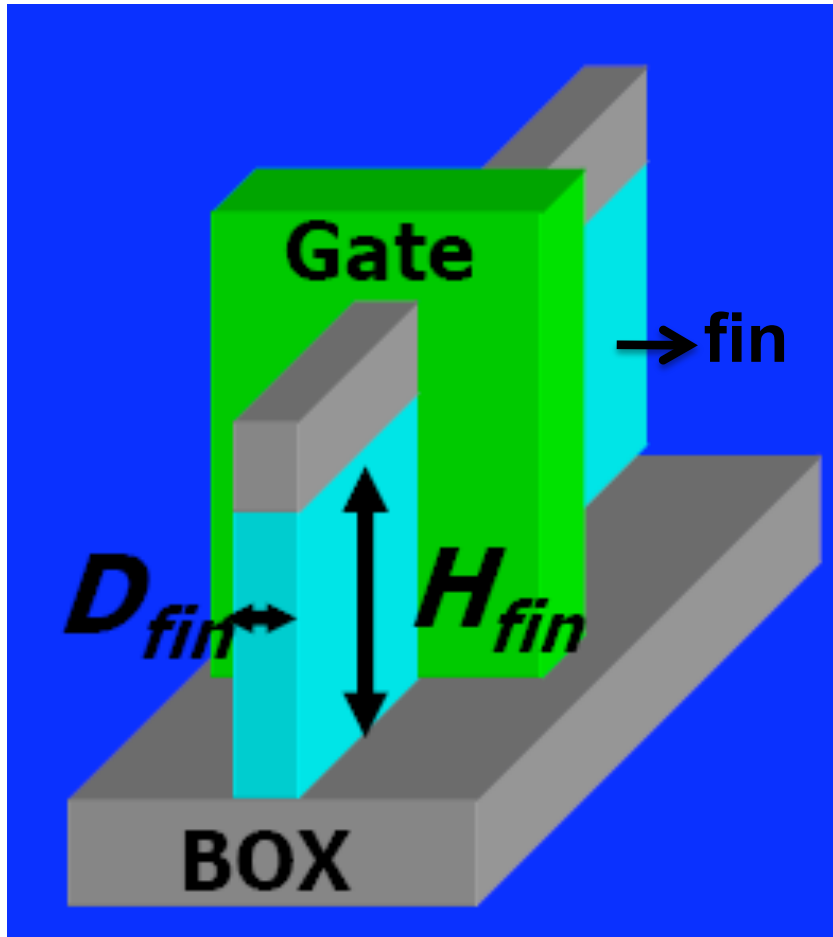


Source: <http://www.freescale.com/webapp/sps/site/overview.jsp?nodeId=0ST287482180CAE>



Source: http://commons.wikimedia.org/wiki/File:Doublegate_FinFET.PNG

Figure 7.1. (a) A bulk planar MOSFET (b) Double gate SOI (silicon on insulator) MOSFET.



Source: H. Kawasaki, Toshiba IEDM 2009

Figure 7.2. Cross section of FINFET. The fin is connected to source and drain.

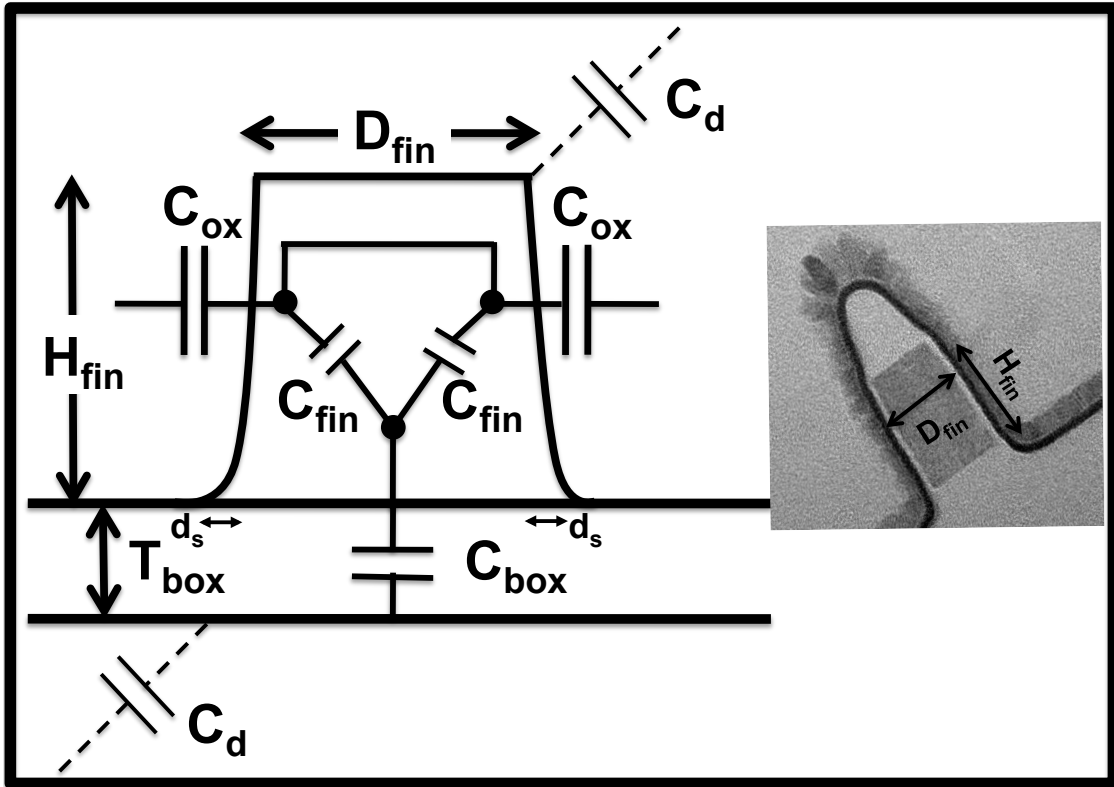


Figure 7.3. Equivalent circuit model and TEM cross-section of fin.

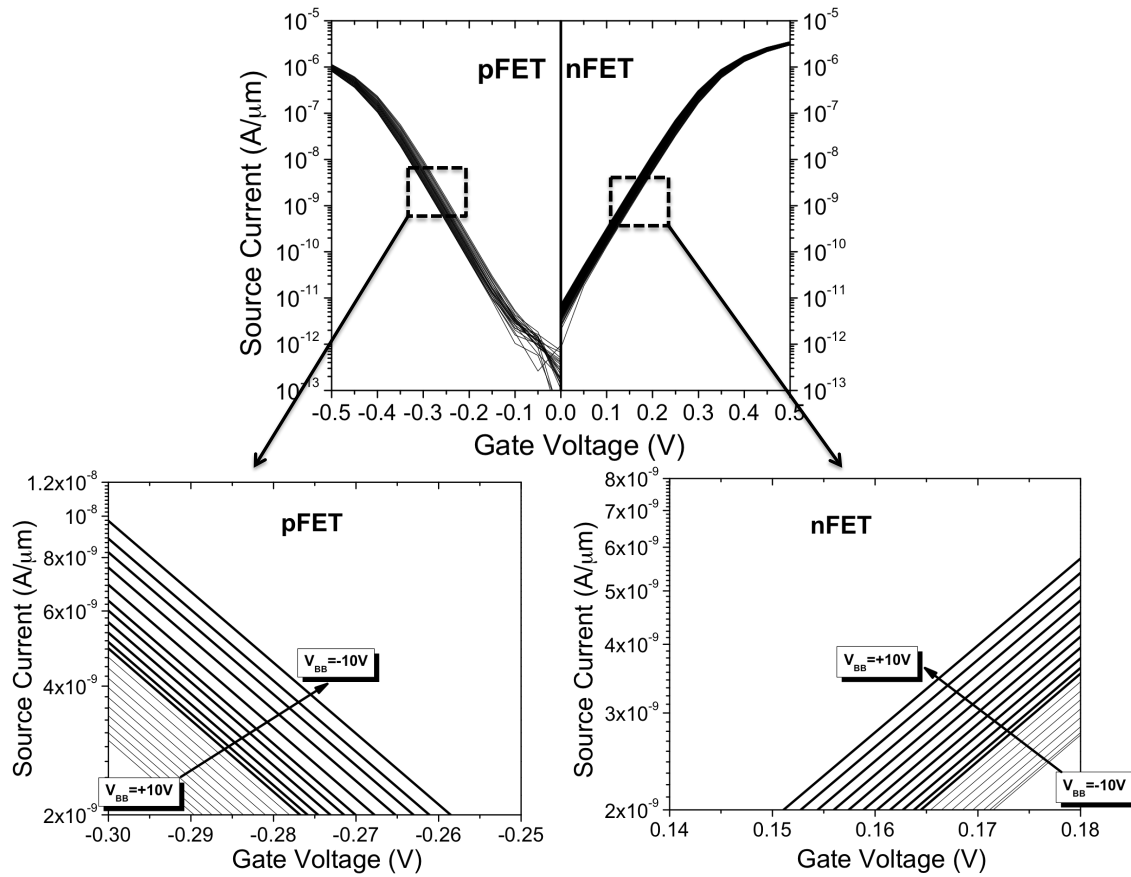


Figure 7.4. Upper panel: I_s - V_g sweeps for different back biases both for n and pFET, Lower panel: The close look of I_s - V_g to show the effect of V_{BB} . Also, the IV's have been color coded to emphasize the “forward bias” regime.

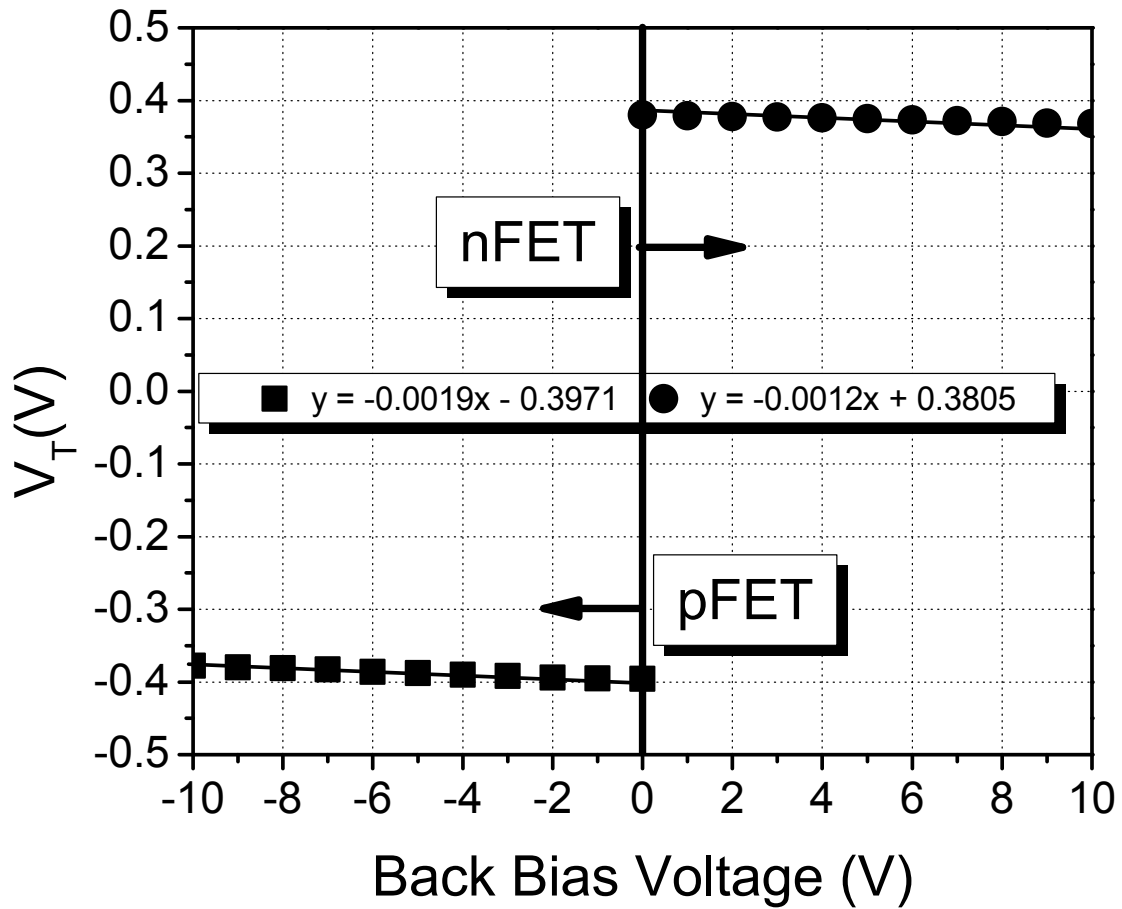


Figure 7.5. Evolution of threshold voltages as a function of back gate voltage. The closed symbol (square: pFET, circle: nFET) represents V_T vs back bias voltage calculated from Figure 7.4. Both pFET and nFET “forward bias” curves, with the different straight line fits used to extract the slopes for estimating T_{inv} 's.

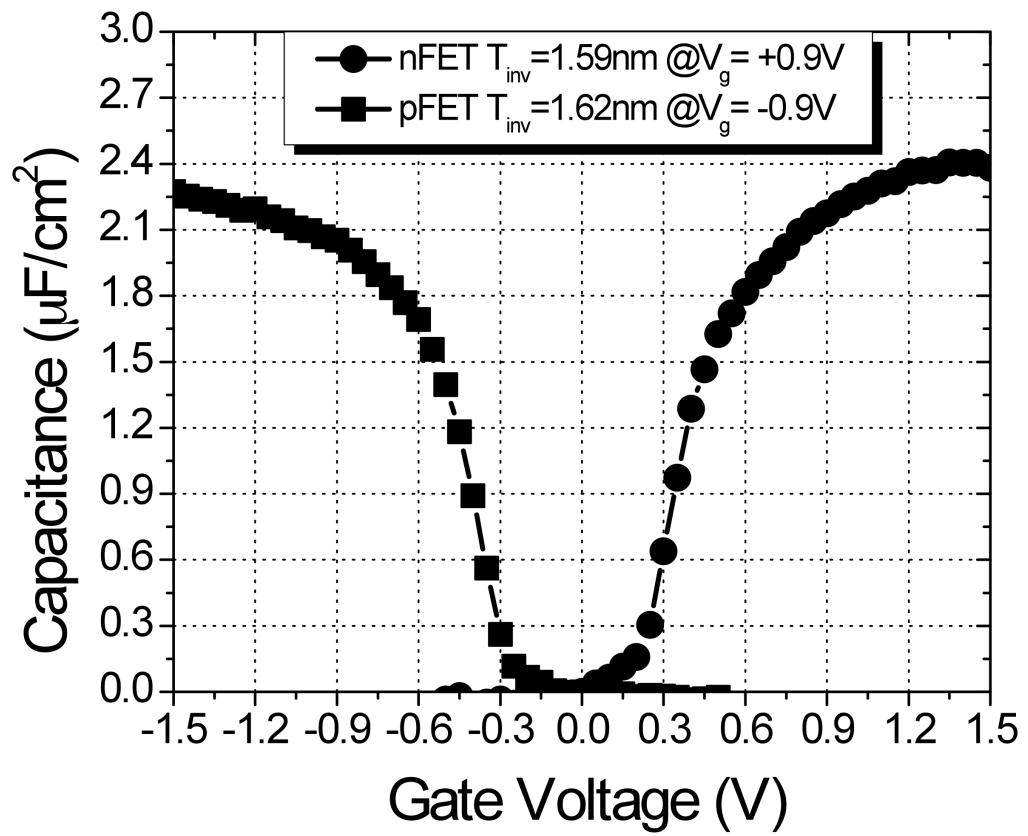


Figure 7.6. Representative CV sweeps for nFET and pFET.

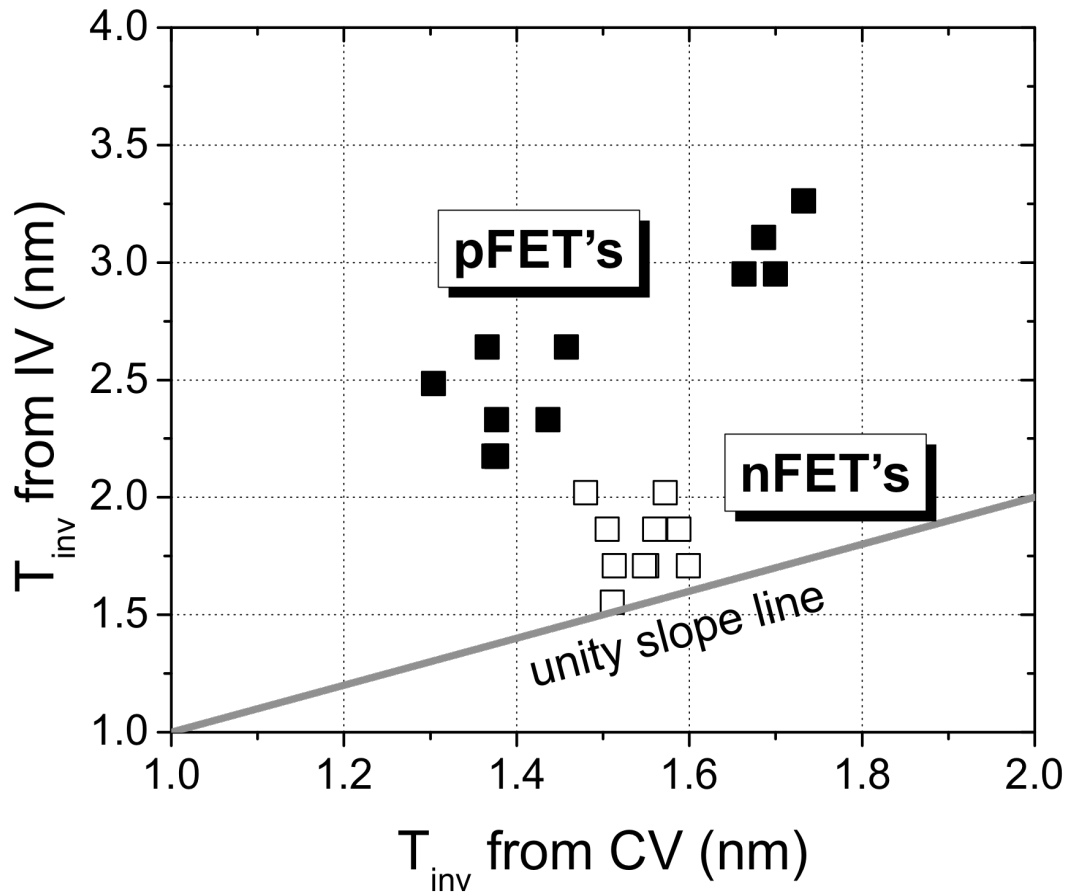


Figure 7.7. Comparison of T_{inv} s determined from back bias and CV sweeps from n and pFETs. A unity slope line illustrating the ideal case i.e $T_{INV}(IV) = T_{INV}(CV)$ is also shown.

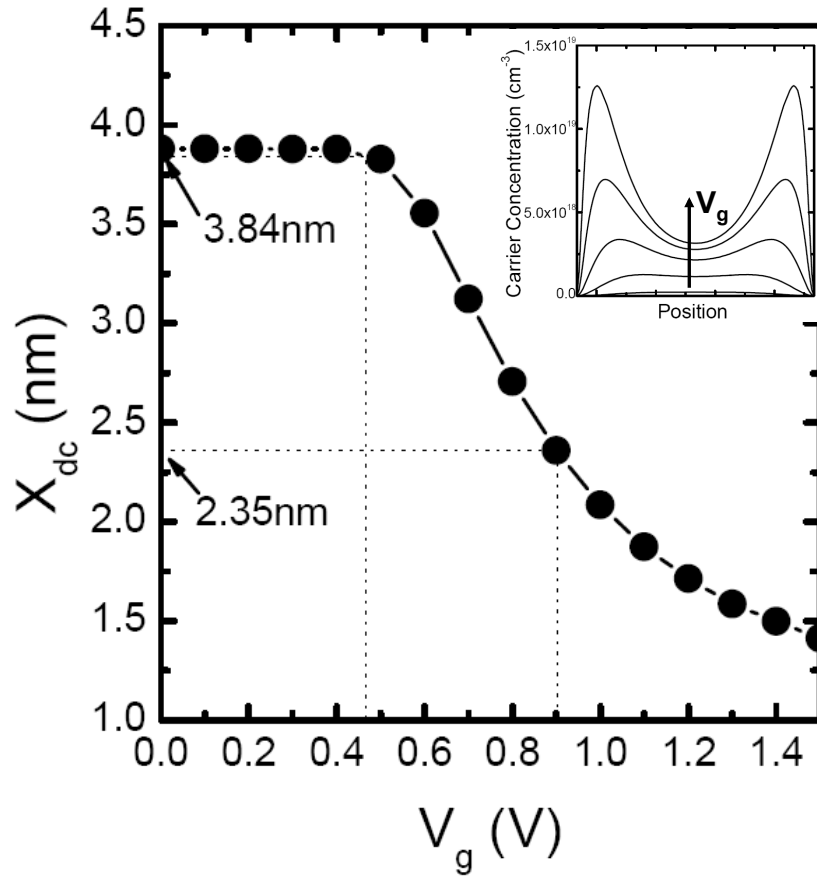


Figure 7.8. Simulation study illustrating the evolution of the location of the charge centroid relative to the gate oxide/Si interface as a function of gate voltage for DC- and AC-type measurements (representative cuts are taken @ $V_g = 0.5$ & 0.9 V to illustrate the difference between the value of charge centroid for low and high gate voltages respectively under DC and AC measurement condition).

References

- ¹ J. P. Colinge, FinFETs and Other Multi-Gate Transistors, Springer, 2007
- ² K. Maitra, "Electron Transport in Bulk-Si nMOSFETs in presence of high-K gate insulator-Charge Trapping and Mobility", Doctoral Dissertation, Department of ECE, North Carolina state university, Raleigh, NC, December 2005 (and references therein)
- ³ J. P. Colinge, Solid State Electronics, Vol. 48, Page 897-905, (2004)
- ⁴ Huang, X. et al., "Sub 50-nm FinFET: PMOS" International Electron Devices Meeting Technical Digest, p. 67. December 5–8, (1999)
- ⁵ Hisamoto, D. et al., "Impact of the vertical SOI 'Delta' Structure on Planar Device Technology" IEEE Trans. Electron. Dev. 41 p. 745 (1991)
- ⁶ J. Frei, C. Johns, A. Vazquez, W. Xiong, C.R. Cleavelin, T. Schulz, N. Chaudhury, G. Gebara, J.R. Zaman, M. Gostkowski, K. Matthews, and J.P. Colinge, "Body Effect in Tri and Pi Gate SOI MOSFETs", IEEE Electron Device Lett., vol. 25, no. 12, pp. 813-815, December 2004. (*We interpret there to be a typographical error in the reference, viz. $C_{OX2} = \left(\frac{\epsilon_{OX}}{t_{OX2}}\right)\left(\frac{W - 2d_s}{W}\right)$ rather than $C_{OX2} = \left(\frac{\epsilon_{OX}}{t_{OX2}}\right)\left(W - \frac{2d_s}{W}\right)$)
- ⁷ H. Shang, L. Chang, X. Wang, M. Rooks, Y. Zhang, B. To, K. Babich, G. Totir, Y. Sun, E. Kiewra, M. Leong and W. Haensch, "Investigation of FinFET devices for 32 nm technologies and beyond", 2006 Symposium on VLSI Technology Digest of Technical Papers

⁸ W. Xiong, C.R. Cleavelin, R. Wise, S. Yu, M. Pas, R.J. Zaman, M. Gostkowaski, K. Matthews, C. Maleville, P. Patruno, T.J. King and J.P. Colinge, “Full/Partial depletion effects in FinFETs”, *Electronics Lett.*, vol. 41, pp., no. 8, April 2005.

⁹ A. Hartstein and N.F. Albert, “Determination of the inversion-layer thickness from capacitance measurements of metal-oxide-semiconductor field-effect transistors with ultrathin oxide layers”, *Physical Review B*, vol. 38, no. 2, pp. 1235-1240, July 1988.

¹⁰ Z. Cheng and C.H. Ling, “Gate-Channel Capacitance Characteristics in the Fully-Depleted SOI MOSFET”, *IEEE Transaction on Electron Devices*, vol. 48, no.2, pp. 388-391, February 2001.

¹¹ Y.C. King, H. Fujiokaf, S. Kamohara, W.C. Lee, and C. Hu, “AC Charge Centroid Model for Quantization of Inversion Layer in n-MOSFET”, *IEEE VLSI TSA*, pp. 245-249, 1997.

¹² K. Yang, Y.C. King, and C. Hu, “Quantum Effect in Oxide thickness Determination From Capacitance Measurements”, *Symposium on VLSI | Technology Digest of Technical Papers*, pp. 77-78, 1999.

Chapter 8

Summary

There are two parts in this dissertation. The layout of the thesis is presented in Figure 8.1. In Part I, we have addressed three different systems and its application; the carbon footprint through CO/CO₂ sequestration/activation and electronic structure of mono and bi-layer graphene. We actively worked on a broad range of problems in first principles simulations of catalysis and chemical reactions, characterization of carbon nanostructures, and surface and interface physics. In our first research project, we have studied the carbon-mediated partial sequestration and selective oxidation of carbon monoxide (CO), both in the presence and absence of hydrogen, on graphitic edges. We have elucidated the atomic scale mechanisms of activation and reduction of carbon dioxide (CO₂) on specifically designed catalytic surfaces via the rational manipulation of the surface properties that can be achieved by combining transition metal thin films on oxide substrates. We have worked in the characterization of the lattice thermal conductivity of ideal mono and bi-layer graphene, demonstrating that their behavior is similar to that observed in graphite,

indicating that the intra-layer coupling does not affect significantly the thermal conductance.

In Part II, I have added the work from summer internships and industrial research opportunities. In the summer of 2009, I worked with IBM Semiconductor Research Development Corporation (SRDC) at Albany Nanotech, Albany, NY. I worked on offline test and characterization of state-of-the-art FINFET devices with high-K/metal gates for 15 nm technology nodes and beyond. Established a novel characterization methodology for estimating electrical oxide thicknesses for these devices, benchmarked it with more conventional techniques for feasibility of being introduced in an automated inline test. I worked with Polymer and Chemical Technologies Division, General Electric Global Research Center, Niskayuna, NY. I worked on the model development and verification of high temperature rechargeable batteries for hybrid-drive systems in transportation applications. This involved intensive experimental activity using advanced electrochemical techniques, analytical engineering transport model of the electrochemical cell, and high performance first principles simulations. In summer 2007 I worked with Physical Sciences Divisions, IBM T. J. Watson Research Center, Yorktown Heights, NY. I worked on modeling of novel phase change materials for application in phase change memories (PCM) for “end-of-roadmap” memory and storage technologies. This project involved high-end numerical computation in IBM’s internal “Blue-Gene” cluster and Oak Ridge National Laboratories’ (ORNL) supercomputing resources.

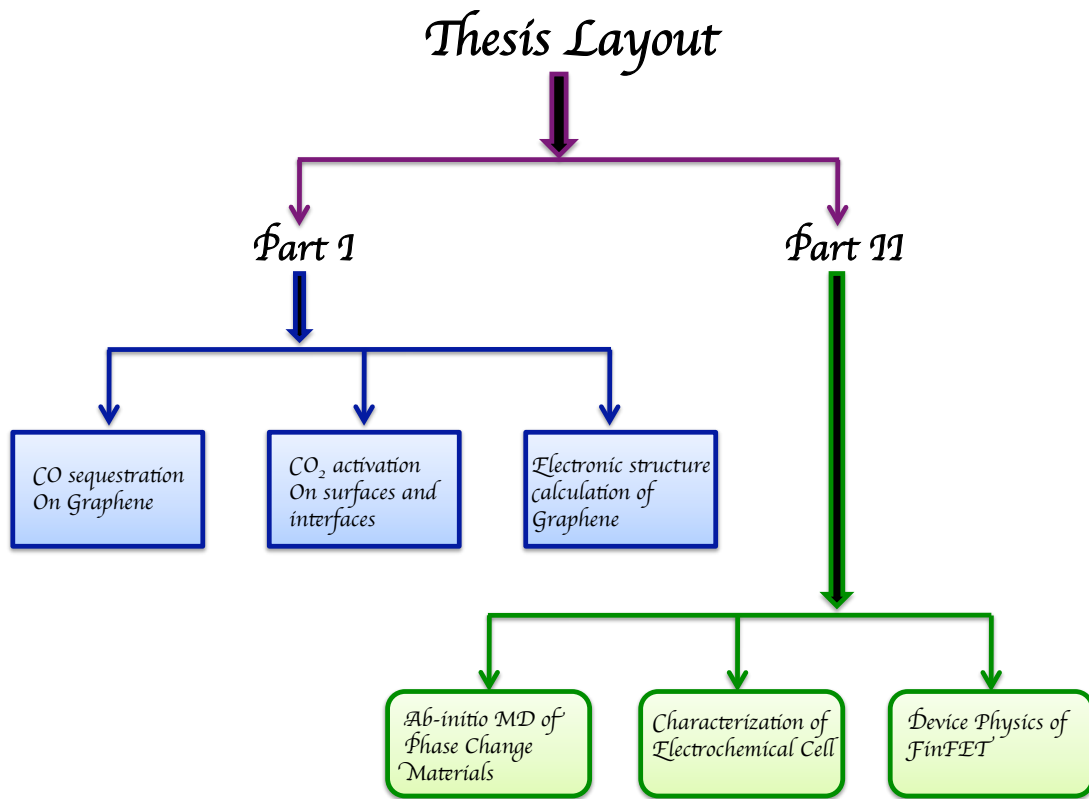


Figure 8.1 Thesis Layout